Towards overall adaptive modeling based on solid-shell and solid-beam approaches for the static and dynamic finite element analysis of structures

Guoqiang Wei

Par **Guoqiang WEI**

Towards overall adaptive modeling based on solid-shell and solid-beam approaches for the static and dynamic finite element analysis of structures

Thèse présentée
pour l'obtention du grade
de Docteur de l'UTC

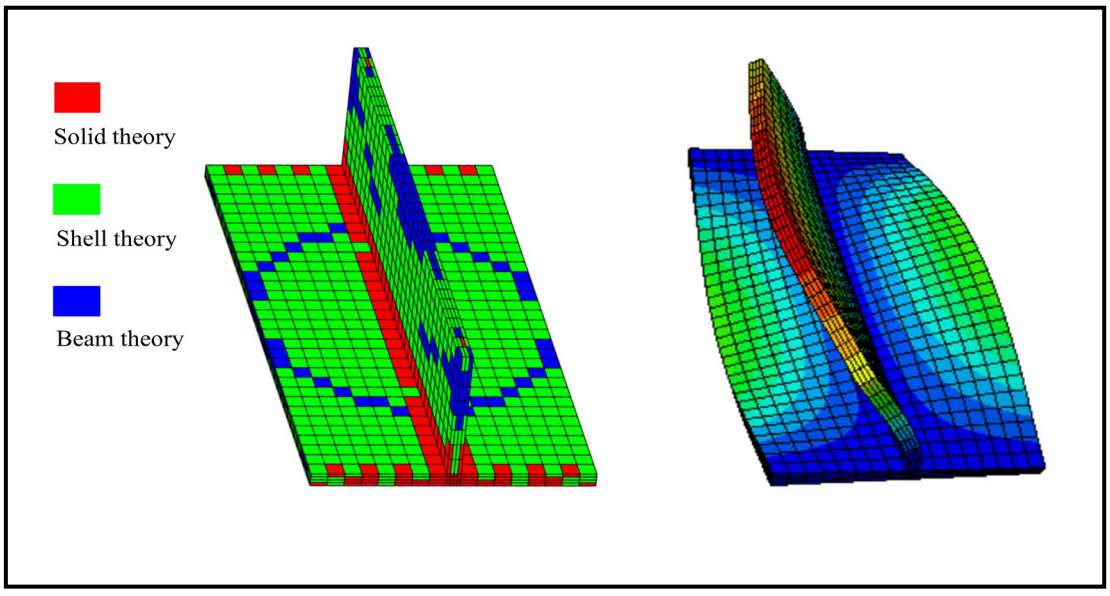

Soutenue le 17 juin 2021
Spécialité : Mécanique Numérique : Unité de recherche en Mécanique - Laboratoire Roberval (FRE UTC - CNRS 2012)
D2618

Towards overall adaptive modeling based on solid-shell and solid-beam approaches for the static and dynamic finite element analysis of structures

Spécialité : Mécanique Numérique

Par Guoqiang Wei

Soutenue le 17 Juin 2021 devant le jury composé de :

M.	J. L. BATOZ
M.	S. BOUABDALLAH
Mme	D. BRANCHERIE
M.	C. NOIRET
M.	M. OUDJENE (Rapporteur)
M.	O. POLIT (Rapporteur)
M.	F. DRUESNE (Directeur de thèse)
M.	P. LARDEUR (Directeur de thèse)

Abstract

The finite element method has been widely used since the 1970s to predict the behavior of structures such as automobiles, airplanes, machines, bridges or buildings. The modeling choices are essential to build a representative model and control the number of degrees of freedom. Many works have sought to optimize the model from a mesh point of view, namely by proposing adaptive meshing techniques. On the other hand, concerning the theory choice, seldom work has been carried out to obtain an optimal finite element model.

In the context of static and vibratory linear analysis, this thesis aims to propose an adaptive modeling methodology in order to obtain an optimal finite element model from the theory choice point of view. The mesh, composed only of solid elements, is refined at each iteration of the methodology. An appropriate choice between beam, shell and 3D elasticity theories is made on each finite element of the model at each analysis. In areas where beam or shell theories are relevant, specific displacement fields are applied. New solid-shell and solid-beam approaches, based respectively on shell theory and beam theory, have been developed for this purpose. For each of these two approaches, first-order and higher-order theories are proposed. In these areas, the application of kinematic relations at nodes of the solid mesh, by using linear equations, leads to a reduction of the number of degrees of freedom. In the context of static and vibratory analysis, several examples are treated to evaluate the methodology of adaptive modeling. The numerical results obtained are always very close to those of a reference solid model and the adaptive modeling method leads to a significant reduction in the model size.

Key words: Adaptive modeling, Solid finite element, Solid-beam element, Solid-shell element, Beam theory, Plate or shell theory, Displacement fields

Résumé

La méthode des éléments finis est couramment utilisée depuis les années 1970 pour prédire le comportement de structures telles que des automobiles, des avions, des machines, des ponts ou des bâtiments. Les choix de modélisation sont essentiels afin de construire un modèle représentatif, tout en maîtrisant le nombre de degrés de liberté. De nombreux travaux ont cherché à optimiser le modèle d'un point de vue du maillage en proposant notamment des techniques de maillage adaptatif. En revanche, concernant le choix de théorie, peu de travaux ont été menés pour obtenir un modèle éléments finis optimal.

Dans le contexte de l'analyse linéaire statique et vibratoire, cette thèse a pour objectif de proposer une méthodologie de modélisation adaptative afin d'obtenir un modèle éléments finis optimal d'un point de vue du choix de théorie. Le maillage, composé uniquement d'éléments volumiques, est raffiné à chaque itération de la méthodologie. Un choix approprié entre les théories de poutre, de coque et d'élasticité 3D est effectué sur chaque élément fini à l'issue de chaque analyse. Dans les zones où les théories de poutre ou de coque sont pertinentes, des champs de déplacements spécifiques sont appliqués. De nouvelles approches volume-coque et volume-poutre, basées respectivement sur la théorie des coques et la théorie des poutres, sont développées à cet effet. Pour chacune de ces approches, des théories de premier ordre et d'ordre supérieur sont proposées. Dans ces zones l'application de relations cinématiques aux nœuds du maillage volumique, se traduisant par des équations linéaires, mène à une réduction du nombre de degrés de liberté. Dans le cadre de l'analyse statique et vibratoire, plusieurs exemples sont traités pour évaluer la méthodologie de modélisation adaptative. Les résultats numériques obtenus sont toujours très proches de ceux d'un modèle volumique de référence et la modélisation adaptative mène à une réduction significative de la taille du modèle.

Mots clés : Modélisation adaptative, Elément fini volumique, Elément fini volume-poutre, Elément fini volume-coque, Théorie de poutre, Théorie de plaque ou coque, Champs de déplacement

Acknowledgments

This thesis was carried out at the Laboratoire Roberval, University of Technology of Compiègne (UTC) under the financial support of the China Scholarship Council (CSC). These organizations are greatly appreciated.

First and foremost, I would like to extend my sincere gratitude to my supervisor Pascal Lardeur, for his tremendous help in guiding my research, for his devotions in correcting my articles and dissertation and for his warm solicitudes in my living. His attitude and passion for the work are impressive and respectable, which deeply inspired me. He organized the meeting to discuss my progress or difficulties every week, which helped me continue my project. Afterward, he always invites us for a cup of hot chocolate that is sweet and comfortable.

Similar cordial gratitude belongs to my supervisor Frédéric Druesne, who also gave useful guidance for my PhD study and supported my academic conference attendance. He always had the patience to modify my dissertation and articles in detail and showed encouragement or criticism at the right time. He is good at hiking and biking and sometimes invites Pascal and me for some forest hikes, helping me recover from a stress-caused depressed mood.

Then, I would like to thank Prof. Olivier Polit and to Prof. Marc Oudjene who accepted to review my thesis report. Great thanks to Prof. Jean-Louis Batoz, Prof. Delphine Brancherie, Dr. Salim Bouabdallah and Dr. Christophe Noiret who took part in the jury of my PhD defense.

I will not forget to thank all my colleagues and friends who have provided me with direct or indirect help and enriched my living in France: Tuan Anh Bui, Hussein Issa, Ernesto III Paruli, Nesrine Ben Hadj Youssef, Jolanthe Verwaerde, Han Guo, Dong Ding, Jishuai Li, Ke Li, Maiqi Xiang, Kaidi Peng, Xingyi Wang, Wenshuai Bai, Dian Wang, Peng Du, Fangtao Yang, Congcong Ma, Rui Zhang, Zhichao Shi, Deyang Zhao, Zhaoyuan Huang, Jianqiang Jin, Xiangjun Kong, Sini Gao, Bo Yang…

I would like to thank my parents with all my heart. Their encouragement and support have been the continuous power for me to keep on studying these years.

I would also like to thank my dear girlfriend Guichuan Li for supporting and accompanying me, making me never fear but move forward in these years. Luckily, we both study in Europe, and 270 kilometers between the Leuven and the Compiègne is never a barrier but a witness to our love.

Finally, great respect belongs to medical staff all over the world. It is their devotion to fighting against the Covid-19 virus that gives us a hopeful tomorrow. Life is not easy but cherished; I wish no more war in the world.

Contents

List of Figures

List of Tables

Chapter 1

General introduction

1.1 Introduction

The complex practical problems in both academic and industrial contexts are usually described by ordinary/partial differential equations (ODEs/PDEs), but it is a challenge to obtain analytical solutions. The numerical simulation technique transforms a physical problem into a discrete mathematical description. Then the algebraic equations derived from ODEs/PDEs are solved by a computer. The Finite Element Method (FEM) is one of the most well established and widespread numerical techniques for multi-physical problems in recent decades. A brief history of FEM is recalled. Some strengths and difficulties are also presented. Finally, some drawbacks of the current finite element modeling process are discussed.

1.1.1 Brief history of FEM

As early as 1870, Rayleigh used assumed "trial functions" to solve complex differential equations. In 1909, Ritz developed it into a numerical approximation method, laying a solid foundation for modern finite element methods. In the 1940s, due to the rapid development of the aviation industry, designers needed to accurately design and calculate the aircrafts structures. Then, they gradually produced matrix mechanics analysis methods in engineering. In 1943, Courant [1] published the first paper using the triangular area's polynomial function to solve the torsion problem. In 1954, Argyris [2] published the first work on energy principles and matrix methods in structural analysis. In 1956, Turner, Clough, Martin, and Topp [3] of Boeing Company systematically studied the element stiffness expressions of discrete trusses, beams, and triangles when analyzing aircraft structures. In 1960, Clough [4, 5] first proposed and used the name "finite element method" when dealing with plane elasticity. In 1967, Zienkiewicz and Cheung [6] published the first monograph on finite element analysis. In 1969, Szabo and Lee [7] pointed out that the weighted residual method, especially the Galerkin method, can be used to derive the standard finite element process from solving non-structural problems. After 1970, the finite element method began to deal with nonlinear and large deformation problems. With the rapid development of computer technology, many software based on the principles of finite element methods have appeared, and they have played an increasingly important role in actual engineering. At present, there are well-known internationally general-purpose finite element analysis software, including ABAQUS, ANSYS, and some specialized finite element analysis software, such as FELAC, DEFORM, etc.

1.1.2 Strengths and difficulties of FEM

As described above, the finite element method (FEM) has attracted a lot of scientists and had a rapid development in recent decades due to its many strengths. From a global viewpoint, the FEM utilizes finite and interrelated elements to simulate complex geometry so that the results can be calculated by modeling and analysis. The FEM succeeds in multiphysics analysis, combining structural analysis and thermal analysis for example. Moreover, the physics fields are accurately approximated by increasing the number of elements or the order of elements. Another strength for the FEM is the ability to combine different types of formulations, namely mixed formulations, which seems difficult in other methods, such as the finite volume method. From the industrial application viewpoint, the FEM provides a simple visualization of results, decreases the design cycle and testing time, and helps to save a lot of costs. For example, it helps engineers with residual stress analysis for predicting failure location. It is not easy to predict without the FEM unless the engineer has years of experience. Fig. 1.1 shows some domains in which the FEM is widely used.

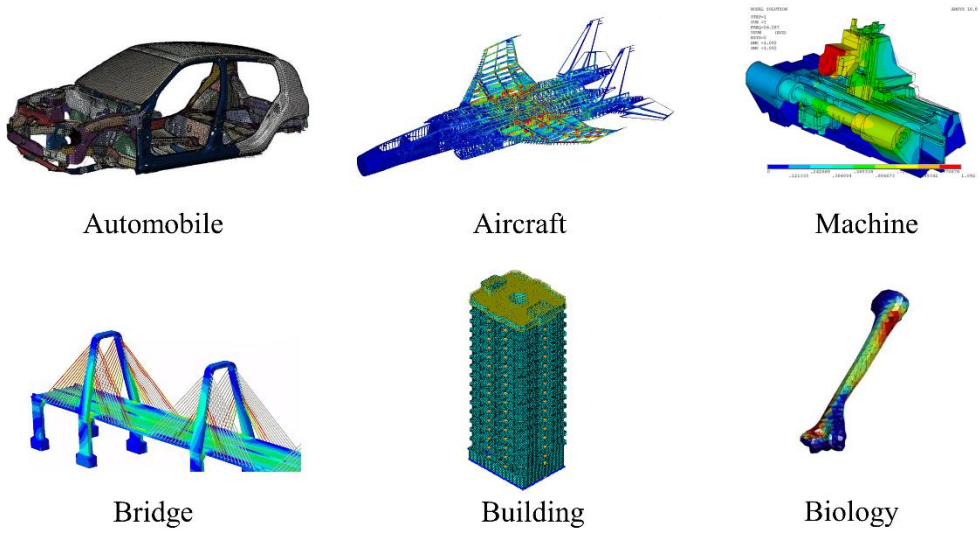

Fig. 1.1. Examples of the FEM applications.

The difficulties of effectively using the FEM are also apparent. The first one is the accuracy of the results mainly depends on the mesh, requiring a high quality of the mesh to obtain good results. The experience of FE modeling, the definition of boundary conditions, and whether the loading meets the physical reality, matter much. Moreover, the computational time for large models is significant, leading to an expensive cost.

1.1.3 Drawbacks of the current finite element modeling process

A finite element analysis is usually composed of three parts [8] with different proportions of effort: pre-processing (70% of total effort), run of program/solver (5% of total effort), post-processing (25% of total effort). The pre-processing step includes preparation of geometry, material properties, loading,

boundary conditions, selection of elements, and mesh creation. The post-processing step consists of the observation and interpretation of the results, but also of the refinement of mesh if convergence of results is not met. All these above are so-called finite element modeling, which is a significant part of finite element analysis.

The current finite element modeling process is summarized in three main steps. Firstly, theory (3D solid, shell, or beam) is selected using rules acquired through experience, and a simulation scenario is defined. In some cases, for complex structures or systems (for example a finite element model of a car), different theories are used in the same model. Secondly, the geometry is created, and material properties are defined. The third step deals with the creation of the mesh. A consistent mesh is obtained thanks to a convergence study. During past decades, numerous studies were performed about the adaptive meshing issue, leading to optimal meshes. In 1978, Babuska and Rheinboldt [9] proposed a pioneering work of error estimation in computational processes, which is a great inspiration for the latter researches of adaptive mesh. A further bibliography study about this issue is highlighted in Chapter 4. In an industrial context, rules acquired from experience are often used to define the mesh size. Deficiencies appear in this existing finite element modeling process.

Some of these difficulties are highlighted through examples, as presented in Fig. 1.2. Choosing an appropriate theory may be difficult when geometry, boundary conditions, loadings, and materials are complex. For instance, the best choice of theory is ambiguous when objects have complex shapes or contain stiffeners (Fig. 1.2a). The limitation of beam and shell theories is also a difficult issue for composite or sandwich structures. For example, even if an automotive windscreen is thin from a geometric viewpoint, shell theory may be inappropriate for this type of sandwich structure. When shell theory is chosen, starting with the solid geometric definition of the object under study, a mid-surface geometry is required. This task is often difficult for an industrial application, and existing tools generally fail in this context. The solid-shell finite elements have been developed to avoid creating a mid-surface geometry. In 1986, Graf et al. [10] firstly presented the “three-dimensional thick shell elements” using solid geometry and displacements, without any rotation degree of freedom. After which, several types of solid-shell elements have been proposed for decades and it is still a promising field until today. A further bibliography study of this aspect is highlighted in Chapter 2. In the same way, when beam theory is chosen, difficulties may appear to make a mid-axis geometry. So solid-beam finite elements have also been developed. In 2013, Frischkorn and Reese [11] introduced the “solid-beam” expression and proposed an eight-node solid-beam element with only displacement degrees of freedom. To our best knowledge, no other solid-beam element has been developed till now. Fig. 1.2b shows a fan blade, which is a combination of massive (cylinder area) and thin structure. The optimal model is certainly made of solid elements and shell elements. But mixing different types of elements in the same model requires some specific numerical treatment. Namely, at the interfaces between solid and shell areas, specific relations between the degrees of freedom are necessary to ensure the compatibility between solid and shell elements.

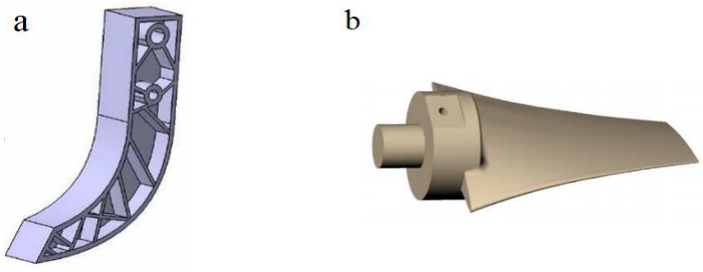

Fig. 1.2. Examples of complex structures: (a) pedal support, (b) fan blade.

1.2 Motivations and outline

Due to the rapid development of 3D geometry software and Reverse Engineering (RE) technology in recent decades, it has become easier to obtain 3D geometries. In finite element analysis, 3D models have many strengths compared with 1D or 2D models. Firstly, the 3D model uses fewer assumptions from the dimension viewpoint, facilitating the application of loads and boundary conditions closer to actual issues. Secondly, 3D models are more convenient when simulating complex structures, especially for some assembled structures. In terms of presenting the results, the 3D model is richer. However, the computational cost for 3D finite element analysis is usually higher than 1D or 2D analysis.

1.2.1 Motivations

The final objective of this research is to define a methodology to identify, in the context of linear static or dynamic analysis, optimal finite element models from both theory and mesh points of view. Indeed, a finite element model is optimal if the choice of the solid, shell, or beam theory and the choice of the mesh are both relevant. As discussed above, many papers have been published about subjects relative to this problem. As far as the authors know, the overall problem proposed here, involving an adaptive choice of theory, has not been described in the literature. This study is performed in the context of the so-called Verification and Validation [12, 13, 14] methodology to improve the predictive capability of finite element models.

An adaptive modeling method should include two aspects: the adaptive meshing and the adaptive choice of theory. As an already relatively reliable technology, the adaptive meshing aspect is not considered in this PhD thesis. On the contrary, the adaptive choice of theory, which was rarely treated before, is discussed here. The methodology is supposed to be based only on solid mesh and elements. The proposed iterative process of the methodology for a given structure contains several steps: the initial finite element analysis of a solid model with coarse mesh, the local choice of appropriate theories, the mesh refinement, the application of solid-shell and solid-beam approaches in the areas concerned, the finite element analysis with a new adaptive model, the calculation of convergence criterion of the methodology.

Our methodology is based on a solid model containing several elements in the different directions of the structure of interest. In particular, in thin-walled areas, the mesh contains several elements through

the thickness or cross-section. In the areas where beam or shell theory is suitable, specific treatments are applied and lead to solid-beam and solid-shell approaches respectively. Therefore, before proposing the overall adaptive modeling method, new solid-shell and solid-beam approaches based on solid elements is first presented. Then it is shown how our methodology exploits a mix of solid, solid-shell and solid-beam areas. One problem may be the compatibility at the interface between the different areas. It is shown that the compatibility conditions are naturally met with our approach.

1.2.2 Outline

The manuscript is organized into five chapters:

- Chapter 1 deals with the general introduction and motivations.
- In the context of adaptive modeling methodology, chapter 2 presents a new solid-shell approach based on the standard solid elements instead of developing a new element. Three plate or shell theories, including the classical first-order plate theory, a modified first-order plate theory and a higher-order plate theory, are considered. The static and vibration examples considering thin to thick structures are treated to verify the relevance and to assess the performances of the approach.
- In chapter 3, we propose a new solid-beam approach in the same way with the solid-shell approach. Beam in a plane, involving membrane and bending effects, is first considered. Then beam in space with rectangular cross-section, taking into account torsion effects. For beam in a plane, three theories including the Timoshenko first-order beam theory, a modified first-order beam theory and a higher-order beam theory, are considered. For beam in space, two variants for the description of warping of the cross-section, are presented. As for the solid-shell approach, static and vibration examples considering thin to thick structures are treated.
- Next, the adaptive modeling methodology is presented in chapter 4. The criterion used to choose the local appropriate theories, the convergence criterion of the methodology, the implementations of the methodology and the special treatment for vibration are described. Cantilever structures and “T” shape plates are considered for both static examples and vibration examples.
- Chapter 5 presents the conclusions and perspectives.

Chapter 2

A new solid-shell approach

In the context of adaptive modeling methodology, a new solid-shell approach dedicated to thin to very thick structures is presented. An original aspect is that plate or shell displacement fields are directly applied on a solid finite element model which contains several elements through the thickness. Moreover any plate or shell theory based on kinematic assumptions can be used, three theories have been considered.

2.1 Introduction

A lot of natural or industrial structures have one dimension small compared to other ones. These structures are called plates and shells. Since the pioneering works of Germain [15] two centuries ago, a lot of researchers, namely Kirchhoff [16] and Love [17], contributed to this theory currently known as the Love-Kirchhoff theory dedicated to thin structures without transverse shear effects. About one century later, Reissner [18] and Mindlin [19] developed the plate theory with transverse shear effects, called the Reissner-Mindlin theory, dedicated to thick as well as thin structures. In these first-order theories, the in-plane and out-of-plane displacements are linear and constant through the thickness respectively. Then higher-order theories were proposed. In the context of the derivation of a shell theory, in 1957 Naghdi [20] proposed a quadratic out-of-plane displacement which includes the transverse normal strain. In 1975, Reissner [21] developed a higher-order theory with cubic in-plane displacements and quadratic out-of-plane displacements. This approach considers out-of-plane effects characterized by the bending phenomenon but neglects in-plane effects. In 1977, Lo, Christensen and Wu [22] enriched the displacement field to take into account in-plane as well as out-of-plane effects. The in-plane displacement contains constant, linear, quadratic and cubic terms, while out-of-plane displacement contains constant, linear and quadratic terms. In 1978, Lo, Christensen and Wu [23] modified the method described above to improve the evaluation of transverse shear and normal stresses using the integration of equilibrium equations. This type of refined theory, or variants, is commented and tested by several authors (Kant [24], Rehfield and Valisetty [25]). Levinson [26] and Reddy [27] used cubic in-plane displacements again, but keep a constant out-of-plane displacement. Voyadjis and Baluch [28] enriched the kinematic assumptions with order five for in-plane displacements and order four for transverse displacements. Levinson [29] developed a higher-order plate theory based on studies in foundation theory. He suggested using of more or less complex shape functions to describe the through-the-

thickness distributions of in-plane and out-of-plane displacements. Other variants of plate theories were proposed, in particular for multilayered composite structures and sandwich ones. The scope of this chapter is limited to homogeneous structures, so multilayered composite structures which have led to a lot of research are not considered in this bibliography study.

The analytical resolution of examples treated with these theories is limited to some academic examples. Consequently, finite element method is widely used for the treatment of plates and shells applications. Since the sixties, an impressive number of formulations have been developed and assessed, to improve the performances of plate and shell finite elements. Most of the formulations concern the Love-Kirchhoff and Reissner-Mindlin first-order theories.

For these finite elements, the most popular approach requires a mesh of the mid-surface and the degrees of freedom are displacements and rotations at nodes. Up to now a lot of literature has been published about this issue, most of the papers dealing with Reissner-Mindlin plate and shell elements. In a review paper containing about 200 references, Cen and Shang [30] describe the state of the art concerning Reissner-Mindlin plate elements. The reader is invited to refer to this paper for detailed information. The reason why a lot of literature deals with these finite elements is that they lead to several specific numerical problems. The most problematic one is transverse shear locking which leads to very bad results when the structure is thin. Another numerical problem, linked to the techniques used for solving the locking phenomenon, is rank deficiency which may cause spurious zero-energy modes. Several techniques were proposed to alleviate these problems. The most popular ones are reduced or selective numerical integration (Zienckiewicz et al. [31], Pawsey and Clough [32], Hughes et al. [33]), Assumed Natural Strain (ANS) method (Hughes and Tezduyar [34]) and its variants, namely the mixed interpolation tensorial components (Bathe and Dvorkin [35]) and the discrete gap method (Bletzinger et al. [36]), Enhanced Assumed Stress (EAS) method (Simo et al. [37]), discrete shear approach (Batoz and Lardeur [38]), mixed or hybrid approach (Spilker and Munir [39], Lee and Pian [40]). In order to prevent spurious modes or zero strain energy modes due to the rank deficiency of the stiffness matrix, stabilization methods have been proposed (Belytschko et al. [41]). Research to improve further and identify best plate and shell finite elements based on first-order theories is still currently an active area (Katili et al. [42]).

Some research has also been carried out for the formulation of finite elements based on higher-order plate theories. The applications of these theories to homogeneous plates and shells are considered here. In 1982, Kant et al. [43] developed a nine-node quadrilateral element based on the Reissner refined theory introduced above [21]. The element only takes bending effects into consideration and has six degrees of freedom per node, compared to three for classical first-order plate elements. Voyadjis and Becquet [44] integrated their theory introduced in [28] in an eight-node quadrilateral element. The number of degrees of freedom is the same as for classical plate elements. Tessler [45] criticized higher-order theories and stated that they are unattractive, namely because they often use a large number of degrees of freedom at each node. Using kinematic assumptions close to those introduced in [20] with

membrane and bending effects and improving the transverse stresses, he described a three-node triangular finite element with five degrees of freedom per node, just like classical plate elements. Up to now, in commercial finite element software, only plate and shell elements based on first-order theories are available.

Another possibility is to exploit only the solid geometry, in this case a mid-surface geometry is not required. As soon as 1970, Ahmad et al. [46] presented an element based on solid geometry but with thick shell assumptions. This leads to a sixteen-node hexahedron element and a twenty-four-node hexahedron element with classical shell degrees of freedom, that is to say three displacements and two rotations. This approach is also known as the degenerated shell element concept. But the so-called solid-shell only uses displacements at nodes, without rotations. This approach has several advantages. First solid and solid-shell elements can be used in the same model, without difficulty. Indeed, sometimes, for the same industrial application, it is justified to use solid theory in some areas of the structure and shell elements in other ones. In this situation, the use of solid and solid-shell elements avoids the development of specific solid-to-shell techniques to correctly connect shell and solid elements. A second advantage is that there is no need to make and exploit a mid-surface mesh, which may lead to severe difficulties and some errors for complex applications. Moreover, in the solid-shell approach, all terms of the strain and stress tensors can be considered and a three-dimensional constitutive law can be used, even if this issue may lead to some difficulties known as the thickness locking phenomenon mentioned below. Finally loading can be naturally applied on the top or bottom faces of the structure. The first contribution was presented in 1986 by Graf et al. [10] who introduced the "three-dimensional thick shell elements" using a solid geometry and displacements, without any rotation. Hexahedral elements with eight, sixteen or eighteen nodes were proposed, with a hybrid/mixed formulation based on the Hellinger-Reissner variational principle. The elements are free from shear or membrane locking phenomena. These numerical problems led to a lot of research for classical plate and shell finite elements and are also relevant for solid-shell elements. Ausserer and Lee [47] also proposed a hexahedral eighteen-node solid element for thin shell analysis based on the same variational principle. The spurious modes problem due to the rank deficiency of the stiffness matrix is discussed and a method to control this numerical problem is detailed. In addition to membrane locking, shear locking and spurious modes, solid-shell elements also suffer from other numerical problems due to the solid nature of these elements. These pathologies include trapezoidal locking, Poisson thickness locking and volumetric locking. Techniques developed to solve these numerical problems are generally similar to those cited above for the development of efficient classical plate and shell elements. Of course, some difficulties as Poisson thickness locking are specific to solid-shell elements and may lead to particular treatments. The main objective of the numerous research works is to control all these numerical difficulties as far as possible. Generally, two or more of the techniques cited above are used together to improve the performances of the elements. Most of the contributions concern the eight-node hexahedral element, see for example Graf et al. [10], Parisch [48], Hauptmann and Schweizerhof [49] who introduced the "solid-shell" expression in 1998,

Sze and Yao [50], Abed-Meraim and Combescure [51, 52], Schwarze and Reese [53], Naceur et al. [54], Ben Bettaieb et al. [55], Bishara and Jabareen [56]. Sixteen-node or eighteen-node hexahedral elements were proposed by Graf et al. [10], Assurer and Lee [47], Parisch [48], Sze et al. [57]. Bassa et al. [58] presented a nine-node hexahedral element which uses an additional node at the center of the element. Twenty-node hexahedral element was proposed by Abed-Meraim et al. [59] and Wang et al. [60]. But for complex geometries, due to difficulties with meshes made up only of hexahedra, prismatic elements are necessary. Abed-Meraim et al. [59] and Wang et al. [60] proposed a fifteen-node prismatic element. As for classical shell elements, research to improve further solid-shell elements finite elements is currently an active area. In 2020 Bishara and Jabareen [56] use the Assumed Natural Inhomogeneous Strain (ANIS) method and the EAS one to improve the eight-node hexahedral element.

In this chapter, a new solid-shell approach, based on applications of first-order or higher-order plate and shell equations to standard solid finite element models, is presented. In Section 2.2, the basic ideas of the methodology proposed, as well as the first-order and higher-order theories of interest, are recalled. In Section 2.3, the approach relying on the master and slave nodes concept is described. In Section 2.4, three static examples with thin and thick cases are treated, and a comparison with solid and shell models in terms of model size is also presented. Two vibration examples with thin and thick cases are presented in Section 2.5. Some conclusions and perspectives are drawn in Section 2.6.

2.2 Presentation of a new solid-shell approach – theoretical aspects

2.2.1 Context and basic ideas

The new solid-shell approach proposed in this chapter is developed in the context of a more general methodology. The aim of this methodology is to propose an adaptive modeling technique based on the use of solid elements, for any type of structure. As stated in Section 1, for the same application, it is sometimes justified to use solid theory in some areas of the structure and shell theory in other ones. The solid-shell approaches developed up to now lead to specific finite elements. Consequently, if it is justified to use both solid and shell theory in the same model, two different finite elements must be managed. Moreover, one characteristic and advantage of classical solid-shell elements is that generally only one finite element is required through the thickness of the structure. On the contrary, in the solid areas, generally due to local effects in the boundary conditions or loading areas, several finite elements through the thickness are necessary to get relevant results meeting the convergence conditions. Consequently, at the interface between the solid and solid-shell areas, severe meshing difficulties may appear. To prevent this problem, our adaptive modeling technique uses only solid elements and the mesh systematically contains several elements through the thickness of the structure. This leads to homogeneous and regular meshes over the whole structure. In solid areas, there is no specific treatment and in the solid-shell areas, plate and shell displacement fields are applied using a specific approach. In this chapter the formulation associated with the solid-shell areas is presented and assessed.

Classically, to develop plate or shell finite element models, equations of the 3D theory of elasticity are modified to give new theoretical equations, characteristic of the plate or shell theory retained. Then, based on these equations, a plate or shell numerical formulation is developed, leading to a surface mesh. The contrary is proposed here. The structure is first modeled with solid finite elements, then through-the-thickness plate or shell equations are applied directly on the solid model to modify the system of algebraic equations and obtain the plate or shell numerical solution.

The main characteristics of the proposed solid-shell approach, dedicated to plate or shell structures, are described below.

- The solid-shell model must give results very close to the reference results given by the solid model.
- The methodology is dedicated to thin to very thick structures and is applicable for statics and dynamics. In the static case presented in this chapter, it must provide correct displacements and stresses. In the thin case, plane stresses $\sigma_{xx}, \sigma_{yy}, \sigma_{xy}$ are concerned. In the thick case, the transverse stresses σ_{xz}, σ_{yz} and σ_{zz} are also of interest.
- Only solid elements are used. The finite element selected must have good performances and must not suffer from severe numerical deficiencies. In particular, the element must be free of severe locking phenomena. In this chapter existing twenty-node hexahedral element is exploited. Some results obtained with eight-node hexahedral element will also be mentioned. Of course, a new solid element formulation could be considered.
- The mesh contains several elements through the thickness. A convergence study makes it possible to choose the appropriate refinement level.
- The 3D constitutive law is used. This means that all strains and stresses are considered in the strain energy. No modification of this constitutive law is allowed. This prohibits for example the use of transverse shear correction coefficients which are classically associated with first-order theories.
- First-order as well as higher-order displacement fields are considered.
- Plate or shell displacement fields are directly applied on the solid finite element model which contains several elements through the thickness.
- From a numerical point of view, kinematic relations between the degrees of freedom of the various nodes through the thickness, are applied. These degrees of freedom are displacements exclusively because solid elements are used, in contrast with plate and shell elements which use rotations and possibly other types of variables, namely in the higher-order theories case. For this purpose, the concept of slave and master nodes is used. After application of equations, only master nodes are kept in the model.
- This process leads to a reduction of the model size compared to the initial solid model.

2.2.2 Displacement fields

2.2.2.1 Classical first-order displacement field

Three displacement fields are considered in this study. The first one, considered in this section, is given by the classical Reissner-Mindlin plate theory. It considers bending effects as well as transverse shear ones. It is widely used in plate and shell finite element formulations. This displacement field is defined by:

$$\begin{cases} u(z) = u_0 - z\varphi_y \\ v(z) = v_0 - z\varphi_x \\ w(z) = w_0 \end{cases} \tag{2.1}$$

where u_0 , v_0 and w_0 are the displacements of a node on the mid-surface, φ_x and φ_y are the rotations around x and y axes respectively.

This displacement field uses displacements as well as rotations. In our approach which relies on solid elements and which is described further in Section 3, only displacements at nodes are used. It is relevant and well suited to rewrite the displacement field of Eq. (2.1) in the simple following form:

$$\begin{cases} u(z) = za_1 + a_2 \\ v(z) = zb_1 + b_2 \\ w(z) = c_1 \end{cases} \tag{2.2}$$

where a_1, a_2, b_1, b_2 and c_1 are coefficients to be determined.

As will be shown and justified in Section 2.4.1, this displacement field does not lead to good results, in the context of our approach.

2.2.2.2 Modified first-order displacement field

To justify a relevant modification of the Reissner-Mindlin theory, it is useful to observe the through-the-thickness displacements of a moderately thin (l/h=20) square plate modeled with solid elements. For the bending case, the plate is clamped along its four edges and subjected to uniform pressure applied on the top face. For the membrane case, the plate is clamped along one edge and submitted to a distributed traction loading at the opposite edge. The through-the-thickness distributions of displacements are shown in Fig. 2.1. For the bending case, in good agreement with the classical first-order theory, the displacements u and v are linear. But the displacement w is quadratic, while the classical first-order theory considers that this component is constant over the entire thickness. For the membrane case, in good agreement with the classical first-order theory, the displacements u and v are constant. But the displacement w is linear, while the classical first-order theory considers that this component is equal to zero over the entire thickness. In summary, to be fully consistent with solid theory, the classical first-order theory must be corrected. The displacement w needs to be enriched and must contain a linear term as well as a quadratic one. This does not mean that the classical Mindlin-Reissner plate theory is not consistent. Indeed, this theory neglects the effect of the transverse strain ε_{zz} and the transverse stress σ_{zz}. Consequently, the assumption stating that w is constant through the thickness has no consequence

on the results. One may say that this theory is self-consistent but does not reproduce all the effects observed in the 3D theory of elasticity.

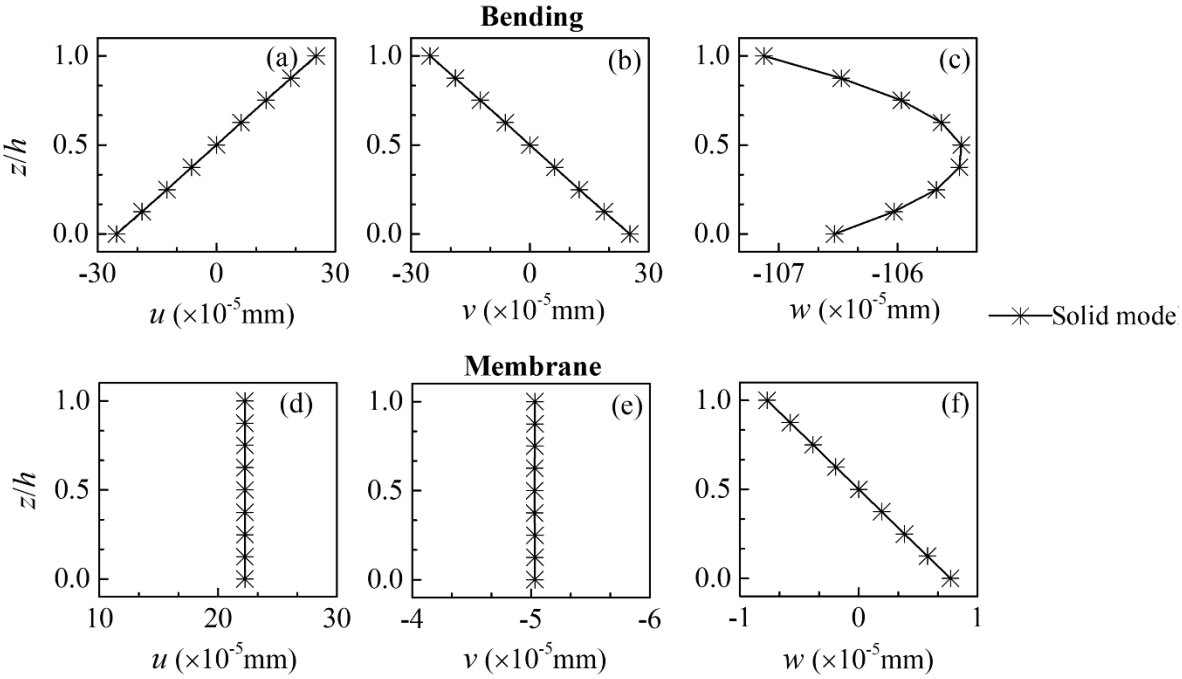

Fig. 2.1. Moderately thin square plate under membrane or bending loading – Distribution of through-the-thickness displacements.

The consistency between linear distribution for *u* and *v* and quadratic distribution for *w* can also be demonstrated. First, as commonly accepted and highlighted in Fig. 2.1, for a given line in the z-direction, assuming that both membrane and bending effects exist, linear through-the-thickness distributions are assumed for *u* and *v*:

$$\begin{cases} u(z) = za_1 + a_2 \\ v(z) = zb_1 + b_2 \end{cases} \tag{2.3}$$

where a_1, a_2, b_1 and b_2 are coefficients to be determined for each line.

Then the strains ε_{xx}, ε_{yy} and γ_{xy} are linear:

$$\begin{cases} \varepsilon_{xx} = u_{,x} = za_3 + a_4 \\ \varepsilon_{yy} = v_{,y} = zb_3 + b_4 \\ \gamma_{xy} = u_{,y} + v_{,x} = zd_1 + d_2 \end{cases} \tag{2.4}$$

where a_3, a_4, b_3, b_4, d_1 and d_2 are coefficients to be determined for each line.

For thin or moderately thick plates, the assumption $\sigma_{zz} = 0$ is acceptable, leading to the classical relation between plane stresses and strains:

$$\begin{Bmatrix} \sigma_{xx} \\ \sigma_{yy} \\ \tau_{xy} \end{Bmatrix} = \frac{E}{1-\nu^2} \begin{bmatrix} 1 & \nu & 0 \\ \nu & 1 & 0 \\ 0 & 0 & \dfrac{1-\nu}{2} \end{bmatrix} \begin{Bmatrix} \varepsilon_{xx} \\ \varepsilon_{yy} \\ \gamma_{xy} \end{Bmatrix} \tag{2.5}$$

In this case, from 3D solid stress-strain relation for isotropic material, the expression of ε_{zz} is deduced:

$$\varepsilon_{zz} = w_{,z} = -\frac{\nu}{E}\left(\sigma_{xx} + \sigma_{yy}\right) \tag{2.6}$$

Eq. (2.5) shows that the stresses σ_{xx}, σ_{yy} and σ_{xy} are linear. From Eq. (2.6), it is deduced that the strain ε_{zz}, which is due to the Poisson effect, is linear. By integration of Eq. (2.6), one highlights the quadratic expression of *w*. The displacement field given in Eq. (2.3) can then be completed as follows:

$$\begin{cases} u(z) = za_1 + a_2 \\ v(z) = zb_1 + b_2 \\ w(z) = z^2c_1 + zc_2 + c_3 \end{cases} \tag{2.7}$$

where $a_1, a_2, b_1, b_2, c_1, c_2$ and c_3 are coefficients to be identified.

This displacement field also corresponds to the theory introduced by Naghdi [20].

2.2.2.3 Higher-order displacement field

The example presented in Section 2.2.2.1 and treated for a moderately thin plate, is now considered for a thick case (*l*/*h*=5). The through-the-thickness distribution of displacements is shown in Fig. 2.2. For the bending case, the displacements *u* and *v* seem to have a cubic variation, while *w* is again almost quadratic. For this bending case, these observations correspond to the displacement field introduced by Reissner [21].

$$\begin{cases} u(z) = z\psi_{\mathrm{x}} + z^3\phi_{\mathrm{x}} \\ v(z) = z\psi_{\mathrm{y}} + z^3\phi_{\mathrm{y}} \\ w(z) = w_0 + z^2\xi_z \end{cases} \tag{2.8}$$

It is worth noting that this displacement field uses classical variables: $w_0, \psi_{\mathrm{x}}, \psi_{\mathrm{y}}$ but also other variables: ϕ_{x}, ϕ_{y}, ξ_z which may be difficult to be interpreted and managed, for example to define boundary conditions or loading. In the approach proposed, displacement field of Eq. (2.8) is rewritten in the simple following form:

$$\begin{cases} u(z) = z^3a_1 + za_2 \\ v(z) = z^3b_1 + zb_2 \\ w(z) = z^2c_1 + c_2 \end{cases} \tag{2.9}$$

where a_1, a_2, b_1, b_2, c_1 and c_2 are coefficients to be identified.

For the membrane case, the displacement *w* is almost linear, while the displacements *u* and *v* have a more complex distribution. Anyway, a quadratic distribution which will be considered hereafter should lead to correct results and seems to be a good choice, even if higher-order terms would certainly have an influence. If one considers membrane and bending effects, compared to the displacement filed proposed by Reissner [21], constant and quadratic terms must be added for *u* and *v*, and linear term must be added for *w*. These observations correspond to the displacement field introduced by Lo et al. [22].

$$\begin{cases} u(z) = u_0 + z\psi_{\mathrm{x}} + z^2\xi_x + z^3\phi_{\mathrm{x}} \\ v(z) = v_0 + z\psi_{\mathrm{y}} + z^2\xi_y + z^3\phi_{\mathrm{y}} \\ w(z) = w_0 + z\psi_{\mathrm{z}} + z^2\xi_z \end{cases} \tag{2.10}$$

One can observe again that this displacement field uses classical variables but also other variables due to higher-order terms. Finally, 11 variables are necessary for this theory. Lo et al. [22] state that this type of theory is not convenient to use. The displacement field of Eq. (2.10) is exploited in the simple following form:

$$\begin{cases} u(z) = z^3 a_1 + z^2 a_3 + z a_2 + a_4 \\ v(z) = z^3 b_1 + z^2 b_3 + z b_2 + b_4 \\ w(z) = z^2 c_1 + z c_3 + c_2 \end{cases} \tag{2.11}$$

where $a_1, a_2, a_3, a_4, b_1, b_2, b_3, b_4, c_1, c_2$ and c_3 are coefficients to be identified.

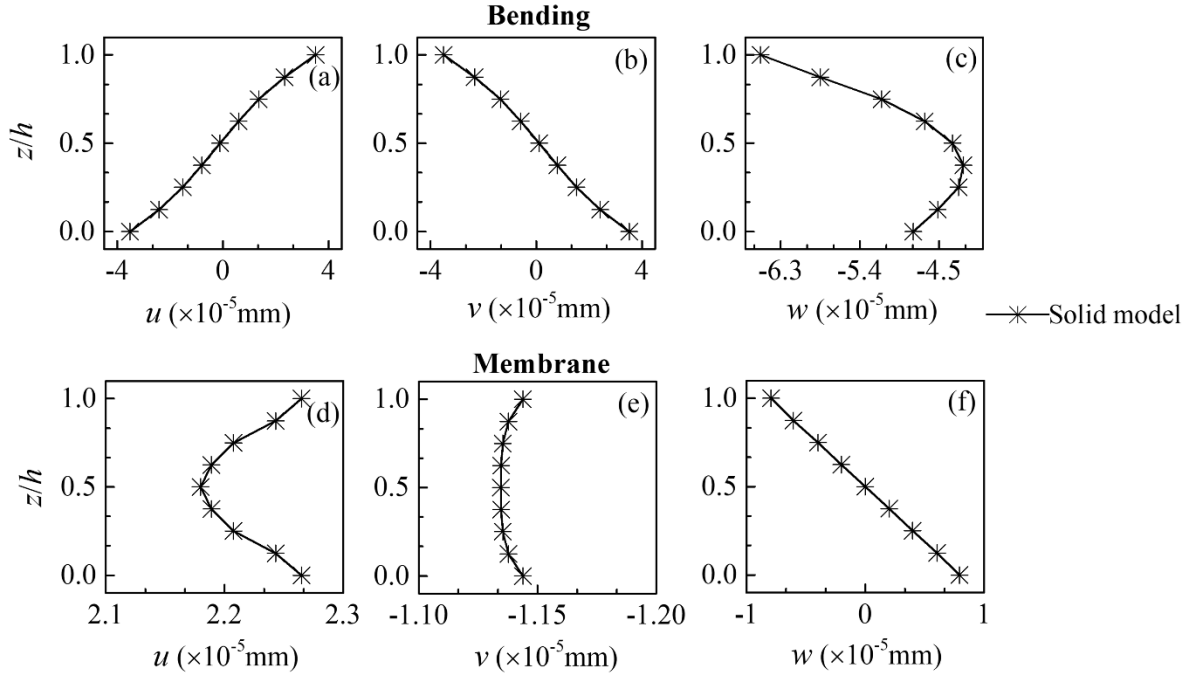

Fig. 2.2. Thick square plate under membrane or bending loading – Distribution of through-the-thickness displacements.

2.3 Presentation of a new solid-shell approach – numerical aspects and implementation

The objective of this section is to explain how the displacement fields presented in Section 2.2.2 are applied on the solid finite element mesh leading to solid-shell models. In all cases, equations are applied on the assembled finite element model. Three solid-shell models are described. Eq. (2.2) leads to the First-Order Solid-Shell (FOSS) model. In the same way, Eq. (2.7) gives the Modified First-Order Solid-Shell (MFOSS) model and Eq. (2.11) the Higher-Order Solid-Shell (HOSS) one. The principle, illustrated in Fig. 2.3, consists in imposing a selected displacement field for each line of nodes in the *z* direction. For each line slave degrees of freedom and master degrees of freedom are defined. Slave degrees of freedom are eliminated from the system of equations to be solved. Each equation leads to the elimination of one degree of freedom. Consequently, the number of degrees of freedom eliminated corresponds exactly to the number of equations applied.

2.3.1 FOSS model

For each through-the-thickness line, the FOSS model uses two master nodes *T* and *B*, the bottom and the top ones, as described in Fig. 2.3. Eq. (2.2) contains two coefficients (a_1 and a_2) to be determined for *u*, two coefficients (b_1 and b_2) for *v* and one coefficient (c_1) for *w*. To identify these five coefficients, the following set of five equations is used:

$$\begin{cases} u(z_B) = u_B = z_B a_1 + a_2 \\ u(z_T) = u_T = z_T a_1 + a_2 \\ v(z_B) = v_B = z_B b_1 + b_2 \\ v(z_T) = v_T = z_T b_1 + b_2 \\ w(z_B) = w_B = c_1 \end{cases} \tag{2.12}$$

where u_B, u_T, v_B, v_T and w_B are displacements at top and bottom nodes; z_B and z_T are the coordinates in the *z* direction of bottom and top nodes respectively.

Solving Eq. (2.12) gives the expressions of coefficients identified for each through-the-thickness line:

$$\begin{cases} a_1 = \dfrac{u_T - u_B}{z_T - z_B} \\ a_2 = -\dfrac{z_T u_B - z_B u_T}{z_T - z_B} \\ b_1 = \dfrac{v_T - v_B}{z_T - z_B} \\ b_2 = -\dfrac{z_T v_B - z_B v_T}{z_T - z_B} \\ c_1 = w_B \end{cases} \tag{2.13}$$

Considering Eq. (2.13) in Eq. (2.2), one obtains:

$$\begin{cases} u(z) = z\dfrac{u_T - u_B}{z_T - z_B} + \dfrac{z_B u_T - z_T u_B}{z_T - z_B} \\ v(z) = z\dfrac{v_T - v_B}{z_T - z_B} + \dfrac{z_B v_T - z_T v_B}{z_T - z_B} \\ w(z) = w_B \end{cases} \tag{2.14}$$

Equations to be applied are obtained by replacing *z* by z_i in Eq. (2.14), z_i being the coordinate of the slave node *i* in the z direction:

$$\begin{cases} u(z_i) = u_i^S = z_i\dfrac{u_T - u_B}{z_T - z_B} + \dfrac{z_B u_T - z_T u_B}{z_T - z_B} \\ v(z_i) = v_i^S = z_i\dfrac{v_T - v_B}{z_T - z_B} + \dfrac{z_B v_T - z_T v_B}{z_T - z_B} \\ w(z_i) = w_i^S = w_B \end{cases} \tag{2.15}$$

For a given line in the *z* direction, the displacements u_B, u_T, v_B, v_T and w_B must be calculated and are the master degrees of freedom. All other degrees of freedom, called the slave degrees of freedom, are expressed in terms of master degrees of freedom and are eliminated using Eq. (2.15). Concerning the displacements *u* and *v*, Eq. (2.15) is applied at all through-the-thickness nodes, except bottom and top ones. The displacements *u* of other nodes of the line are dependent of u_B and u_T. In the same way

the displacements *v* of other nodes of the line are dependent of v_B *and* v_T. Concerning *w*, Eq. (2.15) is applied at all through-the-thickness nodes, except bottom one. The displacement *w* of other nodes is dependent of w_B. This description shows that the methodology relies on slave and master degrees of freedom. For the sake of simplicity, one distinguishes master and slave nodes. It is considered here that a given node is a master node if it contains at least one master degree of freedom. The FOSS model contains five master degrees of freedom per line. It can be observed that Eq. (2.15) defines linear relations between the slave and the master degrees of freedom. One complementary remark is that as far as one needs two master nodes, it seems natural to select the top and bottom nodes, as described here. But two other nodes through the thickness could be selected as well, leading to equivalent results.

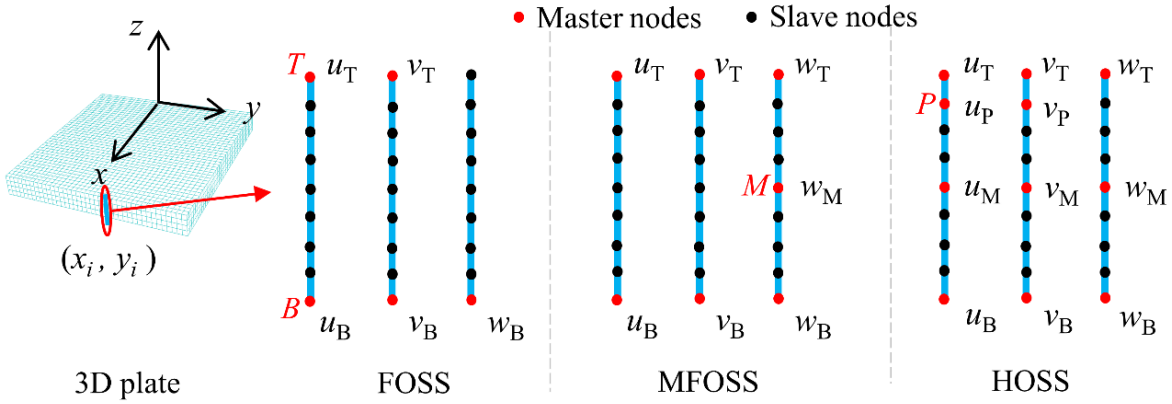

Fig. 2.3. Master nodes and slave nodes through-the-thickness of a 3D plate model.

2.3.2 MFOSS model

The methodology described in Section 2.3.1 for the FOSS model is now applied to build the MFOSS model. This model exploits three master nodes *T*, *B* and *M*, as shown in Fig. 2.3. Eq. (2.7) contains two coefficients (a_1 and a_2) to be determined for *u*, two coefficients (b_1 and b_2) for *v* and three coefficients (c_1, c_2 and c_3) for *w*. The coefficients a_1, a_2, b_1 and b_2 are the same as for the FOSS model. To identify c_1 to c_2 the following equations are used:

$$\begin{cases} w(z_B) = w_B = c_1 z_B^2 + c_3 z_B + c_2 \\ w(z_M) = w_M = c_1 z_M^2 + c_3 z_M + c_2 \\ w(z_T) = w_T = c_1 z_T^2 + c_3 z_T + c_2 \end{cases} \tag{2.16}$$

where w_B, w_M and w_T are displacements at master nodes; z_B, z_M *and* z_T are the coordinates of master nodes in the *z* direction.

The expressions of coefficients identified for each through-the-thickness line are:

$$\begin{cases} a_1 = \dfrac{u_T - u_B}{z_T - z_B} \\ a_2 = -\dfrac{z_T u_B - z_B u_T}{z_T - z_B} \\ b_1 = \dfrac{v_T - v_B}{z_T - z_B} \\ b_2 = -\dfrac{z_T v_B - z_B v_T}{z_T - z_B} \\ c_1 = \dfrac{w_B z_M - w_M z_B - w_B z_T + w_T z_B + w_M z_T - w_T z_M}{(z_B - z_T)(z_B z_M - z_B z_T + z_M z_T - z_M^2)} \\ c_2 = -\dfrac{w_B z_M^2 - w_M z_B^2 - w_B z_T^2 + w_T z_B^2 + w_M z_T^2 - w_T z_M^2}{(z_B - z_T)(z_B z_M - z_B z_T + z_M z_T - z_M^2)} \\ c_3 = -\dfrac{-w_T z_B^2 z_M + w_M z_B^2 z_T + w_T z_B z_M^2 - w_M z_B z_T^2 - w_B z_M^2 z_T + w_B z_M z_T^2}{(z_B - z_T)(z_B z_M - z_B z_T + z_M z_T - z_M^2)} \end{cases} \tag{2.17}$$

Considering Eq. (2.17) and replacing z by z_i in Eq. (2.7), one obtains equations to be applied at slave node i:

$$\begin{cases} u(z_i) = u_i^S = z_i \dfrac{u_T - u_B}{z_T - z_B} + \dfrac{z_B u_T - z_T u_B}{z_T - z_B} \\ v(z_i) = v_i^S = z_i \dfrac{v_T - v_B}{z_T - z_B} + \dfrac{z_B v_T - z_T v_B}{z_T - z_B} \\ w(z_i) = w_i^S = z_i^2 \dfrac{w_B z_M - w_M z_B - w_B z_T + w_T z_B + w_M z_T - w_T z_M}{(z_B - z_T)(z_B z_M - z_B z_T + z_M z_T - z_M^2)} \\ \qquad -z_i \dfrac{w_B z_M^2 - w_M z_B^2 - w_B z_T^2 + w_T z_B^2 + w_M z_T^2 - w_T z_M^2}{(z_B - z_T)(z_B z_M - z_B z_T + z_M z_T - z_M^2)} \\ -\dfrac{-w_T z_B^2 z_M + w_M z_B^2 z_T + w_T z_B z_M^2 - w_M z_B z_T^2 - w_B z_M^2 z_T + w_B z_M z_T^2}{(z_B - z_T)(z_B z_M - z_B z_T + z_M z_T - z_M^2)} \end{cases} \tag{2.18}$$

The MFOSS contains seven master degrees of freedom per through-the-thickness line. As for the FOSS model, Eq. (2.18) describes linear relations between slave and master degrees of freedom.

2.3.3 HOSS model

The methodology is now applied to build the HOSS model. This model requires four master nodes *T*, *B*, *M* and *P*, as described in Fig. 2.3. Eq. (2.11) contains four coefficients (a_1 to a_4) to be determined for *u*, four coefficients (b_1 to b_4) for *v* and three coefficients (c_1 to c_3) for *w*. To identify these eleven coefficients, the following set of eleven equations is used:

$$
\begin{cases}
u(z_B) = u_B = a_1 z_B^3 + a_3 z_B^2 + a_2 z_B + a_4 \\
u(z_M) = u_M = a_1 z_M^3 + a_3 z_M^2 + a_2 z_M + a_4 \\
u(z_P) = u_P = a_1 z_P^3 + a_3 z_P^2 + a_2 z_P + a_4 \\
u(z_T) = u_T = a_1 z_T^3 + a_3 z_T^2 + a_2 z_T + a_4 \\
v(z_B) = v_B = b_1 z_B^3 + b_3 z_B^2 + b_2 z_B + b_4 \\
v(z_M) = v_M = b_1 z_M^3 + b_3 z_M^2 + b_2 z_M + b_4 \\
v(z_P) = v_P = b_1 z_P^3 + b_3 z_P^2 + b_2 z_P + b_4 \\
v(z_T) = v_T = b_1 z_T^3 + b_3 z_T^2 + b_2 z_T + b_4 \\
w(z_B) = w_B = c_1 z_B^2 + c_3 z_B + c_2 \\
w(z_M) = w_M = c_1 z_M^2 + c_3 z_M + c_2 \\
w(z_T) = w_T = c_1 z_T^2 + c_3 z_T + c_2
\end{cases} \tag{2.19}
$$

where $u_B, u_M, u_P, u_T, v_B, v_M, v_P, v_T, w_B, w_M$ and w_T are the displacements at master nodes; z_B, z_M, z_P and z_T are the coordinates of master nodes in the *z* direction.

The expressions of coefficients identified for each through-the-thickness line are:

$$
\begin{cases}
a_1 = -\dfrac{\begin{pmatrix} u_B z_M z_P^2 - u_B z_M^2 z_P - u_M z_B z_P^2 + u_M z_B^2 z_P + u_P z_B z_M^2 - u_P z_B^2 z_M - u_B z_M z_T^2 + u_B z_M^2 z_T \\ +u_M z_B z_T^2 - u_M z_B^2 z_T - u_T z_B z_M^2 + u_T z_B^2 z_M + u_B z_P z_T^2 - u_B z_P^2 z_T - u_P z_B z_T^2 + u_P z_B^2 z_T \\ +u_T z_B z_P^2 - u_T z_B^2 z_P - u_M z_P z_T^2 + u_M z_P^2 z_T + u_P z_M z_T^2 - u_P z_M^2 z_T - u_T z_M z_P^2 + u_T z_M^2 z_P \end{pmatrix}}{\left[(z_P - z_T)(z_M z_P + z_M z_T - z_P z_T - z_M^2)\begin{pmatrix} z_B^2 z_M + z_B^2 z_P + z_B^2 z_T - z_B^3 - z_B z_M z_P \\ -z_B z_M z_T - z_B z_P z_T - z_M z_P z_T \end{pmatrix}\right]} \\
a_3 = \dfrac{\begin{pmatrix} u_B z_M z_P^3 - u_B z_M^3 z_P - u_M z_B z_P^3 + u_M z_B^3 z_P + u_P z_B z_M^3 - u_P z_B^3 z_M - u_B z_M z_T^3 + u_B z_M^3 z_T \\ +u_M z_B z_T^3 - u_M z_B^3 z_T - u_T z_B z_M^3 + u_T z_B^3 z_M + u_B z_P z_T^3 - u_B z_P^3 z_T - u_P z_B z_T^3 + u_P z_B^3 z_T \\ +u_T z_B z_P^3 - u_T z_B^3 z_P - u_M z_P z_T^3 + u_M z_P^3 z_T + u_P z_M z_T^3 - u_P z_M^3 z_T - u_T z_M z_P^3 + u_T z_M^3 z_P \end{pmatrix}}{\left[(z_P - z_T)(z_M z_P + z_M z_T - z_P z_T - z_M^2)\begin{pmatrix} z_B^2 z_M + z_B^2 z_P + z_B^2 z_T - z_B^3 - z_B z_M z_P \\ -z_B z_M z_T - z_B z_P z_T - z_M z_P z_T \end{pmatrix}\right]} \\
a_2 = -\dfrac{\begin{pmatrix} u_B z_M^2 z_P^3 - u_B z_M^3 z_P^2 - u_M z_B^2 z_P^3 + u_M z_B^3 z_P^2 + u_P z_B^2 z_M^3 - u_P z_B^3 z_M^2 - u_B z_M^2 z_T^3 + u_B z_M^3 z_T^2 \\ +u_M z_B^2 z_T^3 - u_M z_B^3 z_T^2 - u_T z_B^2 z_M^3 + u_T z_B^3 z_M^2 + u_B z_P^2 z_T^3 - u_B z_P^3 z_T^2 - u_P z_B^2 z_T^3 + u_P z_B^3 z_T^2 \\ +u_T z_B^2 z_P^3 - u_T z_B^3 z_P^2 - u_M z_P^2 z_T^3 + u_M z_P^3 z_T^2 + u_P z_M^2 z_T^3 - u_P z_M^3 z_T^2 - u_T z_M^2 z_P^3 + u_T z_M^3 z_P^2 \end{pmatrix}}{\left[(z_P - z_T)(z_M z_P + z_M z_T - z_P z_T - z_M^2)\begin{pmatrix} z_B^2 z_M + z_B^2 z_P + z_B^2 z_T - z_B^3 - z_B z_M z_P \\ -z_B z_M z_T - z_B z_P z_T - z_M z_P z_T \end{pmatrix}\right]} \\
a_4 = \dfrac{\begin{pmatrix} u_T z_B^3 z_M^2 z_P - u_P z_B^3 z_M^2 z_T - u_T z_B^3 z_P^2 z_M + u_P z_B^3 z_T^2 z_M + u_M z_B^3 z_P^2 z_T - u_M z_B^3 z_T^2 z_P \\ -u_T z_M^3 z_B^2 z_P + u_P z_M^3 z_B^2 z_T + u_T z_P^3 z_B^2 z_M - u_P z_T^3 z_B^2 z_M - u_M z_P^3 z_B^2 z_T + u_M z_T^3 z_B^2 z_P \\ +u_T z_M^3 z_P^2 z_B - u_P z_M^3 z_T^2 z_B - u_T z_P^3 z_M^2 z_B + u_P z_T^3 z_M^2 z_B + u_M z_P^3 z_T^2 z_B - u_M z_T^3 z_P^2 z_B \\ -u_B z_M^3 z_P^2 z_T + u_B z_M^3 z_T^2 z_P + u_B z_P^3 z_M^2 z_T - u_B z_T^3 z_M^2 z_P - u_B z_P^3 z_T^2 z_M + u_B z_T^3 z_P^2 z_M \end{pmatrix}}{\left[(z_P - z_T)(z_M z_P + z_M z_T - z_P z_T - z_M^2)\begin{pmatrix} z_B^2 z_M + z_B^2 z_P + z_B^2 z_T - z_B^3 - z_B z_M z_P \\ -z_B z_M z_T - z_B z_P z_T - z_M z_P z_T \end{pmatrix}\right]}
\end{cases} \tag{2.20}
$$

$$
\begin{cases}
b_1 = -\dfrac{\begin{pmatrix} v_B z_M z_P^2 - v_B z_M^2 z_P - v_M z_B z_P^2 + v_M z_B^2 z_P + v_P z_B z_M^2 - v_P z_B^2 z_M - v_B z_M z_T^2 + v_B z_M^2 z_T \\ +v_M z_B z_T^2 - v_M z_B^2 z_T - v_T z_B z_M^2 + v_T z_B^2 z_M + v_B z_P z_T^2 - v_B z_P^2 z_T - v_P z_B z_T^2 + v_P z_B^2 z_T \\ +v_T z_B z_P^2 - v_T z_B^2 z_P - v_M z_P z_T^2 + v_M z_P^2 z_T + v_P z_M z_T^2 - v_P z_M^2 z_T - v_T z_M z_P^2 + v_T z_M^2 z_P \end{pmatrix}}{\left[(z_P - z_T)(z_M z_P + z_M z_T - z_P z_T - z_M^2)\begin{pmatrix} z_B^2 z_M + z_B^2 z_P + z_B^2 z_T - z_B^3 - z_B z_M z_P \\ -z_B z_M z_T - z_B z_P z_T - z_M z_P z_T \end{pmatrix}\right]} \\
b_3 = \dfrac{\begin{pmatrix} v_B z_M z_P^3 - v_B z_M^3 z_P - v_M z_B z_P^3 + v_M z_B^3 z_P + v_P z_B z_M^3 - v_P z_B^3 z_M - v_B z_M z_T^3 + v_B z_M^3 z_T \\ +v_M z_B z_T^3 - v_M z_B^3 z_T - v_T z_B z_M^3 + v_T z_B^3 z_M + v_B z_P z_T^3 - v_B z_P^3 z_T - v_P z_B z_T^3 + v_P z_B^3 z_T \\ +v_T z_B z_P^3 - v_T z_B^3 z_P - v_M z_P z_T^3 + v_M z_P^3 z_T + v_P z_M z_T^3 - v_P z_M^3 z_T - v_T z_M z_P^3 + v_T z_M^3 z_P \end{pmatrix}}{\left[(z_P - z_T)(z_M z_P + z_M z_T - z_P z_T - z_M^2)\begin{pmatrix} z_B^2 z_M + z_B^2 z_P + z_B^2 z_T - z_B^3 - z_B z_M z_P \\ -z_B z_M z_T - z_B z_P z_T - z_M z_P z_T \end{pmatrix}\right]} \\
b_2 = -\dfrac{\begin{pmatrix} v_B z_M^2 z_P^3 - v_B z_M^3 z_P^2 - v_M z_B^2 z_P^3 + v_M z_B^3 z_P^2 + v_P z_B^2 z_M^3 - v_P z_B^3 z_M^2 - v_B z_M^2 z_T^3 + v_B z_M^3 z_T^2 \\ +v_M z_B^2 z_T^3 - v_M z_B^3 z_T^2 - v_T z_B^2 z_M^3 + v_T z_B^3 z_M^2 + v_B z_P^2 z_T^3 - v_B z_P^3 z_T^2 - v_P z_B^2 z_T^3 + v_P z_B^3 z_T^2 \\ +v_T z_B^2 z_P^3 - v_T z_B^3 z_P^2 - v_M z_P^2 z_T^3 + v_M z_P^3 z_T^2 + v_P z_M^2 z_T^3 - v_P z_M^3 z_T^2 - v_T z_M^2 z_P^3 + v_T z_M^3 z_P^2 \end{pmatrix}}{\left[(z_P - z_T)(z_M z_P + z_M z_T - z_P z_T - z_M^2)\begin{pmatrix} z_B^2 z_M + z_B^2 z_P + z_B^2 z_T - z_B^3 - z_B z_M z_P \\ -z_B z_M z_T - z_B z_P z_T - z_M z_P z_T \end{pmatrix}\right]} \\
b_4 = \dfrac{\begin{pmatrix} v_T z_B^3 z_M^2 z_P - v_P z_B^3 z_M^2 z_T - v_T z_B^3 z_P^2 z_M + v_P z_B^3 z_T^2 z_M + v_M z_B^3 z_P^2 z_T - v_M z_B^3 z_T^2 z_P \\ -v_T z_M^3 z_B^2 z_P + v_P z_M^3 z_B^2 z_T + v_T z_P^3 z_B^2 z_M - v_P z_T^3 z_B^2 z_M - v_M z_P^3 z_B^2 z_T + v_M z_T^3 z_B^2 z_P \\ +v_T z_M^3 z_P^2 z_B - v_P z_M^3 z_T^2 z_B - v_T z_P^3 z_M^2 z_B + v_P z_T^3 z_M^2 z_B + v_M z_P^3 z_T^2 z_B - v_M z_T^3 z_P^2 z_B \\ -v_B z_M^3 z_P^2 z_T + v_B z_M^3 z_T^2 z_P + v_B z_P^3 z_M^2 z_T - v_B z_T^3 z_M^2 z_P - v_B z_P^3 z_T^2 z_M + v_B z_T^3 z_P^2 z_M \end{pmatrix}}{\left[(z_P - z_T)(z_M z_P + z_M z_T - z_P z_T - z_M^2)\begin{pmatrix} z_B^2 z_M + z_B^2 z_P + z_B^2 z_T - z_B^3 - z_B z_M z_P \\ -z_B z_M z_T - z_B z_P z_T - z_M z_P z_T \end{pmatrix}\right]} \\
c_1 = \dfrac{w_B z_M - w_M z_B - w_B z_T + w_T z_B + w_M z_T - w_T z_M}{(z_B - z_T)(z_B z_M - z_B z_T + z_M z_T - z_M^2)} \\
c_1 = \dfrac{w_B z_M - w_M z_B - w_B z_T + w_T z_B + w_M z_T - w_T z_M}{(z_B - z_T)(z_B z_M - z_B z_T + z_M z_T - z_M^2)} \\
c_2 = -\dfrac{-w_T z_B^2 z_M + w_M z_B^2 z_T + w_T z_B z_M^2 - w_M z_B z_T^2 - w_B z_M^2 z_T + w_B z_M z_T^2}{(z_B - z_T)(z_B z_M - z_B z_T + z_M z_T - z_M^2)}
\end{cases}
$$

After replacing z by z_i in Eq. (2.11), one obtains equations to be applied at slave node *i*:

$$
\begin{cases}
u(z_i) = u_i^S = z_i^3 a_1 + z_i^2 a_3 + z_i a_2 + a_4 \\
v(z_i) = v_i^S = z_i^3 b_1 + z_i^2 b_3 + z_i b_2 + b_4 \\
w(z_i) = w_i^S = z_i^2 c_1 + z_i c_3 + c_2
\end{cases} \tag{2.21}
$$

with coefficients $a_1, a_2, a_3, a_4, b_1, b_2, b_3, b_4, c_1, c_2$ and c_3 defined in Eq. (2.19).

The HOSS model contains 11 master degrees of freedom per through-the-thickness line. Eq. (2.21) describes linear relations between slave and master degrees of freedom.

2.3.4 Remarks

As shown in Sections 2.3.1 to 2.3.3, the methodology is the same for the three theories considered. Only the number of master degrees of freedom per through-the-thickness line is different, namely five,

seven and eleven for the FOSS, MFOSS and HOSS solid-shell models respectively. The number of equations applied is equal to the number of slave degrees of freedom which are systematically eliminated. Consequently, the size of the system to be solved is given by the number of master degrees of freedom and does not depend on the number of nodes through the thickness. The level of mesh refinement in the thickness direction has no consequence on the size of the final model. As highlighted above, the relations between slave and master degrees of freedom are linear. From a practical point of view, in Abaqus [61], the "*EQUATION" keyword is used to consider these linear equations. Of course, in the post-processing step, displacements at slave as well as master nodes are available. Then the stresses can be calculated in all the finite elements of the mesh. The average value at nodes technique is retained to evaluate the stresses.

The solid-shell approach proposed exploits displacements exclusively, without any other type of degree of freedom. This is a hopeful characteristic of our methodology, in particular for higher-order theories which initially use displacements, rotations, but also other types of degrees of freedom (see Eq. (2.10)). Furthermore, there is no limitation for applying other displacement fields in our approach, which means it can be developed for an even higher-order plate or shell theory if necessary.

2.4 Static examples

The new solid-shell approach for FOSS, MFOSS and HOSS models is here used for the treatment of three examples with thin and thick cases in the context of static analysis: a square plate, a quarter of cylinder, and a quarter of hyperboloid. Each static example is presented. A convergence study is made for each example. The displacement and the von Mises stress are studied. The finite element results obtained with the solid-shell models are evaluated by comparison with a reference solid model. The reduction of model size due to the solid-shell approach is discussed. The compatibility of the solid-shell approach with another efficient solid element is also proved.

2.4.1 Clamped square plate under distributed loading

2.4.1.1 Presentation of the example

The first example presented in Fig. 2.4 is a square plate, clamped along its four edges and submitted to a distributed loading applied on the upper surface. Two values of the *l*/*h* ratio are considered: 20 and 5, leading respectively to a relatively thin plate case and a thick plate one.

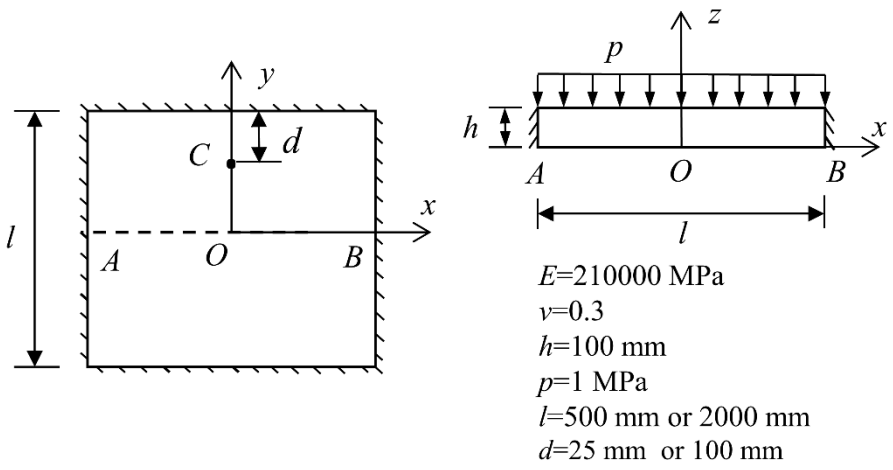

Fig. 2.4. Clamped square plate under distributed loading – Presentation of the example.

2.4.1.2 Convergence study

First a convergence study is presented, to ensure that our approach preserves the convergence quality of the solid finite element used. Namely it is useful to compare the convergence characteristics of models based on the approach proposed and the intrinsic convergence performance of the solid element used. As mentioned before, our approach is compatible with any solid finite element. Here the twenty-node hexahedral element C3D20 of Abaqus [61] is used. The evolution of displacement on the bottom face in the center of the plate (see point *O* in Fig. 2.4) is observed, for several mesh refinement levels. A solid model with a very fine 10×80×80 mesh is chosen to provide the reference results. It is considered here that convergence is achieved if the error is less than 0.5% compared with this reference. Results presented in Fig. 2.5 show that for the HOSS model convergence is obtained with 4×24×24 and 4×16×16 meshes for the thin and thick cases respectively. For both the thin and thick cases, the convergence of the HOSS model is similar to the convergence of the solid model. For the thin or thick plate case, the FOSS model converges to values which are completely wrong compared to the reference solution. The MFOSS model also converges and the result is correct for the thin plate. However, some discrepancy appears in the thick case. This is due to the basic kinematic assumptions used in this MFOSS model.

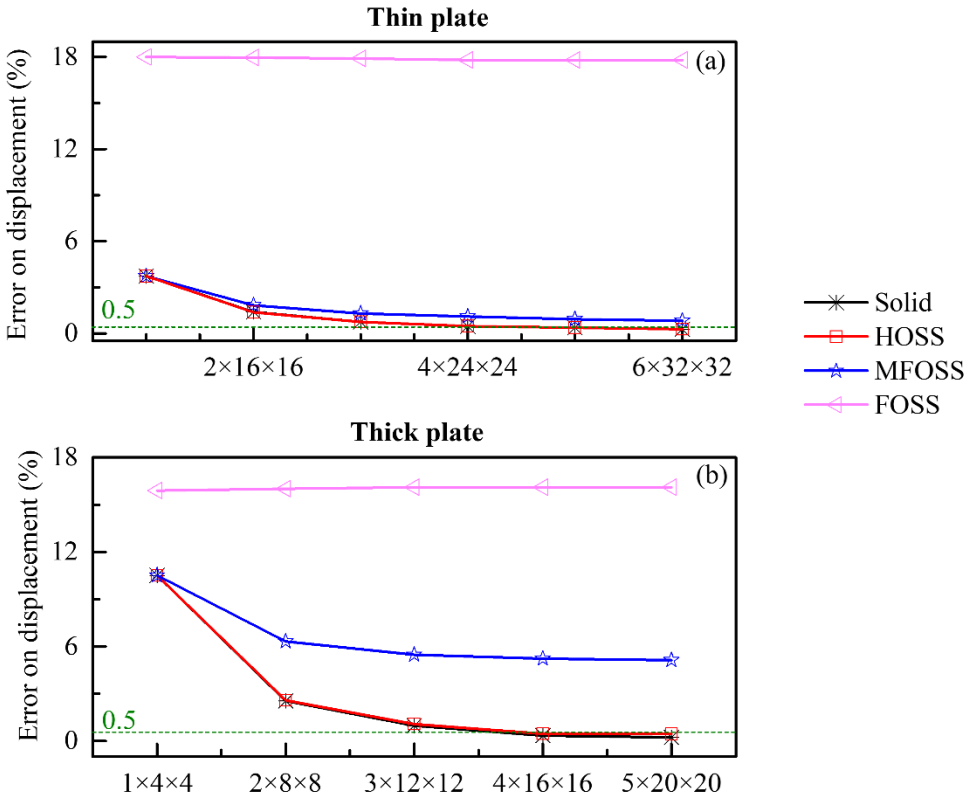

Fig. 2.5. Clamped square plate under distributed loading – Convergence study.

2.4.1.3 Displacements and stresses in the thin plate case

Displacements and stresses are observed over the whole structure. Fig. 2.6 shows a comparison between the results obtained with solid, MFOSS and HOSS models. Due to unsatisfactory convergence results, the FOSS model is not considered in this comparison. Anyway, it will be discussed further for a better analysis of its deficiencies. The results presented in this section are obtained with the 4×24×24 mesh, which meets the convergence criterion as highlighted in Section 2.4.1.2. The three models lead to quite similar results for vertical displacements as well as for von Mises stresses.

Fig. 2.7 shows the distribution of vertical displacement and von Mises stress on the lower face along the AB line defined in Fig. 2.4. The solid-shell models are compared with the solid model and a shell model. Again the 4×24×24 mesh is used for the solid and solid-shell models. For the shell model, a 1×24×24 mesh, which meets the convergence criterion, is considered. All the models give very similar results for displacements and von Mises stress, except the FOSS model which leads to significant errors. These errors are due to a spurious σ_{zz} stress state highlighted and discussed below.

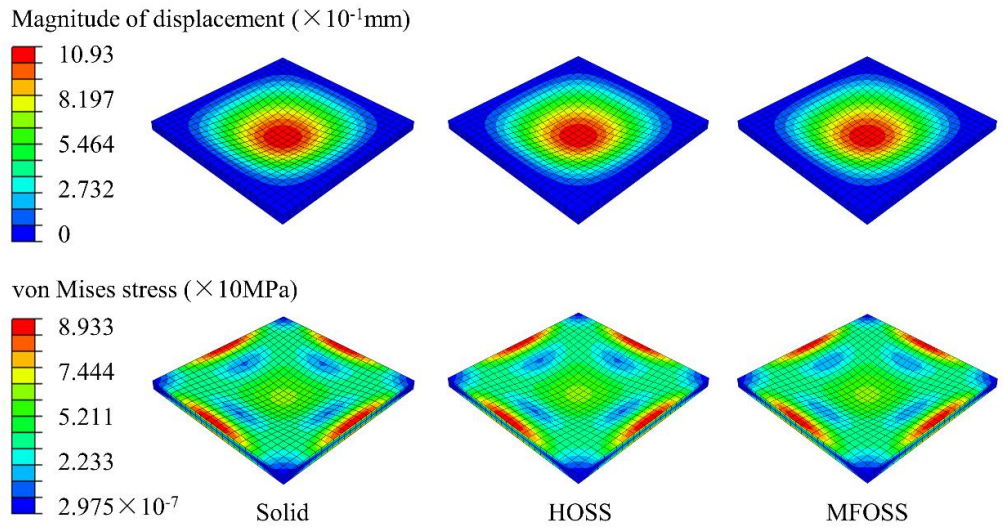

Fig. 2.6. Clamped square plate under distributed loading – Displacement and von Mises stress distributions in the thin plate case.

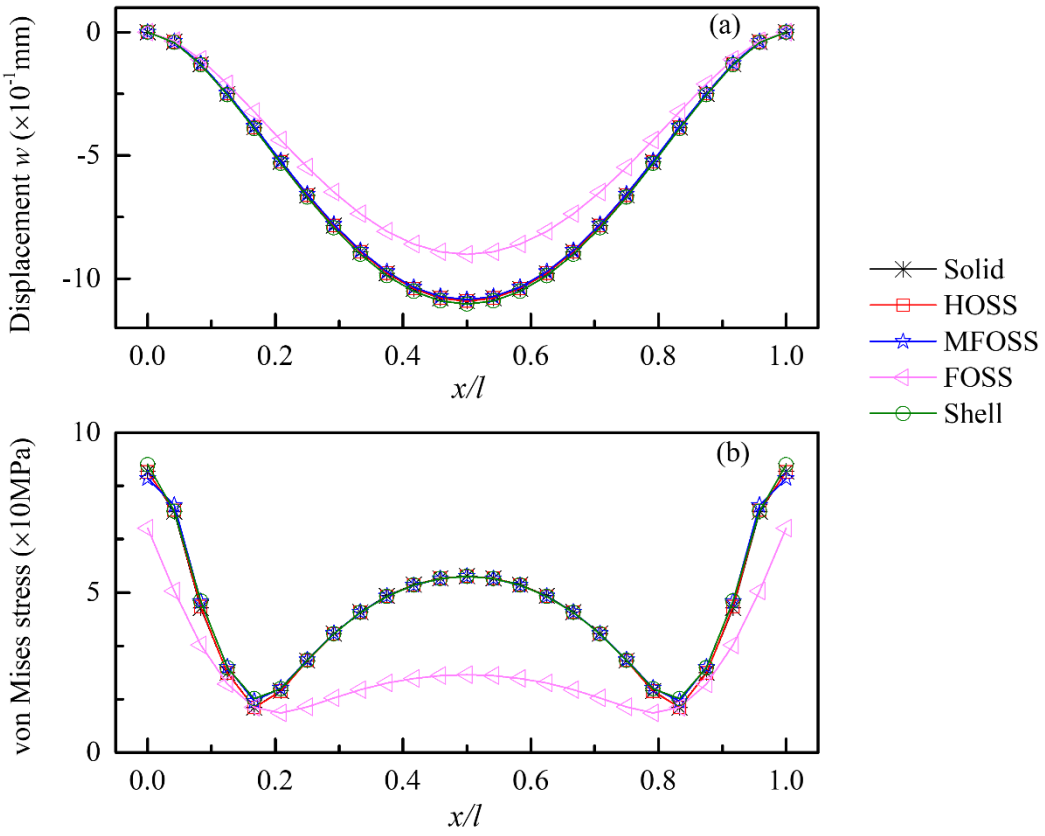

Fig. 2.7. Clamped square plate under distributed loading – Distribution of vertical displacement (a) and von Mises stress (b) along a line on the lower face, in the thin case.

Fig. 2.8 shows the through-the-thickness distribution of displacements and stresses at point *C* (see Fig. 2.4), the reference results being given by the solid model. First, one can see that the FOSS model gives unsatisfactory results. In particular, displacement *w* (Fig. 2.8b) is wrong and a high level σ_{zz} stress

(Fig. 2.8e) is observed. This spurious σ_{zz} stress is due to the fact that *w* is considered as constant through the thickness. Consequently, the ε_{zz} strain which is natural because of the Poisson effect, is prevented. In the context of 3D theory of elasticity, this nonphysical assumption considerably disturbs the state of stress and in particular, it implies large σ_{zz} stresses, while this stress should remain very small in this thin plate case. The von Mises stress which depends on the different stress components is affected by this wrong σ_{zz} stress. These bad results confirm that this kinematic assumption, although valid and consistent in the context of the classical plate theory, is not compatible with the 3D theory of elasticity. This phenomenon is usual for solid-shell elements and is known as the Poisson thickness locking. The FOSS model also leads to a constant σ_{xz} distribution (Fig. 2.8d). This is a well-known result and a limitation of the Mindlin-Reissner plate theory. A usual approach is to use integration of equilibrium equations to obtain a correct and quadratic distribution of transverse shear stresses.

Reference displacement *v* (Fig. 2.8a) is linear through the thickness and one can observe a perfect fit between the solid model and the MFOSS and HOSS models. The distribution of *w* is perfectly predicted as well by these solid-shell models. This distribution seems to be quite constant through the thickness but a detailed observation shows a slight quadratic tendency. The σ_{xx} stress (Fig. 2.8c) is linear through the thickness and again very good results are obtained with the MFOSS and HOSS models. The classical quadratic distribution of σ_{xz} is well reproduced by the HOSS model. Namely, the free-face condition $\sigma_{xz}=0$ is almost met at top and bottom faces. The MFOSS model highlights a quadratic tendency, thanks to the quadratic *w* distribution, but the difference with the reference distribution is significant. Moreover, the free-face condition $\sigma_{xz}=0$ is not met at top and bottom faces. This is not very important for thin structures because transverse shear stresses are generally neglected in this case and influence of transverse shear effects on displacements is small.

In summary, the HOSS model gives excellent results for the thin plate case. The MFOSS model is also satisfactory but it is not able to correctly reproduce the transverse shear effects. Anyway, these effects can be neglected for a thin structure and so this model is quite convenient for thin structures. Finally, the FOSS model gives unacceptable results. Therefore, this model is not considered for the rest of the study.

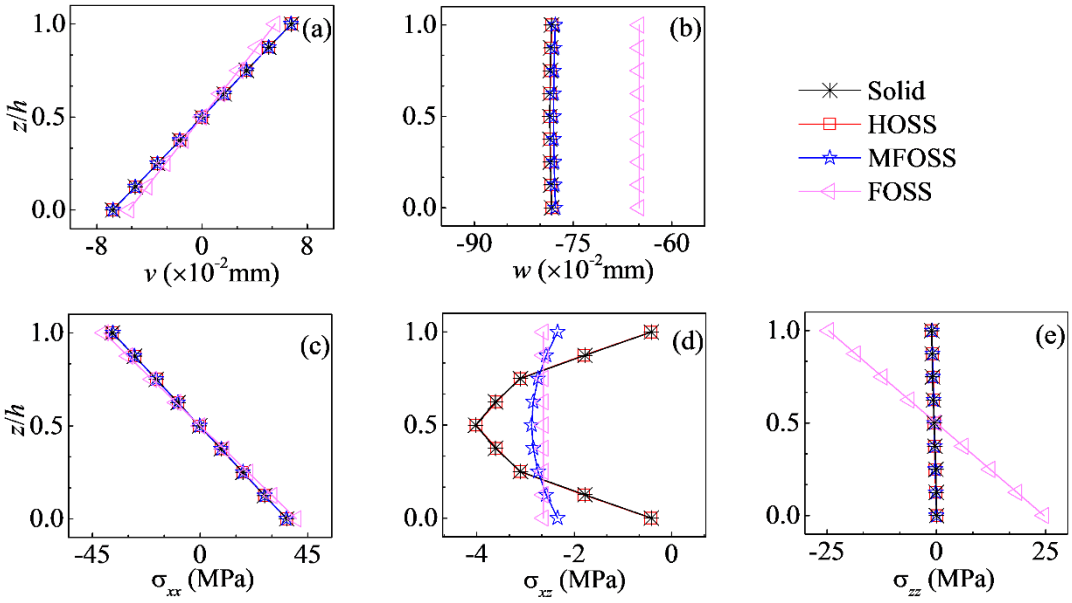

Fig. 2.8. Clamped square plate under distributed loading – Through-the-thickness displacements and stresses at point *C*, in the thin case.

2.4.1.4 Displacements and stresses in the thick plate case

Displacements and stresses are observed over the whole structure. Fig. 2.9 shows a comparison between the results obtained with solid, MFOSS and HOSS models. The 4×16×16 mesh, which meets the convergence criterion, is used. For this global observation, the solid model and the HOSS model highlight similar results. For the MFOSS model, in this very thick plate case, some discrepancy is observed on displacement and von Mises stress.

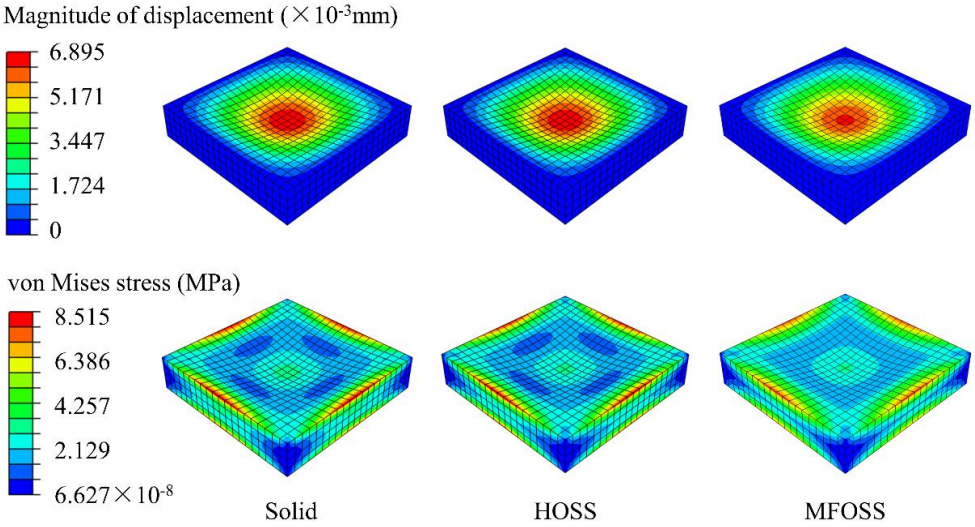

Fig. 2.9. Clamped square plate under distributed loading – Displacement and von Mises stress distribution in the thick plate case.

Fig. 2.10 shows the distribution of vertical displacement and von Mises stress on the lower face along the *AB* line defined in Fig. 2.5. The solid-shell models are compared with the solid model and a

shell model. Again the 4×16×16 mesh is used for the solid and solid-shell models. For the shell model, a 1×20×20 mesh, which meets the convergence criterion, is considered. For displacement, the HOSS model fits very well with the solid one. Some error is obtained with the shell approach and the MFOSS model. For von Mises stress, again the HOSS model fits very well with the solid one. The shell model and the MFOSS models lead to some errors, in particular in the boundary conditions area. Some discrepancy is also observed with the MFOSS model within the plate. This is due to a rough calculation of the transverse stresses which are significant in the thick case, this issue is highlighted and discussed below. These results confirm that the HOSS model is necessary to correctly predict the transverse shear effects and so the mechanical behaviour of a thick plate.

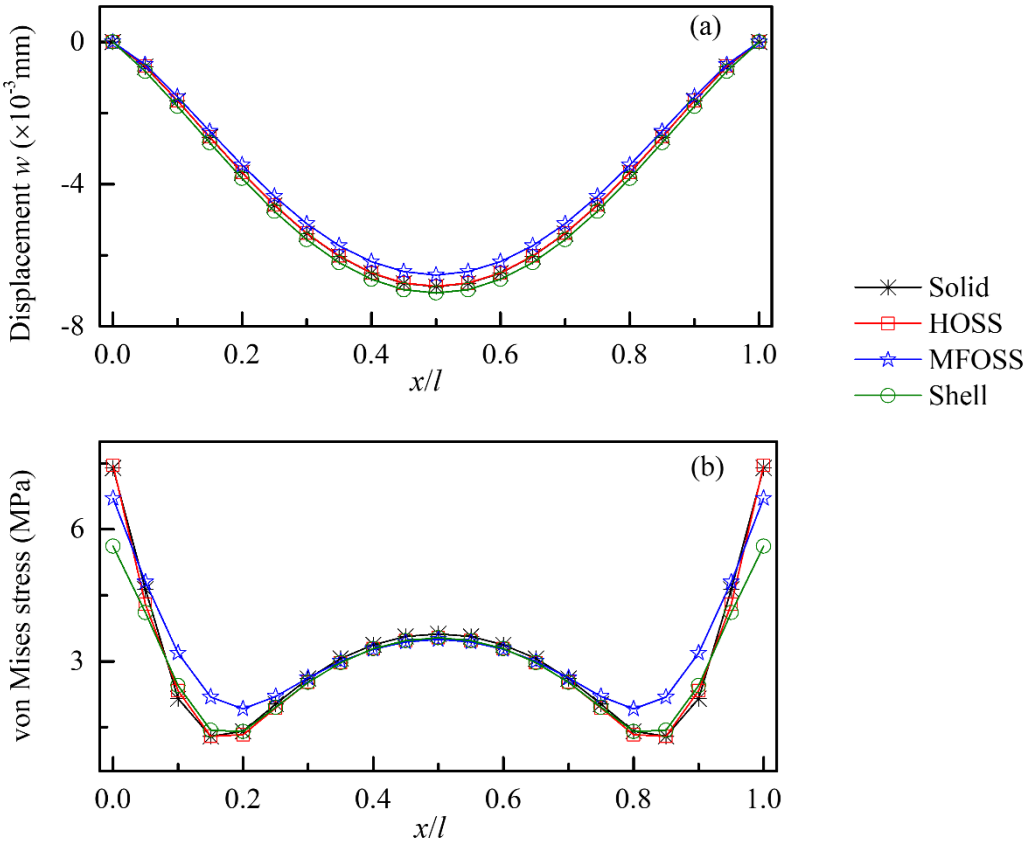

Fig. 2.10. Clamped square plate under distributed loading – Distribution of vertical displacement (a) and von Mises stress (b) along a line on the lower face, in the thick case.

Fig. 2.11 shows the through-the-thickness distribution of displacements and stresses at point *C* (see Fig. 2.4), the reference results being given by the solid model. The MFOSS model has several limitations. The quadratic tendency of *w* (Fig. 2.11b) is well reproduced but the displacement values are not correct, this result means that the stiffness of the structure is not well estimated. This is due to the fact that the transverse shear stiffness, which depends on the through-the-thickness transverse shear strains and stresses, is not precisely calculated. Indeed, the distribution of σ_{xz} (Fig. 2.11d) is not correct. The reference quadratic distribution of σ_{xz} is not well reproduced by the MFOSS model. Namely, as for the thin case, the free-face condition $\sigma_{xz}=0$ is not met at top and bottom faces. And in the thick case with a

small *l/h* ratio, this is a problem because by the contrary of the thin plate case, the transverse shear effects are significant. Classically the Mindlin-Reissner plate theory is associated with shear correction factors to compensate the limitation due to kinematic assumptions. But in our solid-shell approach, no correction factor is used and consequently the MFOSS model suffers from some error concerning the transverse shear stiffness of the structure. Of course, this wrong σ_{xz} distribution also leads to errors on the von Mises stress, as observed in Fig. 2.10. Moreover, this MFOSS model is not able to reproduce the slightly nonlinear distribution of *v* (Fig. 2.11a) and σ_{xx}. On the contrary, one can observe a very good fit between the solid model and the HOSS model. The quadratic distribution of displacements is correctly predicted by this model. The reference stress σ_{xx} (Fig. 2.11c) is also slightly nonlinear and the HOSS model reproduces this result very well. The reference quadratic distribution of σ_{xz} is also well reproduced by the HOSS model. Namely, as for the thick case, the free-face condition $\sigma_{xz}=0$ is almost met at top and bottom faces.

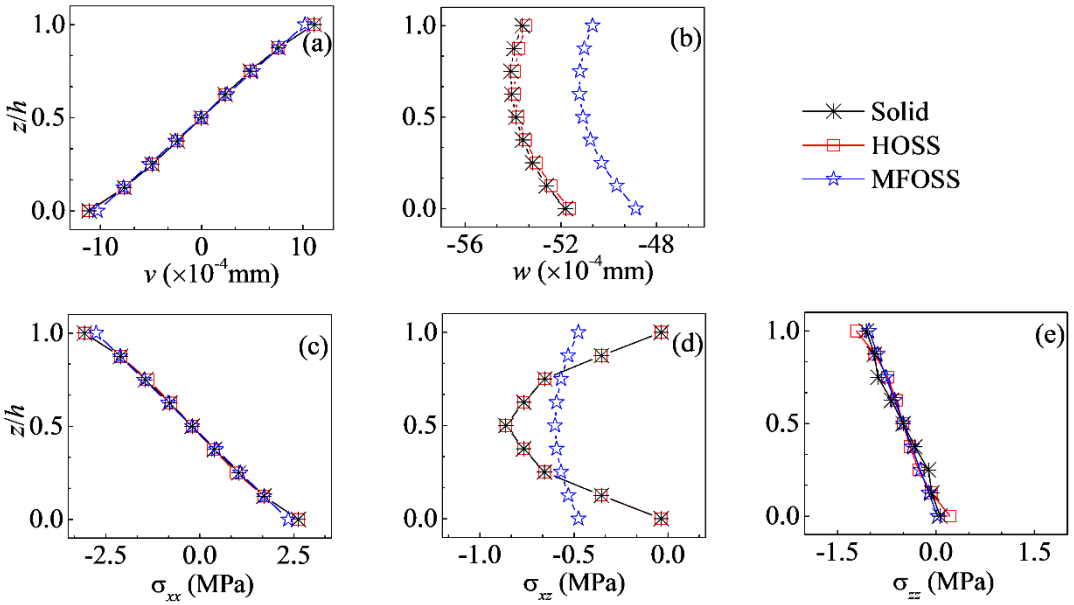

Fig. 2.11. Clamped square plate under distributed loading – Through-the-thickness displacements and stresses at point *C*, in the thick case.

2.4.1.5 Accuracy synthesis of solid-shell models

Table 2.1 summarizes the errors obtained with the solid-shell models, in the thin and thick plate cases. These errors are calculated on the maximal displacement observed at the centre of the plate and on the maximum von Mises stress observed in the boundary conditions area. The MFOSS model gives good results in the thin plate case. The errors are less than 1% for the displacement and the von Mises stress. Anyway, even in this case the HOSS model is better because transverse shear effects are small but not completely negligible. Indeed, the *l/h* ratio is equal to 20, which is not characteristic of a very thin plate. In the thick plate case, the HOSS model remains very satisfactory, the errors do not exceed

1%, while the MFOSS model leads to some discrepancy. With this model the error is about 5% for the displacement and 10% for the von Mises stress.

In summary, the HOSS model gives excellent results in the thin as well as the thick cases, while the MFOSS model is convenient for thin plates only.

In addition, this study was performed again with another type of solid element, the 8-node solid hexahedron element C3D8I [49] of Abaqus, has been used. Similar results have been obtained, demonstrating that the methodology proposed can be applied with any efficient solid finite element.

Table 2.1. Clamped square plate under distributed loading – Accuracy synthesis for maximal displacement and maximal von Mises stress.

Examples	Models	Displacement *w*		von Mises stress	
		Maximum ($\times 10^{-3}$mm)	Error (%)	Maximum (MPa)	Error (%)
Relatively thin plate	Solid	-1093	–	89.33	–
	HOSS	-1093	0.1	88.96	0.4
	MFOSS	-1086	0.6	88.41	1.0
Very thick plate	Solid	-6.895	–	8.515	–
	HOSS	-6.882	0.2	8.424	1.1
	MFOSS	-6.562	4.8	7.671	9.9

2.4.2 Quarter of cylinder under pressure

2.4.2.1 Presentation of the example

The second example presented in Fig. 2.12 is a quarter of cylinder, clamped along its two ends and submitted to a pressure applied on the outer surface. The outside radius is 200 mm and two values: 10 mm and 50 mm, are considered for the thickness, leading respectively to a thin shell case and a thick shell one. The main difference with the first example is that the structure is now curved, allowing natural coupling between membrane and bending effects. For this example, in order to apply kinematic relations on the solid model to obtain a solid-shell model, local coordinate systems are created for each line of nodes through the thickness of the structure. The equations involving the degrees of freedom concerned are applied using these local coordinate systems.

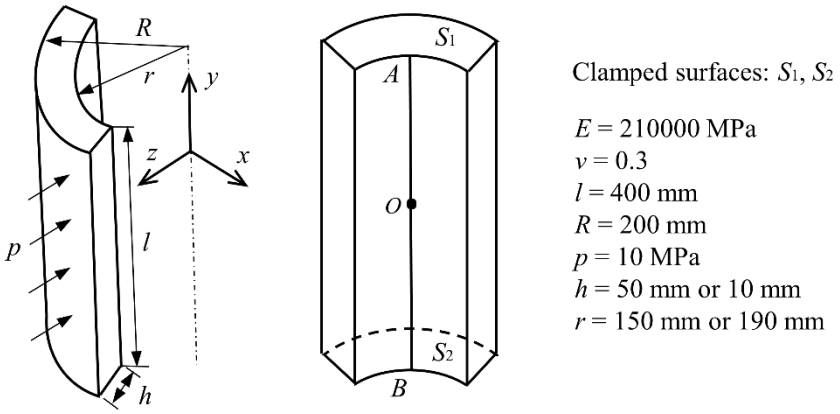

Fig. 2.12. Quarter of cylinder under pressure – Presentation of the example.

2.4.2.2 Convergence study

First a convergence study is presented. The approach already detailed for the first example is repeated here. Again, the twenty-node hexahedron element C3D20 from Abaqus [61] is used. The evolution of displacement on the inner face in the center of the structure (see point *O* in Fig. 2.12) is observed, for several mesh refinement levels. A solid model with a very fine 10×80×80 mesh is chosen to provide the reference results. It is considered that convergence is achieved if the error is less than 0.5% compared with this reference model. Results are reported in Tables 2.2 and 2.3 for the HOSS model. Convergence is obtained with 4×20×20 mesh and 4×16×16 meshes for the thin and thick cases respectively. Moreover, convergence characteristics are similar for the HOSS model and the solid model. As for the first example, due to basic assumptions used, for the MFOSS model the convergence criterion defined above is never achieved because this model does not exactly converge to the reference solution. Indeed, some discrepancy appears concerning the value of displacement, in particular for the thick case. Anyway, convergence is observed also for this model.

Table 2.2. Quarter of cylinder under pressure – Convergence study of displacement *w* at point *O* for the thin shell case.

Mesh	Models	Displacement w ($\times 10^{-1}$mm)	Error (%)
10×80×80	Reference	-5.176	–
1×6×6	Solid	-5.854	13
	HOSS	–	–
2×10×10	Solid	-5.259	1.6
	HOSS	-5.271	1.8
4×20×20	Solid	-5.169	0.1
	HOSS	-5.182	0.1

Table 2.3. Quarter of cylinder under pressure – Convergence study of displacement *w* at point *O* for the thick shell case.

Mesh	Models	Displacement w ($\times 10^{-1}$mm)	Error (%)
10×80×80	Reference	-1.691	–
1×4×4	Solid	-1.509	10
	HOSS	–	–
2×8×8	Solid	-1.656	2.1
	HOSS	-1.652	2.3
4×16×16	Solid	-1.689	0.1
	HOSS	-1.688	0.2

2.4.2.3 Displacements and stresses in the thin shell case

Displacements and stresses are observed over the whole structure. Fig. 2.13 shows a comparison between the results obtained with solid, MFOSS and HOSS models. The results presented in this section are obtained with the 4×20×20 mesh, which meets the convergence criterion as highlighted in Section 2.4.2.2. The three models lead to quite similar results for displacements as well as for von Mises stresses.

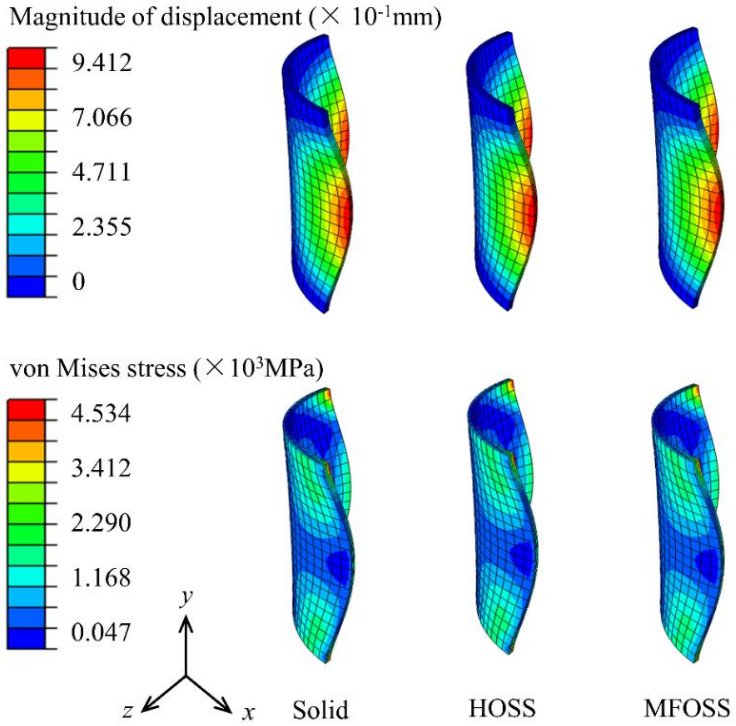

Fig. 2.13. Quarter of cylinder under pressure - Displacement and von Mises stress distributions in the thin shell case.

Fig. 2.14 shows the distribution of vertical displacement in the global coordinate system and von Mises stress on the lower face along the *AB* line defined in Fig. 2.12. The solid-shell models are

compared with the solid model and a shell model. Again the 4×20×20 mesh is used for the solid and solid-shell models. For the shell model, a 1×20×20 mesh, which meets the convergence criterion, is considered. All the models give very similar results for displacements and von Mises stress.

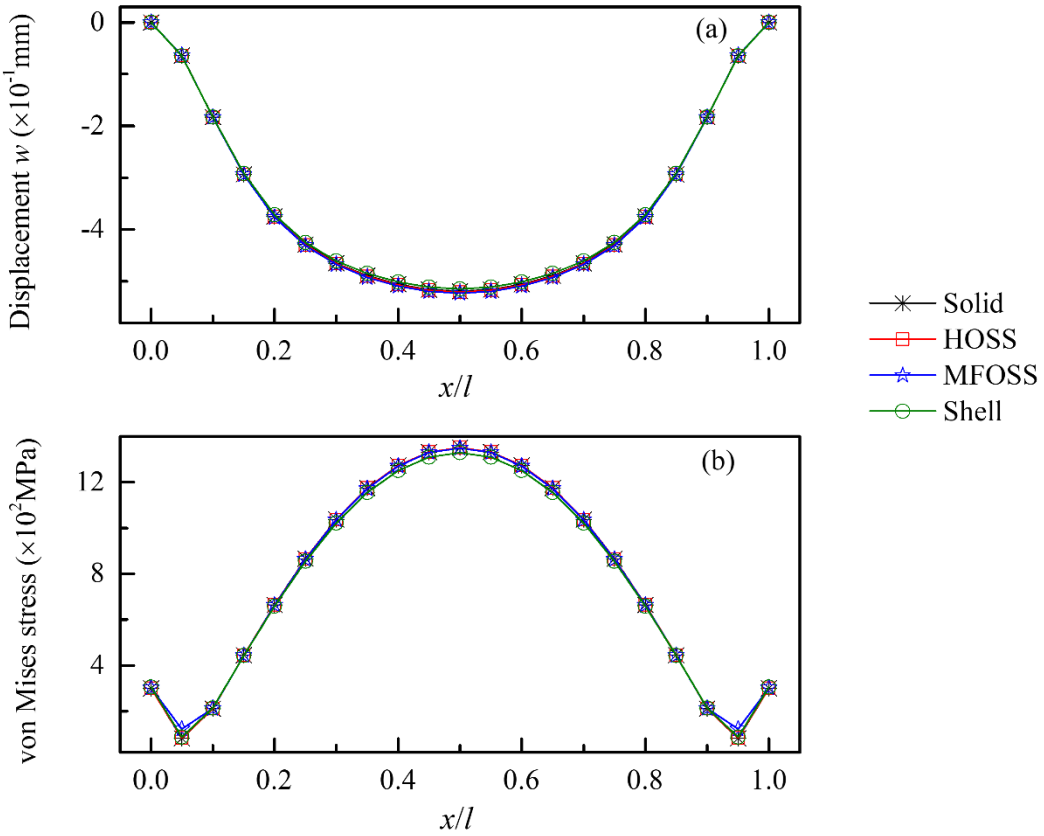

Fig. 2.14. Quarter of cylinder under pressure – Distribution of vertical displacement (a) and von Mises stress (b) along a line on the lower face, in the thin case.

2.4.2.4 Displacements and stresses in the thick shell case

Displacements and stresses are observed over the whole structure. Fig. 2.15 shows a comparison between the results obtained with solid, MFOSS and HOSS models. The results presented in this section are obtained with the 4×16×16 mesh, which meets the convergence criterion. The three models lead to close results, some minor differences can be observed on displacements as well as on von Mises stresses.

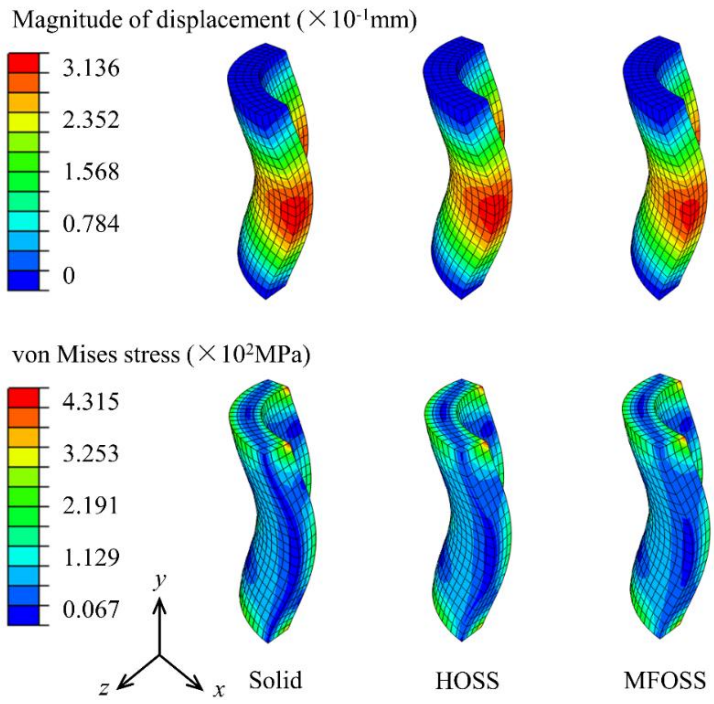

Fig. 2.15. Quarter of cylinder under pressure - Displacement and von Mises stress distributions in the thick shell case.

Fig. 2.16 shows the distribution of vertical displacement in the global coordinate system and von Mises stress on the lower face along the *AB* line defined in Fig. 2.12. The solid-shell models are compared with the solid model and a shell model. Again the 4×16×16 mesh is used for the solid and solid-shell models. For the shell model, a 1×20×20 mesh, which meets the convergence criterion, is considered. For displacement, the HOSS model fits very well with the solid one. Some minor error is observed with the MFOSS model. For von Mises stress, again the HOSS model fits very well with the solid one. The MFOSS model leads to some errors. As explained for the first example, this is due to a rough calculation of the transverse shear stresses which are not negligible in the thick case. These results confirm that the HOSS model is necessary to correctly predict the transverse shear effects and so the mechanical behaviour of a thick shell. Results obtained with the HOSS approach are fully satisfactory. It is worth noting that in this thick shell case, the shell model gives bad displacement and von Mises stress results. This is due to the fact that the distributed pressure loading is applied on a face of the structure. This surface is naturally correct with a solid or solid-shell model, but with the shell approach, the mid-surface is used to define loading. For a curved structure, the area of this mid-surface is significantly wrong in the thick case, leading to an error on loading. This is also a limitation of the shell approach and from this point of view the solid-shell approach is preferable.

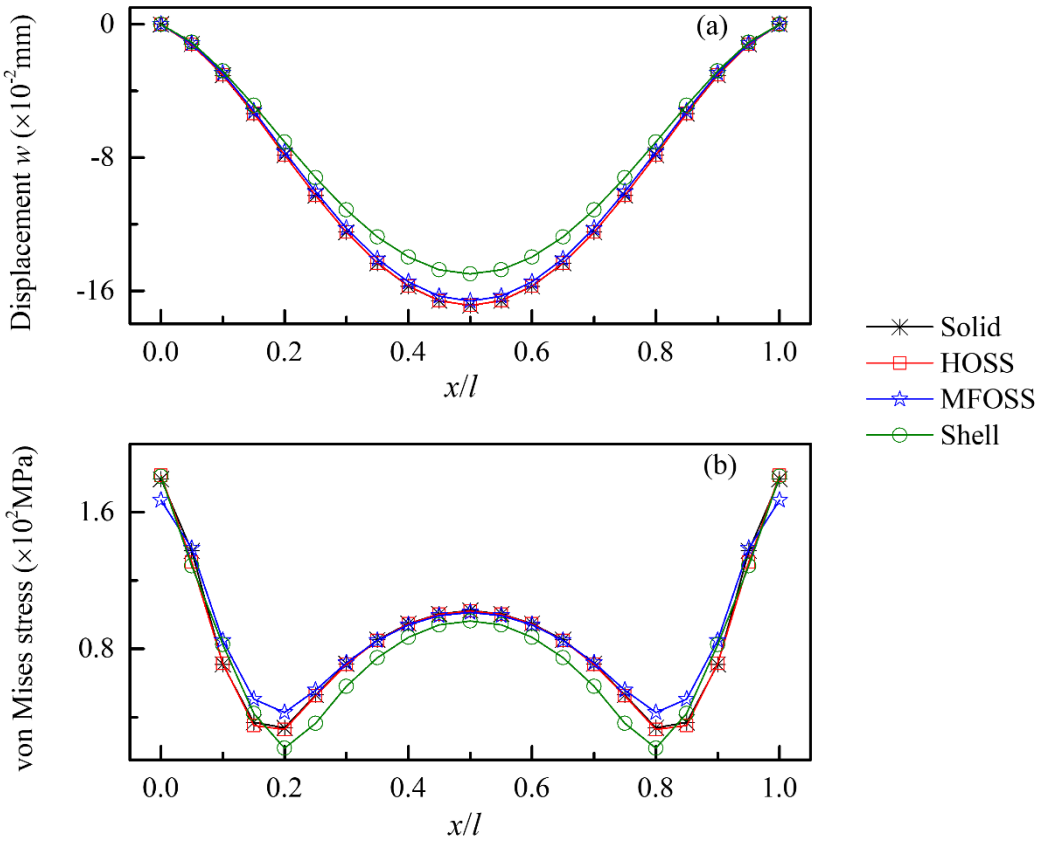

Fig. 2.16. Quarter of cylinder under pressure – Distribution of vertical displacement (a) and von Mises stress (b) along a line on the lower face, in the thick case.

2.4.2.5 Accuracy synthesis of solid-shell models

Table 2.4 summarizes the errors obtained with the solid-shell models, in the thin and thick quarter of cylinder cases. As for example 1, these errors are calculated on the maximal displacement and on the maximum von Mises stress. The results are similar compared with example 1. The MFOSS model gives good results in the thin shell case. The errors are less than 0.5% for the displacement and about 2% for the von Mises stress. As for example 1 even in this case the HOSS model is better because transverse shear effects are small but not completely negligible. In the thick shell case, the HOSS model remains very satisfactory, indeed the errors are limited to about 1%, while the MFOSS model leads to some discrepancy. Indeed, the error is about 2% for the displacement and 7% for the von Mises stress.

In summary, from a theoretical point of view, the HOSS model gives excellent results in the thin as well as the thick cases, while the MFOSS model is convenient for thin structures only. These results show that for thick structures, the higher-order theory introduced by Reissner [21] and Lo et al. [22] is more efficient than the first-order theory. Concerning numerical aspects, the approach based on a solid model constrained by through-the-thickness kinematic relations to obtain a solid-shell model works well. Moreover, the concept of master and slave nodes, involving linear equations between the concerned degrees of freedom, is also efficient.

In addition, this study was performed again with the 8-node solid hexahedral element C3D8I [62] of Abaqus. Similar results have been obtained, demonstrating that the methodology proposed can be applied with any efficient solid finite element.

Table 2.4. Quarter of cylinder under pressure – Accuracy synthesis of maximal displacement and maximal von Mises stress.

Examples	Models	Displacement w		von Mises stress	
		Maximum ($\times 10^{-1}$mm)	Error (%)	Maximum ($\times 10^{2}$MPa)	Error (%)
Thin cylinder	Solid	-8.805	–	45.34	–
	HOSS	-8.792	0.1	45.23	0.2
	MFOSS	-8.773	0.4	44.50	1.9
Thick cylinder	Solid	-2.415	–	4.315	–
	HOSS	-2.406	0.4	4.261	1.3
	MFOSS	-2.369	1.9	4.013	7.0

2.4.3 Quarter of hyperboloid under pressure

2.4.3.1 Presentation of the example

The third example presented in Fig. 2.17 is a quarter of hyperboloid, clamped along its two ends and submitted to a pressure applied on the outer surface. The outside radius at ends is 200 mm and the outside radius in the middle is 150 mm. Two values of thickness: 10mm and 50 mm, lead respectively to thin and thick shell cases. This example also allows natural coupling between membrane and bending effects but with a structure more complex than a quarter of cylinder. To apply kinematic relations on the solid model to obtain a solid-shell model, local coordinate systems are created for each line of nodes through the thickness of the structure. The equations involving the degrees of freedom concerned are applied using these local coordinate systems.

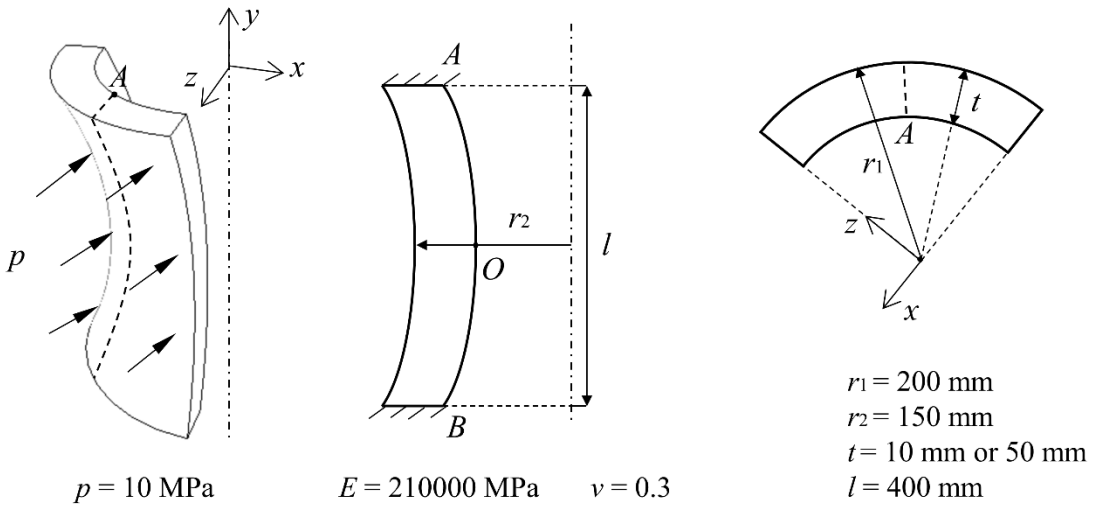

Fig. 2.17. Quarter of hyperboloid under pressure – Presentation of the example.

2.4.3.2 Convergence study

A convergence study of mesh is presented. The approach already detailed for the first and second examples is repeated here. Again, the twenty-node hexahedron element C3D20 from Abaqus is used. The evolution of displacement on the inner surface in the center of the structure (see point *O* in Fig. 2.17) is observed, for several mesh refinement levels. A solid model with a very fine 10×80×80 mesh is chosen to provide the reference results. It is considered that convergence is achieved if the error is less than 0.5% compared with this reference model. Results are reported in Tables 2.5 and 2.6 for the HOSS model. Convergence is obtained with 4×16×20 mesh for the thin and thick cases. Moreover, convergence characteristics are similar for the HOSS model and the solid model. Due to basic assumptions used, for the MFOSS model the convergence criterion defined above is never achieved because this model does not exactly converge to the reference solution. Indeed, some discrepancy appears concerning the value of displacement, in particular for the thick case. Anyway, convergence is observed also for this model.

Table 2.5. Quarter of hyperboloid under pressure – Convergence study of displacement *w* at point *O* for the thin shell case.

Mesh	Models	Displacement *w* ($\times 10^{-1}$mm)	Error (%)
8×32×40	Reference	-7.458	–
1×4×5	Solid	-7.137	4.3
	HOSS	–	–
2×8×10	Solid	-7.384	1.0
	HOSS	-7.379	1.1
4×16×20	Solid	-7.445	0.2
	HOSS	-7.444	0.2

Table 2.6. Quarter of hyperboloid under pressure – Convergence study of displacement *w* at point *O* for the thick shell case.

Mesh	Models	Displacement *w* ($\times 10^{-1}$mm)	Error (%)
8×32×40	Reference	-1.235	–
1×4×5	Solid	-1.155	6.5
	HOSS	–	–
2×8×10	Solid	-1.219	1.3
	HOSS	-1.214	1.7
4×16×20	Solid	-1.232	0.2
	HOSS	-1.229	0.5

2.4.3.3 Displacements and stresses in the thin shell case

Displacements and stresses are observed over the whole structure. Fig. 2.18 shows a comparison between the results obtained with solid, MFOSS and HOSS models. The results presented in this section are obtained with the 4×16×20 mesh, which meets the convergence criterion. The three models lead to quite similar results for displacements as well as for von Mises stresses.

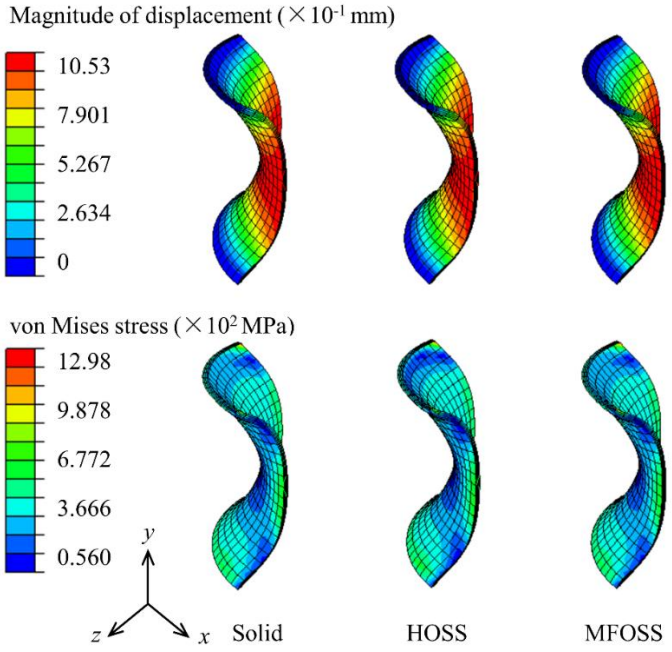

Fig. 2.18. Quarter of hyperboloid under pressure - Displacement and von Mises stress distributions in the thin shell case.

Fig. 2.19 shows the distribution of vertical displacement in the global coordinate system and von Mises stress on the inner surface along the *AB* line defined in Fig. 2.17. The solid-shell models are compared with the solid model and a shell model. The 4×16×20 mesh is used for the solid and solid-shell models. For the shell model, a 1×16×20 mesh, which meets the convergence criterion, is considered. The HOSS model and the reference solid model give very similar results for displacements and von Mises stress. The MFOSS model leads to some errors for stresses, that is due to a rough calculation of the transverse shear stresses which are not negligible in this relatively thin case. The shell model gives different results both for displacements and stresses because it is based on the mid-surface, leading to some geometrical modeling differences at the ends.

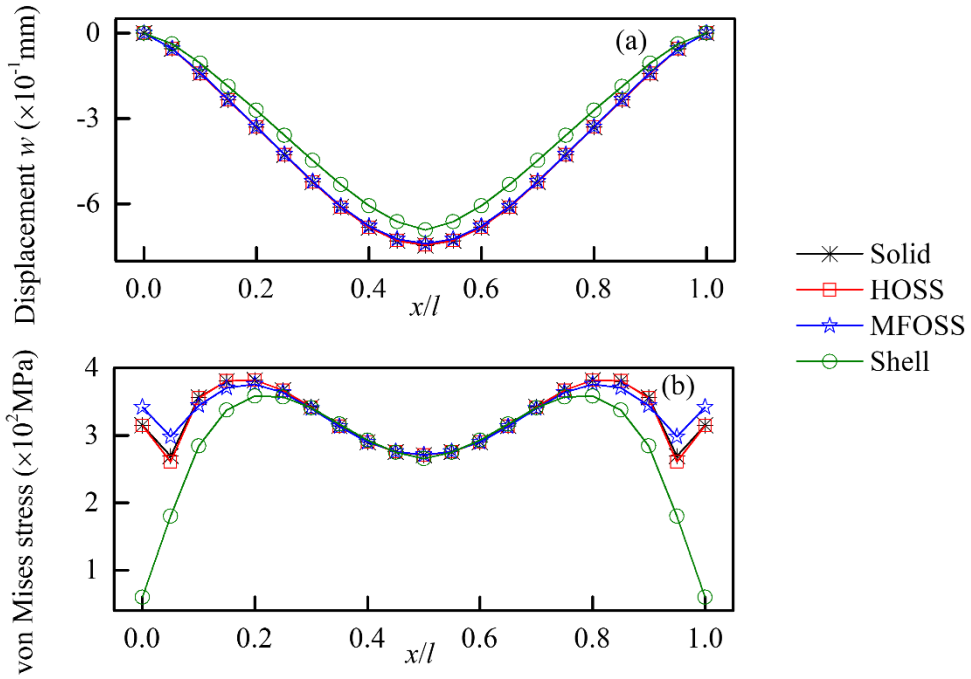

Fig. 2.19. Quarter of hyperboloid under pressure – Distribution of vertical displacement (a) and von Mises stress (b) along a line on the lower face, in the thin case.

2.4.3.4 Displacements and stresses in the thick shell case

Displacements and stresses are observed over the whole structure. Fig. 2.20 shows a comparison between the results obtained with solid, MFOSS and HOSS models. The results presented in this section are obtained with the 4×16×20 mesh. The three models lead to close results, some minor differences can be observed on displacements as well as on von Mises stresses.

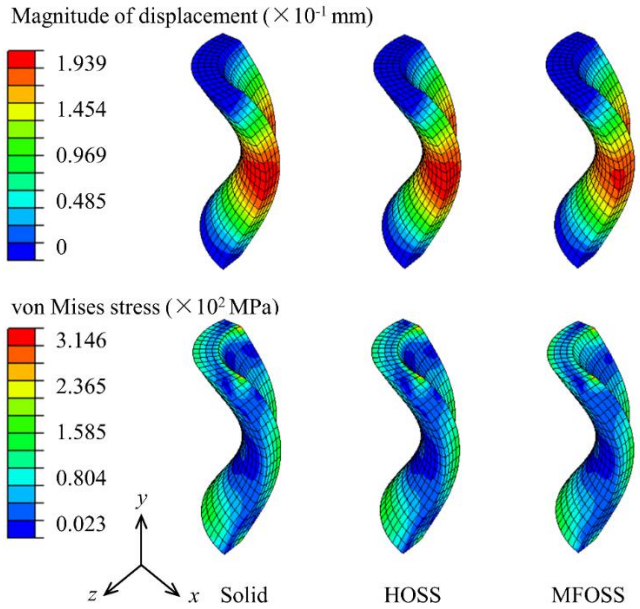

Fig. 2.20. Quarter of hyperboloid under pressure – Displacement and von Mises stress distributions in the thick shell case.

Fig. 2.21 shows the distribution of vertical displacement in the global coordinate system and von Mises stress on the inner surface along the *AB* line defined in Fig. 2.17. The solid-shell models are compared with the solid model and a shell model. Again the 4×16×20 mesh is used for the solid and solid-shell models. For the shell model, a 1×16×20 mesh, which meets the convergence criterion, is considered. For both the displacement and von Mises stress, the HOSS model fits very well with the solid one. Some minor error is observed with the MFOSS model. As explained for the first and second examples, this is due to a rough calculation of the transverse shear stresses which are not negligible in the thick case. These results confirm that the HOSS model is necessary to correctly predict the transverse shear effects and so the mechanical behavior of a thick shell. Results obtained with the HOSS approach are fully satisfactory. It is worth noting that in this thick shell case, the shell model gives bad displacement and von Mises stress results. This is due to the fact that the distributed pressure loading is applied on a face of the structure. This surface is naturally correct with a solid or solid-shell model, but with the shell approach, the mid-surface is used to define loading. For a curved structure, the area of this mid-surface is significantly wrong in the thick case, leading to an error on loading. This is also a limitation of the shell approach and from this point of view the solid-shell approach is preferable. Another reason is as described for the thin case, the shell model is based on the mid-surface, leading to some geometrical modeling differences at the ends. It is also a limitation of the shell approach.

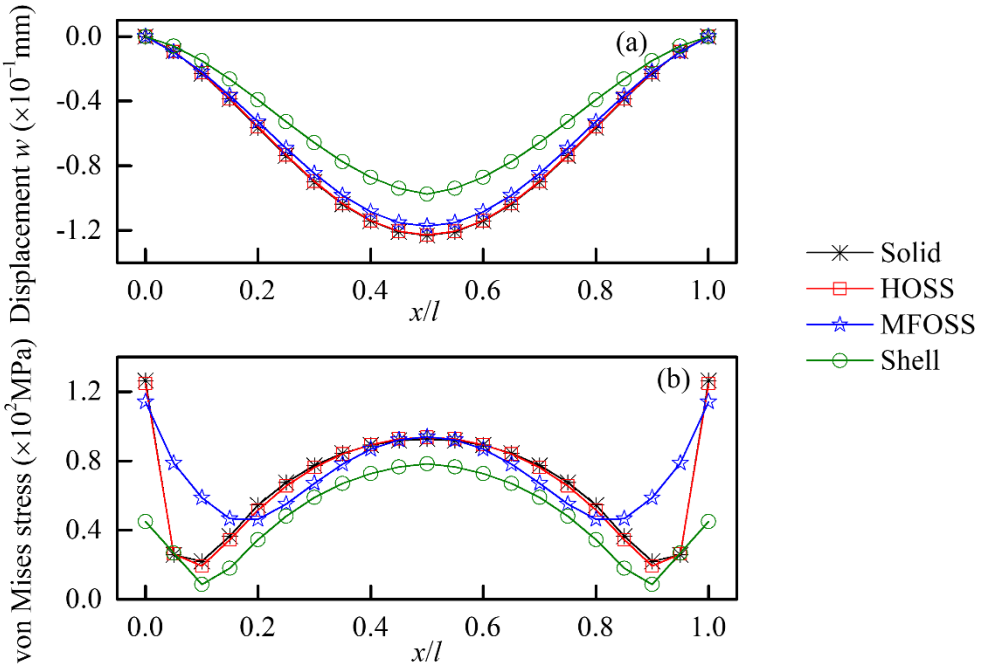

Fig. 2.21. Quarter of hyperboloid under pressure – Distribution of vertical displacement (a) and von Mises stress (b) along a line on the lower face, in the thick case.

2.4.3.5 Accuracy synthesis of solid-shell models

Table 2.7 summarizes the errors obtained with the solid-shell models, in the thin and thick shell cases. As for examples 1 and 2, these errors are calculated on the maximal displacement and on the

maximum von Mises stress. The MFOSS model gives good results in the thin shell case. The errors are less than 0.9% for the displacement and about 0.7% for the von Mises stress. The HOSS model is better because transverse shear effects are small but not completely negligible. In the thick shell case, the HOSS model remains very satisfactory, indeed the errors are limited to about 0.4%, while the MFOSS model leads to some discrepancy. Indeed, the error is about 5% for the displacement and 7% for the von Mises stress. In summary, from a theoretical point of view, the HOSS model gives excellent results in the thin as well as the thick cases, while the MFOSS model is convenient for thin structures only. Concerning numerical aspects, the approach based on a solid model constrained by through-the-thickness kinematic relations to obtain a solid-shell model works well. Moreover, the concept of master and slave nodes, involving linear equations between the concerned degrees of freedom, is also efficient.

Table 2.7. Quarter of hyperboloid under pressure – Accuracy synthesis of maximal displacement and maximal von Mises stress.

Examples	Models	Displacement w		von Mises stress	
		Maximum ($\times 10^{-1}$mm)	Error (%)	Maximum ($\times 10^{2}$MPa)	Error (%)
Thin hyperboloid	Solid	-7.868	–	12.98	–
	HOSS	-7.868	0	12.99	0.1
	MFOSS	-7.797	0.9	13.07	0.7
Thick hyperboloid	Solid	-1.456	–	3.146	–
	HOSS	-1.454	0.1	3.159	0.4
	MFOSS	-1.385	4.9	2.940	6.5

2.4.4 Model size

Compared with the solid model, our solid-shell models lead to a reduction of the number of degrees of freedom, which is interesting from a computational time point of view. Fig. 2.22 shows the comparison of the number of degrees between the solid approach and the solid-shell ones. The results are reported for the plate example, but the same trends can be observed also on other examples. The reduction of the number of degrees of freedom increases with the number of elements, which is a hopeful characteristic of the solid-shell approach proposed. As mentioned in Section 2.3.4, the number of master degrees of freedom remaining after application of equations is independent of the number of nodes through the thickness. Consequently, the size of the final solid-shell model does not depend on the number of nodes through the thickness. For fine meshes, the gain is quite significant with solid-shell models compared with solid models. Of course, the gain obtained with the MFOSS model is bigger compared with the HOSS model because it requires a smaller number of master nodes.

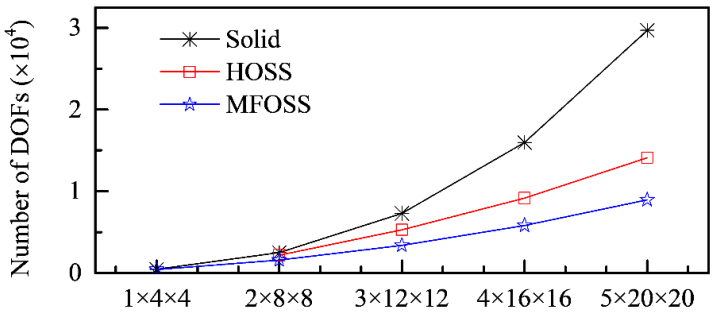

Fig. 2.22. Influence of the meshing refinement level on the number of degrees of freedom for different modeling approaches.

It's useful to compare the MFOSS and HOSS models with classical shell element performances in terms of model size. Fig. 2.23 shows the comparison of the number of degrees of freedom between different modeling approaches. The results are reported for the quarter of cylinder example, but the same trends can be observed also on other examples. For solid and solid-shell models, the results are reported for a mesh which meets the convergence condition, that is to say 4×20×20 and 4×16×16 in the thin and thick cases respectively. In addition, a shell model is also considered, with the same refinement level through the mid-surface of the structure, in order to compare the solid-based approaches and the shell one. The trends observed are the same for the thin and thick cases. Results confirm that solid-shell approach allows quite significant reduction of the problem size, compared with the solid approach. Moreover, the number of degrees of freedom is close for the MFOSS model and the shell one. Indeed, the difference is limited to 15%. This means that in term of model size, these two approaches are comparable. From the model size point of view, the HOSS model is intermediate between the shell model and the solid one.

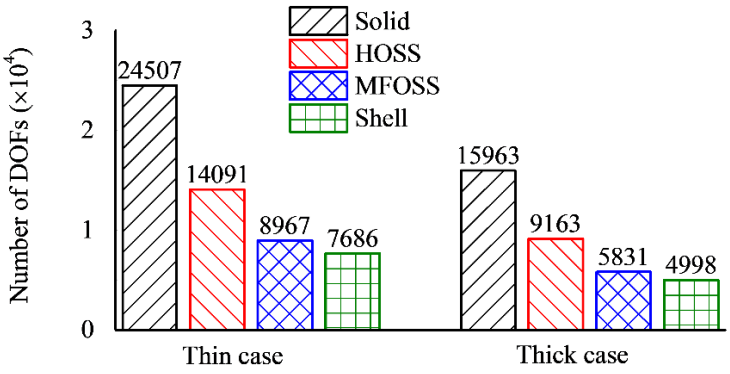

Fig. 2.23. Comparison of the number of degrees of freedom between different modeling approaches.

2.5 Vibration examples

The new proposed solid-shell approach with FOSS, MFOSS and HOSS models is now used for the treatment of two examples in the context of vibration analysis: a square plate and a cylindrical panel, in

both thin and thick cases. A convergence study is made for each example. The frequencies and mode shapes obtained with solid-shell and the reference solid models are compared.

2.5.1 Square plate

2.5.1.1 Presentation of the example

The geometries of square plates described in Fig 2.4 are used here in the context of free-free vibration analysis, with the density equal to 7.89×10^{-9} t/mm^3. The *l*/*h* ratio equals 20 and 5, representing the relatively thin and very thick cases respectively.

2.5.1.2 Convergence study

The thin and very thick structures are discretized with the twenty-node hexahedral element C3D20 in Abaqus. For the two square plates, a convergence study is made for the free-free vibration analysis of the first eight natural frequencies. For the reference solid, HOSS and MFOSS models, the 4×24×24 and 4×16×16 meshes meet the convergence requirement for the relatively thin and very thick plates respectively. For the shell models, the 1×24×24 and 1×16×16 meshes, which meet the convergence criterion, are considered for the relatively thin and very thick plates respectively.

2.5.1.3 Mode shapes

For the reference solid, HOSS, and MFOSS models in the relatively thin plate case, the first eight mode shapes are shown in Fig. 2.24. It is observed the mode 7 is a torsion mode, modes 8, 9, 12, 13 and 14 are bending modes, modes 10 and 11 combine bending and torsional effects. All the models give very similar results for these modes.

The first eight mode shapes for the reference solid, HOSS, and MFOSS models in the very thick plate case, are shown in Fig. 2.25. It is observed mode 7 is a torsion mode, modes 8 and 9 are bending modes, modes 10 and 11 combine the torsion and bending effects, modes 12, 13 and 14 are the membrane modes. All the models presented here lead to similar mode shapes.

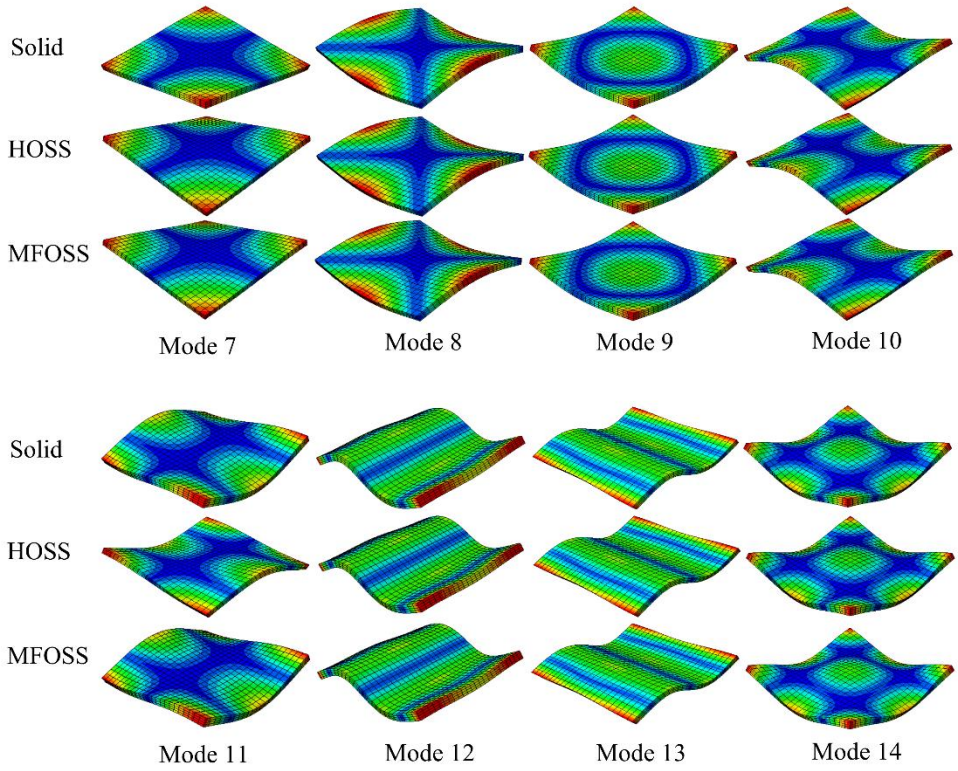

Fig. 2.24. Square plate in free-free vibration – First eight mode shapes obtained with the reference solid, HOSS and MFOSS models for the relatively thin case.

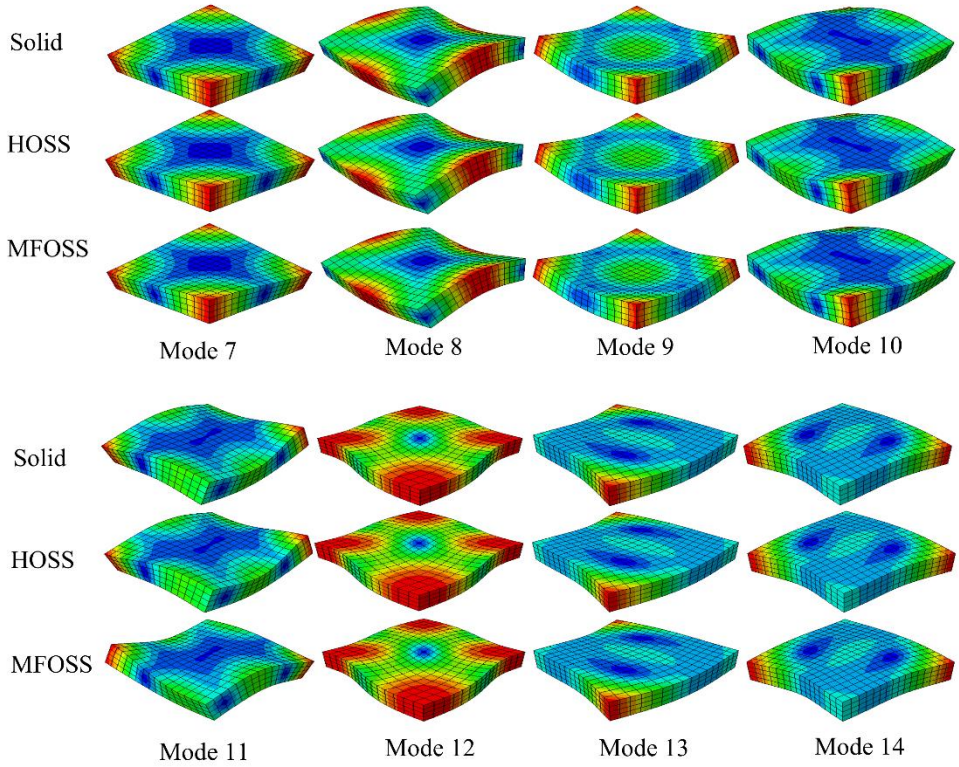

Fig. 2.25. Square plate in free-free vibration – First eight mode shapes obtained with the reference solid, HOSS, and MFOSS models for the very thick case.

For a further comparison of these modes between our solid-shell models and the reference solid models, the Modal Assurance Criterion (MAC) is used. The MAC is expressed as:

$$MAC(\phi_s, \phi_{ss}) = \frac{\phi_s \cdot \phi_{ss}}{\|\phi_s\| \times \|\phi_{ss}\|} \tag{2.22}$$

where ϕ_s and ϕ_{ss} are respectively the eigenvectors for the solid model and the solid-shell model.

The MAC values calculated between the HOSS model and the reference solid model for both the relatively thin and very thick square plates are reported in Fig. 2.26. The MAC values are always greater than 0.9, it indicates strongly correlated modes. Very similar results have been observed for the MAC values between MFOSS model and reference solid model. For both the relatively thin and very thick plates, a perfect consistency is observed between the MFOSS, HOSS and the reference solid models.

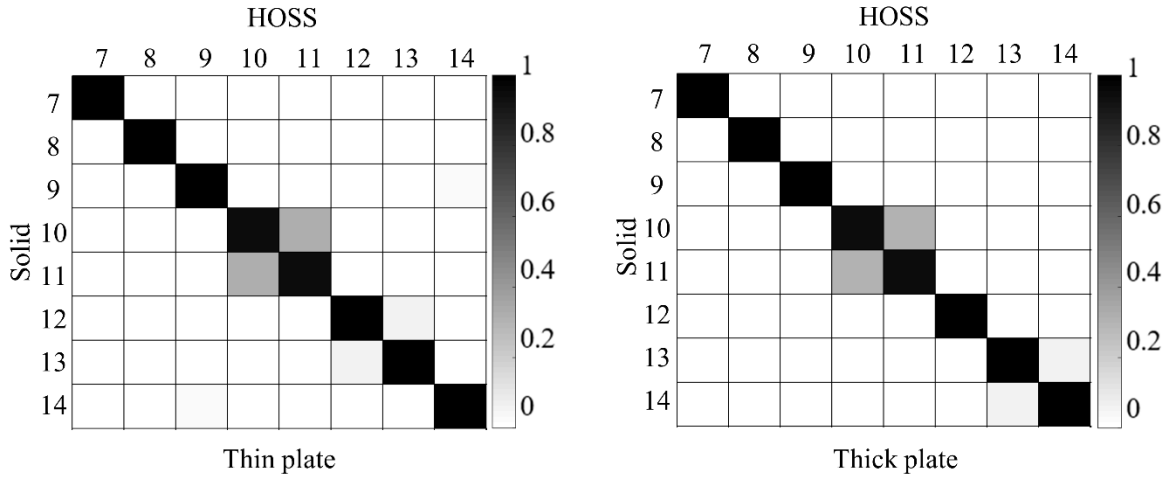

Fig. 2.26. Square plate in free-free vibration – MAC matrix between the solid-shell and the reference models for the relatively thin and very thick plates.

2.5.1.4 Frequencies

The first eight angular frequencies of the square plate are obtained for reference solid, HOSS, MFOSS, FOSS and shell models in the relatively thin case, and for reference solid, HOSS, MFOSS and shell models in the thick case. In order to compare the results of these models with the analytical results of Liew et al. [63] based on Mindlin's plate theory for thick plates, the non-dimensional frequency parameter is introduced. This parameter is expressed as

$$\lambda = \omega l^2 \sqrt{12 \times (1 - \nu^2)\, \rho / E h^2} \tag{2.23}$$

where ω is the angular frequency, ρ is the material density and other quantities are defined in Fig. 2.4.

The non-dimensional frequency parameters are reported in Table 2.8 for the relatively thin and thick cases. Errors on this parameter compared with the reference solid models are presented in Table 2.9 for solid, HOSS, MFOSS, FOSS, shell and Liew's [63] models. It is observed the FOSS model gives bad results for the non-dimensional frequency parameter due to a spurious σ_{zz} stress state, as described in static examples. The FOSS error is systematically significant and greater than 10% for mode 9. The

MFOSS models provide correct results compared with the reference solid models for both the relatively thin plate and very thick plate. But for some complex modes, especially for the very thick plate, errors more than 1% are observed. Indeed, the transverse shear stiffness is not well evaluated in this case. The HOSS models highlight results very close to the reference results, with errors less than 0.1% for both the relatively thin plate and the very thick plate. The shell models also give good results. The results obtained by Liew [63] for the very thick plate have a good consistency with the reference solid, HOSS and shell models.

Table 2.8. Square plate in free-free vibration – Non-dimensional frequency parameters of different models for the relatively thin and very thick plates.

l/*h* ratio	Model	Mode							
		7	8	9	10	11	12	13	14
20	Solid	13.144	19.426	24.018	33.726	33.726	59.470	59.470	60.732
	HOSS	13.144	19.426	24.018	33.726	33.726	59.470	59.470	60.732
	MFOSS	13.170	19.431	24.033	33.808	33.808	59.587	59.587	60.972
	FOSS	13.242	19.802	27.109	34.768	34.768	63.191	64.820	64.820
	Shell	13.144	19.426	24.018	33.721	33.721	59.480	59.480	60.712
5	Solid	11.711	17.434	21.253	27.650	27.650	40.191	42.775	42.775
	HOSS	11.712	17.435	21.256	27.657	27.657	40.191	42.775	42.775
	MFOSS	11.826	17.514	21.402	28.035	28.035	40.198	42.832	42.832
	Shell	11.705	17.413	21.216	27.592	27.592	40.233	42.864	42.864
	Liew et al. [51]	11.701	17.400	21.194	27.574	27.574	–	–	–

Table 2.9. Square plate in free-free vibration – Errors (%) on non-dimensional frequency parameters of different models for the relatively thin and very thick plates.

l/*h* ratio	Model	Mode							
		7	8	9	10	11	12	13	14
20	HOSS	0.0	0.0	0.0	0.0	0.0	0.0	0.0	0.0
	MFOSS	0.2	0.0	0.1	0.2	0.2	0.2	0.2	0.4
	FOSS	0.7	1.9	12.9	3.1	3.1	6.3	9.0	6.7
	Shell	0.0	0.0	0.0	0.0	0.0	0.0	0.0	0.0
5	HOSS	0.0	0.0	0.0	0.0	0.0	0.0	0.0	0.0
	MFOSS	1.0	0.5	0.7	1.4	1.4	0.0	0.1	0.1
	Shell	0.1	0.1	0.2	0.2	0.2	0.1	0.2	0.2
	Liew et al. [51]	0.1	0.2	0.3	0.3	0.3	–	–	–

2.5.2 Cylindrical panel

2.5.2.1 Presentation of the example

The second vibration example presented in Fig. 2.27 is a cylindrical panel clamped along its four edges. Density of the material, characteristic of steel, is equal to 7.89×10^{-9} t/mm^3. Two cases, one with an outside radius of 400 mm and a thickness of 4 mm, the other with an outside radius of 200 mm and a thickness of 50 mm, leading respectively to a thin cylindrical panel (R/t=100) and a thick one (R/t=4). The main difference with the plate example is that the structure is now curved. For this example, to obtain a solid-shell model, local coordinate systems are created for each line of nodes through the thickness of the structure to apply kinematic relations on the solid model. The equations involving the degrees of freedom concerned are applied using these local coordinate systems.

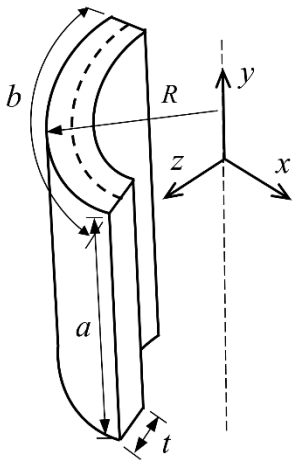

E = 210000 MPa
v = 0.3
$a = b$ = 400 mm
R = 200 mm or 400 mm
t = 50 mm or 4 mm
$\rho = 7.89\times10^{-9}$ t/mm^2

Fig. 2.27. Clamped cylindrical panel in free vibration – Presentation of the example.

2.5.2.2 Convergence study

The thin and thick cylindrical panels are discretized with the twenty-node hexahedral element C3D20 in Abaqus. For the two cases, a convergence study of the first eight natural frequencies is made, considering clamped boundary conditions along the four edges. For the reference solid, HOSS and MFOSS models, the 4×20×20 mesh meets the convergence requirement for both the thin and thick panels. For the shell model, the 1×20×20 mesh, which meets the convergence criterion, is considered for both the thin and thick cases.

2.5.2.3 Mode shapes

For the reference solid, HOSS and MFOSS models in the thin cylindrical panel, the first eight mode shapes are shown in Fig. 2.28. All the models give very similar results for these modes.

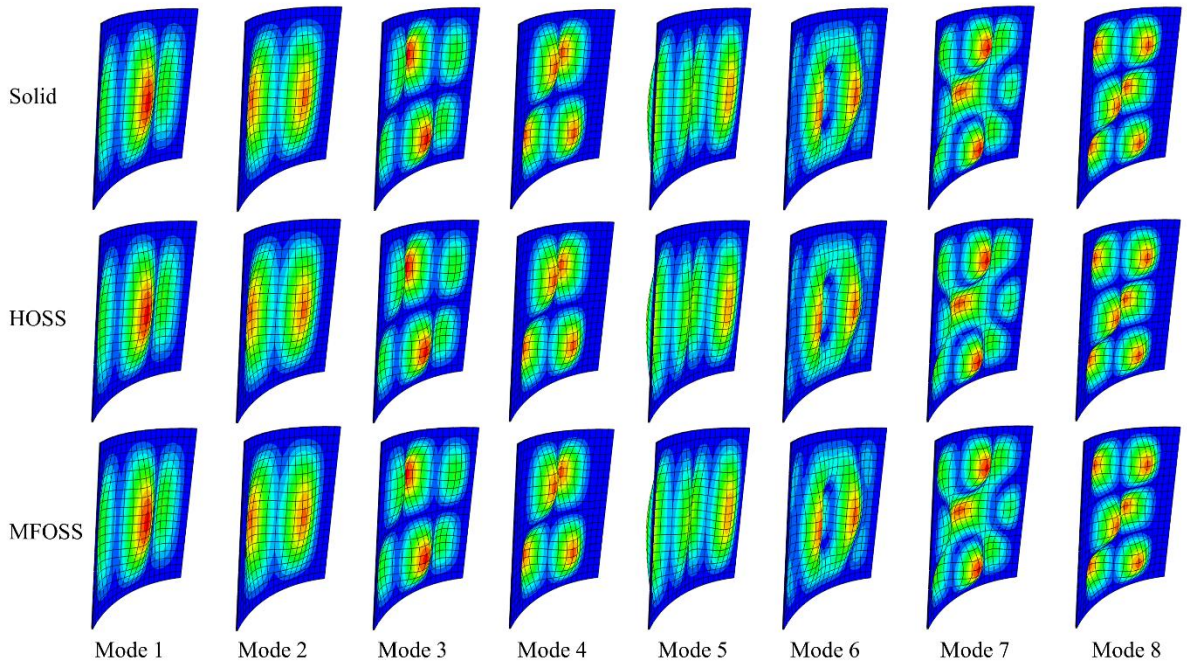

Fig. 2.28. Clamped cylindrical panel in free vibration – First eight mode shapes with the reference solid, HOSS, and MFOSS models for the thin case.

The first eight mode shapes for the reference solid, HOSS and MFOSS models in the thick cylindrical panel are shown in Fig. 2.29. The HOSS and MFOSS models lead to similar model shapes with the reference solid model.

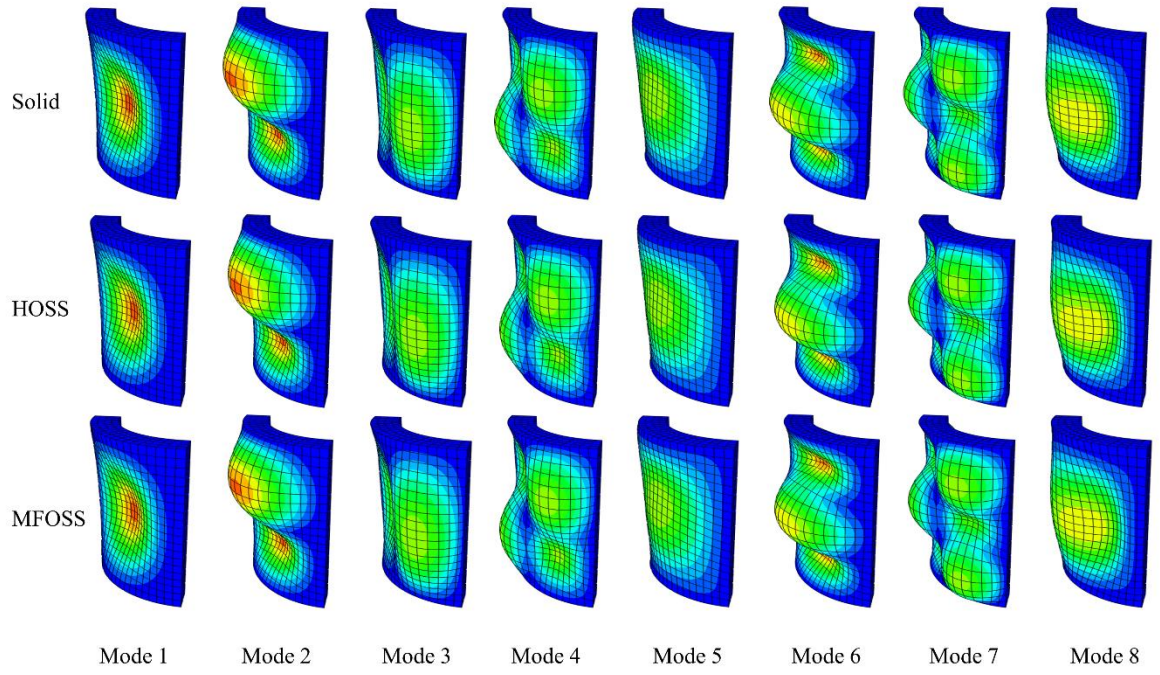

Fig. 2.29. Clamped cylindrical panel in free vibration – First eight mode shapes with the reference solid, HOSS, and MFOSS models for the thick case.

The MAC values calculated between the HOSS model and the reference solid model for both the thin and thick cylindrical panels are reported in Fig. 2.30. The MAC values are always greater than 0.9, it indicates strongly correlated modes. Very similar results have been observed for the MAC values calculated between MFOSS and reference solid. Perfect consistency is observed between the solid-shell models and the reference solid model for both the thin and thick cylindrical panels.

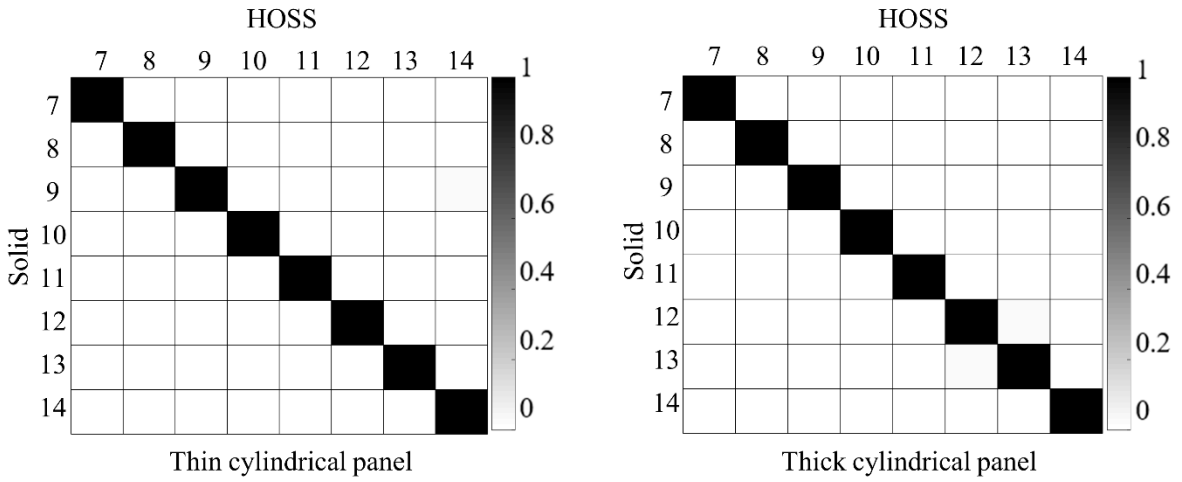

Fig. 2.30. Clamped cylindrical panel in free vibration – MAC matrix between the solid-shell and the reference models for the thin and thick panels.

2.5.2.4 Frequencies

The first eight angular frequencies of the cylindrical panel are obtained for reference solid, HOSS, MFOSS and shell models in the thin and thick cases. In order to compare the results of these models with the analytical results of Li et al. [64], the non-dimensional frequency parameter is calculated. The non-dimensional frequency parameters are reported in Table 2.10 for the thin and thick cases. Errors on this parameter compared with the reference solid models are reported in Table 2.11 for solid, HOSS, MFOSS, shell and Li's [64] models. The MFOSS models provide correct results compared with the reference solid models for the thin cylindrical panel. But in the thick case, moderate errors limited to about 3% are observed. Indeed, the transverse shear stiffness is not well evaluated in the thick case. The HOSS models show almost the same results as the reference solid ones for both the thin and thick cylindrical panels. The shell models provide satisfactory results for the thin cylindrical panel but gives an error limited to 3% for the thick one. The analytical solutions obtained by Li are similar to the results of the shell model for the thin case.

Table 2.10. Clamped cylindrical panel in free vibration – Non-dimensional frequency parameters of different models for the thin and thick panels.

R/*t* ratio	Model	Mode							
		1	2	3	4	5	6	7	8
100	Solid	141.29	144.67	208.43	218.73	229.41	283.76	286.38	289.09
	HOSS	141.35	144.70	208.49	218.79	229.57	283.89	286.46	289.21
	MFOSS	141.46	144.75	208.59	218.90	229.87	284.21	286.61	289.47
	Shell	140.33	144.42	207.87	218.13	227.55	281.82	285.86	287.85
	Li et al. [52]	140.41	144.44	207.76	217.91	226.34	279.92	285.47	286.96
4	Solid	42.72	52.99	54.30	67.49	69.63	70.87	86.76	88.52
	HOSS	42.77	53.05	54.41	67.61	69.65	70.95	86.91	88.60
	MFOSS	43.10	53.73	55.74	69.13	69.72	72.30	88.96	89.04
	Shell	42.10	52.44	52.89	65.87	69.35	70.26	84.84	89.28

Table 2.11. Clamped cylindrical panel in free vibration – Errors (%) on non-dimensional frequency parameters of different models for the thin and thick panels.

R/*t* ratio	Model	Mode							
		1	2	3	4	5	6	7	8
100	HOSS	0.0	0.0	0.0	0.0	0.0	0.0	0.0	0.0
	MFOSS	0.1	0.1	0.1	0.1	0.2	0.2	0.1	0.1
	Shell	0.7	0.2	0.3	0.3	0.8	0.7	0.2	0.4
	Li et al. [52]	0.6	0.2	0.3	0.4	1.3	1.4	0.3	0.7
4	HOSS	0.1	0.1	0.2	0.2	0.0	0.1	0.2	0.1
	MFOSS	0.9	1.4	2.7	2.4	0.1	2.0	2.5	0.6
	Shell	1.5	1.0	2.6	2.4	0.4	0.9	2.2	0.9

2.6 Conclusion

A new and specific solid-shell approach dedicated to thin to very thick structures has been presented. Plate or shell displacement fields are directly applied on a solid finite element model which contains several elements through the thickness. Three theories based on kinematic assumptions have been considered. The classical first-order Mindlin-Reissner theory, a modified first-order theory and a higher-order theory lead to the FOSS, the MFOSS and the HOSS models respectively. Kinematic relations are imposed at nodes to meet through-the-thickness plate or shell displacement fields. From a numerical point of view, linear equations are applied on the assembled finite element model. The methodology relies on the slave and master nodes technique. Slave nodes are eliminated, leading to a reduction of the model size. Consequently, the number of degrees of freedom eliminated corresponds exactly to the number of equations applied. Three static examples have been presented: a clamped square plate under distributed loading, a quarter of cylinder under pressure and a quarter of hyperboloid under pressure. For the thin and thick cases, displacements and von Mises stresses have been observed. The FOSS model suffers from a Poisson thickness locking phenomenon due to an inconsistency between the 3D theory of elasticity and the constant through-the-thickness assumption for displacement *w*. Consequently, this FOSS model leads to unacceptable results. The MFOSS model is satisfactory for thin structures and leads to moderate errors in the thick case. The HOSS model gives excellent results in the thin as well as the thick cases, by comparison with the solid approach. These results show that for thick structures, the higher-order theory introduced by Reissner [21] and Lo et al. [22] leads to a significant gain compared to the first-order theory. Two vibration examples have also been presented. The frequencies obtained by solid, HOSS, MFOSS, FOSS and shell models under different boundary conditions lead to conclusions similar to the static case. The FOSS model leads to bad results. The MFOSS model works well for thin structures but gives less precise results in the thick case, especially for complex modes. The HOSS

model gives excellent frequencies in both thin and thick cases, compared with the solid approach. For the modal shapes, all the models give a good consistency. The approach presented is also efficient from a model size point of view. For the MFOSS model, it is comparable with that induced by the use of shell elements. The model size of the HOSS model is intermediate between the shell model and the solid one.

The perspectives of further applications of this approach are numerous. The results presented have been obtained with a twenty-node solid element but other solid finite elements may be exploited. More complex as well as industrial examples will be treated. The approach will be extended to multilayered composite structures. In this study, for a given finite element model, a choice has been made between first-order or higher-order theory. The application of this methodology is possible with different theories in the same model, in the context of an adaptive modeling approach in which different theories may be required depending on the area concerned. In this chapter, three theories have been considered but the methodology is compatible with any other theory. In particular, it can be exploited to test new higher-order plate and shell theories, avoiding the development of specific new finite elements which may lead to numerous numerical problems.

Chapter 3

A new solid-beam approach

In the context of adaptive modeling methodology, a new solid-beam approach dedicated to thin to very thick structures is presented. An original aspect is that beam displacement fields are directly applied on a solid finite element model which contains several elements within the cross-section. Moreover, any beam theory based on kinematic assumptions can be used, three theories for a beam in plane and two theories for a beam in space have been considered.

3.1 Introduction

A lot of natural or industrial structures have two dimensions small compared to the third one. These structures are called beams. The first beam theory was developed during the 18th century and is known as the Euler-Bernoulli beam theory. The main assumption is that plane sections normal to the undeformed neutral axis remain plane and normal to the deformed neutral axis. Many references describe this theory, see for example [65]. This theory, which does not consider transverse shear effects, is dedicated to thin beams. At the beginning of the 20th century, Timoshenko [66,67] proposed a more general beam theory which considers transverse shear effects as well as rotatory inertia. Sections normal to the undeformed neutral axis remain plane but not necessarily normal to the deformed neutral axis. This theory can be applied to thin and thick beams. The main shortcoming of this theory is that the displacement field leads to a constant transverse shear distribution throughout the cross-section, whereas it is rather quadratic. Timoshenko introduced the so-called transverse shear correction coefficient. Then a lot of research works concerned correction coefficients. Several papers have been specifically dedicated to this issue (Cowper [68], Jensen [69] and Hutchinson [70]).

Many higher-order beam theories were developed to better describe the deformation of beams. In 1975, Essenburg [71] enriched the displacement field with a quadratic transverse displacement assumption, leading to a theory which considers transverse shear and normal strain effects. Stephen and Levinson [72] proposed a second-order beam theory which considers transverse shear stresses, transverse direct stresses and rotatory inertia. It contains two coefficients depending on the cross-section shape. Levinson [73] proposed a higher-order beam theory for rectangular sections. The assumption that cross-sections normal to the undeformed neutral axis remain plane after deformation is abandoned. Indeed, a cubic distribution of axial displacement allows warping of the cross-sections. In this theory no shear coefficient is necessary. Rehfield and Murthy [74] proposed a refined beam theory accounting for

transverse shear and normal effects. In its initial version, the displacement field is order 5 for the axial displacement and order 4 for the transverse displacement. Rehfield and Murthy show that an axial displacement with order 3 and a transverse displacement of order 2 is quite satisfactory and gives results very close to the exact 3D elasticity solutions. Extension to beams in space requires the consideration of other effects. Bending in the second plane can be treated like bending in the first plane. However, torsion justifies specific developments. Initially de Saint-Venant studied this phenomenon leading to the Saint-Venant's uniform torsion theory [75]. Vlasov [76] introduced the non-uniform warping deformation and this theory is suitable for thin-walled open cross-sections. Benscoter [77] proposed a more general theory which is valid for thin-walled open and also for closed cross-sections. These theories were assessed namely by Shakourzadeh et al. [78], for different types of cross-sections. Other 3D beam approaches require cross-section analysis to determine sectional modes to enrich the displacement fields. The so-called Generalized Beam Theory (GBT), proposed by Schardt [79] and namely developed by Habtemariam et al. [80], exploits predetermined cross-sectional deformation modes for the description of warping. The identification of these modes may be obtained by a 2D finite element analysis of the cross-section (El Fatmi [81], Naccache et El Fatmi [82]). In this approach, modes are extracted from the computation of the so-called 3D Saint-Venant's problem. Solving the Saint-Venant problem led to other beam theories (Ladevèze and Simmonds [83], Romano et al. [84], Faghidian [85]). Complementary information about beam theories can be found in the books of Goodier and Timoshenko [86] and Carrera et al. [87]. Other variants of beam theories were proposed, in particular for multilayered composite structures and sandwich ones. The scope of this paper is limited to homogeneous structures, so multilayered composite structures which have led to a lot of research are not considered in this bibliography study.

The analytical resolution of examples treated with these theories is limited to some academic examples. Consequently, finite element method is widely used for the treatment of beam applications. For these finite elements, the most popular approach requires a discretization of the mid-axis and the degrees of freedom are displacements and rotations at nodes. A lot of formulations have been developed and assessed, to improve the performances of beam finite elements. Most of the formulations concern the Euler-Bernoulli and Timoshenko first-order beam theories. Finite elements based on Timoshenko theory or higher-order theories lead to several numerical problems. The most problematic one is locking, in particular transverse shear locking, which leads to very bad results when the structure is thin. Another numerical problem, linked to the techniques used for solving the locking phenomenon, is rank deficiency which may cause spurious zero-energy modes. Several techniques were proposed to alleviate these problems. The same numerical problems exist in plate and shell finite elements and many research works were developed for this type of elements. For further information, the reader can refer to the review paper of Cen and Shang [30] which describes the state of the art concerning Reissner-Mindlin plate elements. The methods and techniques proposed to improve plate and shell elements have also been tested and adapted for beam elements. The most popular ones are reduced or selective numerical

integration (Prathap and Bashyam [88], Reddy [89], Bouclier el al. [90], Adam et al. [91]), assumed natural strain (ANS) method and its variants (Bouclier el al. [90]), mixed approach (Addessi et al. [92]). Yunhua [93] and Reddy [89] presented the field consistence approach to prevent membrane locking as well as transverse shear locking, leading to efficient elements. Some beam elements have the superconvergence character and provide exact displacement and forces, using only one element per structural member (Shakourzadeh et al. [78], Reddy [89]).

Several developments commented hereafter are based on a continuum theory approach but lead to beam elements which finally contain displacements and rotations, that is to say classical beam degrees of freedom. Their geometry is defined by the mid-axis, just like a classical beam element. In some cases, additional degrees of freedom are considered for representing warping of the cross-section. Lee and Kim [95] proposed the discretization of the cross-section of a beam to consider a refined warping effect. Degrees of freedom are displacements and translations, as well as numerous additional degrees of freedom for warping. Zivkovic [96] developed a beam superelement which contains 3D continuum theory for the description of the deformation of the cross-section. Curiel Sosa et al. [97] developed a continuum-based beam element which is an extension of a formulation proposed by Belytschko et al. [98], in the framework of explicit-FEM. This element uses the concept of master and slave nodes to impose beam theory kinematic assumptions. Yoon et al. [99,100] proposed a continuum-based element built from an assemblage of solid elements. Again, beam theory assumptions are applied at cross-sectional nodes.

Another possibility is to exploit only the solid geometry, in this case a mid-axis geometry is not required, leading to the so-called solid-beam element. This approach has several advantages. First solid and solid-beam elements can be used in the same model, without difficulty. On the contrary, using classical beam and solid elements in the same model requires the development of specific solid-to-beam techniques to correctly connect beam and solid elements (Ziyaeifar and Noguchi [94]). A second advantage is that there is no need to make and exploit a mid-axis mesh, which may lead to severe difficulties and some errors for complex applications. Moreover, in the solid-beam approach, all terms of the strain and stress tensors can be considered and a three-dimensional constitutive law can be used, even if this issue may lead to some difficulties known as the thickness locking phenomenon mentioned in this paper. Finally loading can be naturally applied on the top or bottom faces of the structure. On the contrary of elements described above, a solid-beam element looks like a solid element from a geometry point of view. Moreover, degrees of freedom are only displacements. Inspired by solid-shell elements, Frischkorn and Reese [11], who introduced the “solid-beam” expression in 2013, proposed an eight-node solid-beam element with only displacement degrees of freedom. The formulation is derived from the solid-shell formulation of Schwarze and Reese [101]. To prevent locking problems, assumed natural strain and enhanced assumed strain methods embedded in a reduced integration technique, are applied. For several linear or nonlinear examples, good results are obtained by using only one element

within the cross-section. Frischkorn and Reese [102] applied this solid-beam element for the analysis of Nitinol stents.

In this chapter, a new solid-beam approach, based on applications of first-order or higher-order beam equations to standard solid finite element models, is presented. Our approach aims to reduce the number of degrees of freedom of the solid mesh by imposing displacement fields of beam theories. The chapter is organized as follows. In Section 3.2, the basic ideas of the methodology proposed, as well as the first-order and higher-order theories of interest, are recalled. In Section 3.3, the approach relying on master and slave nodes concept is described. In Section 3.4, two static examples, namely a straight beam and a curved beam, in the thin and thick cases, are treated. In Section 3.5, two free-free vibration examples with the same structures as the static examples are treated. Moreover, a comparison with solid and beam models in terms of model size is presented. Some conclusions and perspectives are drawn in Section 3.6.

3.2 Presentation of a new solid-beam approach – theoretical aspects

3.2.1 Basic ideas

The new solid-beam approach is developed in the context of a general adaptive modeling methodology using solid elements only, for any type of structure. As stated above, it is often justified to apply solid theory in some areas affected by local effects, but beam or shell theory is suitable on the rest of the structure. The use of different types of elements in the same model leads to meshing difficulties and mechanical incompatibilities of the displacement field at the interfaces between beam, shell and solid areas. Namely, beam and shell elements contain displacements and rotations but solid elements contain only displacements. Specific numerical treatment is necessary at the interfaces to improve compatibility between the different meshing areas. This approach involves theoretical problems in all cases as well as practical difficulties for complex structures. Our adaptive modeling method uses only solid elements and uniform meshes over the structure. There is no specific treatment in solid areas, and beam or shell displacement fields are applied in the solid-beam or solid-shell areas respectively, by using a specific approach.

In this chapter, the formulation associated with the solid-beam areas is presented and assessed. Classically, to develop beam finite element models, first equations of the 3D theory of elasticity are modified to give new beam theory equations. Then, based on these equations, a beam finite element is developed, leading to a 1D mesh. The contrary is proposed here. The structure is first modeled with solid finite elements, then equations throughout the cross-section are applied directly on the solid model to modify the system of algebraic equations and obtain the beam numerical solution. The main characteristics of the new solid-beam approach are described below.

– The solid-beam model must give results very close to the reference results given by the solid model.

- Only solid elements without severe locking phenomena are used. In this chapter, an existing hexahedral element with twenty nodes is exploited and an eight-node hexahedral element is also mentioned. Moreover, it is possible to consider a new solid element formulation.
- The 3D constitutive law is used. It means all stresses and strains are considered in the strain energy. There is no modification of this constitutive law, consequently no use of transverse shear correction coefficients classically associated with first-order beam theories.
- First-order and higher-order beam displacement fields are considered. The beam displacement fields are directly applied to the solid finite element model which has several elements throughout the cross-section.
- From a numerical point of view, kinematic relations between the degrees of freedom of nodes throughout the cross-section, are applied. These degrees of freedom are displacements exclusively because solid elements are used. For this purpose, slave and master nodes are introduced and only master nodes are kept in the model after the application of equations.
- This process leads to a reduction of the model size and consequently of the computational cost, compared to a reference solid model.

3.2.2 Displacement fields for a beam in plane

3.2.2.1 Classical first-order displacement field

In this chapter totally five displacement fields are considered. The first one is given by the classical Timoshenko beam theory. It considers membrane and bending effects as well as transverse shear ones. It is widely used in beam finite element formulations. This 2D displacement field is defined by:

$$\begin{cases} u(y,z) = u_0 + z\varphi_y \\ v(y,z) = 0 \\ w(y,z) = w_0 \end{cases} \tag{3.1}$$

where u_0 and w_0 are the displacements of a node on the mid-axis, φ_y is the rotation around y axis.

This displacement field uses displacements as well as rotations. In our approach, only displacements at nodes are used. It is relevant and well suited to rewrite the displacement field of Eq. (3.1) in the simple following form:

$$\begin{cases} u(y,z) = za_1 + a_2 \\ v(y,z) = 0 \\ w(y,z) = c_1 \end{cases} \tag{3.2}$$

where a_1, a_2 and c_1 are coefficients to be determined.

As will be shown and justified in Section 3.4.1.3, this displacement field does not lead to good results, in the context of our approach.

3.2.2.2 Modified first-order displacement field

To assess a relevant modification of the classical Timoshenko beam theory, it is helpful to observe the displacements throughout the cross-section of a moderately thin (l/h=20) square-section beam modeled with solid elements. For the bending case, the beam is clamped at its two ends and submitted to a uniform pressure on the top surface. For the membrane case, the beam is clamped at one end and subjected to a distributed traction loading at the opposite end. Fig. 3.1 shows the distribution of displacements through the thickness. For the bending case, the displacements u is linear, which fits well with the classical first-order theory. The displacement w is almost constant with z but with a slight quadratic contribution, while the classical first-order beam theory considers it as constant through the thickness. For the membrane case, the displacements u fits well with the classical first-order theory, showing a constant distribution. But the displacement component w is linear, which is different from the zero through-the-thickness assumption of the classical first-order beam theory. In summary, the classical first-order beam theory should be modified to be completely consistent with solid theory. The displacement w is required to be enriched so linear and quadratic terms are added. This does not mean that the classical first-order beam theory is inconsistent. Indeed, the assumption of constant displacement w in this theory has no consequence on the results due to the fact that the effect of the transverse strain ε_{zz} and the transverse stress σ_{zz} are neglected. One may say that the classical first-order beam theory is self-consistent but cannot reproduce all the effects of the 3D theory of elasticity.

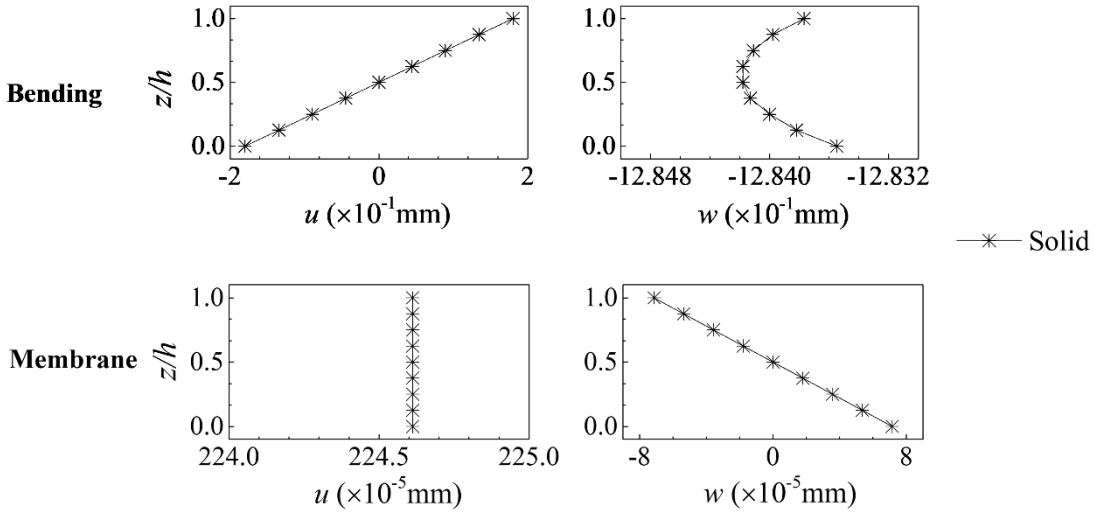

Fig. 3.1. Thin beam under bending or membrane loading – Distribution of through-the-thickness displacements.

The consistency between linear distribution for u and quadratic distribution for w can be demonstrated. First, for a given cross-section, considering both membrane and bending effects in plane x-z, linear through-the-thickness distributions is assumed for u:

$$u(y,z) = za_1 + a_2 \tag{3.3}$$

in which a_1 and a_2 are coefficients to be determined for each cross-section. So the ε_{xx} strain is linear with respect to *z*:

$$\varepsilon_{xx} = u_{,x} = za_3 + a_4 \tag{3.4}$$

where a_3 and a_4 are coefficients to be determined for each cross-section.

For isotropic material, the 3D solid stress-strain relationship is:

$$\begin{Bmatrix} \varepsilon_{xx} \\ \varepsilon_{yy} \\ \varepsilon_{zz} \\ \gamma_{xy} \\ \gamma_{xz} \\ \gamma_{yz} \end{Bmatrix} = \frac{1}{E} \begin{bmatrix} 1 & -\nu & -\nu & 0 & 0 & 0 \\ -\nu & 1 & -\nu & 0 & 0 & 0 \\ -\nu & -\nu & 1 & 0 & 0 & 0 \\ 0 & 0 & 0 & 2(1+\nu) & 0 & 0 \\ 0 & 0 & 0 & 0 & 2(1+\nu) & 0 \\ 0 & 0 & 0 & 0 & 0 & 2(1+\nu) \end{bmatrix} \begin{Bmatrix} \sigma_{xx} \\ \sigma_{yy} \\ \sigma_{zz} \\ \sigma_{xy} \\ \sigma_{xz} \\ \sigma_{yz} \end{Bmatrix} \tag{3.5}$$

For 2D beam structures, the σ_{yy} and σ_{zz} stresses are small and can be neglected, leading to the following relations:

$$\sigma_{xx} = E\varepsilon_{xx} \tag{3.6}$$

$$\varepsilon_{yy} = v_{,y} = -\frac{\nu}{E}\sigma_{xx} = -\nu\varepsilon_{xx} \tag{3.7}$$

$$\varepsilon_{zz} = w_{,z} = -\frac{\nu}{E}\sigma_{xx} = -\nu\varepsilon_{xx} \tag{3.8}$$

Eqs. (3.7) and (3.8) show that ε_{yy} and ε_{zz} are due to the Poisson effect and because ε_{xx} is linear with respect to *z*, ε_{yy} and ε_{zz} must also be linear through the thickness. By integration of Eq. (3.7), one highlights the expression of *v*:

$$v(y,z) = yzb_1 + yb_2 + b_3 + f_1(z) \tag{3.9}$$

where b_1 to b_3 are coefficients and $f_1(z)$ is a function to be determined for each cross-section. The coefficient b_3 represents a global displacement of a cross-section in the *y* direction. This displacement is zero for a beam in a plane, so hereafter $b_3 = 0$ is considered.

In the same way, by integration of Eq. (3.8), one highlights the expression of *w*:

$$w(y,z) = z^2c_1 + zc_2 + c_3 + f_2(y) \tag{3.10}$$

where c_1 to c_3 are coefficients and $f_2(y)$ a function to be determined for each cross-section.

Taking into account the expressions of *v* and *w* given in Eqs. (3.9) and (3.10), the γ_{yz} strain is defined by:

$$\gamma_{yz} = v_{,z} + w_{,y} \tag{3.11}$$

with

$$v_{,z} = yb_1 + f_1(z)_{,z} \tag{3.12}$$

and

$$w_{,y} = f_2(y)_{,y} \tag{3.13}$$

So the γ_{yz} strain is at least linear with respect to *y* and at least constant in the *z* direction. In order to have consistent contributions of the two terms $v_{,z}$ and $w_{,y}$, they must both have a linear variation in the

y direction. The choice to meet this condition is such that $f_1(z) = 0$ and $f_2(y)$ is quadratic with respect to *y*.

Finally the modified first-order displacement field is:

$$\begin{cases} u(y,z) = za_1 + a_2 \\ v(y,z) = yzb_1 + yb_2 \\ w(y,z) = z^2c_1 + y^2c_4 + zc_2 + c_3 \end{cases} \tag{3.14}$$

where a_1 to a_2, b_1 to b_2, c_1 to c_4 are coefficients to be determined.

To verify the relevancy of this displacement field, the deformation of the cross-section of a beam under bending or membrane loading, studied with a solid model, has been observed (see Fig. 3.2). The displacement field given in Eq. (3.14) is consistent with the results observed. In particular, in the bending case, the quadratic contribution of *w* with respect to *y* is highlighted. This displacement field allows the warping of each cross-section. As our best knowledge, this modified first-order displacement field has not been proposed in the literature. However, Hutchinson [70] proposed a similar displacement field without consideration of the membrane effect.

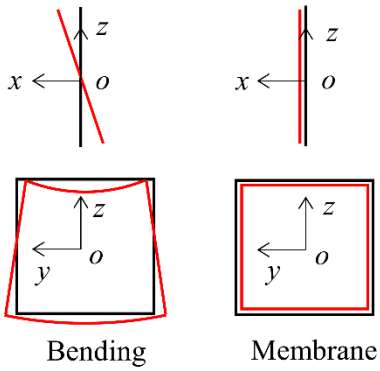

Fig. 3.2. Beam under bending or membrane loading – Deformation of a cross-section.

3.2.2.3 Higher-order displacement field

The example presented above is now considered for a thick beam (*l*/*h*=5). The through-the-thickness distribution of displacements is presented in Fig. 3.3.

For the bending case, the displacements *u* seems to have a cubic variation, while displacement *w* is again almost quadratic. The cubic distribution corresponds to the displacement *u* introduced by Levinson [72].

$$u(y,z) = z^3\phi_x + z\psi_x \tag{3.15}$$

where ϕ_x is the warping function and ψ_x represents the rotation of a cross-section of the beam.

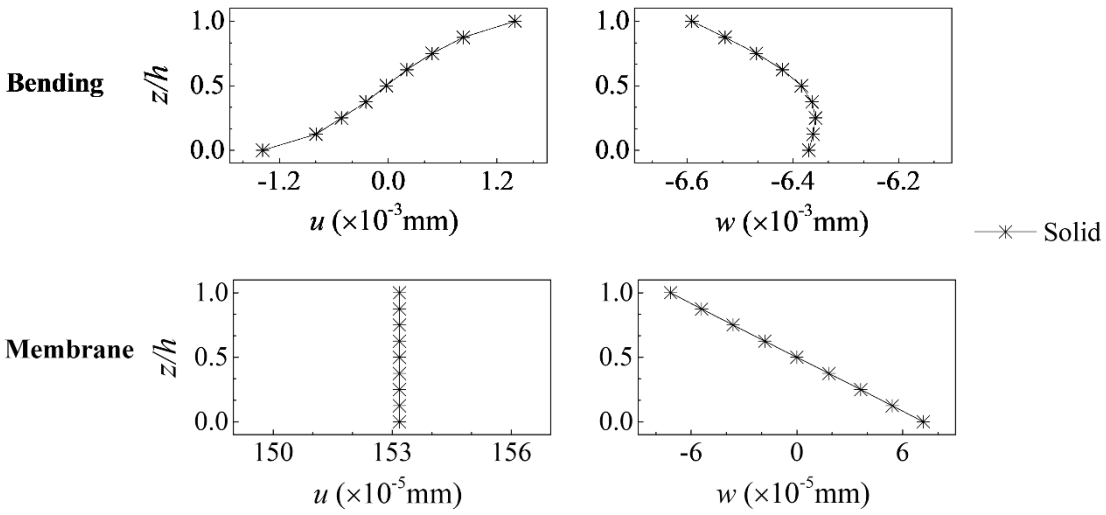

Fig. 3.3. Thick beam under bending or membrane loading – Distribution of through-the-thickness displacements.

This cubic distribution is consistent with results presented in Fig. 3.3. Moreover, it is a relevant choice to obtain a good approximation of transverse shear stresses through the thickness. Indeed, for a 2D beam, the distribution of σ_{xz} transverse shear stress is almost quadratic. This σ_{xz} stress is given by:

$$\sigma_{xz} = G\left(u_{,z} + w_{,x}\right) \tag{3.16}$$

First-order beam theories which use linear variation of *u* and constant variation of *w* through the thickness are not able to reproduce correctly transverse shear effects. Namely these assumptions lead to a constant distribution of σ_{xz} through the thickness, which is not correct. This is the reason why, from the one hand generally integration of equilibrium equations is used for calculating transverse shear stresses, and from the other hand transverse shear correction coefficient is required for the assessment of transverse shear stiffness [68, 69, 70, 71]. If u is cubic and *w* is quadratic with respect to *z*, both terms $u_{,z}$ and $w_{,x}$ can be quadratic with respect to *z*, leading to a consistent and precise distribution of the σ_{xz} stress, without any correction. This point is highlighted in the examples section.

Refined beam theories, namely that proposed by Levinson [72], uses the classical variables ψ_x but also another variable ϕ_x which is difficult to be interpreted and managed, for instance to define loading and boundary conditions. In the approach proposed, this difficulty is prevented because, as highlighted in Section 3.3, only displacements at nodes are exploited, without any other variable. For bending case, the component *u* is directly inspired by the Levinson displacement field. For the general case with membrane and bending effects a constant contribution is added for *u* while *v* and *w* are the same as for the modified first-order theory. The displacement field of the proposed refined beam theory, involving nine terms, is written as:

$$\begin{cases} u(y,z) = z^3 a_1 + z a_2 + a_3 \\ v(y,z) = yz b_1 + y b_2 \\ w(y,z) = z^2 c_1 + y^2 c_4 + z c_2 + c_3 \end{cases} \tag{3.17}$$

where a_1 to a_3, b_1 to b_2, c_1 to c_4 are coefficients to be determined.

This displacement field allows the warping of each cross-section. As our best knowledge, this higher-order displacement field has not been proposed in the literature. Anyway the cubic variation of u had already been proposed, namely by Levinson.

3.2.3 Displacement fields for a beam in space

Two displacement fields including torsion effects are proposed for a square or rectangular cross-section beam in space.

3.2.3.1 Torsion for square or rectangular cross-section beam

To obtain an appropriate displacement field for adequately representing a spatial beam, a torsion state, especially the cross-section deformation, is studied. A spatial beam modeled with solid elements in Abaqus is submitted to a torque. Two different cross-sections: square (a=b) and rectangular (a/b=2) are considered. The warping of the cross-sections is highlighted in Fig. 3.4. A complex and centrosymmetric deformation for both the square and rectangular cross-sections is observed. This means a linear approximation of displacement *u* is not able to reproduce the warping phenomenon. Thus, the *curve fitting toolbox* in Matlab [103] is used to fit these cross-section deformations by polynomials. The interpolation, smoothing splines and localized regression techniques are used for this fitting process. In terms of the contribution to displacement *u*, the terms yz^3 and zy^3 are found useful for a square cross-section and the terms yz^3, zy^3 and yz are important for a rectangular cross-section.

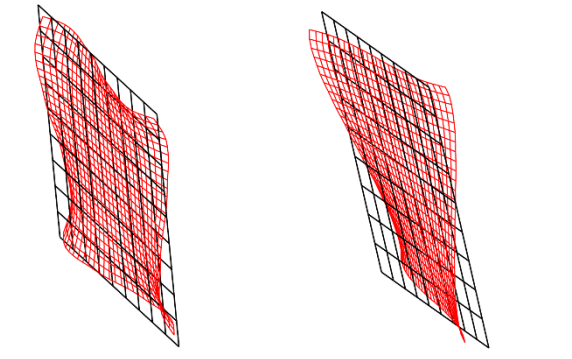

Fig. 3.4. The cross-section deformations of a spatial beam structure under pure torsion.

Fig. 3.5 shows the distribution of displacements *u* and *v* through the thickness for both the square and rectangular cross-sections. The displacement components *v* and *w* are the same in a spatial beam. It is observed at least a cubic relation with respect to *z* for displacement *u* due to the warping effect, and a linear relation with respect to *z* for displacement *v* and so displacement *w*. The three terms (yz^3, zy^3 and yz) of displacement *u* in Eq. (3.18) are consistent with Fig. 3.5, which means they play a significant role for the torsion of a spatial beam with square or rectangular cross-sections. Therefore, by using the

polynomial to represent the cross-section deformation, the displacement field for pure torsion of a spatial beam can be expressed as:

$$\begin{cases} u(y,z) = yz^3a_1 + zy^3a_2 + yza_3 + a_4 \\ v(y,z) = yb_1 + zb_2 + b_3 \\ w(y,z) = yc_1 + zc_2 + c_3 \end{cases} \tag{3.18}$$

where a_1 to a_4, b_1 to b_3, and c_1 to c_3 are coefficients to be determined.

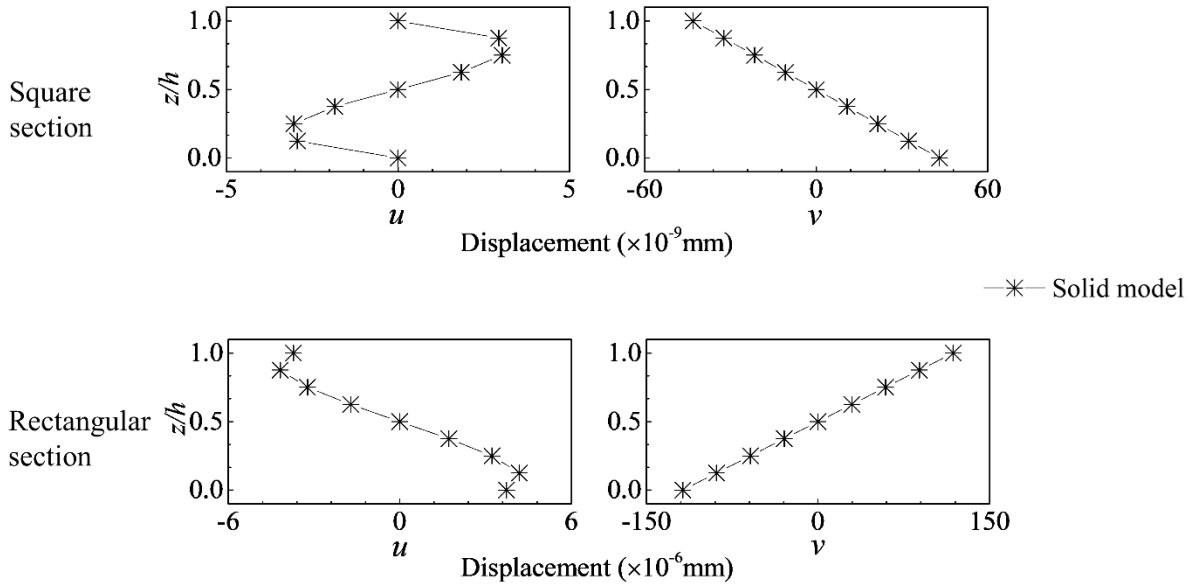

Fig. 3.5. Displacements of nodes through the thickness of spatial beam model for torsion.

3.2.3.2 First displacement field of a beam in space

Considering that for a spatial beam *y* and *z* play the same role, the displacement *w* in Eq. (3.14) can be extended as:

$$w(y,z) = y^2c_1 + z^2c_2 + yzc_3 + yc_4 + zc_5 + c_6 \tag{3.19}$$

where c_1 to c_6 are coefficients to be determined.

Taking Eq. (3.18) into account, the Eq. (3.14) can be extended for a spatial beam displacement field:

$$\begin{cases} u(y,z) = yz^3a_1 + zy^3a_2 + yza_3 + ya_4 + za_5 + a_6 \\ v(y,z) = y^2b_1 + z^2b_2 + yzb_3 + yb_4 + zb_5 + b_6 \\ w(y,z) = y^2c_1 + z^2c_2 + yzc_3 + yc_4 + zc_5 + c_6 \end{cases} \tag{3.20}$$

where a_1 to a_6, b_1 to b_6, and c_1 to c_6 are coefficients to be determined.

3.2.3.3 Second displacement field of a beam in space

Considering the torsion effects, the extension of Eq. (3.17) for a spatial beam with square or rectangular cross-sections can be expressed as:

$$\begin{cases} u(y,z) = y^3 z a_1 + z^3 y a_2 + y^3 a_3 + z^3 a_4 + yz a_5 + y a_6 + z a_7 + a_8 \\ v(y,z) = y^2 b_1 + z^2 b_2 + yz b_3 + y b_4 + z b_5 + b_6 \\ w(y,z) = y^2 c_1 + z^2 c_2 + yz c_3 + y c_4 + z c_5 + c_6 \end{cases} \quad (3.21)$$

where a_1 to a_8, b_1 to b_6, and c_1 to c_6 are coefficients to be determined.

3.3 Presentation of a new solid-beam approach – numerical aspects and implementation

This section explains how the displacement fields presented in Section 3.2.2 and Section 3.2.3 are applied on the solid element mesh, leading to solid-beam models. Equations are applied on the assembled finite element models. Five solid-beam models are described. Eq. (3.2) gives the First-Order Solid-Beam (FOSB) model. In the same way, Eq. (3.14) leads to the Modified First-Order Solid-Beam (MFOSB) model and Eq. (3.17) leads to the Higher-Order Solid-Beam (HOSB) one. Moreover, Eq. (3.20) leads to the first Solid-Beam in space (SB1-3D) model and Eq. (3.21) leads to the second Solid-Beam in space (SB2-3D) one. The principles consisting of imposing a displacement field at nodes throughout the cross-section are illustrated in Fig. 3.6 and Fig. 3.7. Master degrees of freedom and slave degrees of freedom are defined for each cross-section. All slave degrees of freedom can be eliminated from the system of equations to be solved. Each equation leads to the elimination of one degree of freedom. Consequently, the number of degrees of freedom eliminated corresponds exactly to the number of equations applied.

3.3.1 FOSB model

For each cross-section of the beam, the FOSB model uses two master nodes at points *A* and *B* as described in Fig. 3.6. Eq. (3.2) contains two coefficients a_1 and a_2 to be determined for *u* and one coefficient c_1 for *w*. To identify these three coefficients, the following set of three equations is used:

$$\begin{cases} u(y_A, z_A) = u_A = z_A a_1 + a_2 \\ u(y_B, z_B) = u_B = z_B a_1 + a_2 \\ w(y_A, z_A) = w_A = c_1 \end{cases} \quad (3.22)$$

where u_A, u_B, w_A are the displacements at points *A* and *B*, y_A , z_A, y_B , z_B are the coordinates of points *A* and *B* in the *y* and *z* directions.

Solving Eq. (3.22) gives the expressions of coefficients identified for each cross-section:

$$\begin{cases} a_1 = \dfrac{u_A - u_B}{z_A - z_B} \\ a_2 = -\dfrac{z_A u_B - z_B u_A}{z_A - z_B} \\ c_1 = w_A \end{cases} \quad (3.23)$$

By taking into account Eq. (3.23) into Eq. (3.2), one obtains:

$$\begin{cases} u(y,z) = z\dfrac{u_A - u_B}{z_A - z_B} + \dfrac{z_B u_A - z_A u_B}{z_A - z_B} \\ v(y,z) = 0 \\ w(y,z) = w_A \end{cases} \tag{3.24}$$

Equations to be applied are obtained by replacing z by z_i in Eq. (3.24), z_i being the coordinate of the slave node i in the z direction:

$$\begin{cases} u(y_i,z_i) = u_i^S = z\dfrac{u_A - u_B}{z_A - z_B} + \dfrac{z_B u_A - z_A u_B}{z_A - z_B} \\ v(y_i,z_i) = v_i^S = 0 \\ w(y_i,z_i) = w_i^S = w_A \end{cases} \tag{3.25}$$

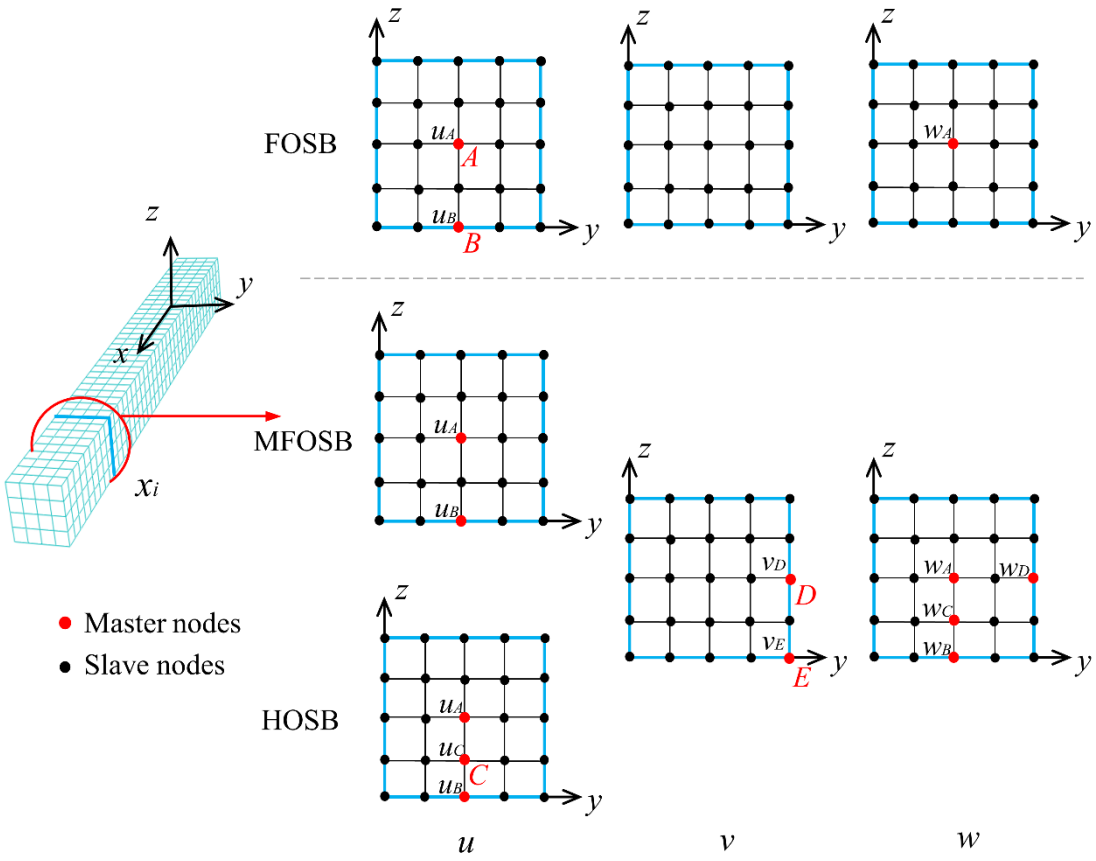

Fig. 3.6. Master nodes and slave nodes in the cross-section of a solid-beam model in a plane.

For a given cross-section of the beam, the displacements u_A, u_B and w_A must be calculated because they are the master degrees of freedom. All other degrees of freedom are the slave degrees of freedom. As highlighted in Eq. (3.25), they can be expressed in terms of master degrees of freedom, so they can be eliminated from the system of equations to be solved. Concerning the displacements u, Eq. (3.25) is applied at all nodes of the cross-sections, except points A and B. The displacements u of other nodes of the cross-section are dependent of u_A and u_B. Eq. (3.24) shows that displacement v is systematically equal to zero, so this equation is applied at all the nodes of the model. Concerning the displacements w, Eq. (3.25) is applied at all nodes of the cross-sections, except point A. The displacement component w

of other nodes is in the same way dependent of w_A. This description shows that the methodology relies on slave and master degrees of freedom. For the sake of simplicity, one distinguishes between master and slave nodes. A given node is considered as a master node if it contains at least one master degree of freedom. This model contains three master degrees of freedom per cross-section. It can be observed that Eq. (3.25) defines linear relations between the slave and the master degrees of freedom. One complementary remark is that if two master nodes are needed, it is natural to select points *A* and *B*. But two other nodes could be selected as well, which leads to equivalent results.

3.3.2 MFOSB model

The methodology described in Section 3.3.1 is now applied to build the MFOSB model. This model exploits five master nodes, as shown in Fig. 3.6. Eq. (3.14) contains two coefficients (a_1 and a_2) to be determined for displacement *u*, two coefficients (b_1 and b_2) for displacement *v* and three coefficients (c_1 , c_2 , c_3 and c_4) for displacement *w*. The coefficients a_1 and a_2 are the same as the FOSB model. To identify other coefficients, the following equations are used:

$$\begin{cases} v(y_D, z_D) = v_D = y_D z_D b_1 + y_D b_2 \\ v(y_E, z_E) = v_E = y_E z_E b_1 + y_E b_2 \\ w(y_A, z_A) = w_A = z_A^2 c_1 + y_A^2 c_4 + z_A c_2 + c_3 \\ w(y_B, z_B) = w_B = z_B^2 c_1 + y_B^2 c_4 + z_B c_2 + c_3 \\ w(y_C, z_C) = w_C = z_C^2 c_1 + y_C^2 c_4 + z_C c_2 + c_3 \\ w(y_D, z_D) = w_D = z_D^2 c_1 + y_D^2 c_4 + z_D c_2 + c_3 \end{cases} \tag{3.26}$$

where v_D, v_E, w_A, w_B, w_C and w_D are displacements at master nodes; y_A, y_B, y_C, y_D, y_E, z_A, z_B, z_C, z_D and z_E are the coordinates of master nodes in the *y* or *z* direction.

The expressions of coefficients identified for each cross-section are:

$$
\begin{cases}
a_1 = \dfrac{u_A - u_B}{z_A - z_B} \\[2ex]
a_2 = -\dfrac{z_A u_B - z_B u_A}{z_A - z_B} \\[2ex]
b_1 = \dfrac{v_D y_E - v_E y_D}{y_D y_E (z_D - z_E)} \\[2ex]
b_2 = \dfrac{v_E y_D z_D - v_D y_E z_E}{y_D y_E (z_D - z_E)} \\[2ex]
c_1 = -\dfrac{\begin{pmatrix} w_A y_B^2 z_C - w_A y_C^2 z_B - w_B y_A^2 z_C + w_B y_C^2 z_A + w_C y_A^2 z_B - w_C y_B^2 z_A - w_A y_B^2 z_D \\ +w_A y_D^2 z_B + w_A y_A^2 z_D - w_B y_D^2 z_A - w_D y_A^2 z_B + w_D y_B^2 z_A - w_C y_B^2 z_A - w_A y_B^2 z_D \\ +w_A y_C^2 z_D - w_A y_D^2 z_C - w_C y_A^2 z_D + w_C y_D^2 z_A + w_D y_A^2 z_C - w_D y_C^2 z_A - w_B y_C^2 z_D \\ +w_B y_D^2 z_C + w_C y_B^2 z_D - w_C y_D^2 z_B - w_D y_B^2 z_C + w_D y_C^2 z_B \end{pmatrix}}{\begin{pmatrix} -y_A^2 z_B^2 z_C + y_A^2 z_B^2 z_D + y_A^2 z_C^2 z_B - y_A^2 z_D^2 z_B - y_A^2 z_C^2 z_D + y_A^2 z_D^2 z_C + y_B^2 z_A^2 z_C - y_B^2 z_A^2 z_D \\ -y_B^2 z_C^2 z_A + y_B^2 z_D^2 z_A + y_B^2 z_C^2 z_D - y_B^2 z_D^2 z_C - y_C^2 z_A^2 z_B + y_C^2 z_A^2 z_D + y_C^2 z_B^2 z_A - y_C^2 z_D^2 z_A \\ -y_C^2 z_B^2 z_D + y_C^2 z_D^2 z_B + y_D^2 z_A^2 z_B - y_D^2 z_A^2 z_C - y_D^2 z_B^2 z_A + y_D^2 z_C^2 z_A + y_D^2 z_B^2 z_C \mp y_D^2 z_C^2 z_B \end{pmatrix}} \\[2ex]
c_4 = -\dfrac{\begin{pmatrix} w_A z_B z_C^2 - w_A z_C z_B^2 - w_B z_A z_C^2 + w_B z_C z_A^2 + w_C z_A z_B^2 - w_C z_B z_A^2 - w_A z_B z_D^2 + w_A z_D z_B^2 \\ +w_B z_A z_D^2 - w_B z_D z_A^2 - w_D z_A z_B^2 + w_B z_B z_A^2 + w_A z_C z_D^2 - w_A z_D z_C^2 - w_C z_A z_D^2 + w_C z_D z_A^2 \\ +w_D z_A z_C^2 - w_D z_C z_A^2 - w_B z_C z_D^2 + w_B z_D z_C^2 + w_C z_B z_D^2 - w_C z_D z_B^2 - w_D z_B z_C^2 + w_D z_C z_B^2 \end{pmatrix}}{\begin{pmatrix} -y_A^2 z_B^2 z_C + y_A^2 z_B^2 z_D + y_A^2 z_C^2 z_B - y_A^2 z_D^2 z_B - y_A^2 z_C^2 z_D + y_A^2 z_D^2 z_C + y_B^2 z_A^2 z_C - y_B^2 z_A^2 z_D \\ -y_B^2 z_C^2 z_A + y_B^2 z_D^2 z_A + y_B^2 z_C^2 z_D - y_B^2 z_D^2 z_C - y_C^2 z_A^2 z_B + y_C^2 z_A^2 z_D + y_C^2 z_B^2 z_A - y_C^2 z_D^2 z_A \\ -y_C^2 z_B^2 z_D + y_C^2 z_D^2 z_B + y_D^2 z_A^2 z_B - y_D^2 z_A^2 z_C - y_D^2 z_B^2 z_A + y_D^2 z_C^2 z_A + y_D^2 z_B^2 z_C \mp y_D^2 z_C^2 z_B \end{pmatrix}} \\[2ex]
c_2 = \dfrac{\begin{pmatrix} w_A y_B^2 z_C^2 - w_A y_C^2 z_B^2 - w_A y_A^2 z_C^2 + w_B y_C^2 z_A^2 + w_C y_A^2 z_B^2 - w_C y_B^2 z_A^2 - w_A y_B^2 z_D^2 + w_A y_D^2 z_B^2 \\ +w_B y_A^2 z_D^2 - w_B y_D^2 z_A^2 - w_D y_A^2 z_B^2 + w_D y_B^2 z_A^2 + w_A y_C^2 z_D^2 - w_A y_D^2 z_C^2 - w_C y_A^2 z_D^2 + w_C y_D^2 z_A^2 \\ +w_D y_A^2 z_C^2 - w_D y_C^2 z_A^2 - w_B y_C^2 z_D^2 + w_B y_D^2 z_C^2 + w_C y_B^2 z_D^2 - w_C y_D^2 z_B^2 - w_D y_B^2 z_C^2 + w_D y_C^2 z_B^2 \end{pmatrix}}{\begin{pmatrix} -y_A^2 z_B^2 z_C + y_A^2 z_B^2 z_D + y_A^2 z_C^2 z_B - y_A^2 z_D^2 z_B - y_A^2 z_C^2 z_D + y_A^2 z_D^2 z_C + y_B^2 z_A^2 z_C - y_B^2 z_A^2 z_D \\ -y_B^2 z_C^2 z_A + y_B^2 z_D^2 z_A + y_B^2 z_C^2 z_D - y_B^2 z_D^2 z_C - y_C^2 z_A^2 z_B + y_C^2 z_A^2 z_D + y_C^2 z_B^2 z_A - y_C^2 z_D^2 z_A \\ -y_C^2 z_B^2 z_D + y_C^2 z_D^2 z_B + y_D^2 z_A^2 z_B - y_D^2 z_A^2 z_C - y_D^2 z_B^2 z_A + y_D^2 z_C^2 z_A + y_D^2 z_B^2 z_C \mp y_D^2 z_C^2 z_B \end{pmatrix}} \\[2ex]
c_3 = \dfrac{\begin{pmatrix} w_D y_A^2 z_B^2 z_C - w_C y_A^2 z_B^2 z_D - w_D y_A^2 z_C^2 z_B + w_C y_A^2 z_D^2 z_B + w_B y_A^2 z_C^2 z_D - w_B y_A^2 z_D^2 z_C \\ -w_D y_B^2 z_A^2 z_C + w_C y_B^2 z_A^2 z_D + w_D y_B^2 z_C^2 z_A - w_C y_B^2 z_D^2 z_A - w_A y_B^2 z_C^2 z_D + w_A y_B^2 z_D^2 z_C \\ +w_D y_C^2 z_A^2 z_B - w_B y_C^2 z_A^2 z_D - w_D y_C^2 z_B^2 z_A + w_B y_C^2 z_D^2 z_A + w_A y_C^2 z_B^2 z_D - w_A y_C^2 z_D^2 z_B \\ -w_C y_D^2 z_A^2 z_B + w_B y_D^2 z_A^2 z_C + w_C y_D^2 z_B^2 z_A - w_B y_D^2 z_C^2 z_A - w_A y_D^2 z_B^2 z_C + w_A y_D^2 z_C^2 z_B \end{pmatrix}}{\begin{pmatrix} -y_A^2 z_B^2 z_C + y_A^2 z_B^2 z_D + y_A^2 z_C^2 z_B - y_A^2 z_D^2 z_B - y_A^2 z_C^2 z_D + y_A^2 z_D^2 z_C + y_B^2 z_A^2 z_C - y_B^2 z_A^2 z_D \\ -y_B^2 z_C^2 z_A + y_B^2 z_D^2 z_A + y_B^2 z_C^2 z_D - y_B^2 z_D^2 z_C - y_C^2 z_A^2 z_B + y_C^2 z_A^2 z_D + y_C^2 z_B^2 z_A - y_C^2 z_D^2 z_A \\ -y_C^2 z_B^2 z_D + y_C^2 z_D^2 z_B + y_D^2 z_A^2 z_B - y_D^2 z_A^2 z_C - y_D^2 z_B^2 z_A + y_D^2 z_C^2 z_A + y_D^2 z_B^2 z_C - +y_D^2 z_C^2 z_B \end{pmatrix}}
\end{cases}
\tag{3.27}
$$

Considering Eq. (3.27) and replacing *y* and *z* by y_i and z_i in Eq. (3.14), one obtains equations to be applied at slave node *i*:

$$\begin{cases} u(y_i, z_i) = u_i^S = z_i a_1 + a_2 \\ v(y_i, z_i) = v_i^S = y_i z_i b_1 + y_i b_2 \\ w(y_i, z_i) = w_i^S = z_i^2 c_1 + y_i^2 c_4 + z_i c_2 + c_3 \end{cases} \tag{3.28}$$

This model contains eight master degrees of freedom per cross-section. Eq. (3.28) describes linear relations between slave and master degrees of freedom.

3.3.3 HOSB model

The methodology is now applied to build the HOSB model. This model exploits five master nodes *A*, *B*, *C*, *D* and *E*, as shown in Fig. 3.6. Eq. (3.17) contains three coefficients (a_1, a_2 and a_3) to be determined for displacement *u*, two coefficients (b_1 and b_2) for displacement *v* and four coefficients (c_1, c_2, c_3 and c_4) for displacement *w*. To identify the nine coefficients, the following equations are used:

$$\begin{cases} u(y_A, z_A) = u_A = a_1 z_A^3 + a_2 z_A + a_3 \\ u(y_B, z_B) = u_B = a_1 z_B^3 + a_2 z_B + a_3 \\ u(y_C, z_C) = u_C = a_1 z_C^3 + a_2 z_C + a_3 \\ v(y_D, z_D) = v_D = y_D z_D b_1 + y_D b_2 \\ v(y_E, z_E) = v_E = y_E z_E b_1 + y_E b_2 \\ w(y_A, z_A) = w_A = z_A^2 c_1 + y_A^2 c_4 + z_A c_2 + c_3 \\ w(y_B, z_B) = w_B = z_B^2 c_1 + y_B^2 c_4 + z_B c_2 + c_3 \\ w(y_C, z_C) = w_C = z_C^2 c_1 + y_C^2 c_4 + z_C c_2 + c_3 \\ w(y_D, z_D) = w_D = z_D^2 c_1 + y_D^2 c_4 + z_D c_2 + c_3 \end{cases} \tag{3.29}$$

where u_A, u_B, u_C, v_D, v_E, w_A, w_B, w_C and w_D are the displacements at master nodes; y_A, y_B, y_C, y_D, y_E, z_A, z_B, z_C, z_D and z_E are the coordinates of master nodes.

The expressions of coefficients b_1, b_2, c_1, c_2, c_3 and c_4 are the same as expressed in Eq. (3.28), coefficients a_1, a_2 and a_3 identified for each cross-section are:

$$\begin{cases} a_1 = \dfrac{u_A z_B - u_B z_A - u_A z_C + u_C z_A + u_B z_C - u_C z_B}{(z_A - z_B)(z_A^2 z_B - z_A^2 z_C + z_A z_B^2 - z_A z_B z_C - z_B^2 z_C + z_C^3)} \\ a_2 = -\dfrac{u_A z_B^3 - u_B z_A^3 - u_A z_C^3 + u_C z_A^3 + u_B z_C^3 - u_C z_B^3}{(z_A - z_B)(z_A^2 z_B - z_A^2 z_C + z_A z_B^2 - z_A z_B z_C - z_B^2 z_C + z_C^3)} \\ a_3 = -\dfrac{-u_C z_A^3 z_B + u_B z_A^3 z_C + u_C z_B^3 z_A - u_B z_C^3 z_A + u_A z_B^3 z_C - u_A z_C^3 z_B}{(z_A - z_B)(z_A^2 z_B - z_A^2 z_C + z_A z_B^2 - z_A z_B z_C - z_B^2 z_C + z_C^3)} \end{cases} \tag{3.30}$$

After considering Eqs. (3.28) and (3.30) and replacing *y* and *z* by y_i and z_i in Eq. (3.17), one obtains equations to be applied at slave node *i*:

$$\begin{cases} u(y_i, z_i) = u_i^S = z_i^3 a_1 + z_i a_2 + a_3 \\ v(y_i, z_i) = v_i^S = y_i z_i b_1 + y_i b_2 \\ w(y_i, z_i) = w_i^S = z_i^2 c_1 + y_i^2 c_4 + z_i c_2 + c_3 \end{cases} \tag{3.31}$$

The HOSB model contains nine master degrees of freedom per cross-section. Eq. (3.31) describes linear relations between slave and master degrees of freedom.

3.3.4 SB1-3D model

The methodology is now applied to build the SB1-3D model. This model exploits six master nodes *A*, *B*, *D*, *E*, *F* and *G*, as shown in Fig. 3.7. Eq. (3.20) contains six coefficients (a_1 to a_6) to be determined for displacement *u*, six coefficients (b_1 to b_6) for displacement *v* and six coefficients (c_1 to c_6) for displacement *w*. To identify the eighteen coefficients, the following equations are used:

$$\begin{cases} u(y_A, z_A) = u_A = y_A z_A^3 a_1 + y_A^3 z_A a_2 + y_A z_A a_3 + y_A a_4 + z_A a_5 + a_6 \\ u(y_B, z_B) = u_B = y_B z_B^3 a_1 + y_B^3 z_B a_2 + y_B z_B a_3 + y_B a_4 + z_B a_5 + a_6 \\ u(y_D, z_D) = u_D = y_D z_D^3 a_1 + y_D^3 z_D a_2 + y_D z_D a_3 + y_D a_4 + z_D a_5 + a_6 \\ u(y_E, z_E) = u_E = y_E z_E^3 a_1 + y_E^3 z_E a_2 + y_E z_E a_3 + y_E a_4 + z_E a_5 + a_6 \\ u(y_F, z_F) = u_F = y_F z_F^3 a_1 + y_F^3 z_F a_2 + y_F z_F a_3 + y_F a_4 + z_F a_5 + a_6 \\ u(y_G, z_G) = u_G = y_G z_G^3 a_1 + y_G^3 z_G a_2 + y_G z_G a_3 + y_G a_4 + z_G a_5 + a_6 \\ v(y_A, z_A) = v_A = y_A^2 b_1 + z_A^2 b_2 + y_A z_A b_3 + y_A b_4 + z_A b_5 + b_6 \\ v(y_B, z_B) = v_B = y_B^2 b_1 + z_B^2 b_2 + y_B z_B b_3 + y_B b_4 + z_B b_5 + b_6 \\ v(y_D, z_D) = v_D = y_D^2 b_1 + z_D^2 b_2 + y_D z_D b_3 + y_D b_4 + z_D b_5 + b_6 \\ v(y_E, z_E) = v_E = y_E^2 b_1 + z_E^2 b_2 + y_E z_E b_3 + y_E b_4 + z_E b_5 + b_6 \\ v(y_F, z_F) = v_F = y_F^2 b_1 + z_F^2 b_2 + y_F z_F b_3 + y_F b_4 + z_F b_5 + b_6 \\ v(y_G, z_G) = v_G = y_G^2 b_1 + z_G^2 b_2 + y_G z_G b_3 + y_G b_4 + z_G b_5 + b_6 \\ w(y_A, z_A) = w_A = y_A^2 c_1 + z_A^2 c_2 + y_A z_A c_3 + y_A c_4 + z_A c_5 + c_6 \\ w(y_B, z_B) = w_B = y_B^2 c_1 + z_B^2 c_2 + y_B z_B c_3 + y_B c_4 + z_B c_5 + c_6 \\ w(y_D, z_D) = w_D = y_D^2 c_1 + z_D^2 c_2 + y_D z_D c_3 + y_D c_4 + z_D c_5 + c_6 \\ w(y_E, z_E) = w_E = y_E^2 c_1 + z_E^2 c_2 + y_E z_E c_3 + y_E c_4 + z_E c_5 + c_6 \\ w(y_F, z_F) = w_F = y_F^2 c_1 + z_F^2 c_2 + y_F z_F c_3 + y_F c_4 + z_F c_5 + c_6 \\ w(y_G, z_G) = w_G = y_G^2 c_1 + z_G^2 c_2 + y_G z_G c_3 + y_G c_4 + z_G c_5 + c_6 \end{cases} \tag{3.32}$$

where $u_A, u_B, u_D, u_E, u_F, u_G, v_A, v_B, v_D, v_E, v_F, v_G, w_A, w_B, w_D, w_E, w_F$ and w_G are the displacements at master nodes; $z_A, z_B, z_D, z_E, z_F, z_G$ and $y_A, y_B, y_D, y_E, y_F, y_G$ are the coordinates of master nodes in the *z* and *y* directions respectively.

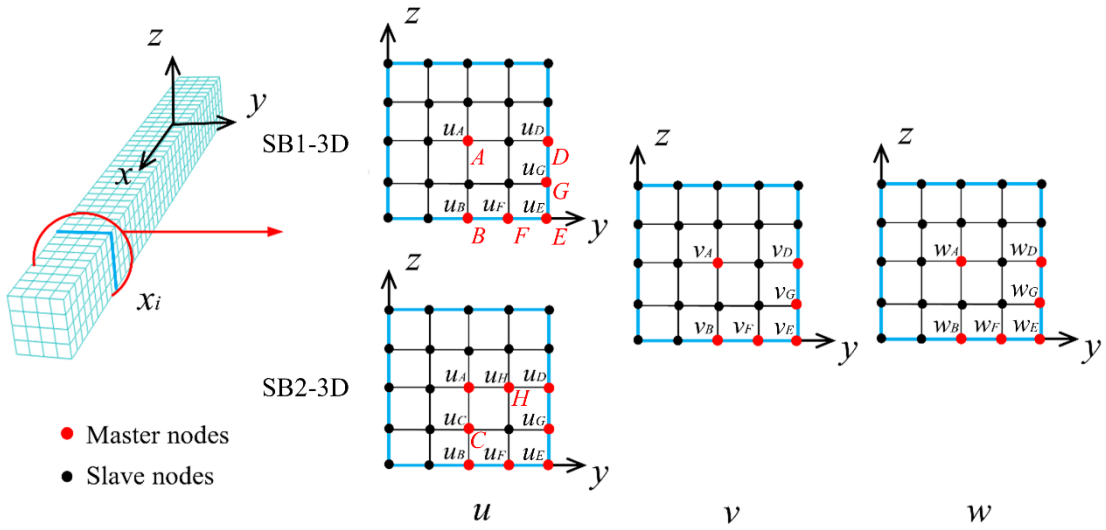

Fig. 3.7. Master nodes and slave nodes in the cross-section of a solid-beam model in space.

For simplification, point *A* in the cross-section can be supposed as the relative origin in the coordinate system. Therefore, some equality relations between the coordinates can be expressed as:

$$\begin{cases} y_B = 0 \\ y_{DA} = y_D - y_A = y_{EA} = y_{GA} \\ y_{FA} = y_F - y_A \\ z_D = 0 \\ z_{BA} = z_B - z_A = z_{FA} = z_{EA} \\ z_{GA} = z_G - z_A \end{cases} \tag{3.33}$$

where $y_{DA}, y_{EA}, y_{FA}, y_{GA}, z_{BA}, z_{EA}, z_{FA}$ and z_{GA} are the relative coordinates of points *B*, *D*, *E*, *F* and *G* to point *A* in the *y* and *z* directions.

Considering Eq. (3.33), the expressions of coefficients identified for each cross-section are:

$$
\begin{cases}
a_1 = \dfrac{(u_D z_{BA} - u_G z_{BA} - u_D z_{GA} + u_E z_{GA})}{y_{DA} z_{BA} z_{GA} (z_{BA} + z_{GA})(z_{BA} - z_{GA})} \\
a_2 = \dfrac{u_B y_{DA} - u_B y_{FA} - u_F y_{DA} + u_E y_{FA}}{y_{DA} y_{FA} z_{BA} (y_{DA}^2 - y_{FA}^2)} \\
a_3 = \dfrac{\begin{pmatrix} u_B y_{DA}^3 z_{GA}^4 + u_A y_{FA}^3 z_{GA}^3 + u_D y_{FA}^3 z_{BA}^3 - u_B y_{FA}^3 z_{GA}^3 - u_G y_{FA}^3 z_{BA}^3 - u_D y_{FA}^3 z_{GA}^3 \\ -u_F y_{DA}^3 z_{GA}^3 + u_E y_{FA}^3 z_{GA}^3 - u_A y_{DA}^2 y_{FA} z_{GA}^3 - u_D y_{DA}^2 y_{FA} z_{BA}^3 + u_G y_{DA}^2 y_{FA} z_{BA}^3 \\ +u_D y_{DA}^2 y_{FA} z_{GA}^3 - u_B y_{DA}^3 z_{BA}^2 z_{GA} - u_A y_{FA}^3 z_{BA}^2 z_{GA} + u_B y_{FA}^3 z_{BA}^2 z_{GA} \\ +u_F y_{DA}^3 z_{BA}^2 z_{GA} + u_A y_{DA}^2 y_{FA} z_{BA}^2 z_{GA} - u_G y_{DA}^2 y_{FA} z_{BA}^2 z_{GA} \end{pmatrix}}{y_{DA} y_{FA} z_{BA} z_{GA} (z_{BA} + z_{GA})(z_{BA} - z_{GA})(y_{DA}^2 - y_{FA}^2)} \\
a_4 = -\dfrac{u_A - u_D}{y_{DA}} \\
a_5 = -\dfrac{u_A - u_B}{z_{BA}} \\
a_6 = u_A \\
b_1 = \dfrac{\begin{pmatrix} v_A y_{DA} z_{GA}^2 - v_D y_{DA} z_{BA}^2 + v_D y_{DA} z_{BA}^3 - v_B y_{DA} z_{GA}^2 + v_G y_{DA} z_{BA}^2 - v_G y_{DA} z_{BA}^3 \\ -v_A y_{FA} z_{GA}^2 + v_D y_{FA} z_{BA}^2 - v_D y_{FA} z_{BA}^3 + v_B y_{FA} z_{GA}^2 - v_G y_{FA} z_{BA}^2 + v_G y_{FA} z_{BA}^3 \\ -v_A y_{DA} z_{BA} z_{GA} + v_B y_{DA} z_{BA} z_{GA} + v_A y_{FA} z_{BA} z_{GA} - v_B y_{FA} z_{BA} z_{GA} + v_D y_{DA} z_{BA} z_{GA} \\ -v_D y_{FA} z_{BA} z_{GA} - v_E y_{DA} z_{BA} z_{GA} + v_E y_{FA} z_{BA} z_{GA} - v_A y_{DA} z_{BA} z_{GA}^2 + v_A y_{DA} z_{BA}^2 z_{GA} \\ +v_A y_{FA} z_{BA} z_{GA}^2 - v_A y_{FA} z_{BA}^2 z_{GA} - v_D y_{DA} z_{BA}^2 z_{GA} + v_D y_{FA} z_{BA}^2 z_{GA} + v_F y_{DA} z_{BA} z_{GA}^2 \\ -v_F y_{DA} z_{BA}^2 z_{GA} + v_E y_{DA} z_{BA}^2 z_{GA} - v_E y_{FA} z_{BA} z_{GA}^2 \end{pmatrix}}{y_{DA} y_{FA} z_{BA} z_{GA} (y_{DA} - y_{FA})(z_{BA} - z_{GA})} \\
b_2 = \dfrac{v_D z_{BA} - v_E z_{BA} - v_D z_{GA} + v_E z_{GA}}{z_{BA} z_{GA} (z_{BA} - z_{GA})} \\
b_3 = -\dfrac{\begin{matrix} v_A z_{GA}^2 - v_D z_{BA}^2 + v_D z_{BA}^3 - v_B z_{GA}^2 + v_G z_{BA}^2 - v_G z_{BA}^3 - v_D z_{BA} z_{GA}^2 + v_E z_{BA} z_{GA}^2 \\ -v_A z_{BA} z_{GA} + v_B z_{BA} z_{GA} + v_D z_{BA} z_{GA} - v_E z_{BA} z_{GA} \end{matrix}}{y_{DA} z_{BA}^2 z_{GA} (z_{BA} - z_{GA})} \\
b_4 = -\dfrac{\begin{pmatrix} v_A y_{DA}^2 z_{GA}^2 - v_D y_{DA}^2 z_{BA}^2 + v_D y_{DA}^2 z_{BA}^3 - v_B y_{DA}^2 z_{GA}^2 + v_G y_{DA}^2 z_{BA}^2 - v_G y_{DA}^2 z_{BA}^3 \\ -v_A y_{DA}^2 z_{BA} z_{GA}^2 + v_A y_{DA}^2 z_{BA}^2 z_{GA} + v_A y_{FA}^2 z_{BA} z_{GA}^2 - v_A y_{FA}^2 z_{BA}^2 z_{GA} - v_D y_{DA}^2 z_{BA}^2 z_{GA} \\ -v_D y_{FA}^2 z_{BA} z_{GA}^2 + v_D y_{FA}^2 z_{BA}^2 z_{GA} + v_F y_{DA}^2 z_{BA} z_{GA}^2 - v_F y_{DA}^2 z_{BA}^2 z_{GA} + v_E y_{DA}^2 z_{BA}^2 z_{GA} \\ -v_A y_{DA} y_{FA} z_{GA}^2 + v_D y_{DA} y_{FA} z_{BA}^2 - v_D y_{DA} y_{FA} z_{BA}^3 + v_B y_{DA} y_{FA} z_{GA}^2 - v_G y_{DA} y_{FA} z_{BA}^2 \\ +v_G y_{DA} y_{FA} z_{BA}^3 - v_A y_{DA}^2 z_{BA} z_{GA} + v_B y_{DA}^2 z_{BA} z_{GA} + v_D y_{DA}^2 z_{BA} z_{GA} - v_E y_{DA}^2 z_{BA} z_{GA} \\ +v_D y_{DA} y_{FA} z_{BA} z_{GA}^2 - v_E y_{DA} y_{FA} z_{BA} z_{GA}^2 + v_A y_{DA} y_{FA} z_{BA} z_{GA} - v_A y_{DA} y_{FA} z_{BA} z_{GA} \\ -v_B y_{DA} y_{FA} z_{BA} z_{GA} - v_D y_{DA} y_{FA} z_{BA} z_{GA} + v_E y_{DA} y_{FA} z_{BA} z_{GA} \end{pmatrix}}{y_{DA} y_{FA} z_{BA} z_{GA} (y_{DA} - y_{FA})(z_{BA} - z_{GA})} \\
b_5 = -\dfrac{(v_A z_{GA}^2 - v_D z_{BA}^2 - v_B z_{GA}^2 + v_G z_{BA}^2 - v_G z_{BA} z_{GA} + v_B z_{BA} z_{GA} + v_D z_{BA} z_{GA} - v_E z_{BA} z_{GA})}{z_{BA} z_{GA} (-z_{BA}^2 + z_{GA} z_{BA})} \\
b_6 = v_A
\end{cases}
\tag{3.34}
$$

$$
\begin{cases}
c_1 = \dfrac{\begin{pmatrix} w_A y_{DA} z_{GA}^2 - w_D y_{DA} z_{BA}^2 + w_D y_{DA} z_{BA}^3 - w_B y_{DA} z_{GA}^2 + w_G y_{DA} z_{BA}^2 - w_G y_{DA} z_{BA}^3 \\ -w_A y_{FA} z_{GA}^2 + w_D y_{FA} z_{BA}^2 - w_D y_{FA} z_{BA}^3 + w_B y_{FA} z_{GA}^2 - w_G y_{FA} z_{BA}^2 + w_G y_{FA} z_{BA}^3 \\ -w_A y_{DA} z_{BA} z_{GA} + w_B y_{DA} z_{BA} z_{GA} + w_A y_{FA} z_{BA} z_{GA} - w_B y_{FA} z_{BA} z_{GA} + w_D y_{DA} z_{BA} z_{GA} \\ -w_D y_{FA} z_{BA} z_{GA} - w_E y_{DA} z_{BA} z_{GA} + w_E y_{FA} z_{BA} z_{GA} - w_A y_{DA} z_{BA} z_{GA}^2 + w_A y_{DA} z_{BA}^2 z_{GA} \\ +w_A y_{FA} z_{BA} z_{GA}^2 - w_A y_{FA} z_{BA}^2 z_{GA} - w_D y_{DA} z_{BA}^2 z_{GA} + w_D y_{FA} z_{BA}^2 z_{GA} + w_F y_{DA} z_{BA} z_{GA}^2 \\ -w_F y_{DA} z_{BA}^2 z_{GA} + w_E y_{DA} z_{BA}^2 z_{GA} - w_E y_{FA} z_{BA} z_{GA}^2 \end{pmatrix}}{y_{DA} y_{FA} z_{BA} z_{GA} (y_{DA} - y_{FA})(z_{BA} - z_{GA})} \\
c_2 = \dfrac{w_D z_{BA} - w_G z_{BA} - w_D z_{EA} + w_E z_{GA}}{z_{BA} z_{GA} (z_{BA} - z_{GA})} \\
c_3 = -\dfrac{\begin{matrix} w_A z_{GA}^2 - w_D z_{BA}^2 + w_D z_{BA}^3 - w_B z_{GA}^2 + w_G z_{BA}^2 - w_G z_{BA}^3 - w_D z_{BA} z_{GA}^2 + w_E z_{BA} z_{GA}^2 \\ -w_A z_{BA} z_{GA} + w_B z_{BA} z_{GA} + w_D z_{BA} z_{GA} - w_E z_{BA} z_{GA} \end{matrix}}{y_{DA} z_{BA}^2 z_{GA} (z_{BA} - z_{GA})} \\
c_4 = -\dfrac{\begin{pmatrix} w_A y_{DA}^2 z_{GA}^2 - w_D y_{DA}^2 z_{BA}^2 + w_D y_{DA}^2 z_{BA}^3 - w_B y_{DA}^2 z_{GA}^2 + w_G y_{DA}^2 z_{BA}^2 - w_G y_{DA}^2 z_{BA}^3 \\ -w_A y_{DA}^2 z_{BA} z_{GA}^2 + w_A y_{DA}^2 z_{BA}^2 z_{GA} + w_A y_{FA}^2 z_{BA} z_{GA}^2 - w_A y_{FA}^2 z_{BA}^2 z_{GA} - w_D y_{DA}^2 z_{BA}^2 z_{GA} \\ -w_D y_{FA}^2 z_{BA} z_{GA}^2 + w_D y_{FA}^2 z_{BA}^2 z_{GA} + w_F y_{DA}^2 z_{BA} z_{GA}^2 - w_F y_{DA}^2 z_{BA}^2 z_{GA} + w_E y_{DA}^2 z_{BA}^2 z_{GA} \\ -w_A y_{DA} y_{FA} z_{GA}^2 + w_D y_{DA} y_{FA} z_{BA}^2 - w_D y_{DA} y_{FA} z_{BA}^3 + w_B y_{DA} y_{FA} z_{GA}^2 - w_G y_{DA} y_{FA} z_{BA}^2 \\ +w_G y_{DA} y_{FA} z_{BA}^3 - w_A y_{DA}^2 z_{BA} z_{GA} + w_B y_{DA}^2 z_{BA} z_{GA} + w_D y_{DA}^2 z_{BA} z_{GA} - w_E y_{DA}^2 z_{BA} z_{GA} \\ +w_D y_{DA} y_{FA} z_{BA} z_{GA}^2 - w_E y_{DA} y_{FA} z_{BA} z_{GA}^2 + w_A y_{DA} y_{FA} z_{BA} z_{GA} - w_A y_{DA} y_{FA} z_{BA} z_{GA} \\ -w_B y_{DA} y_{FA} z_{BA} z_{GA} - w_D y_{DA} y_{FA} z_{BA} z_{GA} + w_E y_{DA} y_{FA} z_{BA} z_{GA} \end{pmatrix}}{y_{DA} y_{FA} z_{BA} z_{GA} (y_{DA} - y_{FA})(z_{BA} - z_{GA})} \\
c_5 = -\dfrac{(w_A z_{GA}^2 - w_D z_{BA}^2 - w_B z_{GA}^2 + w_G z_{BA}^2 - w_G z_{BA} z_{GA} + w_B z_{BA} z_{GA} + w_D z_{BA} z_{GA} - w_E z_{BA} z_{GA})}{z_{BA} z_{GA} (-z_{BA}^2 + z_{GA} z_{BA})} \\
c_6 = w_A
\end{cases}
$$

After replacing y, z by y_i, z_i in Eq. (3.20), one obtains equations to be applied at slave node *i*:

$$
\begin{cases}
u(y_i, z_i) = u_i^S = y_i z_i^3 a_1 + z_i y_i^3 a_2 + y_i z_i a_3 + y_i a_4 + z_i a_5 + a_6 \\
v(y_i, z_i) = v_i^S = y_i^2 b_1 + z_i^2 b_2 + y_i z_i b_3 + y_i b_4 + z_i b_5 + b_6 \\
w(y_i, z_i) = w_i^S = y_i^2 c_1 + z_i^2 c_2 + y_i z_i c_3 + y_i c_4 + z_i c_5 + c_6
\end{cases}
\tag{3.35}
$$

with coefficients a_1 to a_6, b_1 to b_6, and c_1 to c_6 defined in Eq. (3.34).

This model contains eighteen master degrees of freedom per cross-section. Eq. (3.35) describes linear relations between slave and master degrees of freedom.

3.3.5 SB2-3D model

The methodology is now applied to build the SB2-3D model. This model exploits eight master nodes *A*, *B*, *C*, *D*, *E*, *F*, *G* and *H*, as shown in Fig. 3.7. Eq. (3.21) contains eight coefficients (a_1 to a_8) to be determined for displacement *u*, six coefficients (b_1 to b_6) for displacement *v* and six coefficients (c_1 and c_6) for displacement *w*. Besides, the coefficients b_1 to b_6 and c_1 to c_6 are the same as the coefficients defined in Section 3.3.4. To identify the first eight coefficients, the following equations are used:

$$\begin{cases} u(y_A, z_A) = u_A = y_A z_A^3 a_1 + y_A^3 z_A a_2 + y_A^3 a_3 + z_A^3 a_4 + y_A z_A a_5 + y_A a_6 + z_A a_7 + a_8 \\ u(y_B, z_B) = u_B = y_B z_B^3 a_1 + y_B^3 z_B a_2 + y_B^3 a_3 + z_B^3 a_4 + y_B z_A a_5 + y_B a_6 + z_B a_7 + a_8 \\ u(y_C, z_C) = u_C = y_C z_C^3 a_1 + y_C^3 z_A a_2 + y_C^3 a_3 + z_C^3 a_4 + y_C z_C a_5 + y_C a_6 + z_C a_7 + a_8 \\ u(y_D, z_D) = u_D = y_D z_D^3 a_1 + y_D^3 z_D a_2 + y_D^3 a_3 + z_D^3 a_4 + y_D z_A a_5 + y_D a_6 + z_D a_7 + a_8 \\ u(y_E, z_E) = u_E = y_E z_E^3 a_1 + y_E^3 z_E a_2 + y_E^3 a_3 + z_E^3 a_4 + y_E z_E a_5 + y_E a_6 + z_E a_7 + a_8 \\ u(y_F, z_F) = u_F = y_F z_F^3 a_1 + y_F^3 z_F a_2 + y_F^3 a_3 + z_F^3 a_4 + y_F z_A a_5 + y_F a_6 + z_F a_7 + a_8 \\ u(y_G, z_G) = u_G = y_G z_G^3 a_1 + y_G^3 z_G a_2 + y_G^3 a_3 + z_G^3 a_4 + y_G z_G a_5 + y_G a_6 + z_G a_7 + a_8 \\ u(y_H, z_H) = u_H = y_H z_H^3 a_1 + y_H^3 z_H a_2 + y_H^3 a_3 + z_H^3 a_4 + y_H z_H a_5 + y_H a_6 + z_H a_7 + a_8 \end{cases} \quad (3.36)$$

where $u_A, u_B, u_C, u_D, u_E, u_F, u_G, u_H$ are the displacements at master nodes; $z_A, z_B, z_C, z_D, z_E, z_F, z_G, z_H$ and $y_A, y_B, y_C, y_D, y_E, y_F, y_G, y_H$ are the coordinates of master nodes.

For simplification, point *A* on the cross-section can be supposed as the relative origin in the coordinate system. Therefore, some equality relations between the coordinates can be expressed as:

$$\begin{cases} y_B = y_C = 0 \\ y_{DA} = y_D - y_A = y_{EA} = y_{GA} \\ y_{FA} = y_F - y_A = y_{HA} \\ z_D = z_H = 0 \\ z_{BA} = z_B - z_A = z_{FA} = z_{EA} \\ z_{GA} = z_G - z_A = z_C \end{cases} \quad (3.37)$$

where $y_{DA}, y_{EA}, y_{FA}, y_{GA}, y_{HA}, z_{BA}, z_{EA}, z_{FA}, z_{GA}$ and z_{HA} are the relative coordinates of points *B*, *D*, *E*, *F*, *G* and *H* to point *A* in the *y* and *z* directions.

Considering Eq. (3.37), the expressions of coefficients identified for each cross-section are:

$$
\begin{cases}
a_1 = -\dfrac{u_A z_{BA} - u_C z_{BA} - u_A z_{GA} - u_D z_{BA} + u_B z_{GA} + u_G z_{BA} + u_D z_{GA} - u_E z_{GA}}{y_{DA} z_{BA} z_{GA}(z_{BA} + z_{GA})(z_{BA} - z_{GA})} \\
a_2 = -\dfrac{u_A y_{DA} - u_B y_{DA} - u_A y_{FA} + u_B y_{FA} + u_D y_{FA} + u_F y_{DA} - u_H y_{DA} - u_E y_{FA}}{y_{DA} y_{FA} z_{BA}(y_{DA}^2 - y_{FA}^2)} \\
a_3 = \dfrac{u_A y_{DA} - u_A y_{FA} + u_D y_{FA} - u_H y_{DA}}{y_{DA} y_{FA}(y_{DA}^2 - y_{FA}^2)} \\
a_4 = \dfrac{u_A z_{BA} - u_C z_{BA} - u_A z_{GA} + u_B z_{GA}}{z_{BA} z_{GA}(z_{BA}^2 - z_{GA}^2)} \\
a_5 = -\dfrac{\begin{pmatrix} u_A y_{FA}^3 z_{BA}^3 + u_A y_{DA}^3 z_{GA}^3 - u_B y_{DA}^3 z_{GA}^3 - u_C y_{FA}^3 z_{BA}^3 - u_A y_{FA}^3 z_{GA}^3 \\ -u_D y_{FA}^3 z_{BA}^3 + u_B y_{FA}^3 z_{GA}^3 + u_G y_{FA}^3 z_{BA}^3 + u_D y_{FA}^3 z_{GA}^3 + u_F y_{DA}^3 z_{GA}^3 \\ -u_H y_{DA}^3 z_{GA}^3 - u_E y_{FA}^3 z_{GA}^3 - u_A y_{DA}^2 y_{FA} z_{BA}^3 + u_C y_{DA}^2 y_{FA} z_{BA}^3 \\ +u_D y_{DA}^2 y_{FA} z_{BA}^3 - u_G y_{DA}^2 y_{FA} z_{BA}^3 - u_A y_{DA}^3 z_{BA}^2 z_{GA} + u_B y_{DA}^3 z_{BA}^2 z_{GA} \\ -u_F y_{DA}^3 z_{BA}^2 z_{GA} + u_H y_{DA}^3 z_{BA}^2 z_{GA} + u_A y_{DA}^2 y_{FA} z_{BA}^2 z_{GA} - u_B y_{DA}^2 y_{FA} z_{BA}^2 z_{GA} \\ -u_D y_{DA}^2 y_{FA} z_{BA}^2 z_{GA} + u_E y_{DA}^2 y_{FA} z_{BA}^2 z_{GA} \end{pmatrix}}{y_{DA} y_{FA} z_{BA} z_{GA}(z_{BA} + z_{GA})(z_{BA} - z_{GA})(y_{DA}^2 - y_{FA}^2)} \\
a_6 = -\dfrac{u_A y_{DA}^3 - u_A y_{FA}^3 + u_D y_{FA}^3 - u_H y_{DA}^3}{y_{DA} y_{FA}(y_{DA}^2 - y_{FA}^2)} \\
a_7 = -\dfrac{u_A z_{BA}^3 - u_C z_{BA}^3 - u_A z_{GA}^3 + u_B z_{GA}^3}{z_{BA} z_{GA}(z_{BA}^2 - z_{GA}^2)} \\
a_8 = u_A
\end{cases}
\tag{3.38}
$$

As mentioned above, the coefficients b_1 to b_6, c_1 to c_6 are the same as the coefficients defined in Section 3.3.4. After replacing y, z by y_i, z_i in Eq. (3.21), one obtains equations to be applied at slave node *i*:

$$
\begin{cases}
u(y_i, z_i) = u_i^S = y_i z_i^3 a_1 + z_i y_i^3 a_2 + y_i^3 a_3 + z_i^3 a_4 + y_i z_i a_5 + y_i a_6 + z_i a_7 + a_8 \\
v(y_i, z_i) = v_i^S = y_i^2 b_1 + z_i^2 b_2 + y_i z_i b_3 + y_i b_4 + z_i b_5 + b_6 \\
w(y_i, z_i) = w_i^S = y_i^2 c_1 + z_i^2 c_2 + y_i z_i c_3 + y_i c_4 + z_i c_5 + c_6
\end{cases}
\tag{3.39}
$$

with coefficients a_1 to a_8, b_1 to b_6, and c_1 to c_6 defined in Eq. (3.38) and Section 3.3.4.

This model contains twenty master degrees of freedom per cross-section. Eq. (3.39) describes linear relations between slave and master degrees of freedom.

3.3.6 Remarks

The method is the same for the five beam theories considered in Sections 3.3.1 to 3.3.5. The only difference is the number of master degrees of freedom per cross-section, namely three, eight, nine, eighteen and twenty for the FOSB, MFOSB, HOSB, SB1-3D and SB2-3D models respectively. Among them, the first three models for a beam in plane will be assessed through static examples, and the latter

two models for a beam in space will be assessed through vibration examples. The number of equations applied is equal to the number of slave degrees of freedom which are eliminated. Consequently, the model size does not depend on the number of nodes in each cross-section but is given by the number of master degrees of freedom. As described above, all the relations between master and slave degrees of freedom are linear. For implementation, the "*EQUATION" keyword in Abaqus [61] is used to introduce these linear equations. In the post-processing step, displacements are available for all the nodes. Then the stresses can be calculated in all the elements. The average value at nodes is retained to evaluate the stresses.

This new solid-beam approach uses displacements exclusively, without rotations or other types of degrees of freedom. It is an interesting characteristic of our methodology, particularly for higher-order theories that initially use not only displacements and rotations but also other types of degrees of freedom. Moreover, other displacement fields can also be applied in our approach, for instance, an even higher-order beam theory can be considered if necessary.

3.4 Static examples

The new solid-beam approach for FOSB, MFOSB and HOSB models is here used for the treatment of two examples with thin and thick cases in the context of static analysis: a straight beam with square cross-section under distributed loading and a curved beam with square cross-section under distributed loading. A convergence study is made for each example. The displacement and the von Mises stress are studied. The finite element results obtained with the solid-beam models are evaluated by comparison with a reference solid model. The reduction of model size due to the solid-beam approach is discussed. The compatibility of the solid-beam approach with another efficient solid element is also proved.

3.4.1 Straight beam with square cross-section under distributed loading

3.4.1.1 Presentation of the example

The straight beam with square cross-section is presented in Fig. 3.8. The structure is clamped at its two ends and submitted to a distributed loading applied on the upper surface. A relatively thin beam case (l/h=20) as well as a thick beam one (l/h=5), are considered.

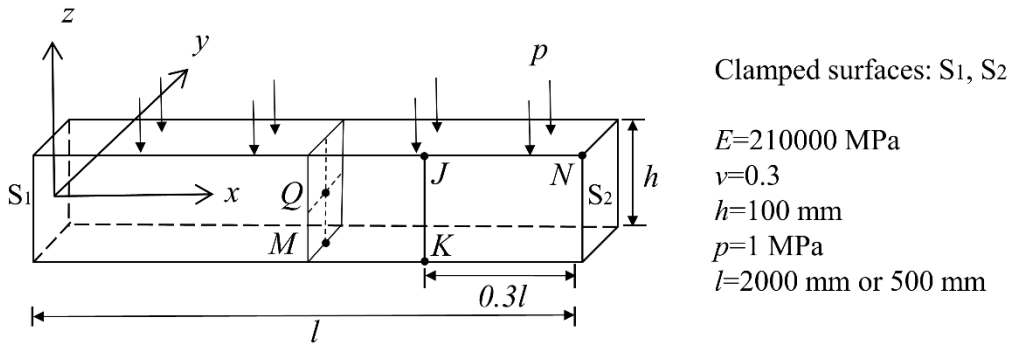

Fig. 3.8. Straight beam with square cross-section under distributed loading – Presentation of the example.

3.4.1.2 Convergence study

A convergence study is presented, to ensure that solid-beam approach meets the convergence conditions and to compare its performances with those of the solid approach. In this example, the twenty-node hexahedral finite element C3D20 of Abaqus [61] is used. The displacement for several mesh refinement levels is observed in the center (point *M* in Fig. 3.8) of the bottom surface. The solid models with very fine 8×8×100 and 8×8×60 meshes are respectively chosen as the reference for thin and thick cases. Convergence is considered to be achieved if the error is less than 0.5% compared with these reference models. The results of thin and thick cases are reported in Table 3.1 and Table 3.2 respectively. The solid model and the HOSB model give very close results and convergence is obtained with a 4×4×40 mesh in the thin case and a 4×4×20 mesh in the thick one. The MFOSB model is satisfactory in the thin case but leads to a small error in the thick one, even for a refined mesh. The FOSB model converges to completely wrong values compared with the reference solid model. Consequently this model is unacceptable.

Table 3.1. Straight beam with square cross-section under distributed loading – Convergence study of displacement *w* at point *M* in the thin case.

Mesh	Models	Displacement *w* (mm)	Error (%)
8×8×100	Reference	-2.427	–
1×1×10	Solid	-2.314	4.7
	HOSB	–	–
	MFOSB	–	–
	FOSB	-1.825	24.8
2×2×20	Solid	-2.400	1.1
	HOSB	-2.406	0.9
	MFOSB	-2.396	1.3
	FOSB	-1.830	24.6
4×4×40	Solid	-2.420	0.3
	HOSB	-2.422	0.2
	MFOSB	-2.417	0.4
	FOSB	-1.831	24.6

Table 3.2. Straight beam with square cross-section under distributed loading – Convergence study of displacement *w* at point *M* in the thick case.

Mesh	Models	Displacement *w* ($\times 10^{-2}$mm)	Error (%)
8×8×60	Reference	-1.316	–
1×1×6	Solid	-1.203	8.6
	HOSB	–	–
	MFOSB	–	–
	FOSB	-1.075	18.3
2×2×10	Solid	-1.288	2.1
	HOSB	-1.285	2.4
	MFOSB	-1.280	2.7
	FOSB	-1.077	18.2
4×4×20	Solid	-1.310	0.5
	HOSB	-1.309	0.5
	MFOSB	-1.299	1.3
	FOSB	-1.078	18.1

3.4.1.3 Displacements and stresses in the thin case

First displacements as well as von Mises stresses are observed over the whole structure. The comparison of the results between solid, HOSB and MFOSB models are presented in Fig. 3.9. The FOSB model is not considered because its convergence performance is not satisfactory. These results are obtained with the 4×4×40 mesh, which meets the convergence criterion as highlighted in Section 3.4.1.2. The vertical displacements and von Mises stresses obtained with the three models are very similar to each other.

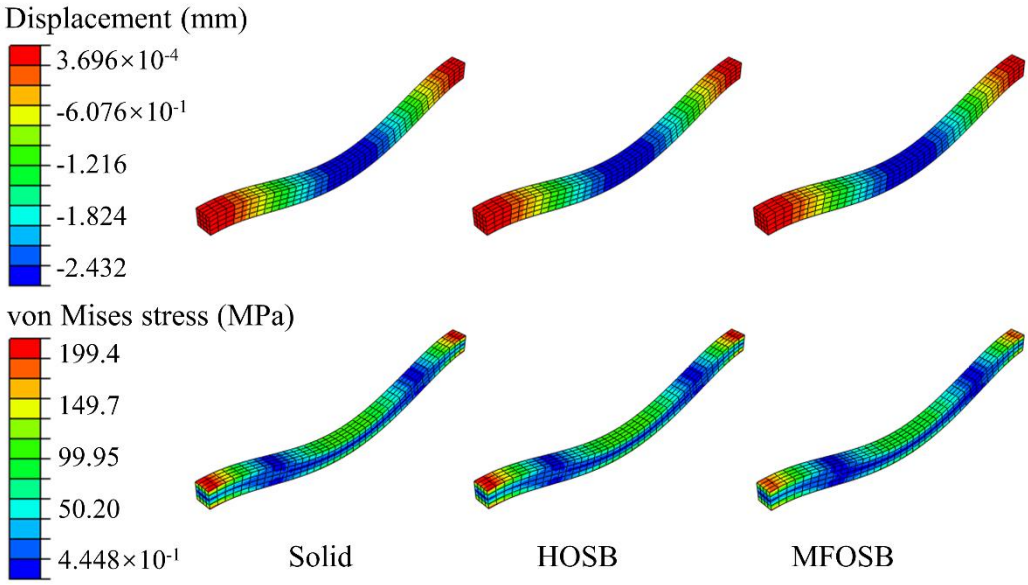

Fig. 3.9. Straight beam with square cross-section under distributed loading – Displacement *w* and von Mises stress distribution in the thin case.

The distribution of vertical displacement along the mid-axis and von Mises stress along a line on the lower surface is shown in Fig. 3.10. The solid-beam models are compared with the solid model and two classical beam models. The elements B21 and B23 in Abaqus are used for representing the thick beam and thin beam models respectively. A mesh containing forty B21 or B23 finite elements, which meets the convergence criterion, is considered for the thin beam and thick beam models. All the models have similar results for displacements and stresses except the FOSB model which shows significant errors. These errors are essentially due to a spurious σ_{zz} stress state being discussed below.

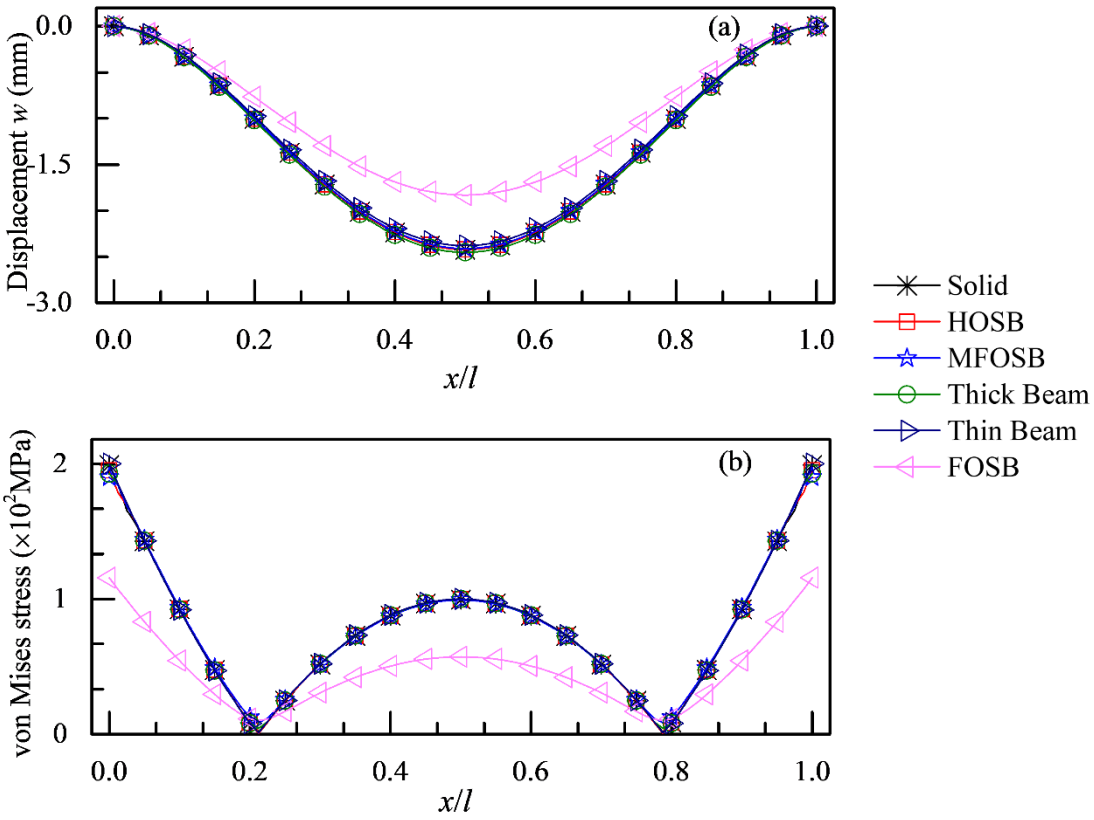

Fig. 3.10. Straight beam with square cross-section under distributed loading – Distribution of vertical displacement along the mid-axis (a) and von Mises stress along a line on the lower surface (b), in the thin case.

Fig. 3.11 presents the through-the-thickness distribution of displacements and stresses along a line *JK* (see Fig. 3.8). The solid model is considered as the reference. Firstly, the FOSB model shows unsatisfactory results, especially for displacement *w* (Fig. 3.11b) and σ_{zz} stress (Fig. 3.11e). Because *w* is considered as constant through the thickness, the ε_{zz} strain is equal to zero, which is not correct due to the Poisson effect. This nonphysical assumption greatly disturbs the state of stress in the 3D elasticity situation. Particularly, it implies large σ_{zz} stress, which should remain very small in this thin beam case. Therefore, the von Mises stress depending on the different stress components is affected and this explains the bad results reported in Fig. 3.10. These poor results confirm that this kinematic assumption is not compatible with 3D theory of elasticity, although consistent and valid in the context of the classical beam theory. Furthermore, the FOSB model also gives a constant σ_{xz} stress distribution (Fig. 3.11d), which is a well-known limitation of the Timoshenko beam theory. Usually, the integration of equilibrium equations is used to obtain a quadratic and correct distribution of transverse shear stresses.

The reference displacement *u* (Fig. 3.11a) is linear and both the MOFSB and HOSB models perfect fit this distribution. The displacement *w* is also well predicted by these two solid-beam models. This component seems to be constant but actually has a slight quadratic tendency. One can observe linear distribution of σ_{xx} stress (Fig. 3.11c) and again the MOFSB and HOSB models provide good results. The HOSB model accurately reproduces the classical quadratic distribution of σ_{xz} stress. Namely, the

free-face condition $\sigma_{xz} = 0$ is almost met at top and bottom surfaces. Thanks to the quadratic distribution of displacement *w*, the MFOSB model also exhibits a quadratic trend, but a significant discrepancy with the reference result is observed. Namely the free-face condition mentioned above is not met. However, it is not important for this thin case since transverse shear stresses are usually neglected in thin structures and the influence of transverse shear effects on displacements is small. In summary the HOSB model gives outstanding results for the thin case, while the MOFSB model is also satisfactory but cannot perfectly reproduce the transverse shear effects. Anyway, one can neglect these effects for a thin structure. Finally, the FOSB model is not able to provide good results, and thus is not considered for the rest of the study.

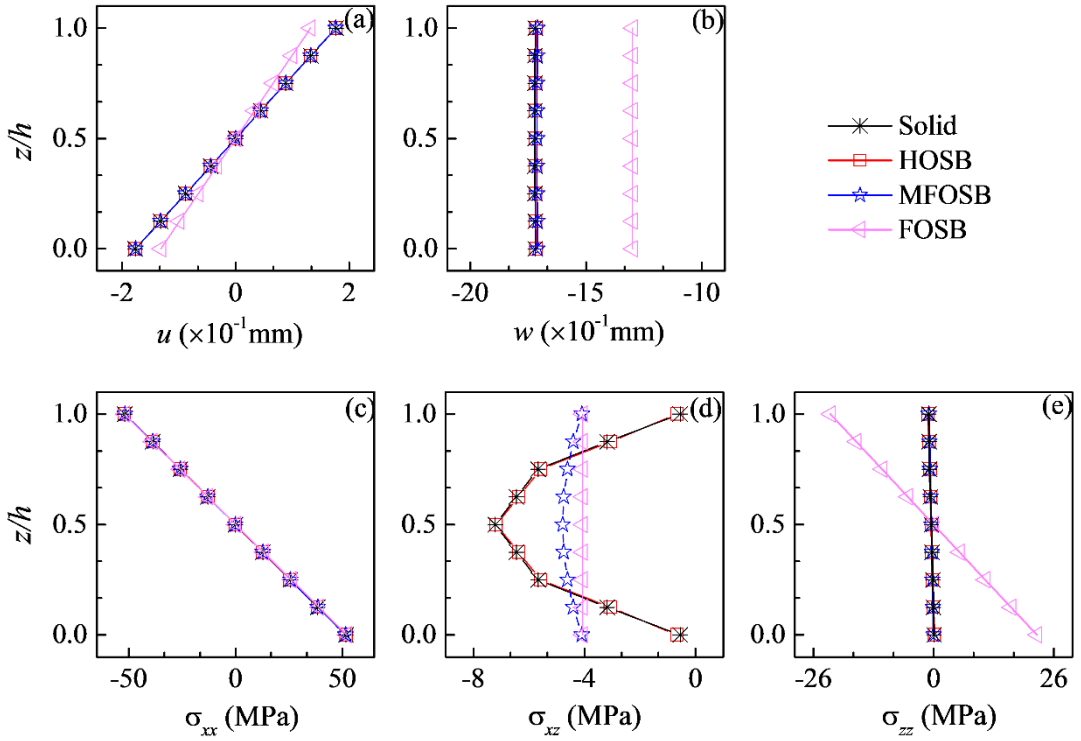

Fig. 3.11. Straight beam with square cross-section under distributed loading – Through-the-thickness displacement and stresses along a line *JK*, in the thin case.

3.4.1.4 Displacements and stresses in the thick case

As for the thin case first of all displacements and von Mises stresses are observed over the whole structure. The comparison of results obtained with the solid, MOFSB and HOSB models are shown in Fig. 3.12. The 4×4×20 mesh, which meets the convergence criterion as highlighted in Section 3.4.1.2, is used. The solid model and the HOSB model perform similar results in this global observation. For the MOFSB model, some little difference appears on displacement and von Mises stress in this thick beam case.

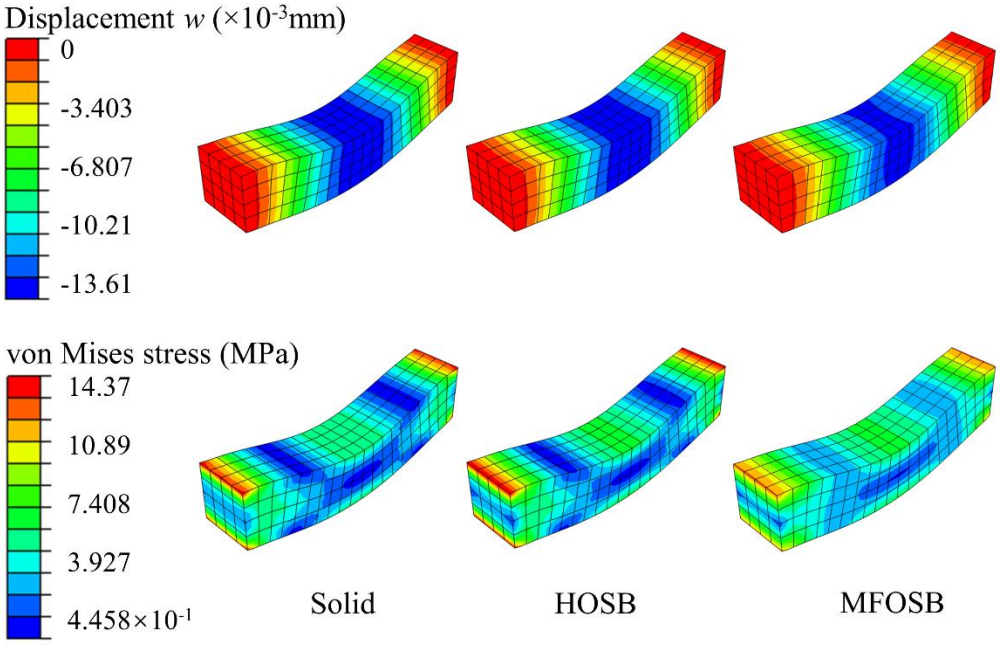

Fig. 3.12. Straight beam with square cross-section under distributed loading – Displacement *w* and von Mises stress distribution in the thick case.

Fig. 3.13 presents the distribution of vertical displacement along the mid-axis and von Mises stress along a line on the lower surface. The solid model and solid-beam models use the 4×4×20 mesh, while the beam models use a mesh with twenty elements, which both satisfy the convergence criterion. For displacement, the HOSB model fits very well with the solid one. Significant error is obtained with the thin beam model which neglects transverse shear effects. Relatively small errors appear with the thick beam model and the MFOSB model. For von Mises stress, again the HOSB model has a perfect fit with the reference, while the beam models lead to small errors in the boundary conditions area. The discrepancy shown with the MFOSB model is due to a rough calculation of transverse stresses which play a significant role in thick structures. Therefore, the HOSB model is confirmed to properly predict the mechanical behavior of a thick beam which is submitted to significant transverse shear effects.

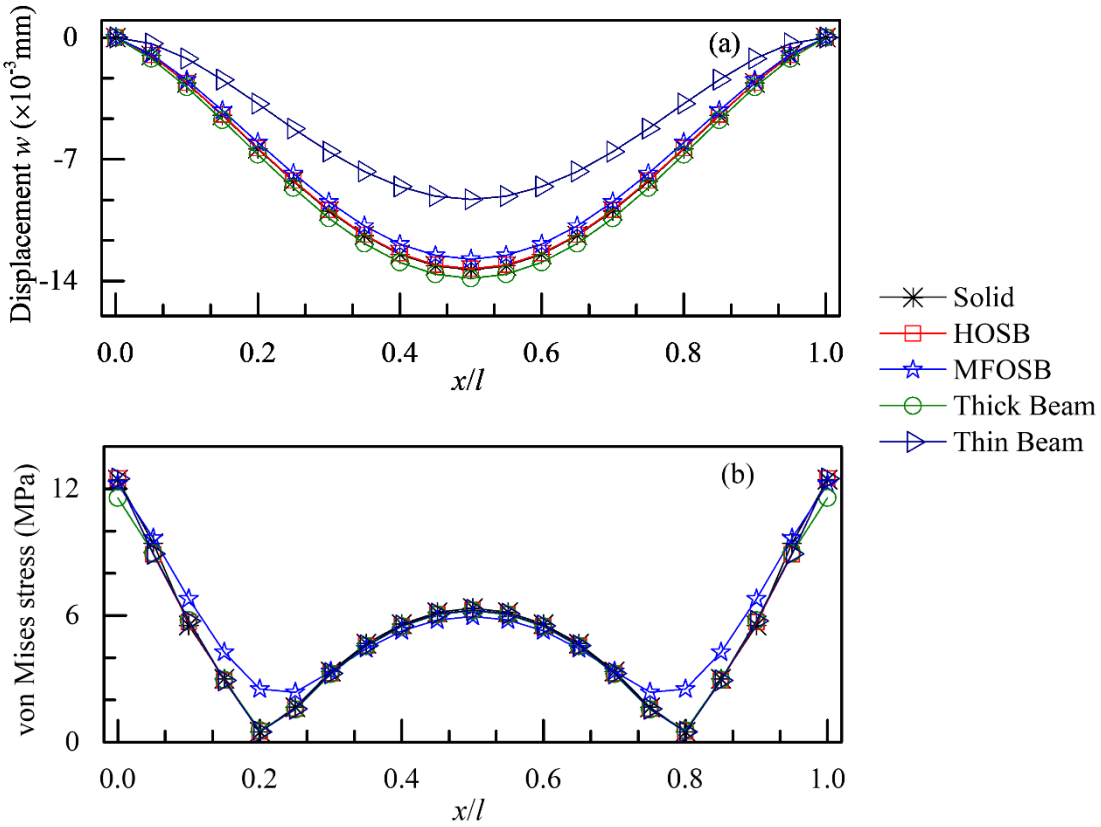

Fig. 3.13. Straight beam with square cross-section under distributed loading – Distribution of vertical displacement along the mid-axis (a) and von Mises stress along a line on the lower surface (b), in the thick case.

Fig. 3.14 shows the distribution of displacements and stresses along a line *JK* (see Fig. 3.8), again the solid model being the reference. Several limitations are shown with the MFOSB model. The quadratic tendency of displacement *w* (Fig. 3.14b) is reproduced but the values are incorrect, which means the stiffness is not well estimated. This is due to the fact that transverse shear stiffness is not precisely calculated. Namely, this model fails in reproducing the quadratic distribution of the reference stress σ_{xz} (Fig. 3.14d). Moreover, the free-face condition $\sigma_{xz} = 0$ is not met at top and bottom surfaces. And obviously, the transverse shear effects play an important role in the thick case. The classical Timoshenko beam theory is associated with shear correction factors to avoid the limitation caused by kinematic assumptions. But in our solid-beam approach, no correction factor is introduced. Of course, this wrong σ_{xz} distribution consequently leads to errors on the von Mises stress, as highlighted in Fig. 3.13. Besides, this MFOSB model cannot replicate the slight nonlinear distribution of displacement *u* (Fig. 3.14a) and stress σ_{xx} (Fig. 3.14c). On the contrary, the HOSB model shows an excellent fit with the solid model. It correctly predicts the quadratic distribution of displacement *w*, the nonlinear distribution of stress σ_{xx} and the quadratic distribution of stress σ_{xz}. In particular, the free-face condition $\sigma_{xz} = 0$ is almost met at top and bottom surfaces. Moreover the distribution of stress σ_{zz} (Fig. 3.14e) is also correctly predicted.

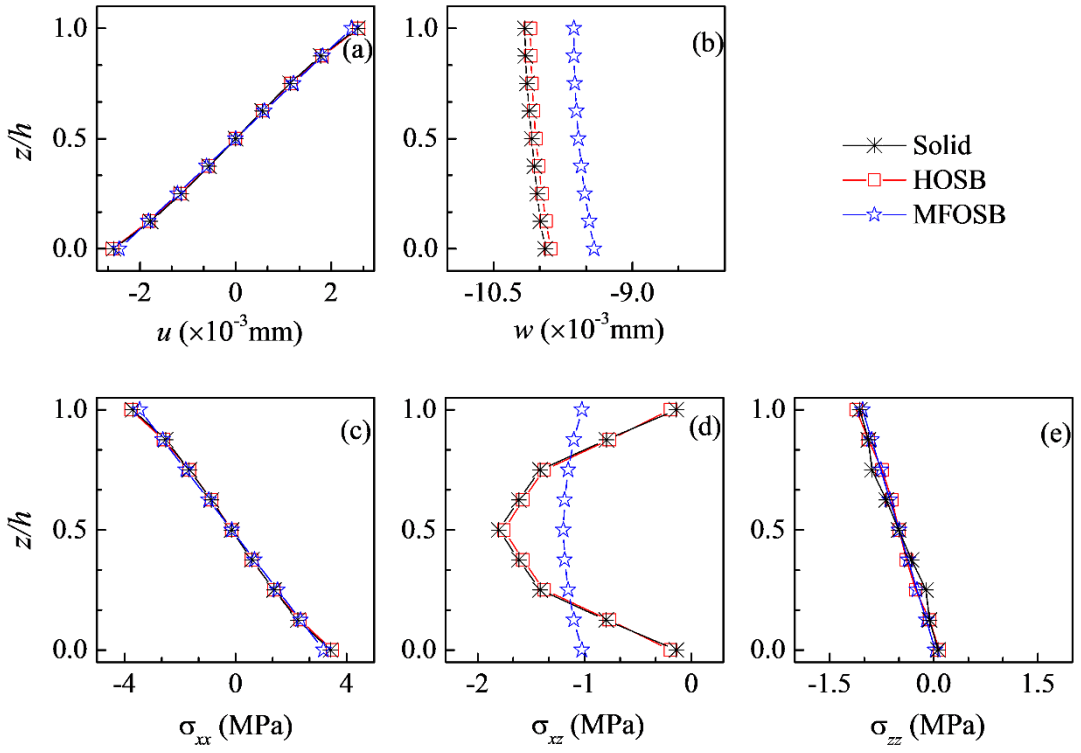

Fig. 3.14. Straight beam with square cross-section under distributed loading – Through-the-thickness displacement and stresses along a line *JK*, in the thick case.

3.4.1.5 Accuracy synthesis of solid-beam models

Table 3.3 summarizes the errors obtained with the solid-beam models in the thin and thick cases. These errors are calculated at center (point *Q* in Fig. 3.8) and corner (point *N* in Fig. 3.8) corresponding to the maximal displacement and von Mises stress respectively. The MFOSB model shows good performance in the thin case, the maximal error being limited to about 1% for the displacement and von Mises stress. The HOSB model even works better because transverse shear effects are not completely negligible in this thin case. Actually, the *l/h* ratio equaling to 20 is not characteristic of a very thin beam. For the thick case, the HOSB model remains satisfactory with errors not exceeding 1.5%. The MFOSB model is less efficient, errors are close to 5% for the displacement and 9% for the von Mises stress. Summarily, the MFOSB model is convenient for the thin case only, while the HOSB model gives excellent results in both the thin and thick cases. Additionally, the same study has been performed with the eight-node hexahedral element C3D8I of Abaqus. Similar results have been obtained showing that the solid-beam methodology can be used with any efficient solid element.

Table 3.3. Straight beam with square cross-section under distributed loading – Errors on maximal displacement and maximal von Mises stress.

Examples	Models	Displacement w		von Mises stress	
		Maximum ($\times 10^{-2}$mm)	Error (%)	Maximum (MPa)	Error (%)
Thin case	Solid	-243.2	–	184.5	–
	HOSB	-242.9	0.1	183.6	0.5
	MFOSB	-242.0	0.5	182.4	1.1
Thick case	Solid	-1.361	–	11.76	–
	HOSB	-1.355	0.4	11.59	1.4
	MFOSB	-1.299	4.6	10.76	8.5

3.4.2 Curved beam with square cross-section under distributed loading

3.4.2.1 Presentation of the example

The second example is a curved beam with a square cross-section. The structure is clamped at its two ends and submitted to a distributed vertical loading applied on the top surface, as shown in Fig. 3.15a. A relatively thin beam case (r/h=10) as well as a thick beam one (r/h=10/3), are considered. This structure is curved, which leads to the coupling of bending and membrane effects, compared with the first example for which the structure is submitted to pure bending effects only. Furthermore, local coordinate systems (see in Fig. 3.15b) are created for each cross-section to apply kinematic relations.

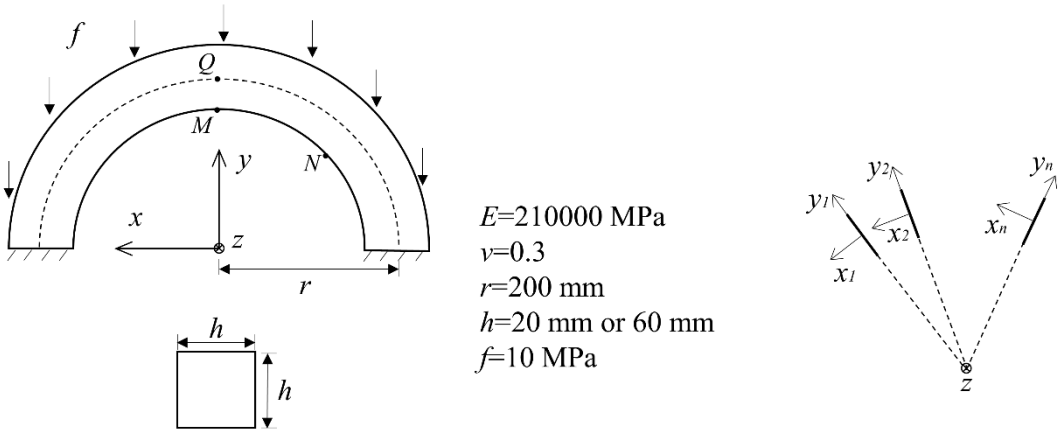

Fig. 3.15. Curved beam with square cross-section under distributed loading – Presentation of the example.

3.4.2.2 Convergence study

The same type of convergence study detailed in Section 3.4.1.2 is presented here. Again, the element C3D20 is used. The evolution of displacement for different mesh refinement levels at point M (see Fig.

3.15a) is observed. A solid model with a very fine 8×8×100 mesh is chosen to be a reference. The convergence is considered to be achieved if the error is less than 0.5% compared with the reference. The results of thin and thick cases are reported in Table 3.4 and Table 3.5 respectively. The observations are similar, compared to the first example. The solid model and the HOSB model give very close results and convergence is obtained with a 4×4×50 mesh in the thin and thick cases. The MFOSB model is satisfactory in the thin case but leads to a small error in the thick one, even for a refined mesh.

Table 3.4. Curved beam with square cross-section under distributed loading – Convergence study of displacement w at point M in the thin case.

Mesh	Models	Displacement w ($\times 10^{-1}$mm)	Error (%)
8×8×100	Reference	-9.723	–
1×1×10	Solid	-8.380	13.8
	HOSB	–	–
	MFOSB	–	–
2×2×30	Solid	-9.632	0.9
	HOSB	-9.615	1.1
	MFOSB	-9.613	1.1
4×4×50	Solid	-9.700	0.2
	HOSB	-9.679	0.4
	MFOSB	-9.676	0.5

Table 3.5. Curved beam with square cross-section under distributed loading – Convergence study of displacement w at point M in the thick case.

Mesh	Models	Displacement w ($\times 10^{-2}$mm)	Error (%)
8×8×100	Reference	-10.23	–
1×1×10	Solid	-9.867	3.6
	HOSB	–	–
	MFOSB	–	–
2×2×30	Solid	-10.17	0.7
	HOSB	-10.12	1.1
	MFOSB	-10.10	1.3
4×4×50	Solid	-10.21	0.2
	HOSB	-10.18	0.5
	MFOSB	-10.15	0.8

3.4.2.3 Displacements and stresses in the thin case

Displacement w and von Mises stress are observed over the whole structure. Fig. 3.16 shows a comparison of results between the solid, MFOSB and HOSB models. The results are obtained with the 4×4×50 mesh, which meets the convergence criterion. Similar displacements and von Mises stress results are obtained with the three models.

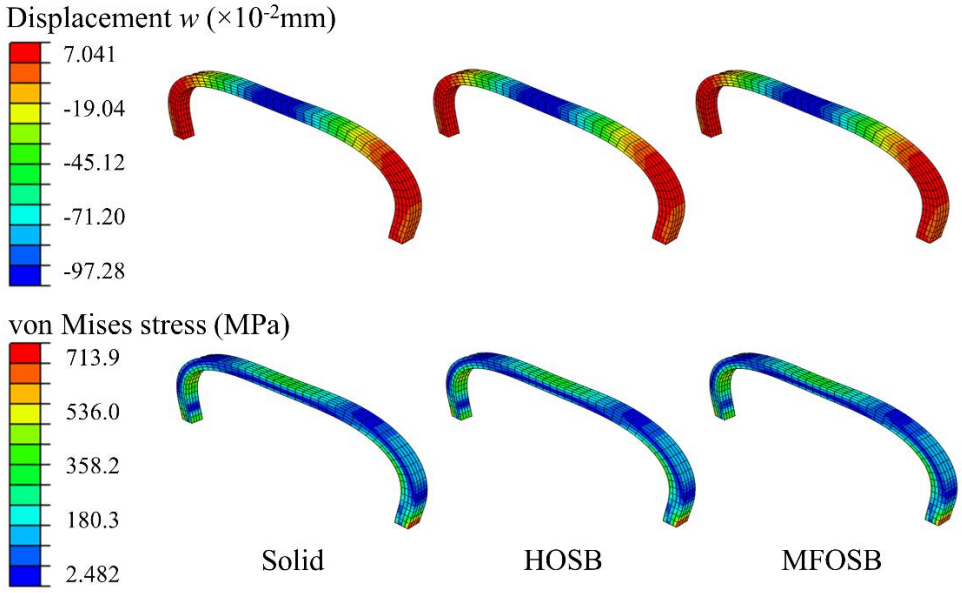

Fig. 3.16. Curved beam with square cross-section under distributed loading – Displacement and von Mises stress distributions in the thin case.

Fig. 3.17 presents the distribution of vertical displacement in the global coordinate system along the mid-axis and von Mises stress along a line on the lower surface. Again the 4×4×50 mesh is chosen for the solid and solid-beam models. For the thin beam and thick beam models, a mesh containing fifty elements is considered. Almost all the models give similar results of displacements and von Mises stress. The thin beam model leads to some minor difference compared with the reference. Indeed the structure is not very thin and consequently, transverse shear effects, which are not taken into account by in the thin beam theory, are not completely negligible.

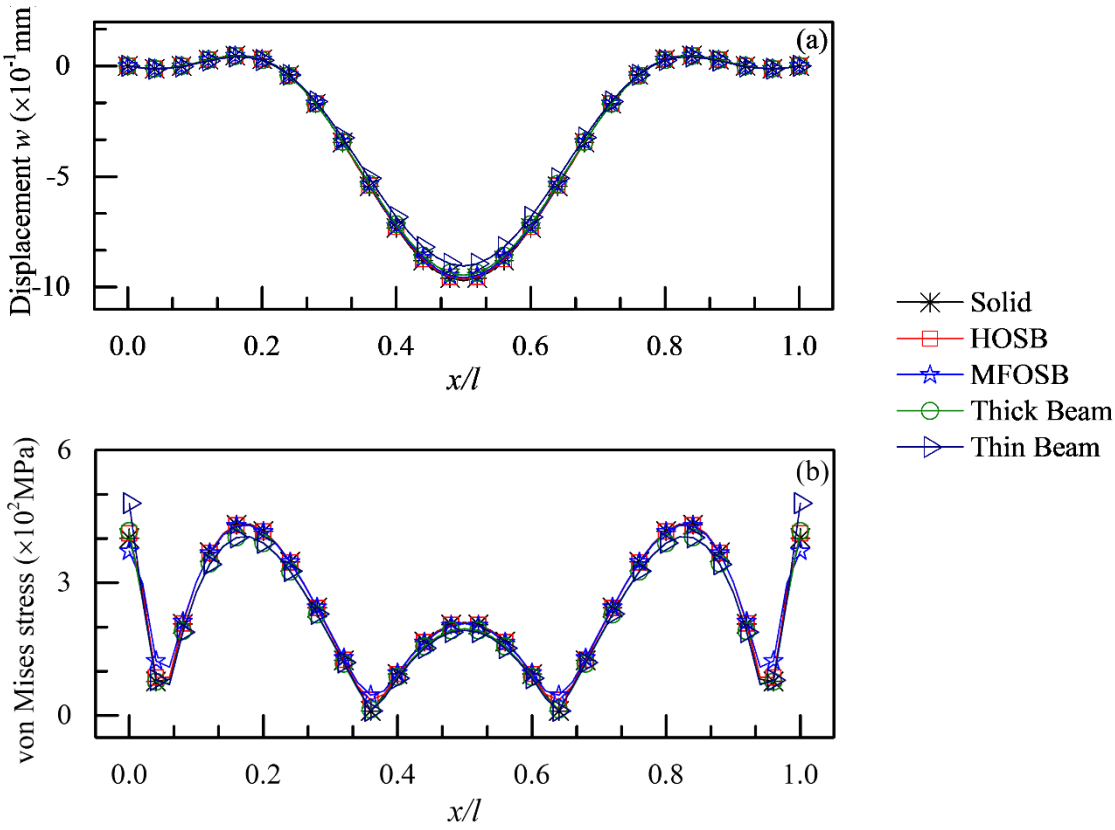

Fig. 3.17. Curved beam with square cross-section under distributed loading – Distribution of vertical displacement along the mid-axis (a) and von Mises stress along a line on the lower surface (b), in the thin case.

3.4.2.4 Displacements and stresses in the thick case

As for the thin case displacements and von Mises stresses are observed over the whole structure. Fig. 3.18 shows a comparison of results obtained with solid, MFOSB and HOSB models. The 4×4×50 mesh, which meets the convergence criterion, is used. The three models show close results, some minor differences on displacements and von Mises stresses can be observed.

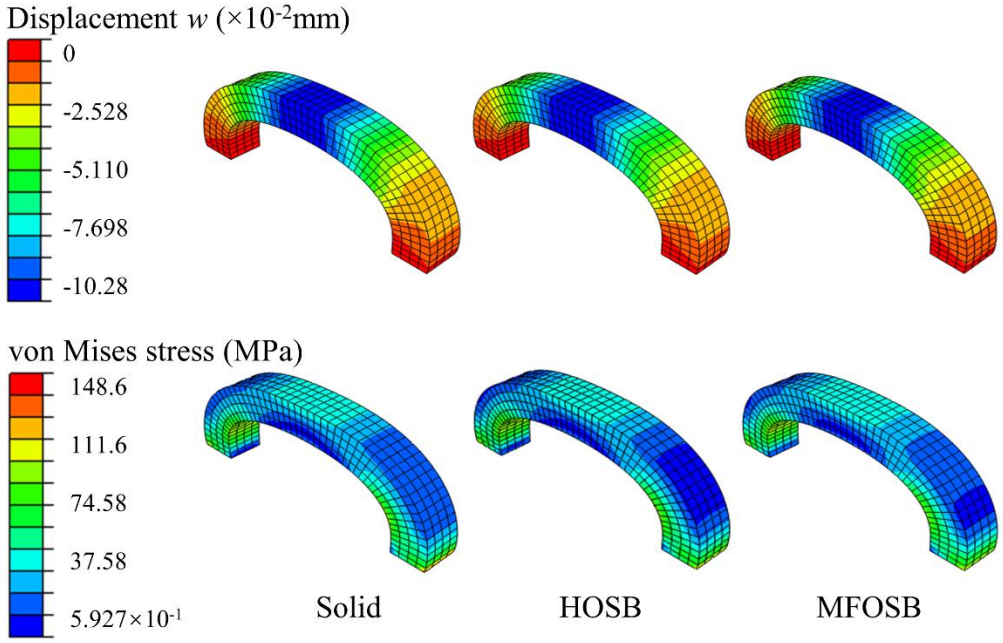

Fig. 3.18. Curved beam with square cross-section under distributed loading – Displacement and von Mises stress distributions in the thick case.

Fig. 3.19 gives the distribution of vertical displacement in the global coordinate system along the mid-axis and von Mises stress along a line on the lower surface. The solid model is considered as a reference. Again the 4×4×50 mesh is used for the solid and solid-beam models. For the beam models, a mesh containing fifty elements is used. The HOSB model fits well with the solid one for displacement, while some minor error is found with the MFOSB model. The HOSB model gives excellent result for von Mises stress, but the MFOSB model leads to some errors. These results confirm that the HOSB model is necessary to better reproduce the transverse shear effects which are significant in the thick beam case. It is worth mentioning that in this thick curved beam case, the thin beam model gives bad displacement and von Mises stress results. Moreover, even the thick beam model appears unsatisfactory for calculating von Mises stress. In Fig. 3.15a, one can see that the distributed loading is applied on the upper face of the structure. This is correctly taken into account with a solid or solid-beam model, but in the beam models, loading is applied on the mid-axis, except if specific techniques are used. For a curved and thick structure, the length of the mid-axis is significantly different from the length of the line on the upper face, leading to a loading error. It is a limitation of the beam approach and so the solid-beam approach is preferable from this point of view.

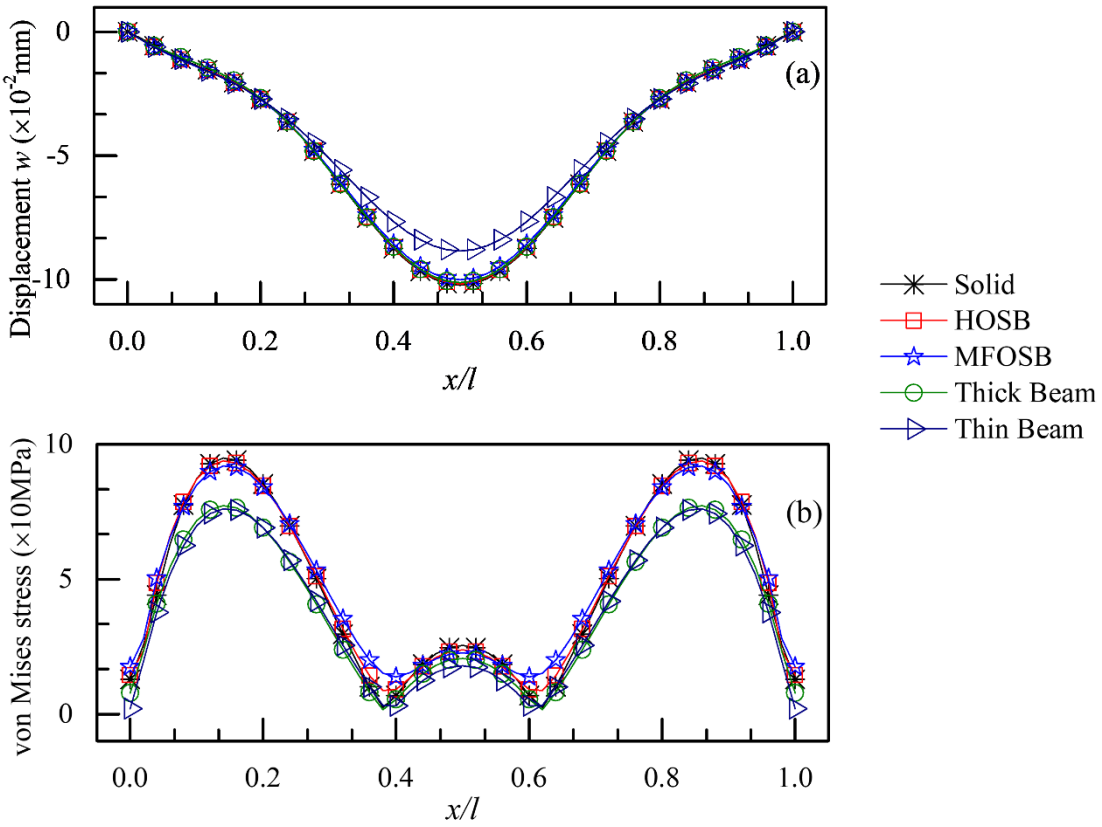

Fig. 19. Curved beam with square cross-section under distributed loading – Distribution of vertical displacement along the mid-axis (a) and von Mises stress along a line on the lower surface (b), in the thick case.

3.4.2.5 Accuracy synthesis of solid-beam models

Table 3.6 summarizes the errors obtained with the solid-beam models, in the thin and thick curved beam cases. These errors are calculated at center (point *Q* in Fig. 3.15a) and point *N* (in Fig. 3.15a) for displacement and von Mises stress, corresponding to the maximal displacement and von Mises stress respectively. The MFOSB model gives good results in the thin case, with errors around 1% for the displacement and von Mises stress. Similar to the first example, the HOSB model performs better. In the thick case, the HOSB model remains satisfactory with the errors limited to about 1%. The MFOSB model leads to some discrepancy, but the errors: about 2% for displacement and 3% for von Mises stress, remain limited. In summary, the HOSB model gives excellent results in both the thin and thick cases, while the MFOSB model is convenient for thin structures only. Again, similar results have been obtained by element C3D8I, which confirms that the methodology can be exploited with any efficient solid finite element.

Table 3.6. Curved beam with square cross-section under distributed loading – Errors on maximal displacement and maximal von Mises stress.

Examples	Models	Displacement w		von Mises stress	
		Maximum ($\times 10^{-2}$mm)	Error (%)	Maximum (MPa)	Error (%)
Thin curved beam	Solid	-97.28	–	432.6	–
	HOSB	-96.75	0.5	430.6	0.5
	MFOSB	-96.03	1.2	429.7	0.7
Thick curved beam	Solid	-10.34	–	94.92	–
	HOSB	-10.28	0.6	93.86	1.1
	MFOSB	-10.11	2.2	91.95	3.2

3.4.3 Model size

Fig. 3.20 compares the number of degrees of freedom between the solid model, and our solid-beam models. The results are obtained for the straight beam example, but other examples share the same trends. The size reduction is due to equations which lead to an elimination of slave degrees of freedom. It is an expected and hopeful characteristic of the solid-beam approach that the reduction of the number of degrees of freedom increases with the number of elements. For fine meshes, the gain is significant with solid-beam models compared with reference solid models. Of course, the gain of the MFOSB model is slightly larger compared with the HOSB model due to a smaller number of master nodes.

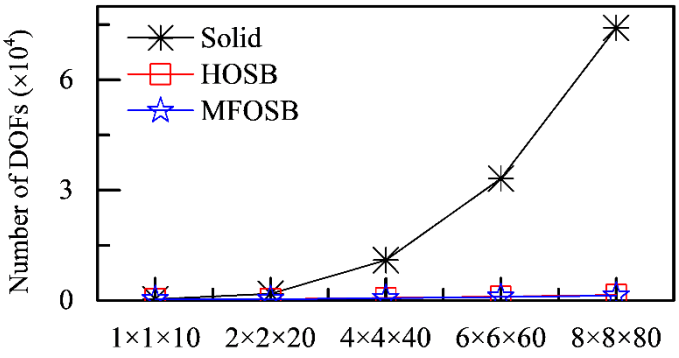

Fig. 3.20. Influence of the meshing refinement level on the number of degrees of freedom between solid, HOSB and MFOSB models.

It's interesting to compare the MFOSB and HOSB models with classical beam elements in terms of computational cost. Fig. 3.21 presents the comparison of the number of degrees of freedom for the curved beam example. For the solid-beam models, the results are reported with a 4×4×50 mesh which meets the convergence condition. The beam model with the same refinement level along the length of the structure is also considered, to compare the solid-beam approaches and the beam one. Results confirm that the beam or solid-beam approach gives a significant gain compared with the solid approach.

It can also be observed that the HOSB model requires only a little more degrees of freedom than the MFOSB model.

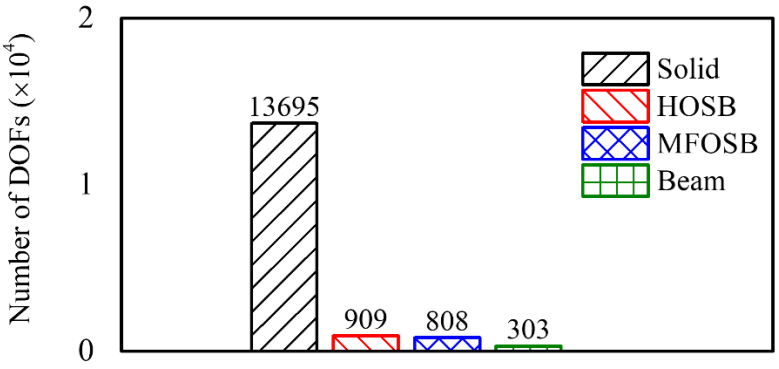

Fig. 3.21. Comparison of the number of degrees of freedom between solid, HOSB, MFOSB and beam models for the curved beam example.

3.5 Vibration examples

The new proposed solid-beam approach with MFOSB-3D and HOSB-3D models is now used for the treatment of two examples in the context of vibration analysis: a straight beam and a curved beam, in both thin and thick cases, described in Fig. 3.8 and Fig. 3.15 respectively. A convergence study is made for each example. The mode shapes and natural frequencies obtained by solid-beam models and reference solid model are compared.

3.5.1 Straight beam with square cross-section

3.5.1.1 Presentation of the example

The geometries of straight beam with square cross-section described in Fig. 3.8 are used in the context of free-free vibration analysis, with the density equal to 7.89×10^{-9} t/mm^3. The *l*/*h* ratio equals 20 or 5, representing the thin and thick cases.

3.5.1.2 Convergence study

The thin and very thick structures are discretized with the twenty-node hexahedral element C3D20 from Abaqus. For the two straight beams, a convergence study is made for the free-free vibration analysis of the first eight natural frequencies. For the reference solid, SB2-3D and SB1-3D models, the 4×4×40 and 4×4×20 meshes meet the convergence requirement for the thin and very thick cases respectively. Meshes containing forty B31 or B33 finite elements, which meet the convergence criterion, are considered for the thin beam models. Meshes containing twenty elements are considered for the thick beam models.

3.5.1.3 Mode shapes

For the reference solid, SB2-3D, and our SB2-3D models in the thin straight beam case, the first eight mode shapes are shown in Fig. 3.22. Mode 13 is a torsion mode and the others are bending modes. It is observed that all the models give very similar results for these modes.

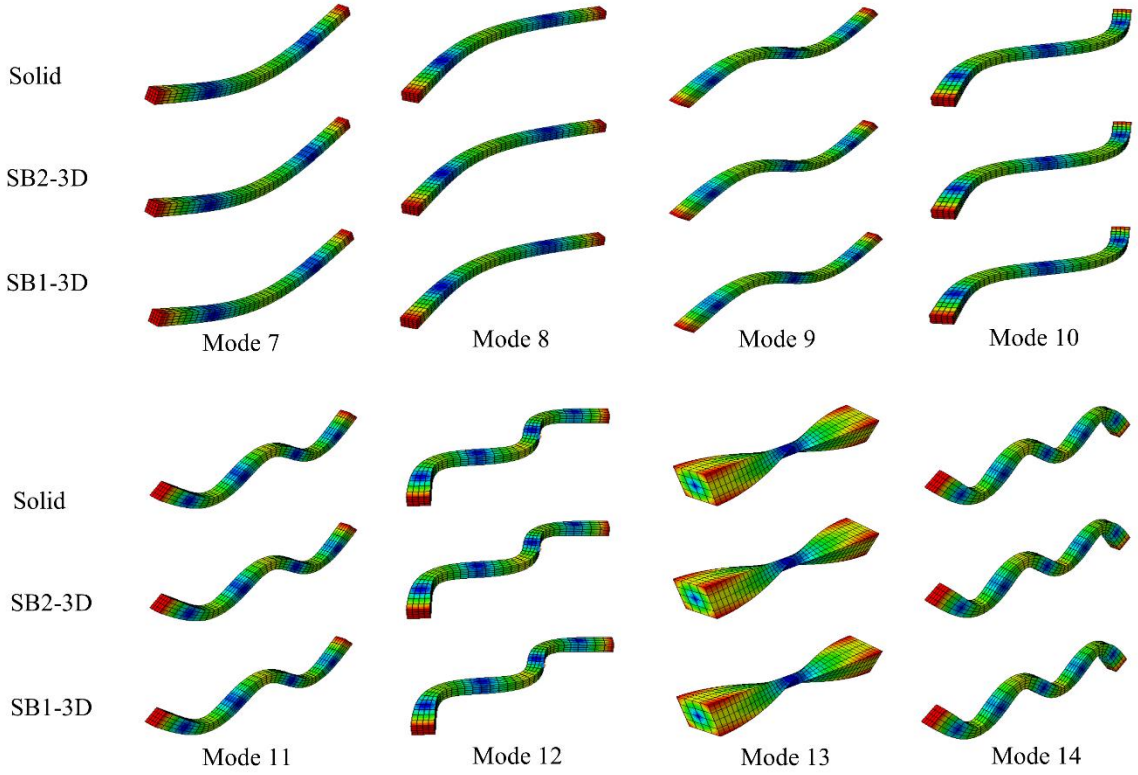

Fig. 3.22. Straight beam in free-free vibration – First eight mode shapes for the reference solid, SB2-3D, and SB1-3D models in the thin case.

The first eight mode shapes for the reference solid, SB2-3D, and SB1-3D models in the thick beam case, are shown in Fig. 3.23. Modes 7, 8, 10, 11 and 14 are bending modes, modes 9 and 13 are torsion modes, and mode 12 is a membrane mode. All the models give very similar results for these modes.

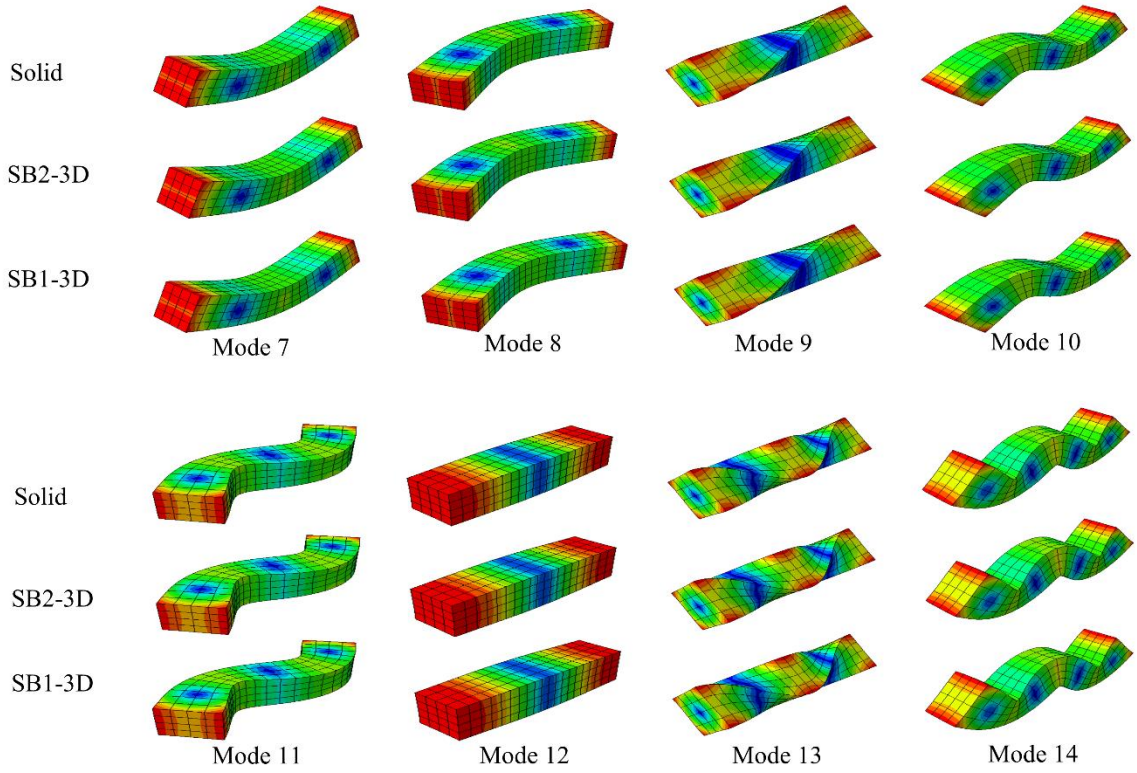

Fig. 3.23. Straight beam in free-free vibration – First eight mode shapes for the reference solid, SB2-3D, and SB1-3D models in the thick case.

The MAC values calculated between the SB2-3D model and the reference solid model for both the thin and thick straight beams, are reported in Fig. 3.24. The MAC values are always greater than 0.9, it indicates strongly correlated modes. Very similar results have been observed for the MAC values calculated between SB1-3D and reference solid models. For both the thin and thick cases, a perfect consistency is observed between the SB1-3D, SB2-3D models and the reference solid model.

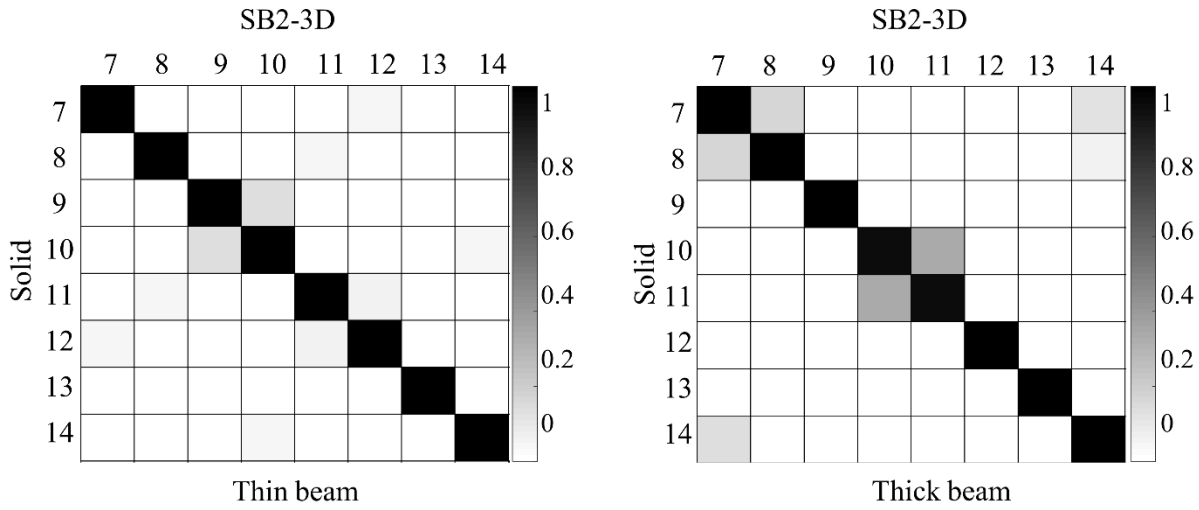

Fig. 3.24. Straight beam in free-free vibration – MAC matrix between the SB2-3D model and the reference models for the thin and thick beams.

3.5.1.4 Natural frequencies

The first eight natural frequencies obtained with the reference solid model, SB2-3D model, SB1-3D model, thin (B33 element in Abaqus) and thick (B31 element in Abaqus) beam models for thin and thick straight beams are presented in Fig. 3.25 and Fig. 3.26 respectively. The errors on natural frequencies are reported in Table 3.7. For the thin case, all the models show results similar to the reference solid ones except the thin beam model for modes 11, 12 and 14. For the thick case, the thin beam model gives incorrect results compared with the reference solid model. The SB1-3D model shows correct results but with errors about 2% for modes 10 and 11 (see Table 3.7), and error about 3% for mode 14, because the transverse shear stiffness is not precisely calculated. The thick beam model also provides a correct result but with errors of 1% for modes 10 and 11, and error about 2% for mode 14. The SB2-3D model gives excellent results with errors less than 0.5% compared to the reference solid one.

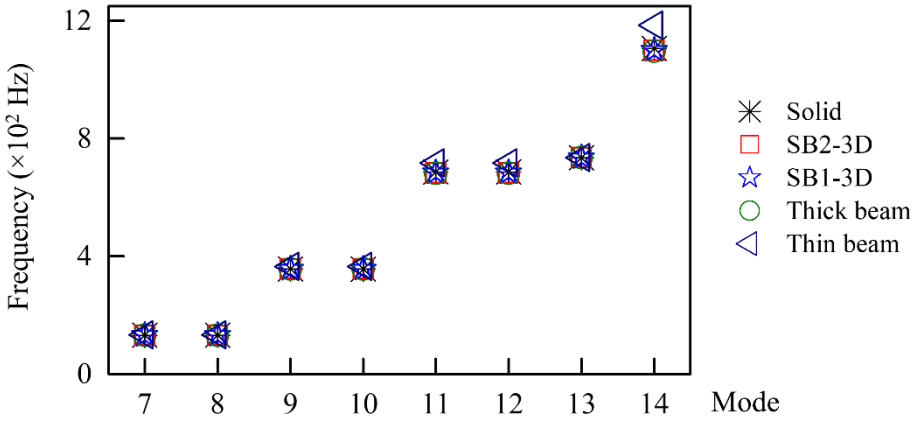

Fig. 3.25. Straight beam in free-free vibration – Natural frequencies for the reference solid model, SB2-3D model, SB1-3D model, thin and thick beam models in the thin case.

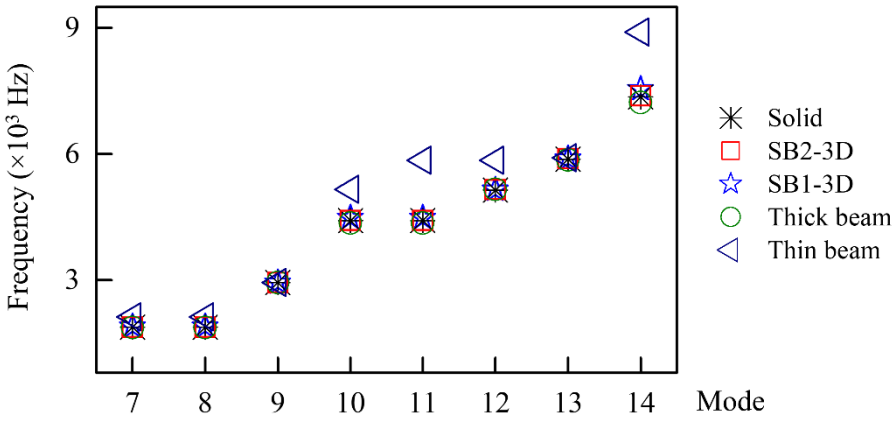

Fig. 3.26. Straight beam in free-free vibration – Natural frequencies for the reference solid model, SB2-3D model, SB1-3D model, thin and thick beam models in the thick case.

Table 3.7. Straight beam in free-free vibration – Errors (%) on natural frequency parameters with different models for the thin and thick cases.

l/*h* ratio	Model	Mode							
		7	8	9	10	11	12	13	14
20	SB2-3D	0.0	0.0	0.0	0.0	0.0	0.0	0.0	0.0
	SB1-3D	0.1	0.1	0.2	0.2	0.4	0.4	0.0	0.6
	Thick beam	0.1	0.1	0.1	0.1	0.2	0.2	0.0	0.3
	Thin beam	0.9	0.9	2.5	2.5	4.8	4.8	0.0	7.8
5	SB2-3D	0.0	0.0	0.1	0.2	0.2	0.1	0.3	0.3
	SB1-3D	0.6	0.6	0.1	1.7	1.7	0.1	0.3	2.6
	Thick beam	0.7	0.7	0.1	1.2	1.2	0.2	0.3	1.8
	Thin beam	12.8	12.8	0.1	16.9	32.5	13.7	0.5	21.0

3.5.2 Curved beam with square cross-section

3.5.2.1 Presentation of the example

The second example with the same geometries as described in Fig. 3.15 are here used in the context of free-free vibration analysis, with the density equal to 7.89×10^{-9} t/mm^3. The ratio *r*/*h* equals 10 or 10/3, representing the thin and thick cases respectively.

3.5.2.2 Convergence study

The thin and thick structures are discretized with the twenty-node hexahedral element C3D20 in Abaqus. For the two curved beams, a convergence study is made for the free-free vibration analysis of the first eight natural frequencies. For the reference solid, SB2-3D and SB1-3D models, the 4×4×50 mesh meets the convergence requirement for the thin and thick beams respectively. A mesh containing fifty B31 or B33 finite elements, which meets the convergence criterion, is considered for the thin and thick cases.

3.5.2.3 Mode shapes

For the reference solid, SB2-3D and SB1-3D models in the thin curved beam case, the first eight mode shapes are shown in Fig. 3.27. They range from simple bending or torsional modes to more complex combined bending and torsional modes. The SB2-3D model and SB1-3D model show similar mode shapes compared with the reference model.

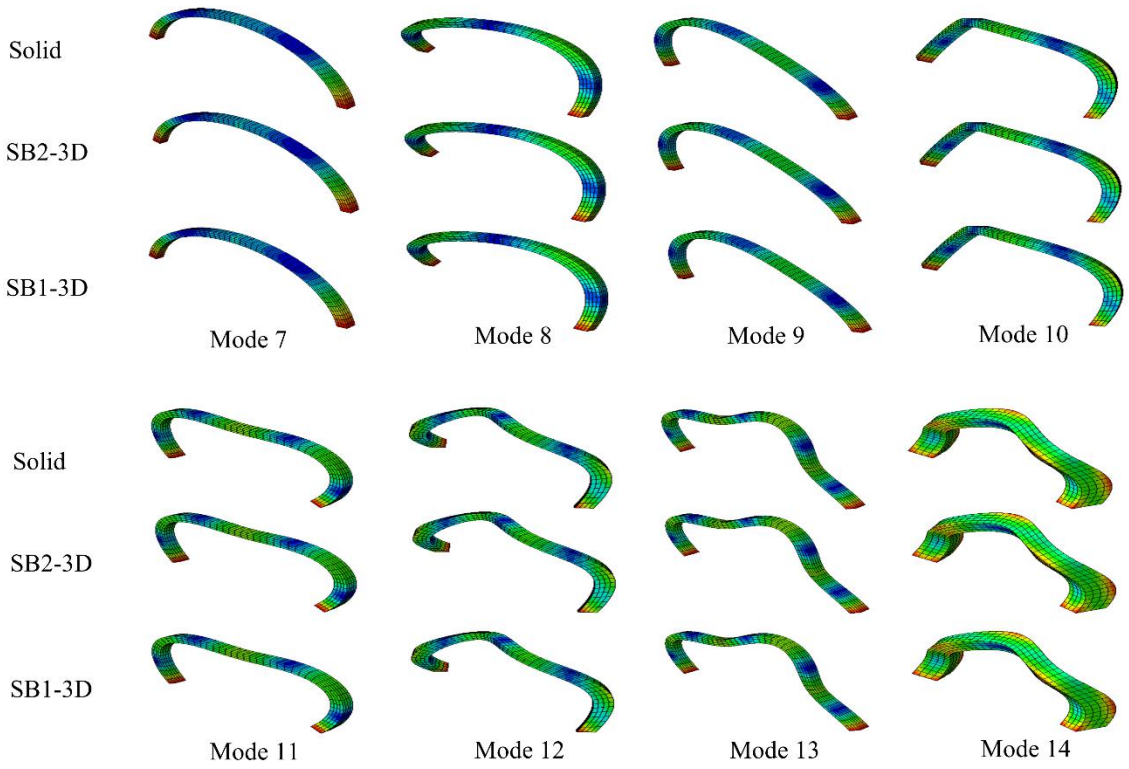

Fig. 3.27. Curved beam in free-free vibration – First eight mode shapes for the reference solid, SB2-3D and SB1-3D models in the thin case.

The first eight mode shapes for the reference solid, SB2-3D, and SB1-3D models in the thick curved beam case, are shown in Fig. 3.28. They range from simple bending or torsional modes to more complex combined bending and torsional modes. All the models presented here lead to similar mode shapes.

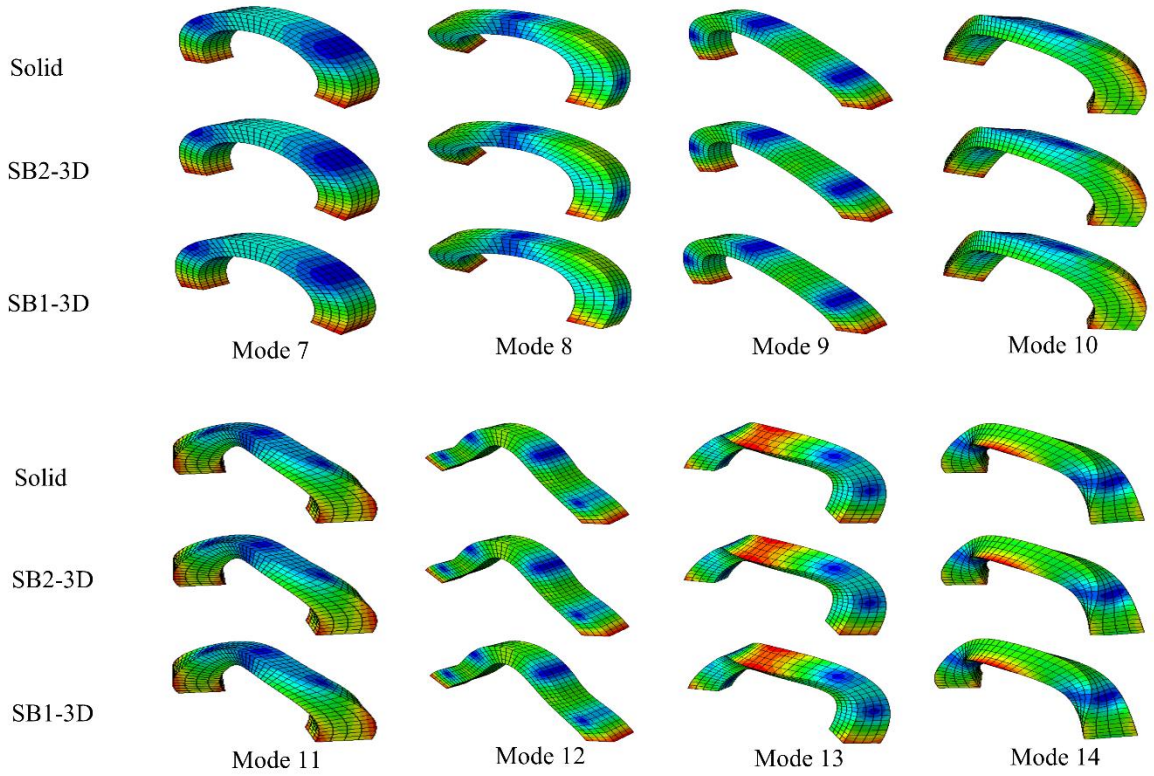

Fig. 3.28. Curved beam in free-free vibration – First eight mode shapes for the reference solid, SB2-3D, and SB1-3D models in the thick case.

The MAC values calculated between the SB2-3D model and the reference solid model for both the thin and thick curved beams, are reported in Fig. 3.29. The MAC values are always greater than 0.9, it indicates strongly correlated modes. Very similar results have been observed for the MAC values calculated between the SB1-3D model and reference solid models. For both the thin and thick cases, a perfect consistency is observed between the solid-beam models and the reference solid model.

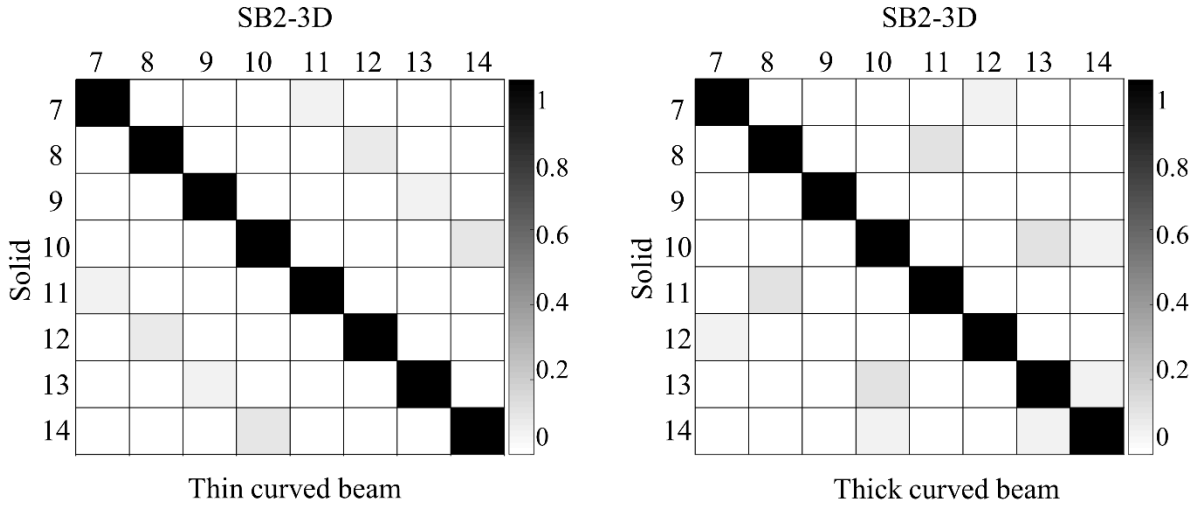

Fig. 3.29. Curved beam in free-free vibration – MAC matrix between the SB2-3D solid-beam and the reference models for the thin and thick beams.

3.5.2.4 Natural frequencies

The first eight natural frequencies for thin and thick curved beam structures are presented in Fig. 3.30 and Fig. 3.31 respectively. The reference solid model, SB2-3D model, SB1-3D model, thin (B33 element in Abaqus) and thick (B31 element in Abaqus) beam models are considered. The errors on natural frequencies are reported in Table 3.8. Results similar to the straight beam example are obtained. For the thin case, all the models show good results except the thin beam model giving slight errors about 2% for modes 10, 11, 12, 13 and 14. For the thick case, the thin beam model gives incorrect results with errors up to 12%. The SB1-3D model shows correct results but with errors more than 2% for modes 10 and 14, and errors about 5% for modes 8 and 11 compared with the reference solid model. The thick beam model also provides the correct result but with errors about 2% for modes 9, 12 and 14. Again, the SB2-3D model gives almost the same results as the reference solid one with errors less than 0.6%.

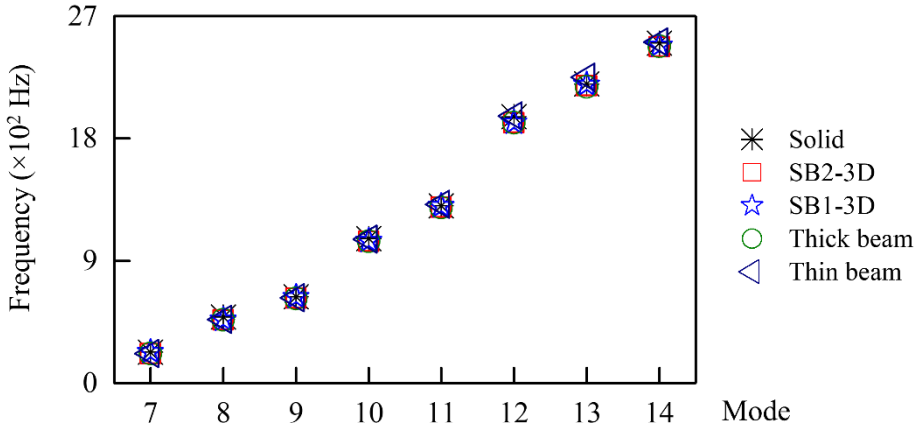

Fig. 3.30. Curved beam in free-free vibration – Natural frequencies for the reference solid model, SB2-3D model, SB1-3D model, thin and thick beam models in the thin case.

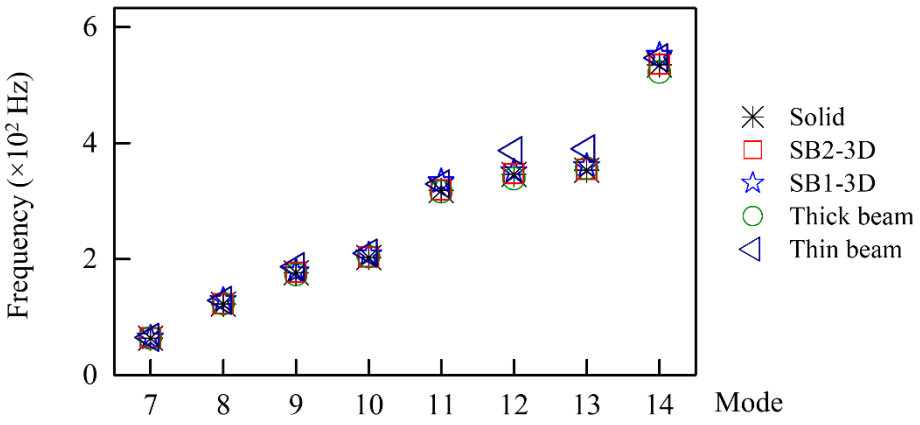

Fig. 3.31. Curved beam in free-free vibration – Natural frequencies for the reference solid model, SB2-3D model, SB1-3D model, thin and thick beam models in the thick case.

Table 3.8. Curved beam in free-free vibration – Errors (%) on natural frequency parameters of different models for the thin and thick cases.

r/*h* ratio	Model	Mode							
		7	8	9	10	11	12	13	14
10	SB2-3D	0.4	0.3	0.2	0.2	0.5	0.1	0.3	0.3
	SB1-3D	0.8	0.3	0.6	0.3	0.8	0.3	0.7	0.4
	Thick beam	0.1	0.0	0.3	0.1	0.3	0.1	0.4	0.0
	Thin beam	0.2	0.8	0.7	1.6	1.6	2.6	2.9	1.3
10/3	SB2-3D	0.6	0.2	0.4	0.2	0.2	0.4	0.3	0.2
	SB1-3D	0.8	5.4	1.0	2.4	4.9	1.4	1.8	3.2
	Thick beam	0.9	0.3	1.9	0.6	0.7	2.1	0.8	2.2
	Thin beam	1.7	5.2	5.9	3.6	3.5	11.9	10.3	2.3

3.5.3 Model size

It's interesting to compare the SB1-3D and SB2-3D models with classical beam elements in terms of model size. Fig. 3.32 presents the comparison of the number of degrees of freedom for the free-free vibration analysis of the curved beam. For the solid-beam models, the results are reported with a 4×4×50 mesh which meets the convergence condition. The beam model with the same refinement level along the length of the structure is also considered, to compare the solid-beam approaches and the beam one. Results confirm that the beam or solid-beam approach gives a significant gain compared with the solid approach. In terms of model size and consequently of computational time, the solid-beam models have a great reduction compared with the reference solid model. It can also be observed that the SB2-3D model requires only a little more degrees of freedom than the SB1-3D model.

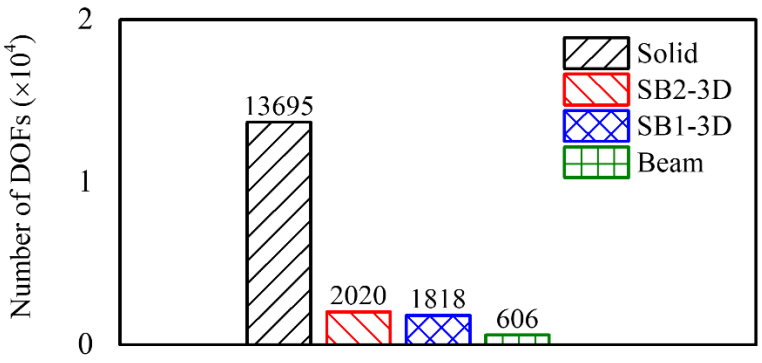

Fig. 3.32. Comparison of the number of degrees of freedom between solid, SB2-3D, SB1-3D and beam models.

3.6 Conclusion

A new solid-beam approach dedicated to thin to thick beam structures under bending, membrane and torsion effects has been presented. Beam displacement fields are directly applied on a solid finite element model which contains several elements throughout the cross-section. Three theories for a beam in plane and two theories for a beam in space, based on kinematic assumptions are considered. For a beam in plane, the classical first-order Timoshenko theory, the modified first-order beam theory and a higher-order beam theory lead to the FOSB, the MFOSB and the HOSB models respectively. For a beam in space, two proposed displacement fields lead to the SB1-3D and SB2-3D models respectively. The methodology relies on the slave and master nodes technique. Kinematic relations are imposed at slave nodes throughout the cross-sections to meet the beam displacement fields. From a numerical point of view, linear equations are applied on the assembled finite element model. All slave nodes are eliminated, resulting in a reduction of the model size. Two static examples have been presented: a straight beam and a curved beam with a square cross-section under distributed loading. Displacements and von Mises stresses have been observed for thin and thick cases. The FOSB model suffers from the Poisson thickness locking phenomenon, leading to wrong results. The HOSB model gives excellent results in both the thin and thick cases, compared with the reference solid approach. The MFOSB model is satisfactory for thin cases and leads to moderate errors for thick beams. These results show that the higher-order beam theory leads to a significant gain compared with the first-order beam theory for thick beams. This new solid-beam approach is efficient from the model size point of view. The MFOSB and HOSB models have considerable model size reduction compared with the reference solid model. Two free-free vibration examples with the same structures as the static examples have also been presented to assess the SB1-3D and SB2-3D models. Mode shapes and natural frequencies have been observed for thin and thick cases. For the natural frequency, the SB2-3D model gives excellent results in both the thin and thick cases, compared with the reference solid approach. The SB1-3D model also gives satisfactory results for thin cases and leads to slight errors for thick beams when higher-order modes are concerned. For the modal shapes, all the models give similar results. The SB1-3D and SB2-3D models also have considerable model size reduction compared with the reference solid model.

Many perspectives of development and applications of this solid-beam approach are possible. The extension to spatial beam with different types of cross-sections, leading to the treatment of more complex examples, is currently in progress. In particular warping namely due to torsion is a complex mechanical phenomenon as highlighted by numerous research works. From this point of view, we are quite confident in the ability of our approach to take into account all possible and complex coupling effects highlighted in literature. Besides the solid elements considered in this chapter, other solid finite elements with good performance could be exploited. This solid-beam approach can be extended to multilayered composite beam structures. An extension of the methodology is possible in the context of an adaptive approach in which different theories may be required depending on the area concerned.

Indeed, several beam, shell, as well as the 3D theory of elasticity, can be taken into account in the same finite element model. Finally, the application to natural and industrial structures is a quite promising perspective.

Chapter 4

Adaptive modeling methodology

In the context of static and vibration linear analysis, an original adaptive modeling methodology is proposed to obtain an optimal finite element model from the theory point of view. For each solid finite element of the mesh, an appropriate choice between the beam theory, the plate or shell theory, and the solid theory is made.

4.1 Introduction

For finite element modeling of academic or industrial structures, rules acquired from experience are often used to choose a type of element and a strategy of mesh refinement. Without specific strategy, the verification of the mesh convergence can lead to a very fine mesh over the whole structure and so to a high computational cost. During past decades, numerous studies investigated the adaptive meshing issue to determine an optimal mesh [104, 105, 106]. Some error estimations [107, 108] are proposed to evaluate an approximation of the exact error in order to optimize the mesh discretization. From an initial coarse mesh, this iterative technique aims an optimal local size of the mesh.

The type of element is associated with the theory to be chosen. This choice can be the beam theory, the plate or shell theory or the solid theory. For thin and thick structures, beam theory and plate or shell theory have been developed to avoid a 3D mesh associated with the solid theory. In this case, the normal to cross-section of a beam or the thickness direction of a plate or shell must be identified when the corresponding theory is chosen. For a complex structure, the automatic identification of these geometrical characteristics of beams or plates from the 3D geometry is difficult. About this issue, techniques have been developed to lead to offset curves [109] and surfaces [110, 111]. Moreover, for a given structure to be modeled, made of thin and 3D parts of geometry, the connection between different types of finite elements is often a challenge. Several modeling techniques [61, 114, 115, 122], leading to specific kinematic relations applied at the interfaces between mesh areas which contain different types of elements, have been proposed. A mesh composed with only solid elements can be chosen to avoid this difficulty, but the 3D elasticity theory is not always relevant.

In order to improve the management of these different aspects, a methodology of adaptive modeling is here introduced in the context of structures modeled by finite elements for static and vibration linear analysis. This methodology is original from the theory choice point of view. To the author's knowledge,

until now finite element modeling dealing with a local and optimal choice of theory has not been investigated in the literature. The methodology proposed is based on a 3D geometry discretized with solid elements, so the initial CAD geometry is kept. This unique type of element avoids the difficulties of connecting different types of finite elements mentioned above. As the methodology is adaptive, several iterations are needed and a local choice of theory is determined at each iteration. Beam or shell displacement fields are directly applied on the solid finite element model. It leads to a possible significant reduction of the number of degrees of freedom when the chosen theories are the beam theory and the plate or shell theory. Concerning mesh strategy during the iterations of the methodology, a basic voxel technique [116, 117] is considered. The first mesh is coarse and the mesh is refined over the whole structure at each iteration without determining an optimal mesh. As the mesh is made up only of hexahedra and the choice of theory can be the beam theory or the shell theory, a first approach is also presented to identify a normal to cross-section of a beam and a thickness direction of a plate or shell when the corresponding theory is chosen.

The outline of this chapter is as follows. In Section 4.2, the general principles of the methodology of adaptive modeling are presented. The criterion for the choice of theory and the convergence criterion of the methodology are respectively introduced in Sections 4.3 and 4.4. Section 4.5 is dedicated to a first proposition to identify the normal to cross-section for a beam structure and the thickness direction for a plate or shell structure. In Section 4.6, the implementation of the methodology is detailed. Section 4.7 gives a specific treatment for vibration analysis. Static examples are presented in Section 4.8, then vibration examples in Section 4.9. Finally, some conclusions and perspectives are drawn in Section 4.10.

4.2 General principles of the proposed methodology

General principles of the adaptive modeling methodology proposed are presented here. The different steps of the procedure are described by the flowchart in Fig. 4.1. An initial finite element analysis of a solid model with a coarse mesh is needed, then the iterative process highlights the adaptive aspect of the methodology. An iteration starts with the optimal choice of theory which exploits a criterion based on the local principal stresses obtained from the previous finite element analysis. Next, a mesh refinement is done according to a basic rule. Afterwards, at nodes of this new solid mesh, displacement fields described in chapter 2 and chapter 3 are applied corresponding to the chosen theory. The new finite element model possibly contains a mix of different theories. For beam theory, a solid-beam approach is used. For plate or shell theory, a solid-shell approach is applied. For solid theory, the original solid element is kept and no specific treatment is necessary. For the adaptive modeling obtained at a given iteration, the analysis of the finite element model is then performed. Finally, a convergence indicator based on strain energy is applied on two successive iterations. The iterative process stops when the convergence is achieved, the model can then be considered as optimal from theory point of view. For a

given structure to be modeled, Fig. 4.2 shows an example of local choice with relevant theories, leading to a mix of solid-beam, solid-shell and solid approaches.

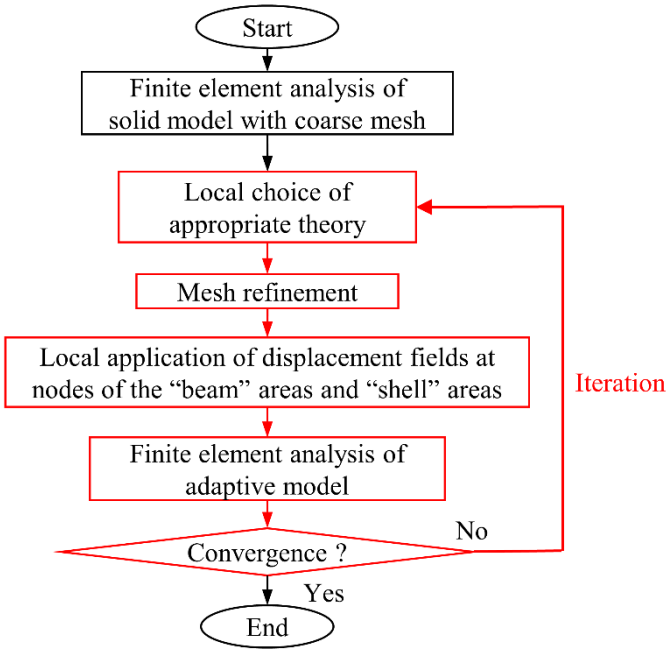

Fig. 4.1. Flowchart of the adaptive modeling process.

After this general description of the adaptive modeling methodology, the main characteristics are highlighted below.

- For any type of structure, the solid geometry is always exploited, regardless of that one or two dimensions are small compared to the others. A mid-axis or mid-surface geometry is never required.
- Only solid finite elements with good performance are used. A twenty-node and an eight-node hexahedral elements from Abaqus have been exploited. Of course, another solid element formulation could also be considered.
- The theory choice criterion is based on the principal stresses in each solid element. Strain energy is also considered to calculate the criterion.
- In the solid-beam and solid-shell areas, beam and shell displacements fields are applied respectively. The criterion is calculated in each element but the displacement fields are applied at nodes. For this purpose, kinematic relations between degrees of freedom are applied at nodes.
- At the interface between two different theories, a conservative approach is applied. For example, at the interface between beam and shell areas, shell theory is applied.
- The approach using solid elements combined with solid-beam, solid-shell or solid approaches allows to avoid all possible connection difficulties between the different areas of the structure.

- The mesh strategy is close to a basic voxel technique, that is well suited to the application of displacement fields at nodes of the solid mesh.
- The adaptive modeling methodology proposed leads to a reduction of the model size compared to a reference solid model when beam and shell theories are chosen in some areas of the structure.

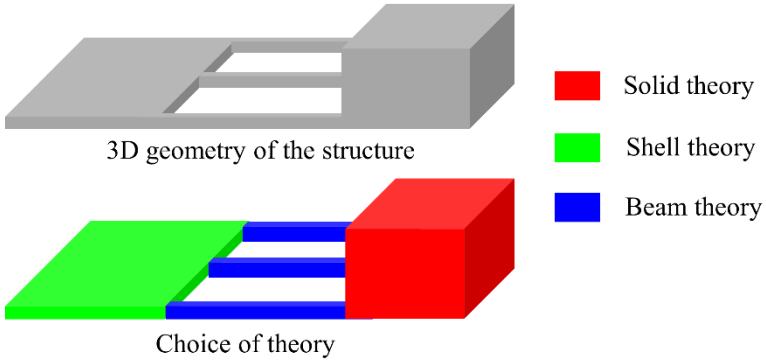

Fig. 4.2. Example of an optimal choice of theory for a given structure.

4.3 Theory choice criterion

The methodology of adaptive modeling needs a criterion to select the most relevant theory in the different areas of the structure. Some criteria from the literature dealing with adaptive mesh issue are available, such as a shape quality criterion [106] or an energy criterion [107, 108]. But these criteria are not well adapted to choose an appropriate theory. Therefore, an original criterion for the choice of theory, based on the principal stresses obtained on each solid element, is introduced to define the relevant modeling of the different areas of the structure by solid-beam, solid-shell or solid approaches. Strain energy is also used as a weighting coefficient to lead to a well-chosen theory choice criterion. First, the calculation of the principal stresses is recalled. Then, a criterion for choosing the adapted theory is presented.

4.3.1 Principal stresses

From the Cauchy stress tensor formulation [118, 119], the relations between the components of stress tensor and the principal stresses are expressed as:

$$\begin{cases} (\sigma_{xx} - \sigma_i) l_i + \tau_{xy} m_i + \tau_{xz} n_i = 0 \\ \tau_{xy} l_i + (\sigma_{yy} - \sigma_i) m_i + \tau_{yz} n_i = 0 \\ \tau_{xz} l_i + \tau_{yz} m_i + (\sigma_{zz} - \sigma_i) n_i = 0 \end{cases} \quad (4.1)$$

where σ_i are the principal stresses with i=1,2,3 and l_i, m_i and n_i are the components along each axis of the corresponding principal directions.

Eq. (4.1) is a homogeneous system of linear equations, the condition for non-zero solution is that the determinant of the resulting matrix is equal to zero:

$$\begin{vmatrix} \sigma_{xx}-\sigma_i & \tau_{xy} & \tau_{xz} \\ \tau_{xy} & \sigma_{yy}-\sigma_i & \tau_{yz} \\ \tau_{xz} & \tau_{yz} & \sigma_{zz}-\sigma_i \end{vmatrix} = 0 \tag{4.2}$$

For 3D stress states, principal stresses equal the roots of the general stress-cubic equation:

$$\sigma^3 - I_1\sigma^2 + I_2\sigma - I_3 = 0 \tag{4.3}$$

where I_1, I_2, and I_3 are known as the stress invariants and are given by:

$$\begin{cases} I_1 = \sigma_{xx} + \sigma_{yy} + \sigma_{zz} \\ I_2 = \sigma_{xx}\sigma_{yy} + \sigma_{yy}\sigma_{zz} + \sigma_{xx}\sigma_{zz} - \tau_{xy}^2 - \tau_{yz}^2 - \tau_{zx}^2 \\ I_3 = \sigma_{xx}\sigma_{yy}\sigma_{zz} + 2\tau_{xy}\tau_{yz}\tau_{zx} - \sigma_{xx}\tau_{yz}^2 - \sigma_{yy}\tau_{xy}^2 - \sigma_{zz}\tau_{zx}^2 \end{cases} \tag{4.4}$$

Therefore, the stresses σ_1, σ_2,and σ_3 are expressed as:

$$\begin{cases} \sigma_1 = \frac{I_1}{3} + 2\sqrt{-\frac{p}{3}}\cos\frac{\theta}{3} \\ \sigma_2 = \frac{I_1}{3} - \sqrt{-\frac{p}{3}}\left(\cos\frac{\theta}{3} - \sqrt{3}\sin\frac{\theta}{3}\right) \\ \sigma_3 = \frac{I_1}{3} - \sqrt{-\frac{p}{3}}\left(\cos\frac{\theta}{3} + \sqrt{3}\sin\frac{\theta}{3}\right) \end{cases} \tag{4.5}$$

with

$$\begin{aligned} \theta &= \arccos\left[-\frac{q}{2}\left(-\frac{p^3}{27}\right)^{-\frac{1}{2}}\right] \\ p &= \frac{3I_2 - I_1^2}{3} \\ q &= \frac{9I_1I_2 - 2I_1^3 - 27I_3}{27} \end{aligned} \tag{4.6}$$

The biggest principal stress is σ_1 and the smallest is σ_3.

4.3.2 Criterion based on principal stresses

In order to choose relevant theory in different areas of the structure, a criterion based on principal stresses is presented here. The three principal stresses calculated at the center of each solid element are compared to define the appropriate solid-beam, solid-shell or solid approach for each of them. The criterion tends to choose the beam theory when only one principal stress is significant. The optimal choice tends to be the shell theory when two principal stresses are significant. Otherwise, the solid theory is chosen when the three principal stresses are of the same order of magnitude. These rules work well if the state of stress is dominated by normal stresses. However, if shear stresses are significant, the situation is more complex. For example, for a beam under pure torsion, one can observe two principal stresses with equal absolute values but opposite signs. When a case closed to this situation is detected, the rule presented above has to be modified. A stress ratio parameter ρ is used to define a critical gap between the three components and a weighting coefficient ω is calculated considering the strain energy. The value of parameter ρ depends on the studied structure and may be different depending on whether it is

a static or vibration analysis. For each example, some preliminary tests allow a relevant choice of this parameter value. Typically, the parameter ρ may be comprised between 20 and 100. The weighting coefficient ω is expressed in terms of strain energy to improve the criterion in different areas of the structure, in order to be less severe in areas where strain energy density is small. The expression of elastic strain energy density per unit volume is recalled:

$$\pi = \frac{1}{2}\sum_{i,j=1}^{3} \sigma_{ij}\varepsilon_{ij} \tag{4.7}$$

where σ_{ij} are the normal or shear stresses and ε_{ij} are the normal or shear strains.

The maximum elementary elastic strain energy density π_{max} is also considered. The weighting coefficient ω is defined by:

$$\omega = (\pi/\pi_{max})^n \tag{4.8}$$

where *n* is a parameter which must be determined for each example.

From the three principal stresses σ_1, σ_2 and σ_3, we define the σ_{max}, σ_{mid} and σ_{min} as the maximum, intermediate and minimum absolute values respectively. Finally, the criterion in order to select the relevant theory for each element is defined by the following rules:

1. If the condition $\sigma_{max} \geq \rho\omega\sigma_{mid}$ is met, the beam theory is selected, leading to a solid-beam approach.
2. If the conditions $\sigma_{max} < \rho\omega\sigma_{mid}$ and $\sigma_{max} \geq \rho\omega\sigma_{min}$ are met, the shell theory is selected, leading to a solid-shell approach. To verify this situation does not correspond to shear stress state, the ratio σ_1/σ_3 is calculated. If this ratio is close to -1, the shear stress is predominant and consequently beam theory is selected, leading to solid-beam approach.
3. If the condition $\sigma_{\text{max}} < \rho\omega\sigma_{\text{mid}}$ and $\sigma_{\text{max}} < \rho\omega\sigma_{\text{min}}$ are met, the solid theory is selected.

4.4 Convergence criterion of the methodology

As described by Fig. 4.1, the convergence of the adaptive modeling process is achieved when an optimal finite element model is obtained from the theory point of view. A convergence criterion is here introduced that exploits the internal strain energy $\mathbf{\Pi}_{int}$ of the system. In the context of the iterative process, the convergence criterion is applied between two successive iterations *i* and *i*+1. Therefore, the strain energy relative error E_r is defined by:

$$E_r = \frac{\left\|\mathbf{\Pi}_{int}^{i+1}\right\| - \left\|\mathbf{\Pi}_{int}^{i}\right\|}{\left\|\mathbf{\Pi}_{int}^{i+1}\right\|} \tag{4.9}$$

with the internal strain energy at the iteration *i* for a mesh composed with *n* elements:

$$\left\|\boldsymbol{\Pi}_{int}^{i}\right\| = \frac{1}{2}\sum_{e=1}^{n}\|\boldsymbol{\varepsilon}^{T}\boldsymbol{\sigma}\|_{e} \tag{4.10}$$

For static and vibration analysis, it is considered that convergence of the methodology is achieved if the error E_r is less than 0.1% between two successive iterations of the adaptive modeling. This criterion is used in the static and vibration examples respectively in Sections 4.8 and 4.9. During the iterations of adaptive modeling process, the stability of theory choice over the whole structure can be observed and it could be considered as another convergence criterion which has not been considered here. Indeed, the local areas of the structure composed of solid-beam, solid-shell, and solid approaches tend to be relatively stable after several iterations. The criterion proposed in Eq (4.9) is a global one. As a perspective, local criteria could also be developed to better take into account local effects.

4.5 Normal to cross-section or thickness direction identification of the structure

For the current classical finite element modeling process, the creation of mid-axis or mid-surface geometry is needed when respectively the beam theory or the shell theory is chosen. For the adaptive modeling methodology proposed, only the solid geometry is exploited. Therefore, the identification of the normal to cross-section or thickness direction is required respectively to apply the solid-beam or solid-shell approaches. A first technique based on the principal directions is here proposed to identify the normal to cross-section or the thickness direction of a structure. Identification of principal directions leads to some difficulties because these directions calculated by finite elements are approximate due to the fact that the stresses are associated with some errors. These difficulties have been highlighted in this research work but further investigations are necessary to improve the implementation of this technique. This issue is one of the perspectives of our methodology. In this research, normal to cross-section and thickness directions are directly imposed.

4.5.1 Calculation of principal directions

The components of principal directions, relative to the principal stresses σ_1, σ_2 and σ_3, are respectively l_i, m_i and n_i with i=1,2,3 and meet the relation:

$$l_i^2 + m_i^2 + n_i^2 = 1 \tag{4.11}$$

with

$$\begin{cases} l_i = \dfrac{A_i}{\sqrt{A_i^2 + B_i^2 + C_i^2}} \\ m_i = \dfrac{B_i}{\sqrt{A_i^2 + B_i^2 + C_i^2}} \\ n_i = \dfrac{C_i}{\sqrt{A_i^2 + B_i^2 + C_i^2}} \end{cases} \tag{4.12}$$

where

$$\begin{cases} A_i = \tau_{xy}\tau_{yz} - (\sigma_y - \sigma_i)\tau_{xz} \\ B_i = \tau_{xy}\tau_{xz} - (\sigma_x - \sigma_i)\tau_{yz} \\ C_i = (\sigma_x - \sigma_i)(\sigma_y - \sigma_i) - \tau_{xy}^2 \end{cases} \tag{4.13}$$

4.5.2 Normal to cross-section or thickness direction

For the solid-beam approach, the normal to cross-section is considered as the principal direction corresponding to the maximum principal stress. For the solid-shell approach, the thickness direction is considered as the principal direction corresponding to the minimum principal stress. As shown in Fig. 4.3, the normal to cross-section is defined by the principal direction (l_1, m_1, n_1) for the solid-beam approach and the thickness direction is defined by the principal direction (l_3, m_3, n_3) for the solid-shell approach.

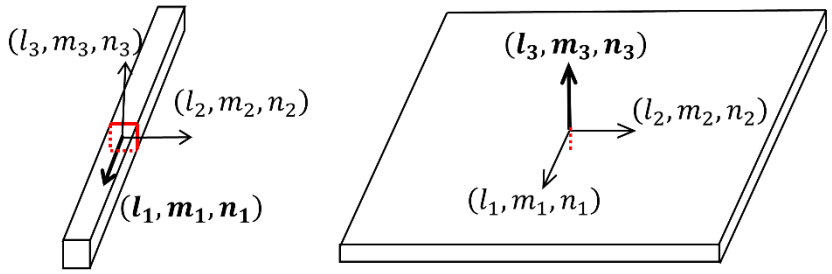

(a) beam (b) plate

Fig. 4.3. Description of the normal to cross-section of a beam (a) and the thickness direction of a plate (b).

This principle of identification is highlighted on a model of cantilever structure described in section 4.7.1 for case 2 of this example. An optimal model has been obtained from the theory point of view. As shown in Fig. 4.4, the arrows indicate the normal to cross-section for the solid-beam area in blue and the thickness direction for the solid-shell area in green. The solid area is described in red. The result of the identification is satisfactory for the bending structure. In solid-beam area, the arrows corresponding to the normal to cross-section are in the direction of the maximum principal stress. In solid-shell area, the arrows corresponding to the thickness direction are in the direction of the minimum principal stress.

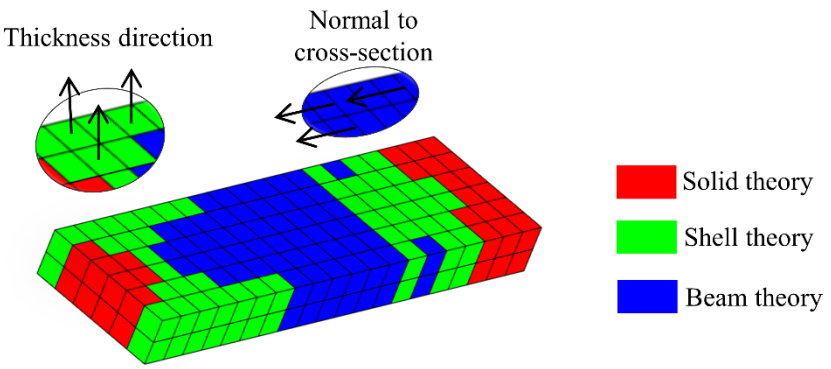

Fig. 4.4. Normal to cross-section of solid-beam approach and thickness direction of solid-shell approach for an optimal model of cantilever structure.

4.6 Implementation of the methodology

The iterations of the methodology described in Fig. 4.1 are composed of a choice of the theory made on each solid element, a mesh refinement and an application of displacement fields at concerned nodes. Some specific aspects of the methodology implementation are here introduced concerning the mesh refinement, the displacement field and rules at the interface between two different theory choices.

4.6.1 Mesh refinement

The meshing strategy for the methodology proposed is basic and is closed to a voxel meshing method [13, 14]. The discretization is defined by a regular three-dimensional mesh with a hexahedral element. The mesh is refined at each iteration to achieve the methodology convergence, with the mesh size divided by two in the three directions. Of course, the adaptive modeling proposed is compatible with adaptive mesh techniques, but it is not implemented here.

4.6.2 Displacement fields

After the mesh refinement at each iteration of the adaptive process, displacement fields are applied at concerned nodes of the solid element. These displacement fields are applied in beam and shell areas, but no treatment is made at nodes of the solid areas. For solid-shell and solid-beam approaches, the displacement fields are respectively described in chapters 2 and 3. Currently, the displacement field of the modified first-order solid-shell approach is chosen for the shell theory. The displacement field of the modified first-order solid-beam approach for 3D beam is chosen for the beam theory. The application of the corresponding equations is achieved by using the master and slave nodes technique. Consequently, solid-shell and solid-beam approaches allow a significant reduction of the problem size, compared to the solid approach.

4.6.3 Special treatment of interface

As it was recalled, a theory choice is made for each solid element and a corresponding displacement field is applied at nodes. At the interface between two types of theory, a conservative rule is used for the concerned nodes. As illustrated in Fig. 4.5, the solid theory is chosen rather than a shell and a beam theory; the shell theory is selected rather than a beam theory.

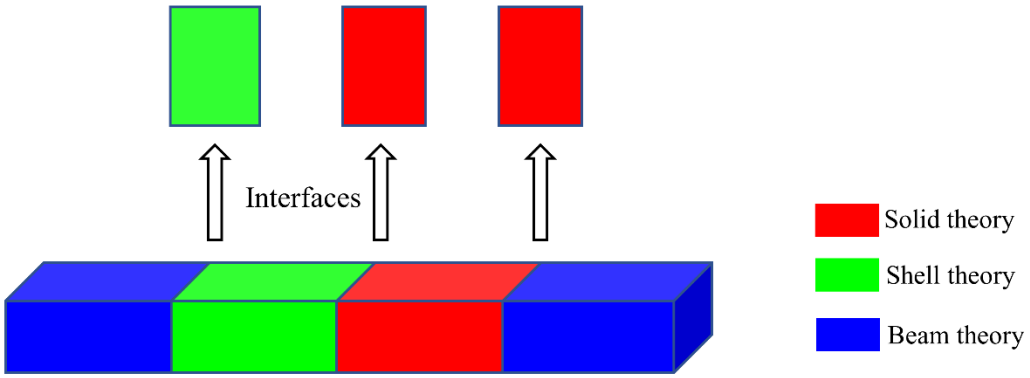

Fig. 4.5. Rules at the interface between two different types of theories.

4.7 Specific step for vibration analysis

The adaptive modeling methodology is proposed in the context of static and vibration linear analysis. A specific step is needed to manage different modes in the case of vibration analysis. Indeed, as mode shapes are different one from other, the choice of theory provides an optimal modeling for each mode. At each iteration of the methodology, a synthesis of these choices is so needed to lead to only one optimal model. The global flowchart of the methodology described in Fig. 4.1 is kept and a step of synthesis is added after the local choice of theory, as shown in Fig. 4.6. This synthesis is conservative, the solid theory is chosen rather than the shell and beam theory; the shell theory is selected rather than the beam theory. An example illustrated by Fig. 4.7 shows the result of synthesis at each iteration process for different modes.

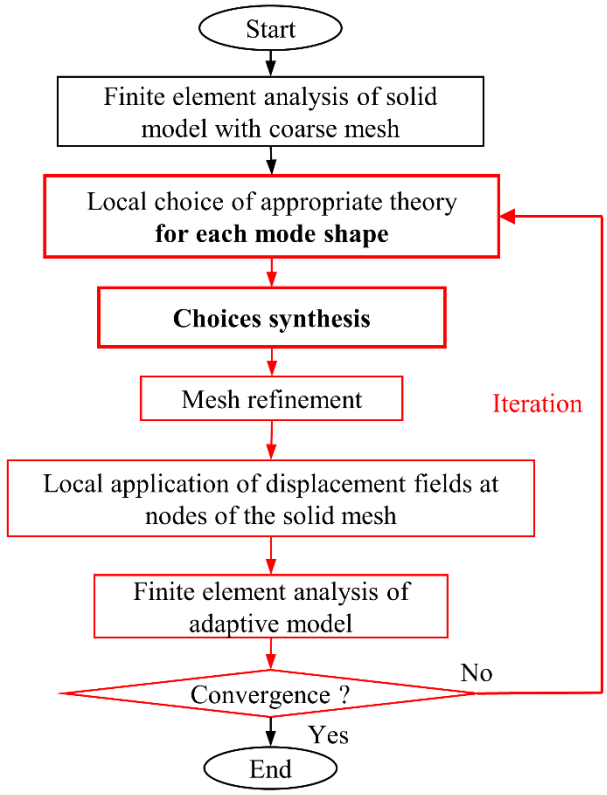

Fig. 4.6. Flowchart of adaptive modeling process for vibration analysis.

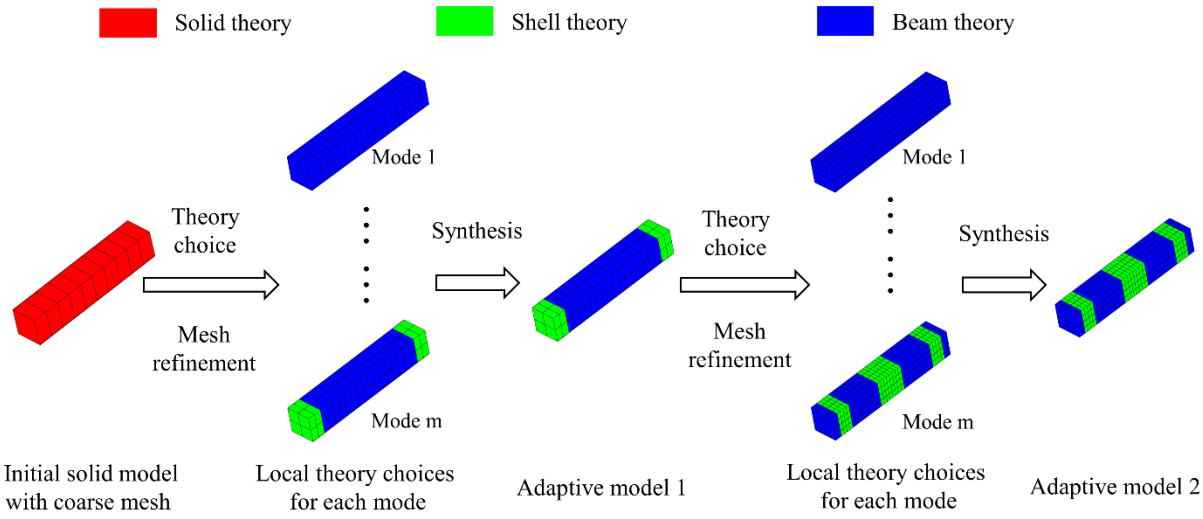

Fig. 4.7. Example of a synthesis concerning the local choice of theory for vibration analysis during the iterative process.

4.8 Static examples

The adaptive modeling methodology is applied here on cantilever structures and on “T” shape plates in the context of static analysis. First each static example is presented. The evolution of theory choice is presented for each iteration of the adaptive modeling process. At convergence the quality of the finite element results obtained with the optimal model is evaluated by comparison with a reference solid model.

The reduction of model size due to the application of solid-shell and solid-beam approaches is discussed. The compatibility of the adaptive modeling methodology with another efficient solid element is also proved.

4.8.1 Cantilever structures with three width/thickness ratios

4.8.1.1 Presentation of the example

Cantilever structures are presented in Fig. 4.8 with three different geometries, three width/thickness ratios are considered. The three structures are clamped at one end and submitted to a distributed loading f at the other end. The first case is a beam-like structure with a square section b_1/h=1. The second case is an intermediate structure with b_2/h=3. The third case is a square plate-like structure with b_3/h=10.

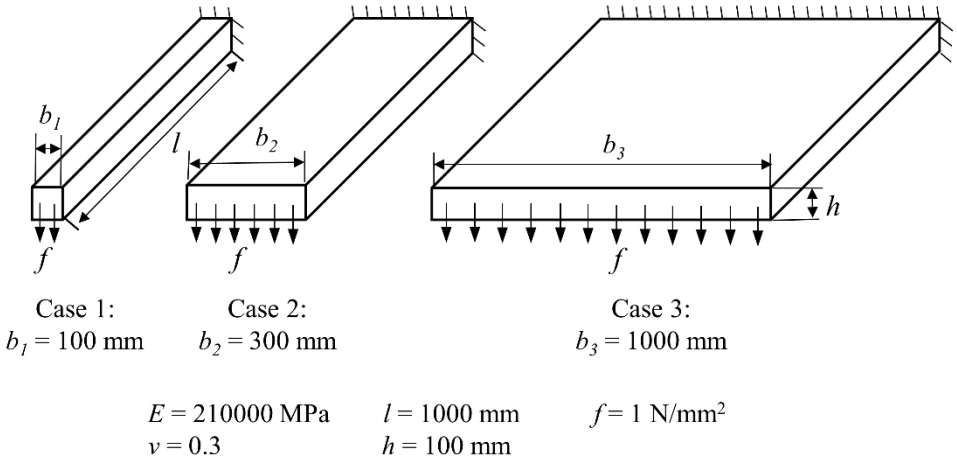

Fig. 4.8. Cantilever structures – Presentation of the example for three width/thickness ratios.

4.8.1.2 Adaptive theory choice

The theory choice is now observed at each iteration of the process for the three cantilever structures. The criterion based on principal stresses and weighted by strain energy provides a distribution of solid-beam, solid-shell and solid areas. The stress ratio parameter ρ described in Section 4.3.2 is equal to 100 for this example. This value is a compromise between small values that lead to larger solid-beam or solid-shell areas and high values that lead to larger solid areas. For the weighting coefficient, n equal to 0.5 has been used in Eq. (4.8). Fig. 4.9 shows the chosen theory in each solid element for the initial model and for two successive adaptive models. The blue, green and red colors correspond respectively to the solid-beam, solid-shell and solid approaches. The obtained results are discussed for the optimal model corresponding to the adaptive model 2. In case 1, a large area of solid-beam approach is obtained for the cantilever beam-like structure with a square section. Some solid-shell and solid approaches are chosen at ends of this structure due to local effects caused by loading and boundary conditions respectively. In case 2 which is intermediate, a mixed distribution of solid-beam, solid-shell and solid areas are observed. In case 3, the solid-shell area predominates except at ends of the square plate-like

structure where boundary conditions and loading are applied, leading to local effects justifying solid elements. A few solid-beam areas are also observed according to the theory choice criterion.

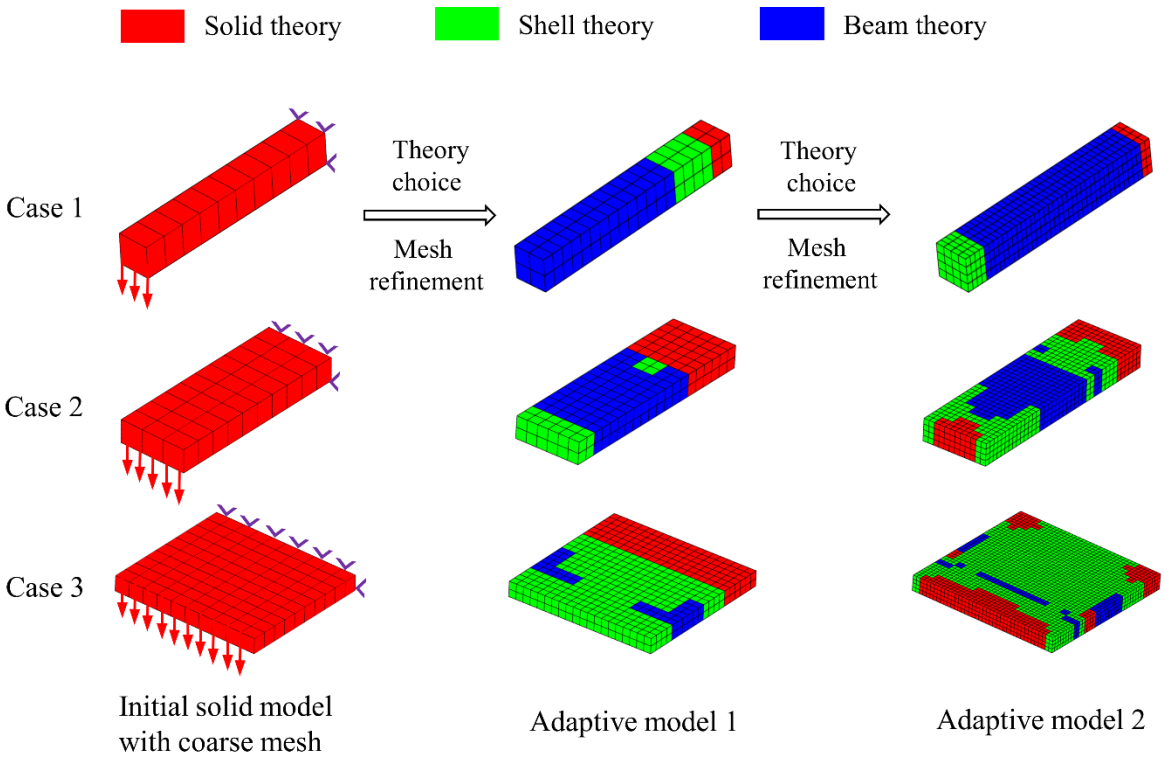

Fig. 4.9. Cantilever structures – Evolution of the theory choice during the iterative process in the three cases.

4.8.1.3 Convergence of the methodology

The three cantilever structures are discretized with the twenty-node hexahedral element C3D20 from Abaqus [120, 121]. An initial coarse and regular mesh is generated to start the adaptive modeling process and the mesh refinement strategy presented in Section 4.6.1 is then applied. The convergence of the methodology is assessed with the strain energy criterion described in Section 4.4. It is considered that convergence is achieved if the error E_r is less than 0.1% between two successive iterations of the adaptive modeling process. For the three cantilever structures, Fig. 4.10 shows the values of strain energy and the convergence criterion values for the first four models. These models are the initial solid model and three adaptive models. Model 3 is the second adaptive model and it corresponds to the optimal model which meets the convergence criterion for the three cases.

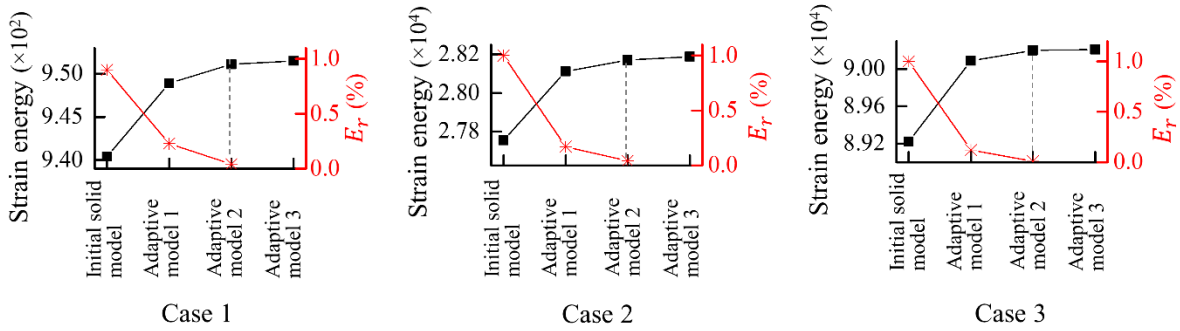

Fig. 4.10. Cantilever structures – Convergence of the methodology in the three cases.

4.8.1.4 Finite element results of the optimal model

The finite element results of the optimal model obtained with the adaptive modeling process is evaluated. The reference model is a solid model that meets the convergence requirements. First, a global comparison of the finite element results is made between the optimal model and reference solid model for the three cantilever structures. Fig. 4.11 shows the distributions of displacement and von Mises stress for the solid and optimal models in the three cases. For the two types of models, these results are quite similar, showing that the adaptive modeling approach seems to be very satisfactory.

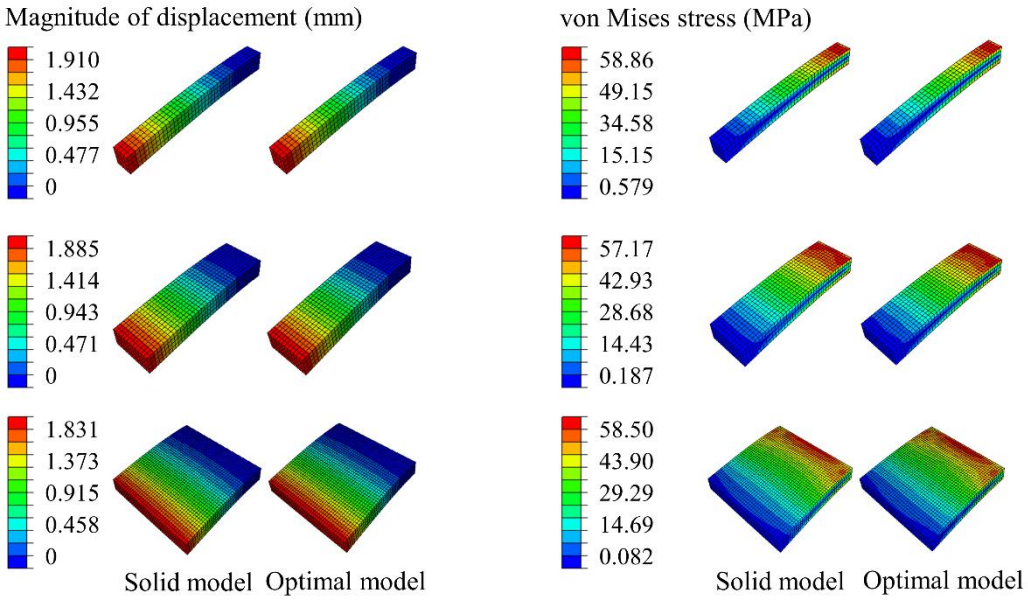

Fig. 4.11. Cantilever structures – Displacement and von Mises stress distributions for the reference solid and optimal models in cases 1, 2 and 3.

In order to quantify the difference on these finite element results, Table 4.1 shows the errors on the maximum displacement and von Mises stress by comparing the optimal and the reference solid models. The errors do not exceed 0.5% for the three cases. These insignificant errors between the optimal and reference solid models confirm the adaptive modelling process is fully satisfactory. It also confirms that new proposed solid-shell and solid-beam approaches work well.

Table 4.1 Cantilever structures – Errors on maximum displacement and von Mises stress between optimal and reference solid models in cases 1, 2 and 3.

Case	Maximum displacement (mm)			Maximum von Mises stress (MPa)		
	Solid model	Optimal model	Error (%)	Solid model	Optimal model	Error (%)
1	-1.904	-1.902	0.1	58.86	58.84	0.1
2	-1.880	-1.877	0.2	57.17	56.84	0.5
3	-1.826	-1.821	0.3	58.50	58.21	0.5

For further understanding the error distribution over the whole structure, the error on displacement at each node and the error on von Mises stress at the center of each element are studied. For the three cantilever structures, Fig. 4.12 shows the errors on displacement and von Mises stress by comparing the optimal model and the reference solid model over the whole structure. The errors on displacement are lower than 0.3%. The analysis of errors on von Mises stress is discussed from global and local aspects. From a global point of view, almost all the errors are smaller than 1%. Especially, the areas of boundary conditions highlight very low errors where the stresses are maximum. From a local point of view, some errors on von Mises stress are slightly higher than 1% in the loading areas (cases 1 and 2) or at free edges (case 3). But these areas are not significant due to small values of stresses, as can be seen in Figure 4.11. Again, for the displacement and von Mises stress, the comparison between the optimal and reference solid models indicates that the adaptive modelling process is entirely satisfactory.

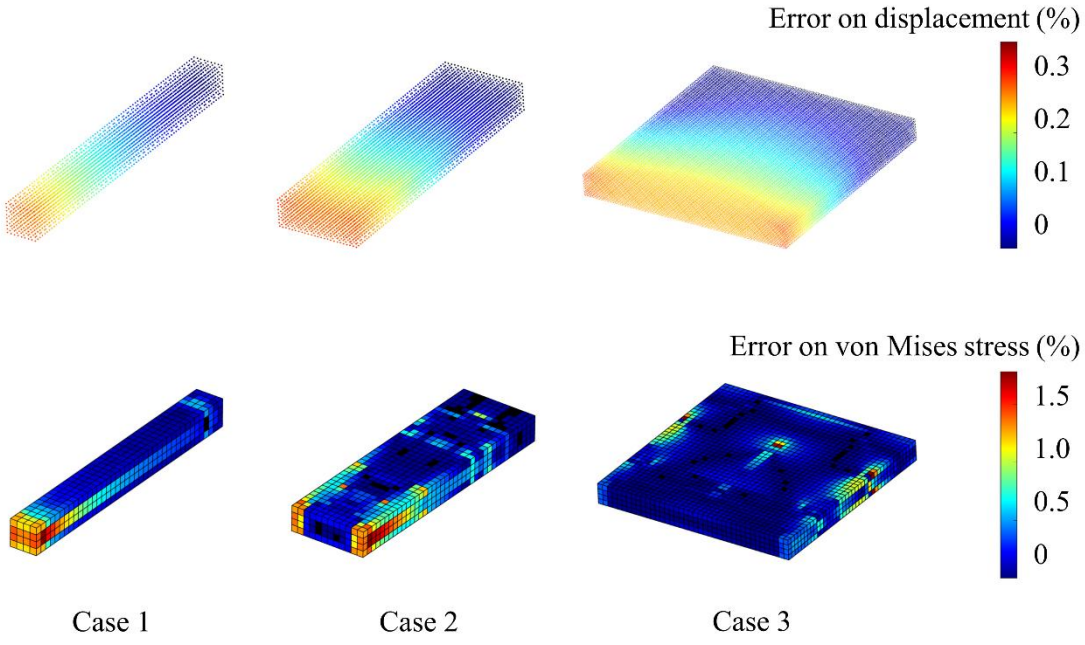

Fig. 4.12. Cantilever structures – Errors on displacement and von Mises stress between optimal and reference models over the whole structure in cases 1, 2 and 3.

4.8.1.5 Reduction of the model size

The optimal model based on solid-beam and solid-shell approaches induces a reduction of the model size compared with the solid model. Fig. 4.13 shows the evolution of the number of degrees of freedom (DOFs) during the adaptive modeling process for the three cases. The initial solid model with a coarse mesh and two adaptive models are considered. The reduction of the number of DOFs for the optimal model compared with the reference solid model is also observed. For the three cases, the second iteration corresponding to model 3 gives the most significant reduction. The gain is calculated as a ratio of the number of DOFs between the reference solid model and the optimal model with same meshes. In cases 1, 2 and 3, the gain is respectively equal to 5.0, 2.6 and 2.1 for the optimal model. The gain is maximal in case 1 because the solid-beam approach, which leads to the larger reduction of the model, is widely applied. Anyway, the gain is significant even when the solid-shell approach predominates, which happens in case 3.

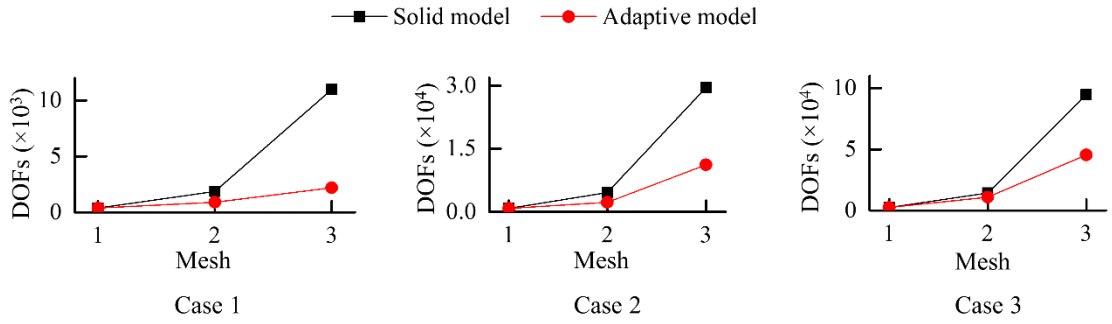

Fig. 4.13. Cantilever structures – Number of degrees of freedom for the adaptive models during the iterative process and for the reference solid models in cases 1, 2 and 3.

4.8.1.6 Adaptive modelling process with another solid element

To prove the adaptive modeling process is compatible with any efficient solid element, the eight-node hexahedral element C3D8I [19] from Abaqus is used here to model the cantilever structures. This solid element with incompatible modes was introduced in 1973 by Wilson et al. [122, 123]. The convergence study of the methodology is quite similar for the element C3D8I and the previous element C3D20. For the three cases, the convergence is achieved for the adaptive model 2. Fig. 4.14 shows the evolution of theory choice during the iterative process using the element C3D8I. From the initial solid model with a coarse mesh to two successive adaptive models, the theory choice criterion provides solid-beam, solid-shell and solid areas respectively illustrated in blue, green and red. The comparison between Figures 4.10 and 4.14 shows that globally in terms of optimal theory choice, the tendencies obtained with the element C3D8I are similar to those obtained with the element C3D20.

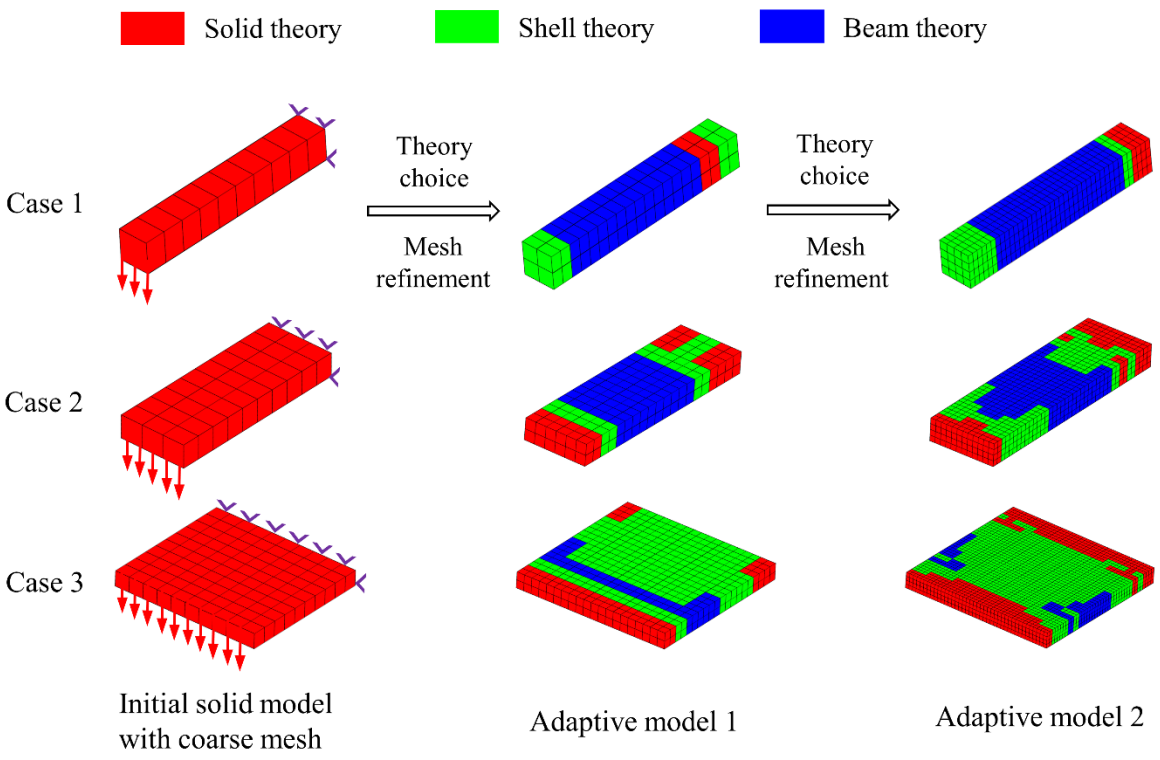

Fig. 4.14. Cantilever structures – Evolution of the theory choice during the iterative process with the element C3D8I.

The finite element results of the optimal model obtained with the adaptive modeling process are evaluated for the element C3D8I. Fig. 4.15 shows the displacement and von Mises stress distributions for the three cantilever structures. Globally, the distributions of the displacements and von Mises stresses obtained with the optimal model are quite similar to those obtained with the reference solid model.

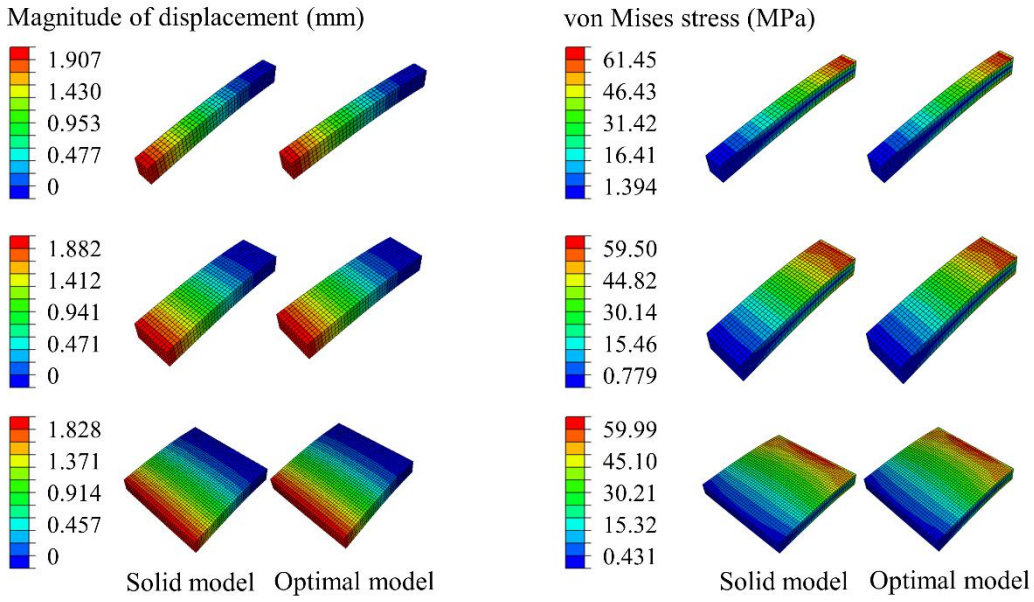

Fig. 4.15. Cantilever structures – Displacement and von Mises stress distributions for the reference solid and optimal models in cases 1, 2 and 3 with the element C3D8I.

Table 4.2 shows the errors on the maximum displacement and von Mises stress by comparing the optimal model and the reference solid model. For the three cases, the errors do not exceed 0.2%. These errors confirm that with the element C3D8I the adaptive modelling process is fully satisfactory as well. It also confirms that the solid-shell and solid-beam approaches work well with this element.

Table 4.2 Cantilever structures – Errors on maximum displacement and von Mises stress by comparing optimal models and reference models with the element C3D8I.

Case	Maximum displacement (mm)			Maximum von Mises stress (MPa)		
	Solid model	Optimal model	Error (%)	Solid model	Optimal model	Error (%)
1	-1.901	-1.900	0.1	61.45	61.39	0.1
2	-1.877	-1.876	0.1	59.50	59.42	0.1
3	-1.826	-1.823	0.2	59.99	59.90	0.2

As for the reduction of model size with the element C3D8I, the same trends can be observed that with the element C3D20. The reduction of the number of degrees of freedom is very significant for case 1 and significant for cases 2 and 3, thanks to solid-beam and the solid-shell approaches.

4.8.2 “T” shape plates

4.8.2.1 Presentation of the example

The second example, presented in Fig. 4.16, is a “T” shape plates assembly in the context of static analysis. One face of the vertical plate is submitted to a pressure p and two edges of the horizontal plate are clamped.

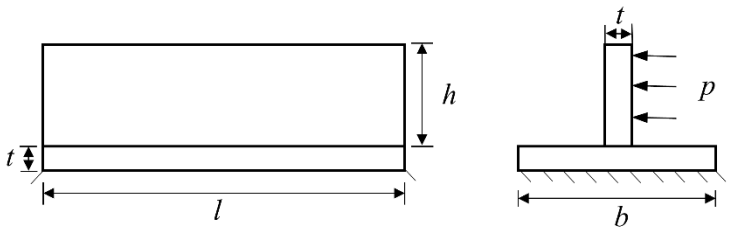

$E = 210000$ MPa
$\nu = 0.3$ $l = 2000$ mm $h = 500$ mm
$p = 0.5$ MPa $b = 1000$ mm $t = 50$ mm

Fig. 4.16. “T” shape plates – Presentation of the example.

4.8.2.2 Adaptive theory choice

The theory choice is presented here at each iteration for the adaptive modeling of “T” shape plates. The criterion based on principal stresses and weighted by strain energy determines solid-beam, solid-shell or solid approaches for each element. Again, the stress ratio parameter ρ is equal to 100 for this

example. For the weighting coefficient, n equal to 0.5 has been used in Eq. (4.8). Fig. 4.17 shows the selected approaches for the initial solid model and three successive adaptive models. The blue, green, and red colors indicate respectively the solid-beam, solid-shell and solid areas. For adaptive model 3, when the convergence of the methodology is achieved, the solid-shell approach is automatically chosen for most of the elements. The solid approach is chosen in the boundary conditions areas and at the junction between the two plates. The current version of theory choice criterion identifies a few solid-beam areas in this example. However, from a theoretical point of view, it seems difficult to justify the beam theory and identify the relevant cross-sections here. Thus, the solid-shell approach is chosen as a replacement.

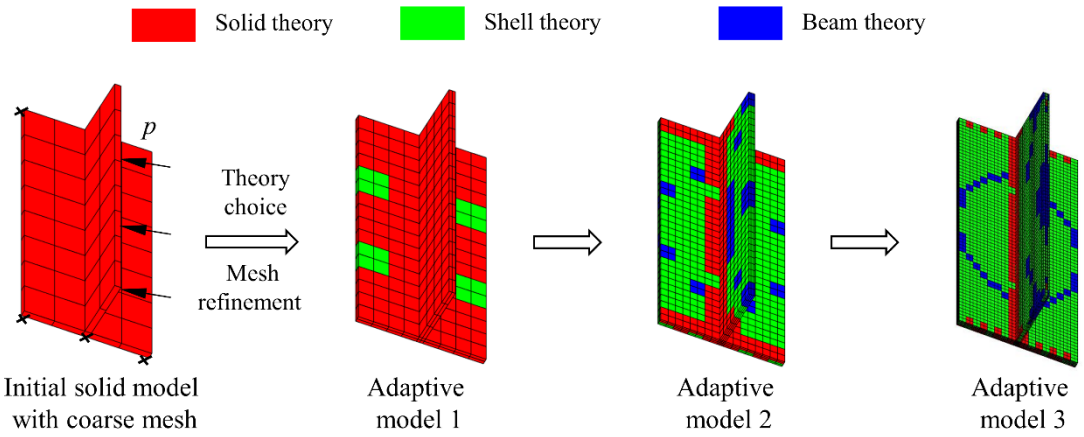

Fig. 4.17. "T" shape plates – Evolution of the theory choice during the iterative process.

4.8.2.3 Convergence of the methodology

The "T" shape plates assembly is discretized with the twenty-node hexahedral element C3D20 from Abaqus. From an initial coarse mesh, the adaptive modeling methodology is applied by taking into account the mesh refinement strategy described in Section 4.6.1. The convergence of the methodology is achieved when the strain energy indicator is less than 0.1% between two iterations of the adaptive modeling process. For "T" shape plates, Fig. 4.18 shows the values of the strain energy and the convergence criterion for an initial solid model with a coarse mesh and four successive adaptive models. The model 4 corresponds to the third adaptive model which meets the convergence criterion, it is the optimal model.

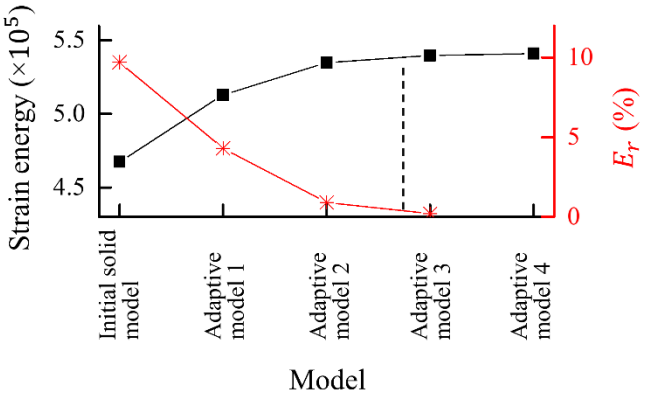

Fig. 4.18. "T" shape plates – Convergence of the methodology.

4.8.2.4 Finite element results of the optimal model

For "T" shape plates, the evaluation of finite element results of the optimal model obtained with the adaptive modeling process is presented here. Again, the reference model is a solid model that meets the convergence requirement. Fig. 4.19 illustrates a global comparison of displacement and von Mises stress distributions between the optimal model and reference solid model. These two models lead to close results, showing the adaptive modeling approach is very satisfactory for modeling the "T" shape plates assembly.

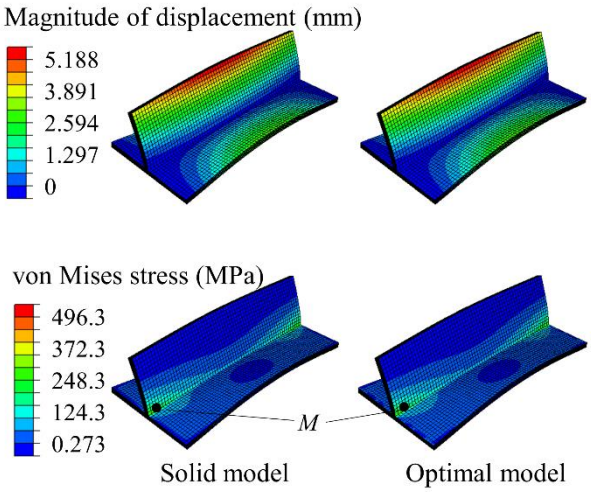

Fig. 4.19. "T" shape plates – Displacement and von Mises stress distributions for the optimal model and reference solid model.

Table 4.3 reports the errors on the maximum displacement and the maximum von Mises stress at point *M* (Fig. 4.19) by comparing the optimal model and the reference solid model. For this example, the error on displacement does not exceed 1% and the error on von Mises stress is close to 1%. These errors can be considered as small.

Table 4.3 "T" shape plates – Errors on maximum displacement and von Mises stress between the optimal model and reference solid model.

Maximum displacement (mm)			Maximum von Mises stress (MPa)		
Solid model	Optimal model	Error (%)	Solid model	Optimal model	Error (%)
5.188	5.146	0.8	305.1	301.8	1.1

The error distribution is now observed over the whole structure. Fig. 4.20 shows the error on displacement at each node and the error on von Mises stress at the center of each element by comparing the optimal and the reference solid models. The errors on displacement are always less than 0.8%. The global observation of errors on von Mises stress highlights almost all the values are smaller than 1%. However, some singularity in the boundary conditions area leads to local errors higher than 1.5%. Thus, the errors between the optimal and the reference solid models can be considered as small. The optimal model of "T" shape plates with a very predominant use of solid-shell approach remains very satisfactory.

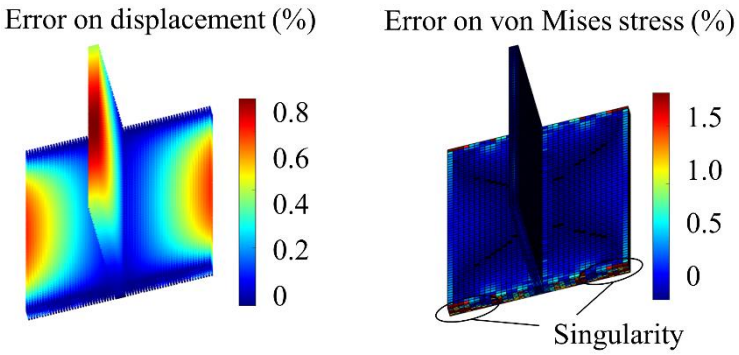

Fig. 4.20. "T" shape plates – Errors on displacement at each node and von Mises stress at the center of each element over the whole structure by comparing the optimal model and the reference solid model.

4.8.2.5 Computational cost

Compared with the reference solid model, the optimal model leads to a reduction of the number of degrees of freedom, which is interesting from a computational cost point of view. For this "T" shape plates example, the optimal model contains a large use of the solid-shell approach. The number of degrees of freedom and CPU time are reported in Table 4.4, the corresponding reduction and gain for the optimal model compared with the reference solid model are also given. All computational times are obtained with a PC i5-8265U @ 1.60GHz, 8GB RAM. In terms of number of DOFs, the gains are 2.5 and 3.1 for the adaptive models 3 and 4 respectively. And in terms of CPU time, the gains are 2.1 and 6.2 for the adaptive models 3 and 4 respectively. The adaptive modeling methodology leads to an optimal model for "T" shape plates with a significant reduction in problem size and computational cost.

Table 4.4 "T" shape plates – Number of degrees of freedom and CPU time for adaptive models and corresponding reference solid models.

No. of mesh	Type of model	Degrees of freedom		CPU time	
		value	gain	value (s)	gain
Mesh 4	Reference model	385731	2.5	133	2.1
	Adaptive model 3	156639		63.6	
Mesh 5	Reference model	2917635	3.1	3997.6	6.2
	Adaptive model 4	929159		640.4	

4.8.2.6 Adaptive modelling process with another solid element

The eight-node hexahedral element C3D8I [61] from Abaqus is used here to model "T" shape plates with the adaptive modeling process to prove its compatibility with another efficient solid element. For element C3D8I, the convergence study of the methodology is quite similar to that of element C3D20. The third adaptive model meets the convergence criterion and corresponds to the optimal model. For the element C3D8I, Fig. 4.21 shows the theory choices during the adaptive modeling process. As for the element C3D20, when convergence of the methodology is achieved, a predominant use of the solid-shell approach is obtained. The solid approach is selected in the boundary conditions areas and the junction between the two plates.

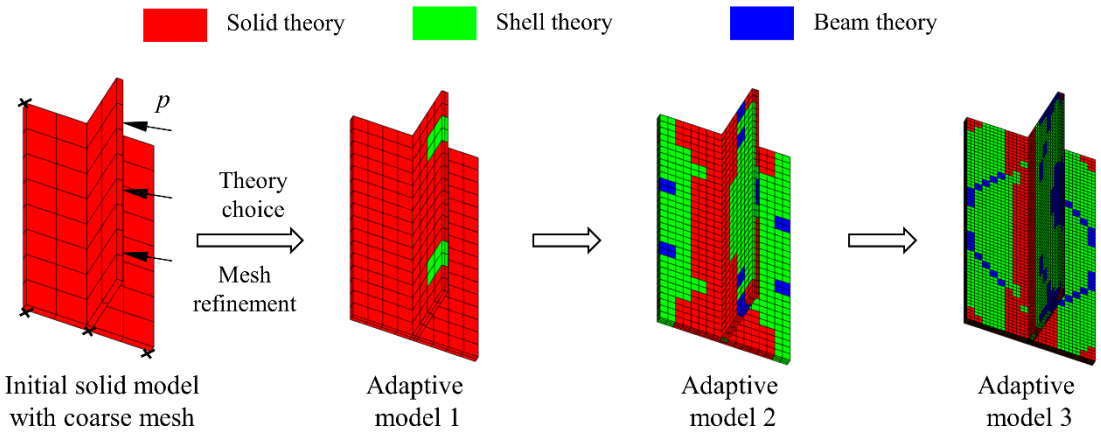

Fig. 4.21. "T" shape plates – Evolution of the choice of theory during the iterative process with the element C3D8I.

For the "T" shape plates example, displacement and von Mises stress distributions obtained with the optimal model and the reference solid model are reported in Fig. 4.22. These finite element results are quite similar, showing that the adaptive modeling approach is globally convincing.

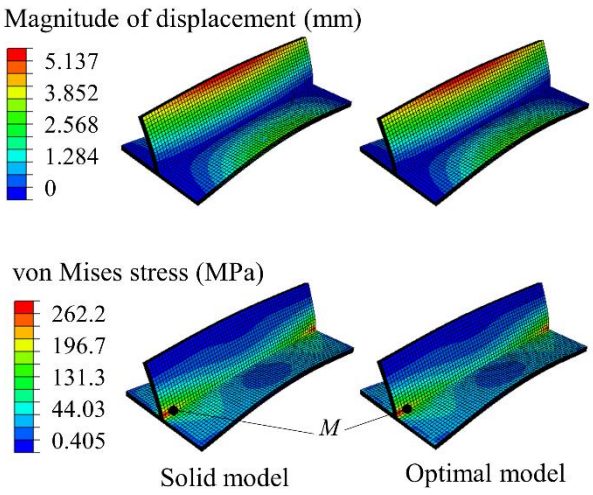

Fig. 4.22. "T" shape plates – Displacement and Von Mises stress distributions for the optimal model and reference solid model with the element C3D8I.

Table 4.5 "T" shape plates – Errors on maximum displacement and von Mises stress between the optimal model and reference solid model with the element C3D8I.

Maximum displacement (mm)			Maximum von Mises stress (MPa)		
Solid model	Optimal model	Error (%)	Solid model	Optimal model	Error (%)
5.137	5.118	0.4	259.9	262.2	0.9

Table 4.5 shows the errors on the maximum displacement and von Mises stress at point *M* (Fig. 4.22) with the element C3D8I. For this "T" shape plates example, the errors do not exceed 0.9%. Finally, in terms of problem size, the number of degrees of freedom are respectively equal to 58399 and 100035 for the optimal model and reference solid model, leading to a gain equal to 1.7 for "T" shape plates with the element C3D8I.

4.9 Vibration examples

The adaptive modeling methodology is now applied on the three structures described in Fig. 4.8 and on "T" shape plates illustrated in Fig. 4.16, in the context of free-free vibration analysis. For each mode, the theory choice is presented and a synthesis of these choices is made. The natural frequencies obtained with the optimal model and a reference solid model are compared. The reduction of the model size due to solid-shell and solid-beam approaches is discussed.

4.9.1 Beam to plate moderately thick structures with three width/thickness ratios

The three structures described in Fig. 4.8 are now studied in free-free vibration, with density equal to 7.89×10^{-9} t/mm^3. For the three cases, the structure is discretized with the twenty-node hexahedral element C3D20 from Abaqus. Concerning the theory choice criterion, the stress ratio parameter ρ and the weighting coefficient ω in Eq. (4.8) have been investigated for this free-free vibration example. According to some preliminary tests, relevant values for parameter ρ are comprised between 20 to 100. Here, taking the result accuracy as a primary goal and considering calculation efficiency, an optimal choice equals 20, 50 and 40 for cases 1, 2 and 3 respectively. For the weighting coefficient, n equal to 1 has been used in Eq. (4.8). The convergence of the methodology is achieved when the strain energy criterion described in Section 4.4 is met for each mode. The first seven modes are retained to evaluate the adaptive modeling process compared with a reference solid model for the cases 1, 2 and 3.

4.9.1.1 Case 1

The first case described in Fig. 4.8 is a beam-like structure with a square section. For a reference solid model, the first seven mode shapes are reported in Fig. 4.23. It is observed that modes 7, 8, 9, 10, 12 and 13 are bending modes, mode 11 is a torsion mode. On the contrary of other modes, this torsion mode corresponds to a state of stress dominated by shear stresses.

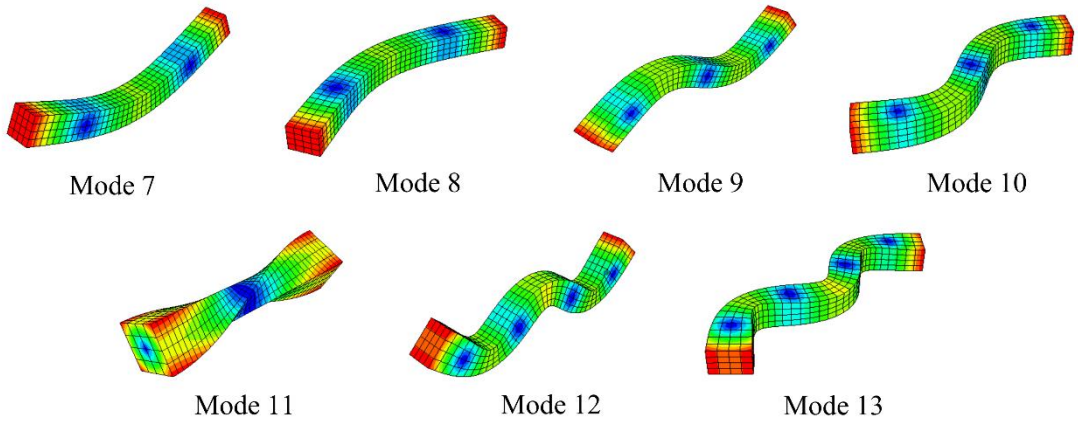

Fig. 4.23. Moderately thick structures – First seven mode shapes for a reference solid model in case 1.

During the process of adaptive modeling in case 1, the theory choice is applied for each mode except the torsion mode. The adaptive model retained will be assessed a posteriori for this torsion mode. From the initial solid model and with two iterations of the adaptive modeling process, Fig. 4.24 shows the theory choice for each mode. For the first modes, beam theory is chosen over the whole structure, but this is not true for higher modes. This is a hopeful characteristic of our adaptive modeling methodology which corresponds to a well-known physical phenomenon relative to the wavelength. Beam theory may be relevant for the first modes but higher modes require refined displacement fields throughout the cross-section. The synthesis of the theory choices leads to only one adaptive model at each iteration, as described in Fig. 4.24. The application of the theory choice criterion leads to large areas of the solid-

beam approach for case 1, but also a fairly large solid area. At the second iteration of the adaptive modeling, the bending modes 9 and 10 highlight a local choice corresponding to the shell theory, with orthogonal thickness directions one from the other. Indeed, for this beam-like structure with a square section, modes 9 and 10 are bending modes in two orthogonal planes. Consequently, for these modes a conservative choice is to use the solid approach. The same type of remark is made for bending modes 12 and 13. For mode 11 which is a torsion mode, we observe that the beam theory has been selected over the whole structure, even if two principal stresses are significant in this case. The convergence of the methodology is achieved for the adaptive model 2 corresponding to the optimal model.

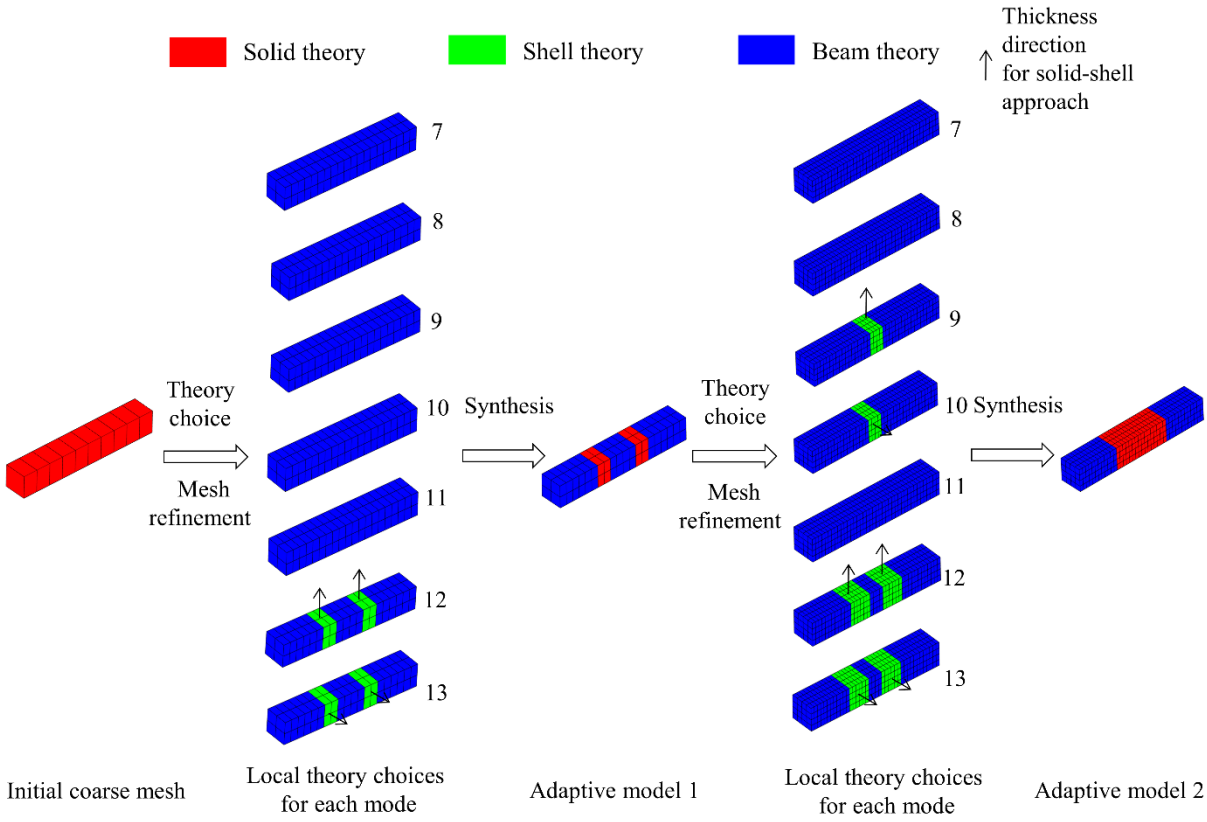

Fig. 4.24. Moderately thick structures – Theory choice for the first seven modes in case 1.

The natural frequencies obtained with the adaptive model are now investigated. The first seven natural frequencies are reported in Fig. 4.25 for the optimal model, the reference solid model, thick beam model (B31 element) and thin beam model (B33 element). The relative errors on natural frequencies between the optimal and reference solid models are calculated, the values are less than 0.5%. It can be noticed a good result is observed for the pure torsion mode (mode 11) because the displacement field used for the solid-beam approach is a 3D beam formulation. The optimal model obtained by the synthesis of theory choices leads to very satisfactory results for the first seven natural frequencies of the beam-like structure with a square section, even for the natural frequency corresponding to the torsion mode. The comparison with a thick beam element, which considers the transverse shear effects, shows that for the first modes all the models give similar results, however slight differences are observed for

higher modes 12 and 13. The comparison with a thin beam element shows more errors because the transverse shear effects has not been considered. These results highlight some discrepancies when beam theory is used.

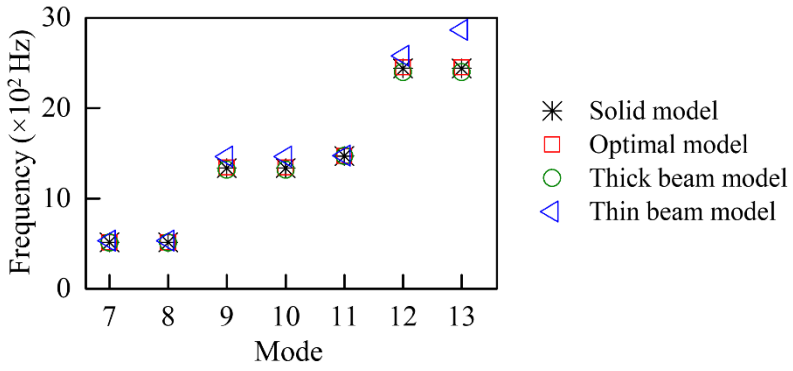

Fig. 4.25. Moderately thick structures – First seven natural frequencies for the beam models, optimal model and reference solid model in case 1.

In terms of problem size, the number of degrees of freedom are respectively equal to 5331 and 10995 for the optimal model and the reference solid model. Thanks to the adaptive modeling methodology, the gain of the number of DOFs is equal to 2.1 for the free-free vibration analysis in case 1. These gains may be increased or decreased depending on the number of modes considered in the adaptive modeling process.

4.9.1.2 Case 2

The second case described in Fig. 4.8 is an intermediate structure between cases 1 and 3. Fig. 4.26 shows the first seven mode shapes obtained with a reference solid model. Modes 7, 9, 10 and 12 are bending modes, mode 8 is a torsion mode, mode 11 combines bending and torsional effects, and mode 13 is a membrane mode.

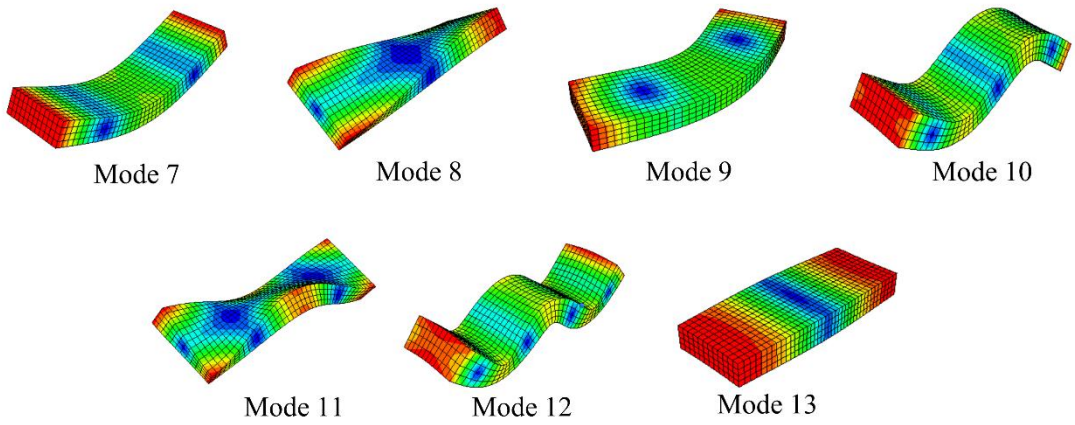

Fig. 4.26. Moderately thick structures – First seven mode shapes for a reference solid model in case 2.

From the initial solid model and two iterations of the adaptive modeling process, the theory choice criterion based on principal stresses is applied to case 2. For the first modes, beam theory or shell theory are chosen over the whole structure, but for higher modes solid theory is chosen in some areas. As for case 1, this is a hopeful characteristic of the adaptive modeling methodology. Fig. 4.27 shows the selected solid-beam, solid-shell or solid areas for modes 7 to 13. When convergence of the methodology is achieved, the synthesis theory choices of the second adaptive model leads to large areas of the solid-shell approach. Nevertheless, the solid theory is selected in the middle of the structure and the beam theory at the corners.

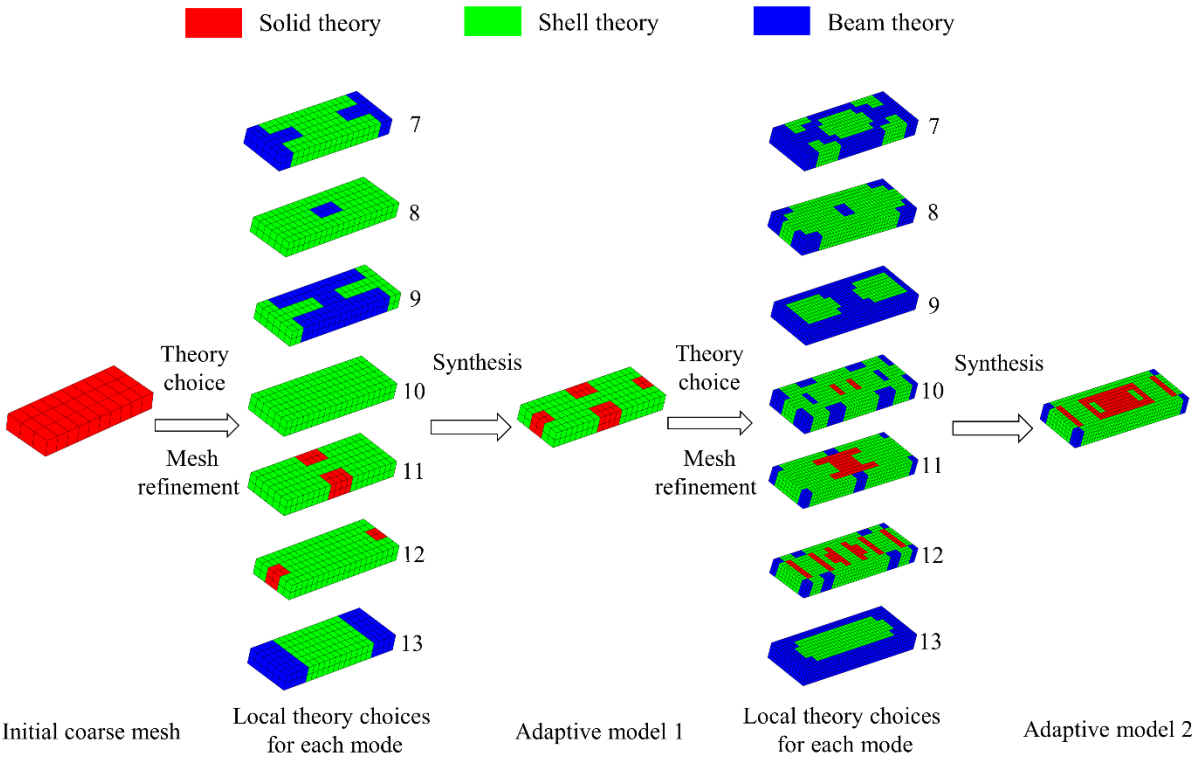

Fig. 4.27. Moderately thick structures – Theory choice for the first seven modes in case 2.

For the optimal model, the finite element results are now investigated. The first seven natural frequencies are reported in Fig. 4.28 for the optimal model and the reference solid model. The relative errors on natural frequencies are less than 0.5%. For case 2, the second choices synthesis leads to an optimal model composed of a predominant solid-shell approach with very satisfactory values of natural frequencies for the first seven modes.

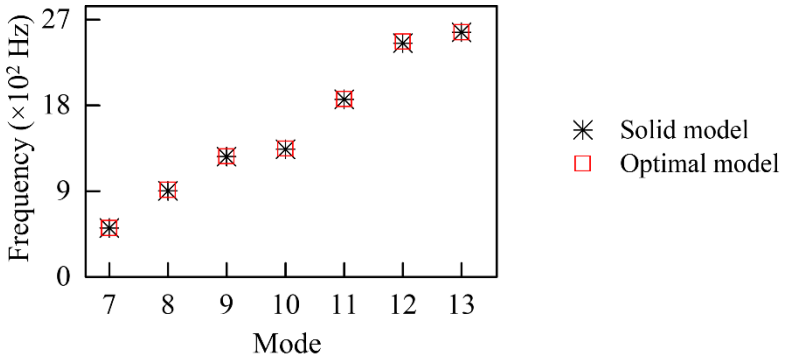

Fig. 4.28. Moderately thick structures – First seven natural frequencies for the optimal model and reference solid model in case 2.

The numbers of degrees of freedom are respectively equal to 18579 and 29571 for the optimal model and the reference solid model. The gain of the problem size reaches 1.6 thanks to the adaptive modeling methodology for the free-free vibration analysis in case 2.

4.9.1.3 Case 3

The third case described in Fig. 4.8 is a square plate-like structure. Fig. 4.29 shows the first seven mode shapes obtained with a reference solid model. Mode 7 is a torsion mode, modes 8, 9, 12 and 13 are bending modes, modes 10 and 11 combine bending and torsional effects.

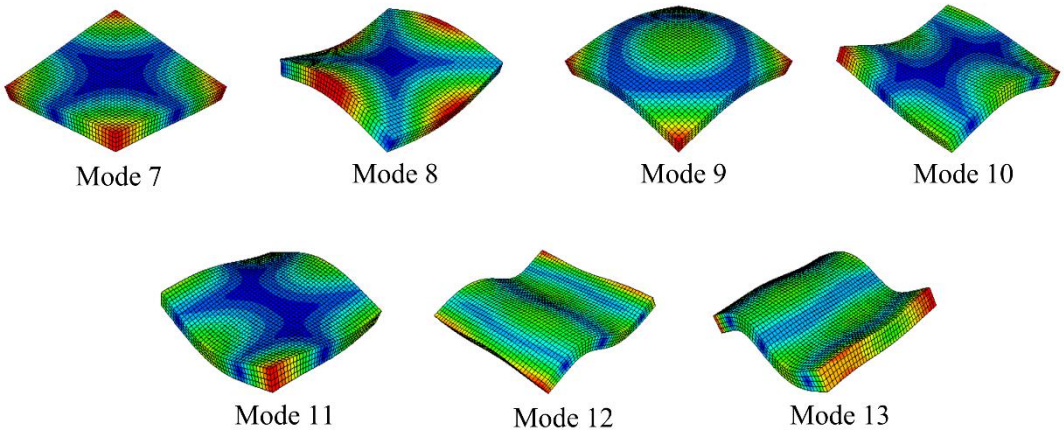

Fig. 4.29. Moderately thick structures – First seven mode shapes for a reference solid model in case 3.

For case 3, the adaptive modeling methodology is applied. For the first modes, shell theory is predominant over the whole structure, but for higher modes solid theory is chosen in some areas. Again,

this is a hopeful characteristic of the adaptive modeling methodology. Fig. 4.30 shows the selected solid-beam, solid-shell or solid areas for modes 7 to 13. After two iterations, the convergence of the methodology is achieved, leading to large areas of the solid-shell and solid approaches.

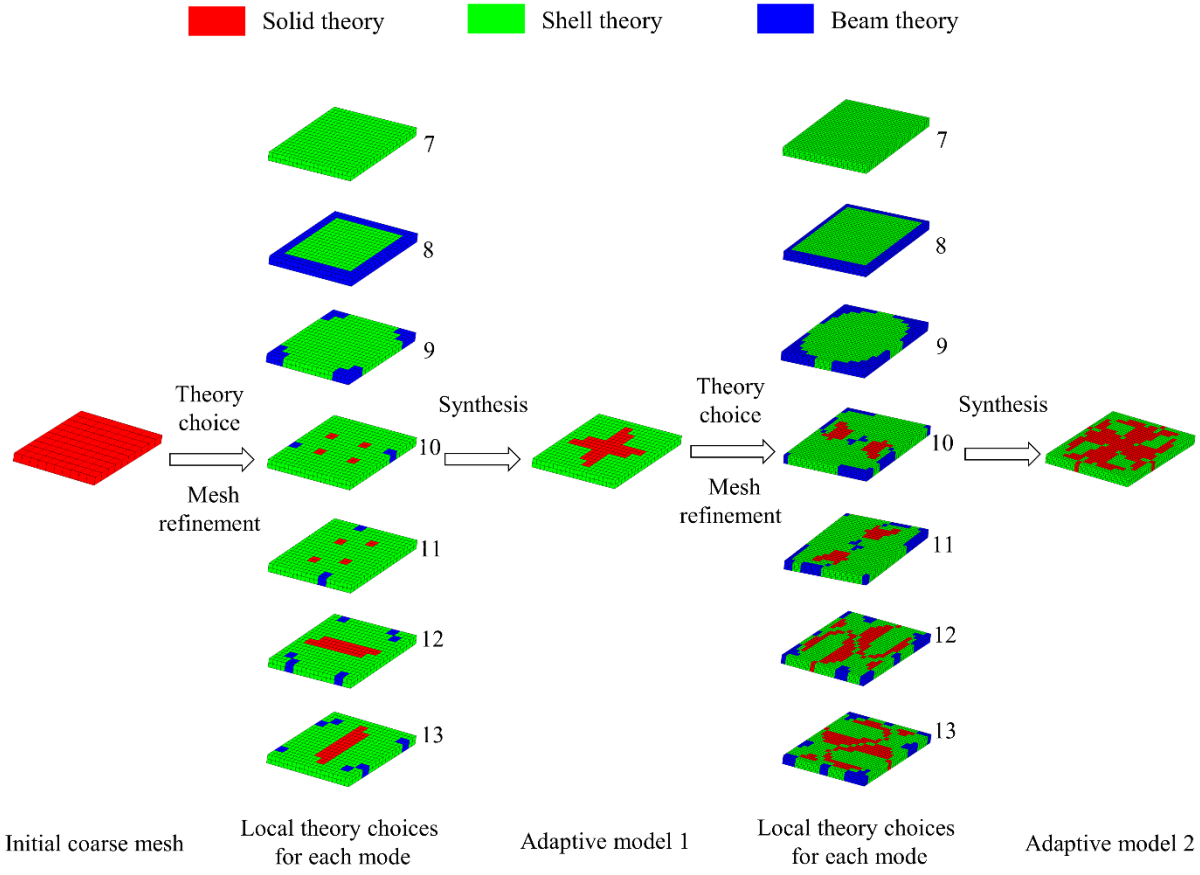

Fig. 4.30. Moderately thick structures – Theory choice for the first seven modes in case 3.

After the second synthesis of the theory choice, the first seven natural frequencies are calculated for the optimal model, shell model (S4R element) and the comparison with the reference solid model is reported in Fig. 4.31. It is observed the relative differences between the optimal and reference solid models are less than 0.5% for the first seven modes in case 3. Again, the results of the optimal model remain very satisfactory in the context of free-free vibration analysis. The comparison with a shell element, which considers the transverse shear effects, shows that for the first modes all the models give similar results, however very slight differences are observed for higher modes 12 and 13.

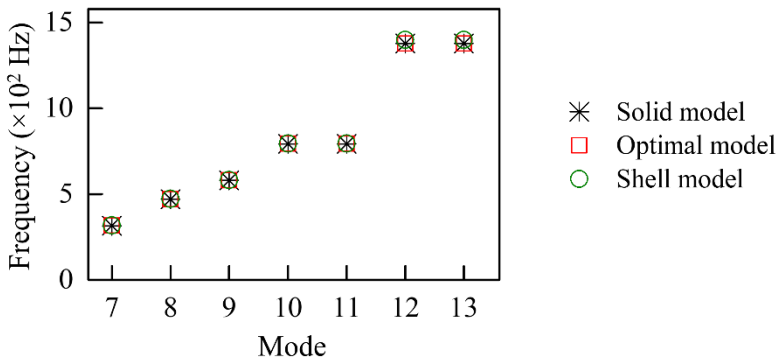

Fig. 4.31. Moderately thick structures – First seven natural frequencies for the shell model, optimal model and reference solid model in case 3.

The number of degrees of freedom are respectively equal to 71291 and 94587 for the optimal model and reference solid model, leading to a gain of the number of DOFs equal to 1.3. The optimal model in case 3 leads to a gain less than for cases 1 and 2, because the solid area is large for case 3.

4.9.2 "T" shape plates

The adaptive modeling methodology is applied here on "T" shape plates described in Fig. 4.16 in the context of free-free vibration analysis, with density equal to 7.89×10^{-9} t/mm^3. The structure is discretized with the twenty-node hexahedral element C3D20 from Abaqus. The first seven modes are studied, Fig. 4.32 illustrates mode shapes obtained with a reference solid model, they range from simple bending or torsional modes to more complex combined bending and torsional modes. For the choice criterion of theory, the value of n in Eq. (4.8) is equal to 0.5 and the stress ratio parameter ρ is equal to 100 for this example. The convergence of the methodology is achieved for each mode, the adaptive model 2 meets the convergence criterion.

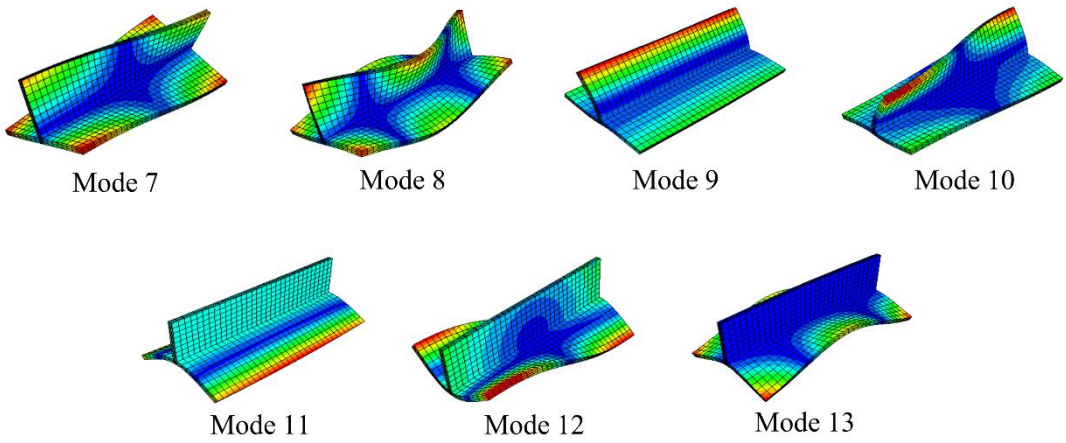

Fig. 4.32. "T" shape plates – First seven mode shapes for a reference solid model.

For the initial solid model and two iterations of the adaptive modeling process, Fig. 4.33 shows the selected solid-beam, solid-shell and solid areas for modes 7 to 13. The second synthesis of the theory

choices leads to a large solid-shell area and some solid area in the vicinity of the junction of the two plates.

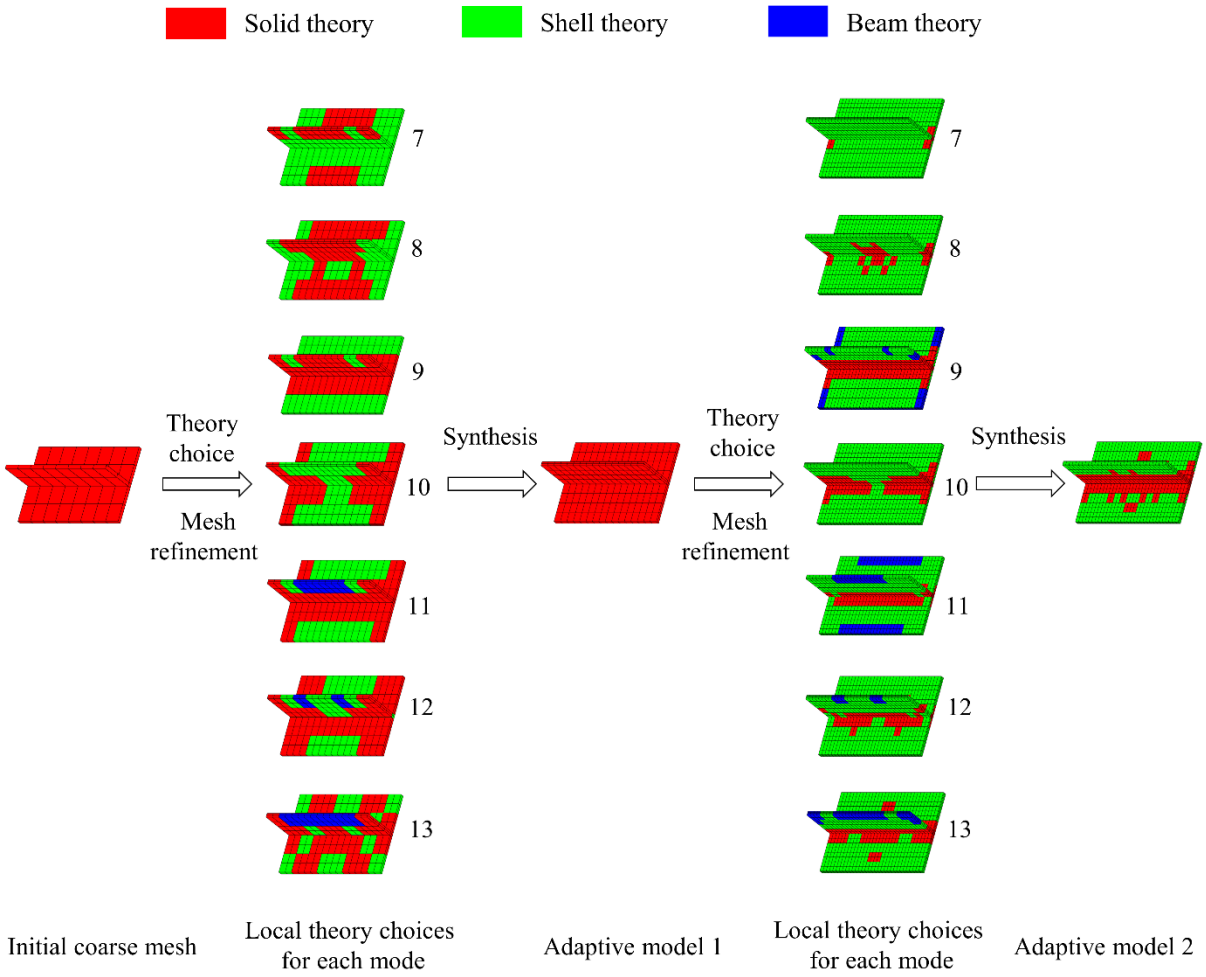

Fig. 4.33. "T" shape plates – Theory choice for the first seven modes.

The first seven natural frequencies are reported in Fig. 4.34 for the optimal model, shell model (S4R element) and the reference solid model. It is observed the relative differences between the optimal model and reference solid model are less than 0.5% for the first seven modes of "T" shape plates. In the context of free-free vibration analysis, the optimal model provides again very satisfactory results. The natural frequencies obtained with the shell model lead to slight differences for modes 9 to 13, compared with the reference solid model. In this example, a problem is highlighted due to the junction between two plates. The shell geometry is based on mid-surfaces, a local treatment is necessary to correctly connect the plates at the junction. This treatment involves some errors on the stiffness and on the mass of the structure. For example, in this "T" shape plates, the error on the mass is about 2%. In summary, a junction between two plates is better modeled with solid geometry, in particular, when the plates are thick.

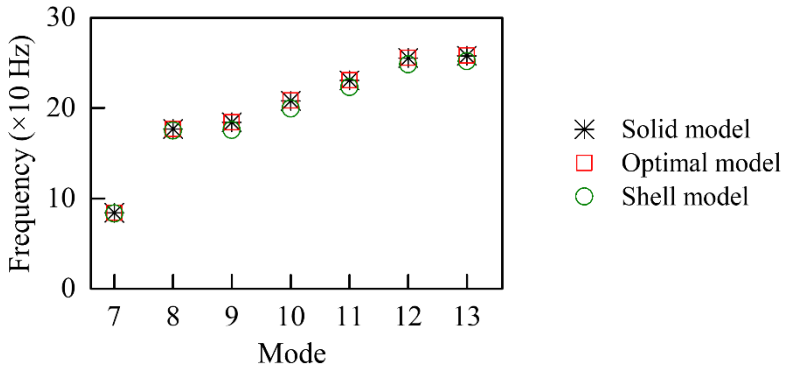

Fig. 4.34. "T" shape plates – First seven natural frequencies for the shell model, optimal model and reference solid model.

In terms of problem size, the number of degrees of freedom are respectively equal to 38075 and 53619 for the optimal model and reference solid model of the "T" shape plates. The gain of the number of DOFs is equal to 1.4. Compared with the cases 1 and 2 of the previous example, this reduction is less significant, essentially due to the fact that the vicinity of the junction between the two plates is modeled with solid approach.

4.10 Conclusions

In the context of linear static and vibration analysis, an original methodology of adaptive modeling has been proposed to lead to an optimal model from theory choice point of view in the different areas of the structure. The 3D geometry is discretized with solid elements. A criterion of theory choice based on principal stresses and weighted by strain energy is applied on each element. Depending on the stress state, the obtained optimal model possibly contains solid-beam, solid-shell and solid areas. The modified first-order displacement fields proposed in chapters 2 and 3 are applied at concerned nodes of the mesh when respectively solid-shell and solid-beam approaches are selected. For vibration analysis, a specific synthesis of theory choice is needed at each iteration of the process to define a single optimal model for all the modes studied. The convergence of the methodology is achieved when a strain energy criterion is met.

For three cantilever structures and a "T" shape plates assembly, this iterative process has been applied and has provided an optimal model in the context of static analysis. The obtained displacement and von Mises stress are very close to the results given by a reference solid model. The optimal model leads to a significant reduction of the number of degrees of freedom and an interesting CPU time gain. The reduction of the problem size depends on the number of elements corresponding to solid-beam and solid-shell approaches.

For three beam to plate moderately thick structures and a "T" shape plates assembly, the adaptive modeling methodology has led to an optimal model in the context of free-free vibration analysis. For

the first seven mode shapes of these structures, the natural frequencies of the optimal model are very satisfactory compared with a reference solid model. A significant gain in terms of the number of degrees of freedom is obtained. These gains may be increased or decreased depending on the number of modes considered in the adaptive modeling process.

In perspective, the methodology of adaptive modeling is a promising approach based on new displacement fields proposed in chapters 2 and 3. We can distinguish two types of perspectives, first on the one hand, different aspects of the methodology should be improved and from the other hand further applications are numerous. Concerning the theory choice criterion, the principal stresses work well but still can be optimized for some special situation, for example pure torsion of a beam, consequently the criterion should be improved. The stress ratio parameter plays an important role in this criterion and depends on the studied structure. The choice of this parameter could be identified in an automatic way, for example by using machine learning techniques. An error indicator could also be proposed to evaluate the theory choice. Currently, a global criterion is used to assess the convergence of the methodology, a local criterion could also be developed to better take into account local effects. As the methodology associates a solid mesh with beam theory or shell theory, the identification of the normal to cross-section for a beam and the thickness direction for a shell requires complementary research. An approach based on principal directions of the stress tensor has been proposed, but this issue needs new investigations for complex structures. Also, the mesh refinement uses a basic voxel technique and can be improved by coupling the iterative methodology with adaptive mesh technique. Finally, the extension of development and applications of the adaptive modeling are numerous, especially for composite structures.

Chapter 5

Conclusions and perspectives

5.1 Conclusions

An adaptive modeling methodology for the optimal finite element static and dynamic analysis of structures has been proposed. In the context of which, the present works have been focused on the local adaptive choice of appropriate theories. A new solid-shell approach and a new solid-beam approach are presented since only solid geometry, mesh, and element are preserved in this methodology. As far as the author knows, both the proposed new solid-shell or solid-beam approaches and the proposed adaptive local choice of appropriate theory are original.

A new and specific solid-shell approach dedicated to thin to very thick structures has been presented. The classical first-order Mindlin-Reissner theory, a modified first-order plate theory, and a higher-order plate theory have been considered for this approach. These three theories are based on kinematic relations, and the plate or shell displacement fields are directly imposed at the through-the-thickness nodes of solid model which contains several elements through the thickness. This leads to the first-order solid-shell (FOSS), modified first-order solid-shell (MFOSS), and higher-order solid-shell (HOSS) models respectively. The master and slave nodes technique is used. Linear equations based on displacement fields eliminate degrees of freedom of slave nodes, resulting in a reduction of model size. Consequently, the number of degrees of freedom eliminated corresponds exactly to the number of equations applied. In static examples, the FOSS model fails in both thin and thick plate or shell structures due to the Poisson thickness locking phenomenon. The MFOSS model gives a satisfactory performance in the thin cases but shows moderate errors in the thick ones. The through-the-thickness linear assumptions of the displacement components u and v cannot accurately reproduce reference results. The HOSS model shows excellent results both in the thin and thick structures compared with the reference solid model. In dynamics, the frequencies obtained by solid, HOSS, MFOSS, FOSS and shell models under different boundary conditions lead to conclusions similar to the static case. The FOSS model leads to bad results. The MFOSS model works well for thin structures but gives less precise results in the thick case, especially for higher-order modes. The HOSS model gives excellent frequencies in both thin and thick cases, compared with the solid approach. For the modal shapes, all the solid-shell models give results close to the reference. Moreover, the solid-shell models are efficient from a model size point of view thanks to the reduction of the number of degrees of freedom. From this point of view, the MFOSS model is comparable with that induced by the use of shell elements, and the HOSS model is intermediate between the shell model and the solid one.

Up to now, few solid-beam elements have been developed. For the new solid-beam approach, a beam in plane and a beam in space are presented separately. Similar to the solid-shell approach, the classical first-order Timoshenko theory, a modified first-order beam theory, and a higher-order beam theory are considered for a beam in plane. It leads to the first-order solid-beam (FOSB), modified first-order solid-beam (MFOSB), and higher-order solid-beam (HOSB) models respectively. These models take into account membrane, bending and transverse shear effects. For a beam in space, a modified first-order beam theory and a higher-order beam theory, which contain the torsion effect for rectangular cross-sections, are considered. This leads to the SB1-3D model and the SB2-3D model respectively. The implementation of this solid-beam approach is quite similar to the solid-shell approach, except that kinematic relations are imposed at the nodes throughout the cross-section for a beam instead of the nodes through the thickness for a shell. Static examples have been studied to verify the solid-beam approach for a beam in plane. The FOSB, MFOSB and HOSB models for beam structures give similar performances to the FOSS, MFOSS and HOSS models respectively for plate or shell structures described above. Two free-free vibration analyses allowed assessment to the performances of SB1-3D and SB2-3D models. Again, similar tendencies are observed to the MFOSS and HOSS models described above for the solid-shell approach. In terms of model size, the solid-beam models have considerable reduction compared with the reference solid model.

In the context of linear static and vibration analysis, an original methodology of adaptive modeling has been proposed to lead to an optimal model from a theory choice point of view in the different areas of the structure. The 3D geometry is discretized with the solid element. A criterion of theory choice based on principal stresses and weighted by strain energy is applied on each element. Depending on the thin, thick or solid 3D areas of the structure, the obtained optimal model possibly contains solid-beam, solid-shell and solid approaches. The modified first-order displacement fields proposed in chapters 2 and 3 are applied at the nodes of the mesh when respectively solid-shell and solid-beam approaches are selected. For vibration analysis, a specific synthesis of theory choice is needed at each iteration of the process to define only one optimal model for all the modes studied. The convergence of the methodology is achieved when a strain energy criterion is met. In the context of static analysis, the iterative process has been applied on three cantilever structures and "T" shape plates, leading to optimal models. The obtained displacements and von Mises stresses are very close to the reference results given by a reference solid model. In the context of free-free vibration analysis, the methodology of adaptive modeling has led to optimal models for three moderately thick structures and "T" shape plates. For the first seven mode shapes of these structures, the natural frequencies of the optimal model are very satisfactory compared with a reference solid model. The optimal model results in a significant reduction of the number of degrees of freedom and an interesting CPU time gain. The reduction of the problem size depends on the number of elements corresponding to solid-beam and solid-shell approaches.

The main characteristics and strengths of the overall adaptive modeling methodology are summarized as: (1) The proposed iterative process leads to an optimal model considering the local choice of appropriate theory. Beam, shell and solid theories can be used simultaneously in this optimal model. (2) Compared with the reference solid model, our optimal model achieves almost the same results with less computational cost due to the reduced number of degrees of freedom. (3) For the beam or shell areas of the optimal model, compared with the shell or beam approach (shell or beam models), no mid-surface or mid-axis geometries are required in our proposed approach, which leads to fewer difficulties concerning the link between Computer Aided Design (CAD) and Computer Aided Engineering (CAE). (4) For the beam or shell areas of the optimal model, compared with the solid-shell or solid-beam elements of the literatures, our method uses only standard solid elements, leading to more adaptabilities to commercial finite element software. (5) Moreover, the interfaces difficulties due to the different types of elements or different mesh refinements are also avoided. There are also some difficulties and shortcomings of the current version of our methodology. For example, the criterion of theory choice is limited and should be improved. The normal to cross-section for a beam and the thickness direction for a shell should be clearly identified for complex structures. The adaptive modeling method should be considered from an optimal mesh point of view.

5.2 Perspectives

Three original methods, including the new solid-shell, solid-beam approaches, and the adaptive modeling methodology, have been proposed. Thus, it gives a possibility to numerous perspectives.

- Other refined plate or shell theories can be applied in the solid-shell or solid-beam approach.
- An extension of the proposed solid-shell or solid-beam approach to multilayered composite structures is possible.
- Other cross-section shapes can be considered in the solid-beam approach.
- The criterion for theory choice has to be improved. A criterion based on principal stresses is not perfect and needs special treatment for some cases, namely pure torsion for a beam. The optimal stress ratio parameter of this criterion depends on the studied structure, the choice of this parameter could be identified by using machine learning techniques.
- An error indicator could also be proposed to evaluate the choice of theory.
- As the methodology associates a solid mesh with beam theory or shell theory, the identification of the normal to cross-section for a beam and the thickness direction for a shell requires further works. This aspect needs new investigations for complex structures.
- The refinement of the mesh uses a basic voxel technique and can be improved by coupling the iterative methodology with adaptive mesh technique.
- The adaptive modeling methodology has to be applied to more complex structures, in particular industrial examples.

References

[1] R. Courant, Variational methods for the solution of problems of equilibrium and vibrations, Bull. Amer. Math. Soc. 49 (1943) 1–23.

[2] J. H. Argyris, Energy Theorems and Structural Analysis: A Generalized Discourse with Applications on Energy Principles of Structural Analysis Including the Effects of Temperature and Non-Linear Stress-Strain Relations, Aircr. Eng. Aerosp. Technol. 26 (10) (1954) 347–356.

[3] M. J. Turner, R. W. Clough, H. C. Martin, L. J. Topp, Stiffness and deflection analysis of complex structures, Journal of the Aeronautical Sciences, 23 (9) (1956) 805–823.

[4] R. W. Clough, The finite element method in plane stress analysis, Proceedings of 2nd ASCE Conference on Electronic Computation, Pittsburgh, PA, 1960.

[5] A. Adini, R. W. Clough, Analysis of plate bending by the finite element method, University of California, 1960.

[6] O. C. Zienkiewicz, Y. K. Cheung, The Finite Element in Structural and Continuum Mechanics, McGraw-Hill publishing Coy Ltd, London, 1967.

[7] B. A. Szabo, G. C. Lee, Derivation of stiffness matrices for problems in plane elasticity by Galerkin's method, Int. J. Numer. Methods Eng. 1 (3) (1969) 301–310.

[8] Outline of the finite element analysis process: structural analysis. (2019 September 12). Retrieved October 1, 2020, from OpenLearn: https://www.open.edu/openlearn/science-maths-technology/introduction-finite-element-analysis/content-section-1.6

[9] I. Babuška, W. C. Rheinboldt, A-posteriori error estimates for the finite element method, Int. J. Numer. Methods Eng. 12 (10) (1978) 1597–1615.

[10] W. Graf, T. Y. Chang, A. F. Saleeb, On the numerical performance of three-dimensional thick shell elements using a hybrid/mixed formulation, Finite Elem. Anal. Des. 2 (1986) 357–375.

[11] J. Frischkorn, S. Reese, A solid-beam finite element and non-linear constitutive modelling, Comput. Methods Appl. Mech. Eng. 265 (2013) 195–212.

[12] P. J. Roache, Verification and validation in computational science and engineering, Hermosa, 1998.

[13] R. Scigliano, M. Scionti, P. Lardeur, Verification, validation and variability for the vibration study of a car windscreen modeled by finite elements, Finite Elem. Anal. Des. 47 (1) (2011) 17–29.

[14] P. Lardeur, R. Scigliano, M. Scionti, Verification and validation for the vibration study of automotive structures modelled by finite elements, J. Strain Anal. Eng. Des. 48 (1) (2013) 59–72.

[15] S. Germain, Recherches sur la théorie des structures élastiques, Paris, 1821.

[16] G. Kirchhoff, Über das gleichgewicht und die bewegung einer elastischen scheibe, Journal für reine und angewandte Mathematik 40 (1850) 51–88.

[17] A. E. H. Love, A treatise on the mathematical theory of elasticity, Cambridge University Press, Cambridge, 1906.

[18] E. Reissner, The effect of transverse shear deformation on the bending of elastic plates, J. Appl. Mech. 12 (1945) A69–A77.

[19] R. D. Mindlin, Influence of rotatory inertia and shear on flexural motion of isotropic elastic plates, J. Appl. Mech. 18 (1951) 31–38.

[20] P. M. Naghdi, On the theory of thin elastic shells, Quarterly of Applied mathematics 14 (1957) 369–380.

[21] E. Reissner, On transverse bending of plates, including the effect of transverse shear deformation, Int. J. Solids Struct. 11 (5) (1975) 569–573.

[22] K. H. Lo, R. M. Christensen, E. M. Wu, A high-order theory of plate deformation, Part 1: Homogeneous plates, J. Appl. Mech. 44 (1977) 663–668.

[23] K. H. Lo, R. M. Christensen, E. M. Wu, Stress solution determination for higher-order plate theory, Int. J. Solids Struct. 14 (1978) 655–662.

[24] T. Kant, Numerical analysis of thick plates, Comput. Methods Appl. Mech. Eng. 31 (1982) 1–18.

[25] L. W. Rehfield, R. R. Valisetty, A simple, refined theory for bending and stretching of homogeneous plates, AIAA Journal 22 (1) (1984) 90–95.

[26] M. Levinson, An accurate, simple theory of the statics and dynamics of elastic plates, Mech. Res. Commun. 7 (6) (1980) 343–350.

[27] J. N. Reddy, A refined nonlinear theory of plates with transverse shear deformation, Int. J. Solids Struct. 20 (1984) 88l–896.

[28] G. Z. Voyiadjis, M. H. Baluch, Refined theory for flexural motions of isotropic elastic plates, J. Sound Vib. 76 (1) (1981) 57–64.

[29] M. Levinson, A novel approach to thick plate theory suggested by studies in foundation theory, Int. J. Mech. Sci. 26 (1984) 427–436.

[30] S. Cen, Y. Shang, Developments of Mindlin-Reissner plate elements, Math. Probl. Eng. (2015) 1–12.

[31] O. C. Zienkiewicz, R. L. Taylor, J. M. Too, Reduced integration technique in general analysis of plates and shells, Int. J. Numer. Methods Eng. 3 (2) (1971) 275–290.

[32] S. F. Pawsey, R. W. Clough, Improved numerical integration of thick shell finite elements, Int. J. Numer. Methods Eng. 3 (4) (1971) 575–586.

[33] T. J. R. Hughes, R. L. Taylor, W. Kanoknukulchai, Simple and efficient finite element for plate bending, Int. J. Numer. Methods Eng. 11 (10) (1977) 1529–1543.

[34] T. J. R. Hughes, T. E. Tezduyar, Finite elements based upon Mindlin plate theory with particular reference to the four-node bilinear isoparametric element, J. Appl. Mech. – Trans. ASME 48 (3) (1981) 587–596.

[35] K. J. Bathe, E. N. Dvorkin, A formulation of general shell elements – the use of mixed interpolation of tensorial components, Int. J. Numer. Methods Eng. 22 (3) (1986) 697–722.

[36] K. U. Bletzinger, M. Bischoff, E. Ramm, A unified approach for shear-locking-free triangular and rectangular shell finite elements, Comput. Struct. 75 (3) (2000) 321–334.

[37] J. C. Simo, D. D. Fox, M. S. Rifai, On a stress resultant geometrically exact shell model Part 3: computational aspects of the non-linear theory. Comput. Methods Appl. Mech. Eng. 79 (1990) 91–126.

[38] J. L. Batoz, P. Lardeur, A discrete shear triangular nine D.O.F. element for the analysis of thick to very thin plates, Int. J. Numer. Methods Eng. 28 (3) (1989) 533–560.

[39] R. L. Spilker, N. I. Munir, A hybrid-stress quadratic serendipity displacement Mindlin plate bending element, Comput. Struct. 12 (1) (1980) 11–21.

[40] S. W. Lee, T. H. H. Pian, Improvement of plate and shell finite elements by mixed formulations, AIAA Journal, 16 (1) (1978) 29–34.

[41] T. Belytschko, C. S. Tsay, W. K. Liu, A stabilization matrix for the bilinear Mindlin plate element, Comput. Methods Appl. Mech. Eng. 29 (3) 1981 313–327.

[42] I. Katili, J. L. Batoz, I. J. Maknun, P. Lardeur, A comparative formulation of DKMQ, DSQ and MITC4 quadrilateral plate elements with new numerical results based on s-norm tests, Comput. Struct. 204 (2018) 48–64.

[43] T. Kant, D. R. J. Owen, O. C. Zienkiewicz, A refined higher-order C° plate bending element, Comput. Struct. 15 (2) (1982) 177–183.

[44] G. Z. Voyiadjis, R. W. Pecquet, Isotropic plate elements with shear and normal strain deformations, Int. J. Numer. Methods Eng. 24 (1987) 1671–1695.

[45] A. Tessler, A higher-order plate theory with ideal finite element suitability, Comput. Methods Appl. Mech. Eng. 85 (1991) 183–205.

[46] S. Ahmad, B. M. Irons, O. C. Zienkiewicz, Analysis of thick and thin shell structures by curved finite elements, Int. J. Numer. Methods Eng. 2 (1970) 419–451.

[47] M. F. Ausserer, S. W. Lee, An eighteen-node solid element for thin shell analysis, Int. J. Numer. Methods Eng. 26 (1988) 1345–1364.

[48] H. Parisch, A continuum-based shell theory for non-linear applications, Int. J. Numer. Methods Eng. 38 (1995) 1855–1883.

[49] R. Hauptmann, K. Schweizerhof, A systematic development of solid shell element formulations for linear and nonlinear analysis employing only displacement degrees of freedom, Int. J. Numer. Methods Eng. 42 (1998) 49–69.

[50] K. Y. Sze, L. Q. Yao, Hybrid stress ANS solid-shell element and its generalization for smart structure modelling. Part I – solid-shell element formulation, Int. J. Numer. Methods Eng. 48 (2000) 545–564.

[51] F. Abed-Meraim, A. Combescure, SHB8PS - a new adaptive, assumed-strain continuum mechanics shell element for impact analysis, Comput. Struct. 80 (2002) 791–803.

[52] F. Abed-Meraim, A. Combescure, An improved assumed strain solid–shell element formulation with physical stabilization for geometric non-linear applications and elastic–plastic stability analysis, Int. J. Numer. Methods Eng. 80 (2009) 1640–1686.

[53] M. Schwarze, S. Reese, A reduced integration solid-shell finite element based on the EAS and the ANS concept—Geometrically linear problems, Int. J. Numer. Methods Eng. 80 (2009) 1322–1355.

[54] H. Naceur, S. Shiri, D. Coutellier, J. L. Batoz, On the modeling and design of composite multilayered structures using solid-shell finite element model, Finite Elem. Anal. Des. 70 (2013) 1–14.

[55] A. Ben Bettaieb, J. Velosa de Sena, R. J. Alves de Sousa, R. A. F. Valente, A. M. Habraken, L. Duchêne, On the comparison of two solid-shell formulations based on in-plane reduced and full integration schemes in linear and non-linear applications, Finite Elem. Anal. Des. 107 (2015) 44–59.

[56] D. Bishara, M. Jabareen, Does the classical solid-shell element with the assumed natural strain method satisfy the three-dimensional patch test for arbitrary geometry? Finite Elem. Anal. Des. 168 (2020) 103331.

[57] K. Y. Sze, S. Yi, M. H. Tay, An explicit hybrid stabilized eighteen-node solid element for thin shell analysis, Int. J. Numer. Methods Eng. 40 (1997) 1839–1856.

[58] B. Bassa, F. Sabourin, M. Brunet, A new nine-node solid-shell finite element using complete 3D constitutive laws, Int. J. Numer. Methods Eng. 92 (2012) 589–636.

[59] F. Abed-Meraim, V. D. Trinh, A. Combescure, New quadratic solid-shell elements and their evaluation on linear benchmark problems, Computing 95 (5) (2013) 373–394.

[60] P. Wang, H. Chalal, F. Abed-Meraim, Quadratic prismatic and hexahedral solid–shell elements for geometric nonlinear analysis of laminated composite structures, Composite Structures 172 (2017) 282–296.

[61] Abaqus Analysis User's Guide, Abaqus 6.14, Dassault Systèmes Simulia, 2014.

[62] J. C. Simo, M. S. Rifai, A class of assumed strain methods and the method of incompatible modes, Int. J. Numer. Methods Eng. 29 (1990) 1595–1638.

[63] K. M. Liew, Y. Xiang, S. Kitipornchai, Transverse vibration of thick rectangular plates-I. comprehensive sets of boundary conditions, Comput. Struct. 49 (1993) 1–29.

[64] R. Li, X. Zheng, Y. Yang, M. Huang, X. Huang, Hamiltonian system-based new analytic free vibration solutions of cylindrical shell panels, Appl. Math. Model. 76 (2019) 900–917.

[65] W. A. Oldfather, C. A. Ellis, D. M. Brown, Leonhard Euler' s elastic curves, Isis, 20 (1) (1933) 72–160.

[66] S. P. Timoshenko, On the corrections for shear of the differential equation for transverse vibrations of prismatic bars, Philos. Mag. 41 (1921) 744–746.

[67] S. P. Timoshenko, On the transverse vibrations of bars of uniform cross section, Philos. Mag. 43 (1922) 125–131.

[68] G. R. Cowper, The shear coefficient in Timoshenko's beam theory, J. Appl. Mech. 33 (2) (1966) 335–340.

[69] J. J. Jensen, On the shear coefficient in Timoshenko's beam theory, J. Sound Vib. 87 (4) (1983) 621–635.

[70] J. R. Hutchinson, Shear coefficients for Timoshenko beam theory, J. Appl. Mech. 68 (1) (2001) 87–92.

[71] F. Essenburg, On the significance of the inclusion of the effect of transverse normal strain in problems involving beams with surface constraints, J. Appl. Mech. 42 (1) (1975) 127–132.

[72] N. G. Stephen, M. Levinson, A second order beam theory, J. Sound Vib. 67 (3) (1979) 293–305.

[73] M. Levinson, A new rectangular beam theory, J. Sound Vib. 74 (1) (1981) 81–87.

[74] L. W. Rehfield, P. L. N. Murthy, Toward a new engineering theory of bending: Fundamentals, AIAA J. 20 (5) (1982) 693–699.

[75] A. B. de Saint-Venant, Mémoire sur la torsion des prismes, Mémoires Des Savants Etrangers, 14 (1855) 233–560.

[76] V. Z. Vlasov, Thin walled elastic beams. Israel Program for Scientific Translations, Jerusalem, 1961.

[77] S. U. Benscoter, A theory of torsion bending for multicell beams, J. appl. Mech. 21 (1954) 25–34.

[78] H. Shakourzadeh, Y. Q. Guo, J. L. Batoz, A torsion bending element for thin-walled beams with open and closed cross sections, Comput. Struct. 55 (6) (1995) 1045–1054.

[79] R. Schardt, Generalized beam theory – an adequate method for coupled stability problems, Thin-Walled Struct. 19 (2–4) (1994) 161–180.

[80] A. K. Habtemariam, C. Könke, V. Zabel, M. J. Bianco, Generalized Beam Theory formulation for thin-walled pipes with circular axis, Thin-Walled Struct. 159 (2021) 107243.

[81] R. El Fatmi, A refined 1D beam theory built on 3D Saint-Venant's solution to compute homogeneous and composite beams, J. Mech. Mater. Struct. 11 (4) (2016) 345–378.

[82] F. Naccache, R. El Fatmi, Numerical free vibration analysis of homogeneous or composite beam using a refined beam theory built on Saint Venant's solution, Comput. Struct. 210 (2018) 102–121.

[83] P. Ladevèze, J. Simmonds, New concepts for linear beam theory with arbitrary geometry and loading, Eur. J. Mech. A Solids 17 (3) (1998) 377–402.

[84] G. Romano, A. Barretta, R. Barretta, On torsion and shear of Saint-Venant beams, Eur. J. Mech. A Solids 35 (2012) 47–60.

[85] S. A. Faghidian, Unified formulation of the stress field of Saint-Venant's flexure problem for symmetric cross-sections, Int. J. Mech. Sci. 111–112 (2016) 65–72.

[86] J. N. Goodier, S. P. Timoshenko, Theory of Elasticity, McGraw-Hill, NY, 1970.

[87] E. Carrera, G. Giunta, M. Petrolo, Beam structures, classical and advanced theories, John Willey & Sons Inc., NY, 2011.

[88] G. Prathap, G. R. Bhashyam, Reduced integration and the shear-flexible beam element, Int. J. Numer. Methods Eng. 18 (2) (1982) 195-210.

[89] J. N. Reddy, On locking-free shear deformable beam finite elements, Comput. Methods Appl. Mech. Eng. 149 (1–4) (1997) 113–132.

[90] R. Bouclier, T. Elguedj, A. Combescure, Locking free isogeometric formulations of curved thick beams, Comput. Methods Appl. Mech. Eng. 245–246 (2012) 144–162.

[91] C. Adam, S. Bouabdallah, M. Zarroug, H. Maitournam, Improved numerical integration for locking treatment in isogeometric structural elements, Part I: Beams, Comput. Methods Appl. Mech. Eng. 279 (2014) 1–28.

[92] D. Addessi, P. Di Re, G. Cimarello, Enriched beam finite element models with torsion and shear warping for the analysis of thin-walled structures, Thin-Walled Struct. 159 (2021) 107259.

[93] L. Yunhua, Explanation and elimination of shear locking and membrane locking with field consistence approach, Comput. Methods Appl. Mech. Eng. 162 (1–4) (1998) 249–269.

[94] M. Ziyaeifar, H. Noguchi, A refined model for beam elements and beam-column joints, Comput. Struct. 76 (4) (2000) 551–564.

[95] S. W. Lee, Y. H. Kim, A new approach to the finite element modelling of beams with warping effect, Int. J. Numer. Methods Eng. 24 (12) (1987) 2327–2341.

[96] M. Zivkovic, M. Kojic, R. Slavkovic, N. Grujovic, A general beam finite element with deformable cross-section, Comput. Methods Appl. Mech. Eng. 190 (20–21) (2001), 2651–2680.

[97] J. L. Curiel Sosa, A. J. Gil, Analysis of a continuum-based beam element in the framework of explicit-FEM, Finite Elem. Anal. Des. 45 (8-9) (2009) 583–591.

[98] T. Belytschko, W. K. Liu, B. Moran, Nonlinear finite elements for continua and structures, John Wiley & Sons, Ltd, Chichester, 2000.

[99] K. Yoon, Y. Lee, P. S. Lee, A continuum mechanics based 3-D beam finite element with warping displacements and its modeling capabilities, Struct. Eng. Mech. 43 (4) (2012) 411−437.

[100] K. Yoon, P. S. Lee, Nonlinear performance of continuum mechanics based beam elements focusing on large twisting behaviors, Comput. Methods Appl. Mech. Eng. 281 (2014) 106–130.

[101] M. Schwarze, S. Reese, A reduced integration solid-shell finite element based on the EAS and the ANS concept–large deformation problems, Int. J. Numer. Methods Eng. 85 (3) (2011) 289–329.

[102] J. Frischkorn, S. Reese, Solid-beam finite element analysis of nitinol stents, Comput. Methods Appl. Mech. Eng. 291 (2015) 42–63.

[103] I. The MathWorks, Curve Fitting Toolbox, Natick, Massachusetts, United State, 2020. https://www.mathworks.com/products/curvefitting.html.

[104] M. J. Berger, J. Oliger, Adaptive mesh refinement for hyperbolic partial differential equations, J. Comput. Phys. 53 (1984) 484–512.

[105] M. C. Rivara, Selective refinement/derefinement algorithms for sequences of nested triangulations, Int. J. Numer. Methods Eng. 28 (1989) 2889–2906.

[106] A. Rassineux, 3D mesh adaptation. Optimization of tetrahedral meshes by advancing front technique, Comput. Methods Appl. Mech. Eng. 141 (1997) 335–354.

[107] C. Zienkiewicz, J. Z. Zhu, A simple error estimator and adaptive procedure for practical engineering analysis, Int. J. Numer. Methods Eng. 24 (1987) 337–357.

[108] P. Ladeveze, J. P. Pelle, P. Rougeot, Error estimation and mesh optimization for classical finite elements, Eng. Comput. 8 (1991) 69–80.

[109] J. Hoschek, Offset curves in the plane, Comput. Des. 17 (1985) 77–82.
[110] S. Aomura, T. Uehara, Self-intersection of an offset surface, Comput. Des. 22 (1990) 417–421.
[111] T. Maekawa, Overview of offset curves and surfaces, Comput. Des. 31 (1999) 165–173.
[112] P. Lardeur, Presentation of a linear or nonlinear analysis method for multilayered composite plates and shells with edge effects influence, in: C. Hirsch (Ed.), Numer. Methods Eng., Elsevier Science Publisher B.V., 1992: pp. 637–644.
[113] R. Krueger, T. K. O. Brien, A shell / 3D modeling technique for the analysis of delaminated composite laminates, Compos. Part A. 32 (2001) 25–44.
[114] Z. Tonkovic, A. Rodic, M. Surjak, I. Garašic, Numerical analysis and experimental investigation of welding residual stresses and distortions in a T-joint fillet weld, Mater. Des. 53 (2014) 1052–1063.
[115] W. Dou, L. Zhang, G. Chen, S. Stichel, A boundary-condition-transfer method for shell-to-solid submodeling and its application in high-speed trains, Int. J. Mech. Sci. 177 (2020) 105542.
[116] H. J. Kim, C. C. Swan, Voxel-based meshing and unit-cell analysis of textile composites, Int. J. Numer. Methods Eng. 56 (2003) 977–1006.
[117] Z. L. Wang, J. C. M. Teo, C. K. Chui, S. H. Ong, C. H. Yan, S. C. Wang, H. K. Wong, S. H. Teoh, Computational biomechanical modelling of the lumbar spine using marching-cubes surface smoothened finite element voxel meshing, Comput. Methods Programs Biomed. 80 (2005) 25–35.
[118] J. M. Gere, B. J. Goodno, Mechanics of Materials, 7th ed., Stamford, CA, 2009.
[119] K. Wang, The calculation formulae of direction cosines for principal stresses, Mech. Eng. 37 (2015) 378–380.
[120] O. C. Zienkiewicz, R. L. Taylor, The finite element method, McGraw-Hill Book Company, NY, 1989.
[121] L. Lapidus, G. F. Pinder, Numerical solution of partial differential equations in science and engineering, John Wiley & Sons, NY, 1999.
[122] E. L. Wilson, R. L. Taylor, W. P. Doherty, J. Ghaboussi, Incompatible displacement models. In Numerical and computer methods in structural mechanics, Academic Press., MA, 1973.
[123] A. Ibrahimbegovic, E. L. Wilson, Modified method of incompatible modes, Commun. Appl. Numer. Methods. 7 (1991) 187–194.